LEABHARLANN CHOLÁISTE NA TRÍONÓIDE, BAILE ÁTHA CLIATH | TRINITY COLLEGE LIBRARY DUBLIN
Ollscoil Átha Cliath | The University of Dublin

Terms and Conditions of Use of Digitised Theses from Trinity College Library Dublin

Copyright statement

All material supplied by Trinity College Library is protected by copyright (under the Copyright and Related Rights Act, 2000 as amended) and other relevant Intellectual Property Rights. By accessing and using a Digitised Thesis from Trinity College Library you acknowledge that all Intellectual Property Rights in any Works supplied are the sole and exclusive property of the copyright and/or other IPR holder. Specific copyright holders may not be explicitly identified. Use of materials from other sources within a thesis should not be construed as a claim over them.

A non-exclusive, non-transferable licence is hereby granted to those using or reproducing, in whole or in part, the material for valid purposes, providing the copyright owners are acknowledged using the normal conventions. Where specific permission to use material is required, this is identified and such permission must be sought from the copyright holder or agency cited.

Liability statement

By using a Digitised Thesis, I accept that Trinity College Dublin bears no legal responsibility for the accuracy, legality or comprehensiveness of materials contained within the thesis, and that Trinity College Dublin accepts no liability for indirect, consequential, or incidental, damages or losses arising from use of the thesis for whatever reason. Information located in a thesis may be subject to specific use constraints, details of which may not be explicitly described. It is the responsibility of potential and actual users to be aware of such constraints and to abide by them. By making use of material from a digitised thesis, you accept these copyright and disclaimer provisions. Where it is brought to the attention of Trinity College Library that there may be a breach of copyright or other restraint, it is the policy to withdraw or take down access to a thesis while the issue is being resolved.

Access Agreement

By using a Digitised Thesis from Trinity College Library you are bound by the following Terms & Conditions. Please read them carefully.

I have read and I understand the following statement: All material supplied via a Digitised Thesis from Trinity College Library is protected by copyright and other intellectual property rights, and duplication or sale of all or part of any of a thesis is not permitted, except that material may be duplicated by you for your research use or for educational purposes in electronic or print form providing the copyright owners are acknowledged using the normal conventions. You must obtain permission for any other use. Electronic or print copies may not be offered, whether for sale or otherwise to anyone. This copy has been supplied on the understanding that it is copyright material and that no quotation from the thesis may be published without proper acknowledgement.

Spin-Dependent Transport
in
Multifunctional Tunnel Junctions

by

Nuala Mai Caffrey

A thesis submitted for the degree of
Doctor of Philosophy

School of Physics
Trinity College Dublin

2012

Declaration

I, Nuala Mai Caffrey, hereby declare that this dissertation has not been submitted as an exercise for a degree at this or any other University.

It comprises work performed entirely by myself during the course of my Ph.D. studies at Trinity College Dublin. I was involved in a number of collaborations, and where it is appropriate my collaborators are acknowledged for their contributions.

A copy of this thesis may be lended or copied by the Trinity College Library upon request by a third party provided it spans single copies made for study purposes only, subject to normal conditions of acknowledgement.

Abstract

Spin-dependent tunnelling between ferromagnetic electrodes separated by insulating oxide barriers has long attracted scientific and commercial interest. In the last decade it became evident that the insulating layer was more than just a simple barrier through which electrons tunnel. It is wave-function symmetry selective, making the tunnelling process sensitive to its electronic structure. The understanding of such a concept suggests that one can engineer the transport properties of a tunnel junction by carefully selecting the insulating barrier and the metallic electrodes. Ferroelectric materials are of particular interest as barriers due to additional functionality offered by the electric polarisation. Indeed, the inclusion of a ferroelectric barrier in a ferromagnetic tunnel junction is predicted to become the basis for a novel resistive based memory.

Density functional theory (DFT) has emerged as one of the most powerful methods for computing the ground state properties of many-body systems. Here, the structural and electronic properties are determined using the SIESTA implementation of DFT. The transport properties are then studied using the non-equilibrium Green's function formalism as implemented in the SMEAGOL code.

We first investigate the properties of a multifunctional tunnel junction combining two materials with different ferroic states (ferromagnetic and ferroelectric). This has the prospect of enabling one to actively manipulate the tunnelling current with both external magnetic and electric fields. We demonstrate massive tunnelling magnetoresistance (TMR) in a $SrRuO_3/BaTiO_3/SrRuO_3$ junction. We also consider the implications of introducing structural asymmetry into this junction by using a thin layer of dielectric material at one interface. In such a junction we demonstrate a sizable tunnelling electroresistance (TER) that increases with the thickness of the dielectric layer.

The choice of barrier similarly plays an important role in spin-photodiodes where circularly polarised light is converted into a spin-polarised electrical signal. We show that by the careful choice of insulating barrier and ferromagnetic electrode, the photocurrent spin polarisation in such a device can be manipulated. We explain the high spin-filtering asymmetry that has been experimentally achieved in a Fe/MgO/Ge tunnel junction based on an analysis of the electronic band structure of Ge and the spin filtering effect of the Fe/MgO interface.

Further functionality can be introduced into a tunnel junction by using a ferromagnetic insulator as a barrier. The exchange split electronic states of the magnetic barrier will yield different tunnelling barrier heights for spin up and spin down electrons. As a result, electrons will be transmitted differently depending on their spin. We investigate how the complex band structure of the insulating spinel ferrites could influence transport in such a junction.

Acknowledgements

"I not only use all the brains I have, but all I can borrow"

Woodrow Wilson

Undoubtedly, this thesis would not have been possible without the support and encouragement of a great number of people.

First and foremost, I would like to take this opportunity to extend a sincere thanks to my supervisor, Prof. Stefano Sanvito. His enthusiasm and energy made working within his group a pleasure and his encouragement and guidance were invaluable throughout the last four years. His detailed corrections of various versions of this thesis, to the extent of putting in missing commas, was very much appreciated. This attention to detail was evident in all areas of his supervision, and for that I am indebted.

I would like to thank all the postgrads and postdocs who make the 'Computational Spintronics' group what it is. The group is now too large to thank everyone individually but it has been a pleasure to work with all of you. There are, however, a few people whose contribution was vital to the work presented in this thesis: Dr. Thomas Archer and Dr. Ivan Rungger; thank you for all your help, guidance and suggestions. A special thanks must also go to the CRANN cohort of the group. Mauro, Sankar, Aaron, Nadjib, Igor and Xihua - thanks for being such terrific office mates.

I am grateful to Prof. Nicola Spaldin and her group for hosting me in UC Santa Barbara for six weeks before I had technically begun my PhD, and for the opportunity it offered me to learn about multiferroic materials from one of the leaders in the field.

The calculations presented in this thesis were performed in the Trinity Centre for High Performance Computing (TCHPC) and the Irish Centre for High End Computing. I wish to also thank TCHPC for computer administration and technical assistance. In addition, many thanks to Stefania, for booking flights and accommodation and for dealing with paperwork I probably never even saw. None of the research presented here could have been possible without the assistance of the Science Foundation of Ireland (grant number 07/IN.1/I945 - Quantum Design of FUnctional Nanodevices) and Seagate who paid my fees and maintenance, and also provided support for attending conferences. I am also thankful for and would like to acknowledge many collaborators who helped me along the way by sharing their results and expert knowledge - Dr. Claude Ederer, Dr. Daniel Fritsch, Eva Kalivoda, Prof. Riccardo Bertacco, James Rondinelli and Prof. Nicola Spaldin.

Many thanks to everyone who met for lunch in the Lloyd common room, who were never too busy for a tea-break and who made the whole PhD process enjoyable. A special thanks to the TPs whose friendship, from undergrad all the way through postgrad, meant the world to me.

My deepest thanks and gratitude to my parents and family for their support throughout my studies. It was, and continues to be, much appreciated. And if nothing else, perhaps this thesis will convince Ann that 'computational physics' isn't code for 'playing Solitaire'!

Finally, I must thank Stephen, whose support and encouragement was worth more to me than I could ever adequately express.

Contents

CHAPTER 1

Introduction

The twin phenomena of electricity and magnetism have been known to mankind for thousands of years, long before there was any concept of the electron. In ancient Greece, Egypt and Rome it was observed that certain eels inflicted shocks and furthermore, that these shocks could be conducted by other objects. The effects of lightning were also well known. The ancient Chinese observed that a certain stone, known as loadstone, could attract iron. Although they did not understand the mechanism behind this effect, attributing the phenomenon in some cases to a 'soul' within the material, they were nonetheless able to utilise it in rudimentary compasses. It was not until the turn of the last century that it was recognised that both electricity and magnetism could in fact be attributed to a single particle - the electron. Electrons were first discovered by J. J. Thompson in 1897 to be particles carrying negative charge ($-e$). It took almost another 30 years to realise that they have another degree of freedom, related to their angular momentum, called spin ($S = \pm\frac{1}{2}$). Uncompensated spins can be used to explain why atoms possess local magnetic moments. Exchange coupling between neighbouring local magnetic moments can then result in magnetic order on a macroscopic scale. For a long time, investigations into the charge and spin of an electron were carried out independently with no thought to any correlation between the two, so that the fields of magnetism and electronic transport progressed almost completely independently. Sir Nevill Mott first introduced the 'two current' model which assumes that the electron current is in fact comprised of two independent spin currents carried by both majority and minority electrons [1]. These two species coexist independently and so remain conserved in the absence of spin-flip events.

Spintronics (short for spin electronics) is a field of research based on harnessing the spin degree of freedom of an electron together with its electronic charge. While conventional electronics relies solely on the electron charge, the significance of spintronics lies in the breakthroughs that can be achieved beyond simply enhancing traditional electronics. These can include all-spin logic devices with ultra-low power consumption[2], domain wall 'race-track' memories [3], spin transfer torque memories [4] and graphene-based devices [5]. Such advances are indeed necessary as the electronics industry is reaching its limit in scalability [6].

1.1 Tunnel Junctions

The discovery of the giant magnetoresistance (GMR) effect in magnetic multilayers by Fert [7] and simultaneously by Grünberg [8] in 1988 is considered by many to be the founding step of spintronics. This effect relies on the relative magnetisation alignment of the two ferromagnetic layers sandwiching a thin non-magnetic metallic spacer. When the magnetisation of the two ferromagnetic layers is parallel, the current experiences low resistance. When the two layers are antiparallel the structure is in a high resistance state. This is shown in Fig. 1.1. In practice, the magnetisation of one of the ferromagnets is pinned by exchange bias to an antiferromagnetic layer while the other is free to rotate in an external magnetic field. The ability of such a 'spin valve' to detect a magnetic field meant it could be used as a detector in the magnetic recording industry. When they were first introduced in 1997 as reading elements in the heads of hard-disk drives, they lead to a dramatic increase in areal storage density of up to 100% per year [9].

Following on from this, remarkable progress can be made by replacing the non-magnetic metallic spacer by a non-magnetic insulator, creating a magnetic tunnel junction (MTJ). This device was originally proposed by Jullière in 1975 [10]. However, experimental difficulties meant that reproducibly was poor and research on the tunnelling magnetoresistance (TMR) effect was shelved until the 1990s. Since then, there has been significantly progress in thin-film deposition techniques such as sputtering, pulsed laser deposition and molecular beam epitaxy to the point that high quality coherent oxide thin films can be created with crystalline quality on a par with that of single crystals. In-situ reflection high-energy electron diffraction (RHEED) has been very successful at monitoring the growth of thin film oxides in real time which makes it possible to grow films as thin as a few unit cells, either alone or as part of a superlattice. Miyazaki and Tezuka first observed a large TMR effect in a Fe/Al_2O_3/Fe junction of 30% at 4K [11]. Replacing the amorphous barrier with a

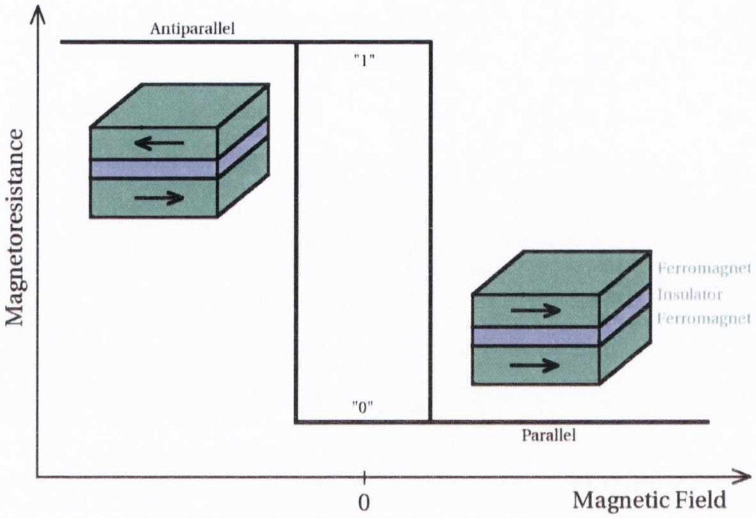

Figure 1.1: Schematic of a magnetic tunnel junction consisting of two ferromagnetic electrodes separated by a thin layer of insulating material. The low (parallel magnetic alignment) and high (antiparallel magnetic alignment) resistance states correspond to '0' and '1' in a memory device.

single crystal MgO barrier generated another big step forward as TMR values of up to 1010% have been found at low temperatures [12].

Continued technological advancement in the field of spintronics is divided into two approaches. One is based on the improvement of current technologies by using materials with higher spin polarisations or by perfecting the device structure. The second approach is focused on finding and using novel functional materials. To date, the search for such materials has encompassed a wide range and includes semiconductors, ferromagnetic insulators [13], organic materials including molecules [14, 15, 16], carbon nanotubes [17], graphene [5] and ferroelectrics among others [18]. The ambition behind investigations such as these is to find materials that can integrate multiple functionalities into a single device. These can include ferromagnetism, ferroelectricity, ferroelasticity and ferroterroicidy. If a material exhibits magnetoelectric coupling [19], it may be possible to write magnetic information with an electric field. This would allow information to be written faster and with less power consumption than conventional magnetic storage devices. However, materials which exhibit two or more ferroic orders in a single phase, known as multiferroics, are relatively scarce and almost all of them are antiferromagnetic or only weakly ferromagnetic [20], which is not ideal for device purposes. In an effort to circumvent the problems presented by these so-called single phase multiferroics, artificial component multiferroics have been designed that combine ferroelectric materials with ferromagnetic materials in a heterostructure [21].

The component materials for these heterostructures are generally drawn from the diverse family of complex oxides. Their impressive range of properties and degrees of freedom makes them exceptionally suited to the search for multifunctional materials. They show ferroic behaviour including ferromagnetism and ferroelectricity while their transport properties span insulating, semiconducting, metallic and even superconducting. It is possible to tune and control some of these properties by using strain or by doping appropriately. In fact, even a slight change in material composition or crystal structure can result in properties changing by several orders of magnitude. In addition, the behaviour of thin film oxides may exhibit considerably different properties than that which would be expected from their bulk properties.

While thin film oxides have the potential to transform the electronics industry, several outstanding problems need to be resolved before they are incorporated into devices on an industrial scale. In this thesis we address several of these open questions including the effect of combining several complex oxides with different properties into one heterostructure, the effect of strain on such a structure and the effect of a ferroelectric polarisation in a magnetic tunnel junction. We discuss, in particular, the possibility of manipulating the tunnelling current across such a device.

1.2 Spin Injection

Despite some outstanding problems, magnetic tunnel junctions have been successfully commercialised. However, spin injection devices, where a spin polarised current is injected into a non-magnetic semiconductor, are yet to enjoy widespread commercial success. Several obstacles remain to be overcome before they can be implemented into spintronic devices. Research in this field is motivated by the prospect that integrated spin injection and detection could lead to the large-scale adoption of semiconductor-based spintronic devices. Although a high spin injection has been achieved at low temperatures, problems arise when attempts are made to achieve efficient spin injection at room temperature. The main difficulty is that the materials required have very different electron affinities so that a high Schottky barrier forms at the interface between the two, impeding efficient electronic transport. The introduction of a thin insulating layer between the ferromagnet and the semiconductor resolves this issue along with the so-called ‘conductivity mismatch’ problem [22]. Therefore, it is of fundamental importance to adequately describe electron spin transport from a ferromagnet into a semiconductor via an insulating barrier. Several experimental methods have been developed in order to have integrated injection and detection of a spin polarised current. Here, we concentrate on the implications of optically exciting a spin polarised current in semiconducting germanium and detecting it electrically in the same device. We consider especially the effect of the tunnel barrier on spin injection efficiency.

1.3 Complex Band Structure

All of the phenomena discussed above rely on the layering of a ferromagnetic metal and an insulating material. In many instances, the interface between the two can dictate the properties of the whole device. This can be due to interface states, interfacial bonding or the creation of interfacial dipoles. At the interface, travelling Bloch states in the metal decay as evanescent states into the band gap of the insulator. The decay rate of such carriers, injected at energies corresponding to the band gap, can be determined by allowing complex solutions to the Bloch-Schrödinger equation. The result is the so-called complex band structure. The decay rates can also be symmetry dependent. That is, the symmetry of the injected electrons will determine which evanescent state they can couple to and hence their decay rate. In order to thoroughly describe the spin-dependent current in a tunnelling junction, both the symmetry of the Bloch states in the metal and the complex band structure of the insulator are required. The implications of this were first noticed in a Fe/MgO/Fe heterostructure [23, 24], where symmetry-dependent tunnelling results in half-metallic behaviour of the Fe/MgO(001) interface. Since then, the complex band structure is predicted to account for many, otherwise unexplained, experimental results in spin-dependent tunnel junctions. For instance, the sign of spin polarisation in several spinel ferrites is opposite to what would be expected from a cursory glance at the electronic density of states of these materials. In this thesis, we outline how the complex band structure can indeed influence the tunnelling properties of such a device.

1.4 Electronic Transport at the Nanoscale

Electronic transport at the nanoscale is an extremely complex theoretical problem as it is an inherently non-equilibrium process occurring in an open system. Ideally, a full many-body quantum mechanical description should be applied. However, this is beyond the capabilities of even the most modern computers, except for processes involving only a small number of particles. Instead, several approximations must be taken in order to make the problem more manageable. There are several approaches available to describe electronic transport and the choice of approach depends on the length scale of the system involved.

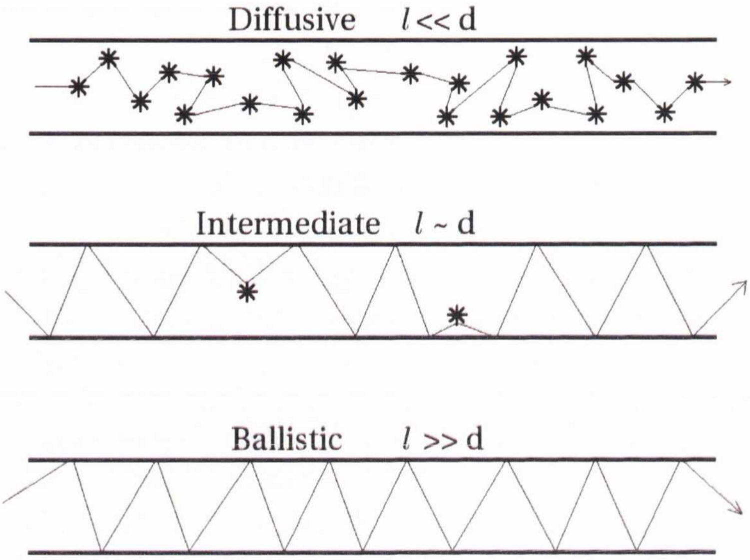

Figure 1.2: Representation of the effects of length scale on the transport properties of nanoscale systems. The mean free path of the carriers is denoted ℓ and the device is of length d. Inelastic scattering events are illustrated as $*$.

At macroscopic length scales, where the mean free path, ℓ, of the electrons is much smaller than the size of the device, d, Ohm-Kirchoff's laws are sufficient to describe the system. The mean free path of typical transition metals is approximately 100 Å. Transport in such a system falls within the so-called diffusive regime. As d becomes comparable or less than ℓ, Ohm's law is no longer valid. A ballistic regime is entered within which inelastic electron scattering processes can be neglected. The conductance is now independent of the mean free path of the electrons and depends on the device geometry. At such small length scales, the quantum mechanical nature of the electrons must be taken into account. In this work we assume the transport process occurs in the ballistic regime and all calculations are carried out in the steady state.

Several methods have been developed to determine electron transport in a nanoscale device in the presence of a time independent external bias. These include the non-equilibrium Green's function (NEGF) formalism, tight binding empirical methods, many-body theory and time-independent density functional theory. The NEGF formalism allows one to calculate the electronic charge density at a given applied bias. In order to do this, a detailed description of the electronic structure is required. This is generally provided using the density functional theory (DFT) introduced by Hohenberg and Kohn. DFT has proved to be an extremely powerful method for describing the ground state properties such as the structural, magnetic and electronic properties of realistic nanoscale systems. In this method the exchange and correlation energy of the interacting system of electrons must be approximated. Several approximations are possible and the choice between them is, in general, system dependent. The validity of these approximations is generally tested by comparison with experiment. However, DFT is a ground state theory. Even with the exact functional, it cannot describe dynamical properties, including non-equilibrium transport. Notwithstanding, for a wide range of materials and systems, the errors involved are small. The DFT-NEGF formalism has been numerically implemented in a number of codes. Here we use the *ab initio* electron transport code SMEAGOL. The tight-binding-like Hamiltonian required in the NEGF method is obtained with the DFT code SIESTA. SIESTA uses a flexible, numerical linear combination of atomic orbitals basis set, allowing systems with a large number of atoms to be treated efficiently. SMEAGOL was designed to treat the spin-dependent transport of magnetic systems and it is capable of calculating currents and transmission coefficients with a very high degree of accuracy.

1.5 Outline of Dissertation

The main focus of this work is to examine the spin-dependent transport behaviour of multifunctional devices using the DFT-NEGF formalism. We consider in particular the so-called multiferroic tunnel junctions where a ferroelectric barrier is used to manipulate the current in a magnetic tunnel junction. The mechanisms by which the ferroelectric polarisation can modify the tunnelling current are discussed and we suggest possible device structures to maximise both the tunnelling magentoresistance and the tunnelling electroresistance. The problem of spin injection from a ferromagnet into a semiconductor is also discussed. We show explicitly how the electronic structure of both the electrodes and barrier material must be taken into account in order to accurately predict the transport properties of such devices as it is not sufficient to simply model the insulating region as a potential barrier through which electrons must pass.

Chapter 2

In this chapter, the theoretical concepts and models required to investigate spin transport in magnetic tunnel junctions are introduced. The many body problem is discussed and an overview is given of density functional theory. The Hohenberg-Kohn and Kohn-Sham theorems are presented along with several of the most popular approximations to the exchange-correlation functional. The self-interaction problem is introduced along with the approximate method by which this error is removed. The implementation of DFT in the SIESTA program is briefly outlined. We also introduce the NEGF formalism required to solve the non-equilibrium transport problem for an open system, along with its implementation in the SMEAGOL program.

Chapter 3

In this chapter I look in detail at the electronic, structural and magnetic properties of two perovskite oxides that form the basis for much of the work in later chapters, namely $SrRuO_3$ and $BaTiO_3$. In recent years there have been several experimental investigations that suggested $SrRuO_3$ shows features associated with strongly correlated electrons. As such, we discuss the effect of electronic correlations on its electronic structure. As a ferroelectric perovskite, $BaTiO_3$ exhibits strong coupling between its structural and electronic properties. The implication of this sensitivity is that careful consideration must be given to the exchange correlation functional used to describe it. We discuss such descriptions of $BaTiO_3$ with the intention of finding the best computational strategy for investigating its transport properties when included in a tunnel junction.

Chapter 4

In this chapter I describe the multiferroic $SrRuO_3/BaTiO_3/SrRuO_3$ tunnel junction, investigating in particular the effect of the magnetic degree of freedom on the tunnelling current. We demonstrate theoretically a huge TMR that can be reversed with the application of an external bias. By comparison with an artificial centrosymmetric structure we isolate the contribution of the ferroelectric polarisation on the TMR. All results are rationalised by considering the electronic band structure and alignment between the magnetic electrodes and the ferroelectric insulator.

Chapter 5

Here we extend the work of the previous chapter by considering the effects of asymmetry on an $SrRuO_3/BaTiO_3/SrRuO_3$ tunnel junction. We discuss the effects of including a thin layer of dielectric material ($SrTiO_3$) on the potential barrier presented to the tunnelling electrons and suggest methods to enhance the subsequent tunnelling electroresistance. The coexistence of the TMR and TER in such a device is discussed in relation to a possible four state memory.

Chapter 6

In chapter 6 we examine the Ge/MgO/Fe heterostructure. This heterostructure has been considered experimentally for the efficient and integrated electric detection of photon helicity at room temperature. We present *ab initio* calculations of the spin-dependent electronic transmission through the MgO barrier, concentrating on the spin filtering of both holes and electrons through particular regions of the Brillouin Zone.

Chapter 7

In this chapter we investigate the possible effects of an insulator's complex band structure on spin-dependent transport by considering two different systems. In the first we look at the complex band structure of two spinel ferrites. These are insulating ferrimagnets that have been proposed to be efficient spin filters. We determine the spin selection associated with the symmetry dependent decay rates in the band gap. For the second structure, we return again to ferroelectric tunnel junctions and discuss how asymmetric electrodes can influence the complex band structure of the ferroelectric insulator and hence the transport properties of the junction.

Finally, we conclude this dissertation with a brief summary of the work presented here and highlight some outstanding problems in this field that require further investigation.

CHAPTER 2

Theoretical Framework: DFT and Electronic Transport

2.1 Introduction

The aim of this Chapter is to provide a brief overview of the theoretical methods used in the thesis. Section 2.2 details the basic concepts behind density functional theory followed by a description of its implementation in the SIESTA code. For a more thorough account of the subject the reader is referred to one of the several books that are now published on DFT [25, 26, 27]. Section 2.3 presents the main concepts of electronic transport theory and in particular the non-equilibrium Green's function formalism. In both cases, formal derivations of the fundamental equations and mathematical details of their implementation are not presented in order to show more transparently the general framework.

2.2 Density Functional Theory

The central problem in condensed matter physics concerns the solution of the Schrödinger equation for a solid consisting of a huge number of nuclei and electrons. Many different methods have been developed in order to tackle this many-body problem as it is impossible to solve it analytically for non-trivial systems. Field-theoretical many-body techniques have been applied to solid state problems beginning with the seminal paper by Gell-Mann and Brueckner [28]. Such methods, however, are best suited to systems with small numbers of particles. As such, their applicability to real systems with hundreds, if not thousands, of atoms is limited. Therefore, several approximations have to be introduced in order to make a realistic problem more tractable. Firstly, one can assume that the relevant electrons travel at non-relativistic speeds so that the dynamics of the system are governed by the time-dependent non-relativistic Schrödinger equation. The problem can then be described by the time-independent Schrödinger equation:

$$\hat{H}\Psi = E\Psi,$$

where E is the energy and $\psi = \psi(\boldsymbol{r}_1, \boldsymbol{r}_2, \ldots, \boldsymbol{r}_N)$ is the many-body wavefunction. The coordinates of the ith electron is $\boldsymbol{r}_i$. $\hat{H}$ is the Hamiltonian operator for a system consisting of N_e electrons of mass m_e, moving in a potential generated by N_N nuclei of mass Z_I and position coordinates $\boldsymbol{R}_I$. It is comprised of several independent contributions:

$$\hat{H} = T_e(\boldsymbol{r}) + T_n(\boldsymbol{R}) + V_{ee}(\boldsymbol{r}) + V_{en}(\boldsymbol{r}, \boldsymbol{R}) + V_{nn}(\boldsymbol{R}),$$

where

$$\begin{array}{rlr}
T_e(\boldsymbol{r}) = & \displaystyle\sum_{i=0}^{N_e} -\frac{\hbar^2}{2m_e}\nabla^2_{\boldsymbol{r}_i} & \text{Electron Kinetic Energy} \\
T_n(\boldsymbol{R}) = & \displaystyle\sum_{I=0}^{N_N} -\frac{\hbar^2}{2M_I}\nabla^2_{\boldsymbol{R}_I} & \text{Nuclei Kinetic Energy} \\
V_{ee}(\boldsymbol{r}) = & \displaystyle\frac{1}{2}\sum_{i \neq j}^{N_n} \frac{e^2}{|\boldsymbol{r}_i - \boldsymbol{r}_j|} & \text{Electron - Electron Coulomb Repulsion} \\
V_{en}(\boldsymbol{r}, \boldsymbol{R}) = & \displaystyle -\frac{1}{2}\sum_{i,j}^{N_n, N_N} \frac{e^2 Z_I}{|\boldsymbol{r}_i - \boldsymbol{R}_I|} & \text{Electron - Core Coulomb Repulsion} \\
V_{nn}(\boldsymbol{R}) = & \displaystyle\sum_{i,j} \frac{Z_I Z_J}{|\boldsymbol{R}_i - \boldsymbol{R}_J|} & \text{Core - Core Coulomb Repulsion}
\end{array}$$

The second approximation assumes that, because the mass of the nucleus is many times heavier than the mass of the electrons, nuclear dynamics occurs at a time scale much longer than that of the electrons. This is the Born-Oppenheimer approximation [29, 30], whereby the nuclei are described as classical particles and remain stationary. They generate a static potential in which the electrons, described quantum mechanically, must move. The total wavefunction, Ψ, can then be separated into two parts

$$\Psi = \psi(\boldsymbol{r}; \boldsymbol{R})\zeta(\boldsymbol{R}),$$

such that

$$\begin{aligned} \hat{H}_e\psi(\boldsymbol{r}; \boldsymbol{R}) &= E_e(\boldsymbol{R})\psi(\boldsymbol{r}; \boldsymbol{R}) \qquad (2.1) \\ &= (T_e + V_{ee} + V_{en})\psi(\boldsymbol{r}; \boldsymbol{R}), \\ \hat{H}_N\zeta(\boldsymbol{R}) &= E\zeta(\boldsymbol{R}) \\ &= (T_n + V_{nn} + E_e(\boldsymbol{R}))\zeta(\boldsymbol{R}), \end{aligned}$$

where $\zeta(\boldsymbol{R})$ is the nuclear wavefunction and $\psi(\boldsymbol{r}; \boldsymbol{R})$ is the electronic wavefunction depending parametrically on the nuclear positions. $E_e(\boldsymbol{R})$ is the total electron energy for the nuclei configuration $\{\boldsymbol{R}\}$. E is the total energy of the system.

The Schrödinger equation for the electronic system, Eqn. (2.1), still contains $3N_e$ degrees of freedom. In order to deal with systems with hundreds of atoms a different approach is then required. Density Functional Theory (DFT) replaces the many-body wavefunction with the electron density $n(\boldsymbol{r})$, simplifying the problem enormously. This powerful method relates all the ground state properties of the system to a functional of the ground state electronic density.

2.2.1 Hohenberg Kohn theorem

The foundations of DFT were laid down in the 1960s with the work of Hohenberg and Kohn [31]. The basic idea is to take the intricate many-body wavefunction and replace it with the ground state electronic density $n(\boldsymbol{r})$, which becomes the fundamental quantity of the theory. This is a much simpler quantity to deal with as it depends only on the 3 spatial coordinate variables as opposed to the $3N_e$ variables of the many-body wavefunction. The electron density is defined as the probability to find an electron at a position $\boldsymbol{r}$:

$$n(\boldsymbol{r}) = \int |\Psi(\boldsymbol{x}_1, \boldsymbol{x}_2, \ldots, \boldsymbol{x}_N)|^2 d\boldsymbol{r}_2 d\boldsymbol{r}_3 \ldots d\boldsymbol{r}_N.$$

The first Hohenberg-Kohn theorem states that the external potential $\mathrm{V}_{ext}(\boldsymbol{r})$ is, within a constant, a unique functional of $n(\boldsymbol{r})$. From this one can conclude that the electron density determines both the number of electrons in the system and the external potential $\mathrm{V}_{ext}(\boldsymbol{r})$, i.e., the two quantities which fix the Hamiltonian. In other words, the Hamiltonian and all the quantities that can be derived from it are determined uniquely by $n(\boldsymbol{r})$.

The kinetic energy can now be written as a functional of the density, $T[n]$, as can the electron-nuclei potential energy, $V_{en}[n]$, and the electron-electron interaction, $V_{ee}[n]$, so that the total energy functional for a given external potential is given as

$$E[n] = T[n] + V_{ne}[n] + V_{ee}[n].$$

The second theorem of Hohenberg-Kohn states that the total ground state energy is a functional of the electron density for a given external potential and the energy functional is minimised for the true ground state density, n_0. If $n \neq n_0$ then $E_0 = E[n_0] < E[n]$. This variational principle provides the means to determine the ground state density, assuming that the form of the total energy functional is known. The Hohenberg-Kohn theorems, however, provide no prescription for determining the universal functional.

2.2.2 Kohn-Sham scheme

In 1965, Kohn and Sham [32] proposed a method to formulate the total energy functional that remains the basis for all modern DFT calculations. They introduced an auxiliary system of non-interacting electrons with the requisite that it must have the same ground state density, and therefore the same ground state energy, as the interacting system under consideration.

The density of a system of non-interacting electrons in an external potential, V_{ext}, can be expressed in terms of single particle wavefunctions, ψ_i

$$n(\boldsymbol{r}) = \sum_{i=1}^{N_e} |\psi_i(\boldsymbol{r})|^2.$$

The total Kohn-Sham energy functional can now be formulated as

$$E_{KS}[n] = T_s[n] + \int n(\boldsymbol{r}) V_{ext}(\boldsymbol{r}) d\boldsymbol{r} + E_H + E_{xc}, \tag{2.2}$$

where

$$T_s[n] = -\frac{\hbar^2}{2m} \sum_i \langle \psi_i | \nabla^2 | \psi_i \rangle,$$

is the kinetic energy of the non-interacting electron system. The second term describes the interaction of the electrons with the external potential V_{ext}. The classical

Coulomb repulsion (Hartree) energy is given by

$$E_H = \frac{e^2}{2} \int \frac{n(\boldsymbol{r})n(\boldsymbol{r'})}{|\boldsymbol{r} - \boldsymbol{r'}|} d\boldsymbol{r} d\boldsymbol{r'}.$$

E_{xc} is the exchange and correlation (xc) energy. All of these terms are known explicitly except the last. The exchange-correlation energy functional is defined so as to include all the contributions to the kinetic and potential energy that are omitted in Eqn. (2.2). The exact functional dependence of E_{xc} on the density is unknown and must be approximated. These approximations will be discussed later.

In order to find the ground state energy, Eqn. (2.2) must be minimised under the constraint that the wavefunctions are normalised ($\langle \psi_i | \psi_j \rangle = \delta_{ij}$) or equivalently that the density integrates to the correct number of electrons. This leads to the Kohn-Sham equations

$$\hat{H}_{KS}\, \psi_i(\boldsymbol{r}) = \varepsilon_i \psi_i(\boldsymbol{r}), \tag{2.3}$$

$$[-\frac{\hbar^2}{2m_e} \nabla^2 + V_{eff}(\boldsymbol{r})]\, \psi_i(\boldsymbol{r}) = \varepsilon_i \psi_i(\boldsymbol{r}). \tag{2.4}$$

The effective Kohn-Sham potential, V_{eff}, is defined by the functional derivative of the energy functional. It can be written as

$$V_{eff}(\boldsymbol{r}) = V_{ext}(\boldsymbol{r}) + V_H(\boldsymbol{r}) + V_{xc}(\boldsymbol{r}),$$

where

$$V_H(\boldsymbol{r}) = e^2 \int \frac{n(\boldsymbol{r'})}{|\boldsymbol{r} - \boldsymbol{r'}|} d\boldsymbol{r'},$$

is the electrostatic Hartree potential and

$$V_{xc}(\boldsymbol{r}) = \frac{\delta E_{xc}[n]}{\delta n(\boldsymbol{r})}$$

is the exchange-correlation potential. The eigenvalues, ε_i, which are introduced in the minimisation process as Lagrange multipliers, are the Kohn-Sham single particle energies (see later for a discussion on how to intrepret the Kohn-Sham eigenvalues).

It is clear that the effective potential, $V_{eff}(\boldsymbol{r})$, depends on the wavefunctions via the dependence of the Hartree and exchange-correlation potentials on the density. Therefore, the Kohn-Sham equations must be solved self-consistently. The general iterative scheme is shown in Fig. 2.1.

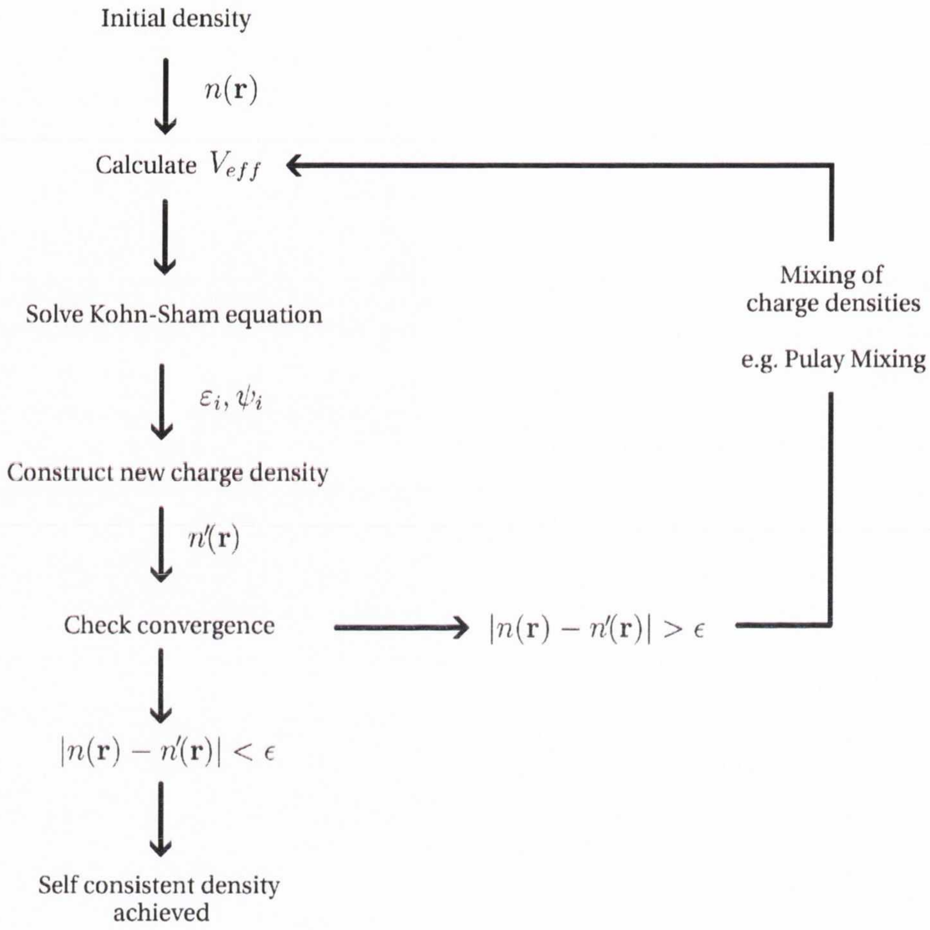

Figure 2.1: Schematic outline of the iterative solution of the Kohn-Sham equations

2.2.3 Spin-DFT

All the equations written in the previous section can be extended to the spin polarised case by decomposing the charge density, n($\boldsymbol{r}$), into its two spin components

$$n(\boldsymbol{r}) = n^{\uparrow}(\boldsymbol{r}) + n^{\downarrow}(\boldsymbol{r}),$$

where $n^{\uparrow}(\boldsymbol{r})$ is the density of the majority electrons and $n^{\downarrow}(\boldsymbol{r})$ is the density of the minority ones. This allows us to define a magnetisation density

$$m(\boldsymbol{r}) = n^{\uparrow}(\boldsymbol{r}) - n^{\downarrow}(\boldsymbol{r}).$$

Majority and minority spins now satisfy two independent Kohn-Sham equations [33]:

$$\hat{H}^{\sigma}_{KS}\, \psi^{\sigma}_i = \varepsilon^{\sigma}_i\, \psi^{\sigma}_i,$$

where σ is the spin index, $\sigma = (\uparrow, \downarrow)$. The spin-dependent effective potential is now defined as

$$V^{\sigma}_{eff}(\boldsymbol{r}) = V(\boldsymbol{r}) + \int \frac{e^2 n(\boldsymbol{r'})}{|\boldsymbol{r} - \boldsymbol{r'}|} d\boldsymbol{r} + \frac{\delta E_{xc}[n^{\uparrow}(\boldsymbol{r}), n^{\downarrow}(\boldsymbol{r})]}{\delta n^{\sigma}(\boldsymbol{r})} .$$

The Kohn-Sham equations have also been extended to account for non-collinear magnetism [34, 35] via the introduction of the two-component spinor wavefunctions. However, the materials under consideration in this thesis do not exhibit non-collinear magnetism and so this will not be discussed further.

2.2.4 Approximate density functionals

In principle, the DFT Kohn-Sham formalism is exact, that is the ground state total energy and density of the interacting system produced by solving the Kohn-Sham equations in Eqn. (2.2) are exact. This would only be true if the exact functional dependence of E_{xc} on n is known but unfortunately this is not the case. However, there are several approximations for this energy available that work well for a wide variety of materials.

One of these is the Local Density Approximation (LDA) and its extension to polarised systems (LSDA). The LDA was proposed in the original work of Kohn and Sham and remains one of the most widely used functionals to date. Although in general the value of $\mathrm{V}_{xc}[n]$ at a point $\boldsymbol{r}$ depends on the value $n(\boldsymbol{r'})$ for all $\boldsymbol{r'}$, the LDA assumes that it depends only on $n(\boldsymbol{r})$, i.e., on the density at that point only. The resultant exchange-correlation energy is assumed to be the same as that of a homogeneous electron gas with the same density, which is known.

$$E^{LDA}_{xc}[n] = \int n(\boldsymbol{r}) \varepsilon^{hom}_{xc}(n(\boldsymbol{r})) d\boldsymbol{r},$$

where $\varepsilon^{hom}_{xc}(n(\boldsymbol{r}))$ is the known exchange-correlation energy density of the uniform gas. As one would expect, this approximation works well for systems with slowly varying densities but it also works remarkably well for many materials where this is not the case. The exchange part of the energy is given by

$$\varepsilon_x = -\frac{e^2}{4\pi\varepsilon_0} \frac{3}{4} \left(\frac{3n}{\pi} \right)^{\frac{1}{3}},$$

but there is no exact expression for the correlation part, ε_c. For this, one uses a numerical expression with values generally tabulated using results from Monte-Carlo simulations. Several parametrisations exist for the LDA but the most commonly used is that of Perdew and Zunger [36, 37]. The success of the LDA in situations where the electron density is far from homogeneous can be attributed to the fact that it gives the correct sum rule to the exchange-correlation hole. This means that there is one electron excluded from the neighbourhood of an electron at $\boldsymbol{r}$. The various strengths and weaknesses of the LDA have been well documented: structural and vibrational properties such as bond lengths, bond angles and phonon vibrational frequencies are generally quite good. Bond lengths, bulk moduli and vibrational frequencies are all accurate to within a few percent. However, cohesive energies of solids and ionisation energies of molecules are less accurately described, typically to within 10 or 20%. One serious shortcoming of the LDA is the estimation of the bandgap of semiconductors and insulators. This is routinely underestimated by up to 50% and in some cases a metallic ground state is found for semiconducing or insulating materials.

Several extensions to the LDA have also been developed. If the density is far from homogeneous it is sensible to take its first derivative into account. Such a semilocal approach is taken in the Generalised Gradient Approximation (GGA) where the exchange-correlation energy is now a functional of the density and its gradient to fulfill a maximum number of exact constraints.

$$E_{xc}^{GGA} = \int f(n(\boldsymbol{r}), \nabla n(\boldsymbol{r})).$$

The exchange-correlation potential is given by

$$V_{xc}[n(\boldsymbol{r})] = \frac{\partial E_{xc}[n]}{\partial n(\boldsymbol{r})} - \nabla . \frac{\partial E_{xc}[n]}{\partial(\nabla n(\boldsymbol{r}))},$$

where the gradient of the density is usually determined numerically. The GGA has proved successful in some instances where the assumption of a uniform electron density is dubious, for example in molecules, but in general it does not provide the systematic improvement over LDA that would be expected. Several flavours of GGA have been developed, the most popular of which is the construction of Perdew, Burke and Ernzerhof (PBE) [38].

Another popular method, especially within the chemistry community, is to create a 'hybrid' functional, incorporating part of the Hartree-Fock exact-exchange with the DFT exchange and correlation energy [39]. Such a method introduces external parameters as the various weights defining the functional. These must be determined by fitting to experimental or thermochemical data. The exchange-correlation energy functional in this case is given by

$$E_{xc}^{hyb} = aE_x^{exact} + (1-a)E_x^{GGA} + E_c^{GGA},$$

where a is either estimated theoretically or fitted empirically. An example of this class of functionals is the B3LYP one [40].

2.2.5 Dealing with Strongly Correlated Systems

For systems with weakly correlated electrons the LDA and GGA work remarkably well. However, they fail for strongly correlated materials with localised states. Several attempts have been made to improve upon the LDA and GGA for strong electronic correlations.

Local Density Approximation + Hubbard U

One of the most popular functionals, in particular for materials where the correct description of the band gap is vital, is the local density approximation + Hubbard U (LDA+U) [41]. The starting point of this description is the standard LDA energy functional. An orbital dependent term is then added to the LDA to correct for the missing on-site Coulomb interaction. Then a 'double-counting' term subtracts the electron-electron interaction already included in the LDA in some approximate mean-field way. As such, the LDA+U energy functional becomes

$$E_{LDA+U}[n(\boldsymbol{r})] = E_{LDA}[n(\boldsymbol{r})] + E_{Hub}[n_{mm'}^{I\sigma}] - E_{dc}[n^{I\sigma}],$$

where $E_{Hub}[n_{mm'}^{I\sigma}]$ is the 'corrected' on-site correlation functional at site I, $n_{mm'}$ are the generalised orbital occupations and E_{dc} is the mean field approach to correlation already accounted for in the LDA and so must be subtracted out. The general result is that occupied orbitals are shifted to lower energies and unoccupied orbitals are shifted higher in energy. This increases the band gap of semiconductors and insulators to be more in line with experimental expectations. In practice, however, the corrections added to the LDA energy functional depend on two parameters: U the Hubbard repulsion and J the intra-atomic exchange for electrons with the angular momentum of interest. These are usually chosen in such a way as to reproduce some particular feature or property of the material in question. As such the LDA+U scheme is not a fully *ab initio* method.

A second approach to increasing the band-gap of materials is the self-interaction correction (SIC), which is parameter free. This method is used extensively in this thesis and so will be discussed in more detail in the next section.

Atomic Self Interaction Correction

Self-interaction (SI) is, as the name suggests, the spurious electrostatic interaction of an electron with itself. Its presence is behind many of the failures of the LDA and the GGA. For example, LDA and GGA fail to describe the dissociative behaviour of symmetric radicals correctly, most famously for the simplest one-electron molecule H_2^+ [42]. Within the Hartree Fock method, the self-interaction of occupied orbitals is explicitly cancelled by the exchange energy. As the exchange potential in LDA and GGA is approximated, the cancellation is now no longer exact and so some unphysical self-interaction remains. These self-interaction errors are small for materials with delocalized electronic states but can be significant in systems with localized electrons, where the interaction of an electron with itself is large.

SIC methods aim at removing the self-interaction from semi-local potentials. Since the SIC in a periodic extended system is not uniquely defined, many different methods have been proposed to remove SI in DFT calculations for solids (for a review see Ref. [43]). These are generally based on the work of Perdew and Zunger [44]. In this work, the computationally inexpensive 'atomic-SIC' (ASIC) approximation is used. This is described in Ref. [45]. The method is based on the work of Vogel et al. [46], extended by Filippetti and Spaldin [47]. The approach taken is to incorporate the SIC into the generation of the pseudopotentials (discussed in more detail in Section 2.2.7). The procedure is as follows:

1. Project the occupied Bloch states onto the basis of the pseudoatomic orbitals.

2. Correct the Kohn-Sham potential for each Bloch state by the SIC for the pseudoatomic orbital weighted by the projection, and scaled to account for the relaxation energy.

Note that only the valence bands are corrected since the empty conduction bands, derived from orbitals where the occupation numbers are close to zero, are not self-interacting. This is in contrast to the LSDA+U method, in which the occupied bands are lowered in energy and the unoccupied bands raised. In principle, however, the two formalisms would yield equivalent results if suitable U and J parameters (corresponding to the SIC energy) were applied to all orbitals in the LSDA+U calculation. Indeed, whether the deficiencies of LSDA for strongly correlated systems derive from the absence of Hubbard U or the self-interaction error or both remains an open question and the answer may be material specific. The ASIC method has some advantages over LSDA+U, since it is not required to choose which orbitals to correct, nor the value of the U and J parameters. Furthermore, it can be applied readily to both magnetic and nonmagnetic systems.

The ASIC approach has been used with success for a variety of systems [48, 49, 50], most notably the band gap of wide-gap insulators and transition metal oxides are significantly improved compared to their experimental values. However, for some metals, including Fe, it gives unphysical results.

2.2.6 Interpretation of the Kohn-Sham Eigenvalues

The physical meaning of the Kohn-Sham eigenvalues is a very prominent question withing DFT. As we saw earlier, ε_i enter simply as Lagrange multipliers during the minimisation of the total energy functional. As it might be initially presumed, the sum of the eigenvalues does not equal the total Kohn-Sham energy. This can be seen by multiplying the Kohn-Sham equation, Eqn. (2.2) by $\psi^*(\boldsymbol{r})$, by integrating over space and summing over all i

$$\sum_{i=1}^{N_e} \varepsilon_i = T_s[n] + \int V_{eff} n(\boldsymbol{r}) d\boldsymbol{r}.$$

The difference between $\sum \varepsilon_i$ and the total energy is then given by

$$\Delta E = \sum_i \varepsilon_i - E_{KS}[n] = \frac{e^2}{2} \int \frac{n(\boldsymbol{r})n(\boldsymbol{r'})}{|\boldsymbol{r} - \boldsymbol{r'}|} + E_{xc}[n] - \int V_{xc}(\boldsymbol{r}) n(\boldsymbol{r}) d\boldsymbol{r}.$$

Despite the lack of any physical meaning it has been found that, in practice, the Kohn-Sham eigenvalues give an excellent description of the experimental band structure of metals. With this empirical justification, it is now standard practice to interpret the ε_is as estimates of the excitation energies. Janak [51] first showed that the Kohn-Sham eigenvalues correspond to the derivative of the total energy E with respect to the occupation number f_i of the state ψ_i

$$\varepsilon_i^{KS} = \frac{\partial E}{\partial f_i},$$

where f_i are defined as follows

$$n(\boldsymbol{r}) = \sum_{i=1}^{occupied} |\psi_i|^2 = \sum_{i=1}^{\infty} f_i |\psi_i|^2.$$

Although in general the Kohn-Sham eigenvalues do not have any physical meaning, the highest occupied molecular orbital (HOMO) with Kohn-Sham eigenvalue ε^{HOMO} is equal to the negative of the ionisation energy of the real system

$$I = -\varepsilon^{HOMO}. \tag{2.5}$$

The Kohn-Sham band gap differs from the real band gap due to the the derivative discontinuity in E_{xc} [52]

$$E_g^{real} - E_g^{KS} \equiv \Delta > 0.$$

Therefore, unless the exchange correlation functional can accurately describe the derivative discontinuity one must be conscious that the DFT band gap will be incorrect. Similarly, Eqn. (2.5) is only approximate for functionals that do not describe the derivative discontinuity correctly.

2.2.7 The SIESTA Code

All DFT calculations presented in this thesis were performed using the SIESTA code. Pseudopotentials are used to describe the nuclei and core electrons and the wavefunction is expanded as a linear combination of atomic orbitals. In this section only a brief overview of the SIESTA numerical implementation is given; a more detailed description of it can be found in Refs. [53, 54, 55, 56].

Basis Sets

In order to solve the Kohn-Sham equations, the Kohn-Sham eigenstates must be expanded over some finite basis set. Several varieties of basis sets exist including planewaves, local orbitals, linearised augmented planewaves and linearised muffin-tin orbitals.

Planewave basis sets are conceptually simple and are convenient in that the wavefunction can be expanded as a Fourier expansion over a set of planewaves

$$\psi_j(\boldsymbol{r}) = \sum_k A_{\boldsymbol{k}}^j e^{i\boldsymbol{k}\boldsymbol{r}}.$$

In practice, the number of $\boldsymbol{k}$-vectors is chosen so that $\psi_i(\boldsymbol{r})$ is represented to the required accuracy. This is decided by an energy cutoff, $E_{cut} = \frac{\hbar^2|\boldsymbol{k}|^2}{2m}$, describing the maximum kinetic energy of any planewave used in the expansion. For systems with highly localised electron states (and thus large kinetic energies), calculations can become computational unwieldy due the large E_{cut} required. Planewave basis sets are also inefficient for describing isolated molecules as many planewaves are used to describe vacuum regions where the charge density vanishes.

A second popular approach, and the one used in SIESTA, is to expand the wavefunction over a linear combination of localised, atomic-like orbitals

$$\psi_j(\boldsymbol{r}) = \sum_a C_a^j \phi_a(\boldsymbol{r}),$$

where $\phi_a(\boldsymbol{r})$ are radial numerical functions that have a finite radius and are strictly zero beyond that radius. This approach describes localised orbitals well and the number of basis functions required is relatively small. A disadvantage is that, in comparison to planewaves in particular, the approach lacks a systematic route to convergence, i.e., there is not a single parameter to tune the convergence. A basis set of atomic orbitals can be defined by three main features: size, range and radial shape.

- **Size** A single-ς (SZ) basis set has one single radial function per angular momentum channel. A double-ς (DZ) basis set includes a second function per channel, usually via the split valence scheme [55]. Polarisation orbitals can also be included. These are generated by polarising the basis orbitals with an electric field [53].

- **Range** The atomic-like orbitals must be strictly localised in order to obtain the sparse Hamiltonian essential for calculation efficiency. A cut-off radius is defined for each orbital beyond which the orbital goes strictly to zero.

- **Shape** Within the pseudopotential framework, the basis orbitals are generally chosen as the solutions of the same pseudopotential in the free atom (pseudo-atoms).

Pseudopotentials

It is well known that most physical properties of a material do not depend on the tightly bound core-electrons but rather on the valence electrons that are responsible for chemical binding. Also, the core electrons are only slightly affected by changes in the chemical environment so it can be assumed that the configuration of core electrons within a crystal or a molecule is the same as it would be in an isolated atom. For this reason, the pseudopotential approximation is introduced [57], where all the core electron potentials are replaced by single effective potentials that describe their effect on the valence electrons. In this way the wavefunctions remain unchanged with respect to the all-electron wavefunction beyond a certain radius but they are replaced by a smoothly varying function in the core region.

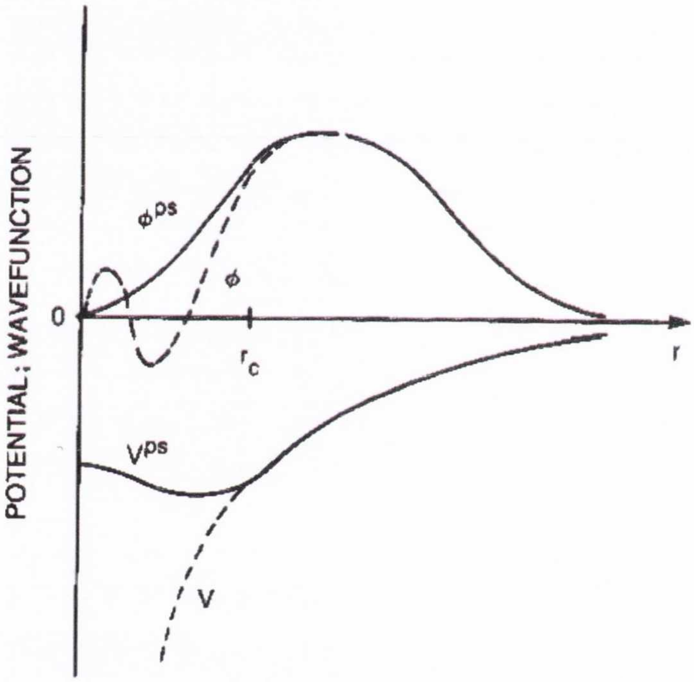

Figure 2.2: Schematic representation of the pseudopotential method. The all-electron potential V and orbital ϕ, are replaced with the pseudopotential V^{ps} and the pseudo-orbital ψ^{ps} inside the core radius r_c. Figure taken from Ref. [58].

There are several methods available for generating pseudopotentials; all results in this thesis were obtained using norm-conserving Troullier-Martins pseudopotentials [59, 60]. In general, one begins by solving the atomic radial Schrödinger equation in a spherically symmetric potential V[ρ](r) for a particular valence shell (n, ℓ)

$$\Big[-\frac{1}{2}\frac{d^2}{dr^2}+\frac{\ell(\ell+1)}{2r^2}+V[\rho](r)\Big]r\psi_{n\ell}^{AE}=\varepsilon_{n\ell}r\psi_{n\ell}^{AE},$$

where V[ρ](r) is the Kohn-Sham effective potential for the atomic density $\rho(r)$

$$V[\rho](r)=-\frac{Z}{r}+V_H[\rho](r)+V_{xc}[\rho](r).$$

The real all-electron wavefunction $\psi_{n\ell}^{AE}$ oscillates wildly in the core region and it is thus replaced by the smooth nodeless pseudo wavefunction $\psi_{n\ell}^{PS}$ which is constructed in such a way as to match the real wavefunction outside the chosen matching radius. From $\psi_{n\ell}^{PS}$, the pseudopotential can be determined by inverting the Schrödinger equation:

$$V_{n\ell}^{PS}(r) = \varepsilon_{n\ell} - \frac{\ell(\ell+1)}{2r^2} + \frac{1}{2r\psi_{n\ell}^{PS}(r)}\frac{d^2}{dr^2}r\psi_{n\ell}^{PS}(r)$$

A more detailed discussion on pseudopotentials can be found in Refs. [58, 61, 59].

k-points (Monkhorst Pack Method)

For periodic systems, by virtue of Bloch's theorem, any real-space integral over the infinite system can be replaced by an integral over the (finite) first Brillouin zone. Integrations are then performed by summing the function values of the integrand over a finite mesh of $\boldsymbol{k}$-points, i.e.

$$\int_{BZ} F(\boldsymbol{k})d\boldsymbol{k} = \frac{1}{\Omega}\sum_j w_j F(k_j),$$

where $F(\boldsymbol{k})$ is the Fourier transform of $f(\boldsymbol{r})$, Ω is the cell volume and w_j are weighting factors. The $\boldsymbol{k}$-point mesh must be sufficiently dense in order to achieve convergence to the correct result (note however that the total energy convergence is not necessarily monotonous with respect to the $\boldsymbol{k}$-point density). For all calculations presented in this work the unbiased method of Monkhorst-Pack was employed. The chosen $\boldsymbol{k}$-points comprise of rectangular grid of points distributed homogeneously throughout the Brillouin zone. In some cases the symmetry of the crystal is exploited in order to reduce the number of $\boldsymbol{k}$-points used.

2.3 Electronic Transport at the Nanoscale

A theoretical description of electronic transport over length scales less than an electron's mean free path is a very challenging problem. Ohm's Law is no longer valid and quantum transport dominates. Any description must take not only the system geometry and the electronic structure into account but also the fact that the system is no longer in equilibrium. Technological developments have meant that there are now accurate electrical measurements carried out on a variety of systems over a wide range of temperatures and scales. Achieving a theoretical understanding of these experimental results requires the development of methods to model electronic transport. The Boltzmann formalism to treat electronic transport is one of the most well known. A non-equilibrium distribution function is used to describe the occupation probability of the phase space. The equations of motion for this distribution function can then be constructed such that in the steady state the effect of the electric field is balanced by the effect of collisions. However, this method is limited to cases where the system size is much larger than the mean free path. The time dependent Kubo formalism describes the current as a response to an applied electric field. However in its most rigorous formulation it can be difficult to apply it to realistic systems. Landauer first related the conductance to the quantum mechanical transmission coefficient in a simple 1D single channel formula [62]. A more general treatment, now including higher dimensions and multiple conductance channels, was given by Büttiker [63].

2.3.1 Toy Model of Transport

In order to capture some of the key aspects behind the *ab initio* description of electronic transport, I will initially follow the 'bottom up' approach taken by Datta [64], where the key concepts are introduced via a simple toy model of transport at the atomic scale in an archetypical molecular system.

Such a system generally consists of a molecule, represented for simplicity by a single energy level, ε, sandwiched between two metallic leads kept at two different chemical potentials, μ_L and μ_R (see Fig. 2.3). As at low biases only a small number of molecular orbitals participate in the transport, this simple model already incorporates much of the physics required. The energy difference between μ_L and μ_R is described by the potential difference, V, applied across the two electrodes

$$\mu_L - \mu_R = eV.$$

For $\mu_L = \mu_R$ the system is in equilibrium with the occupation of the molecular energy

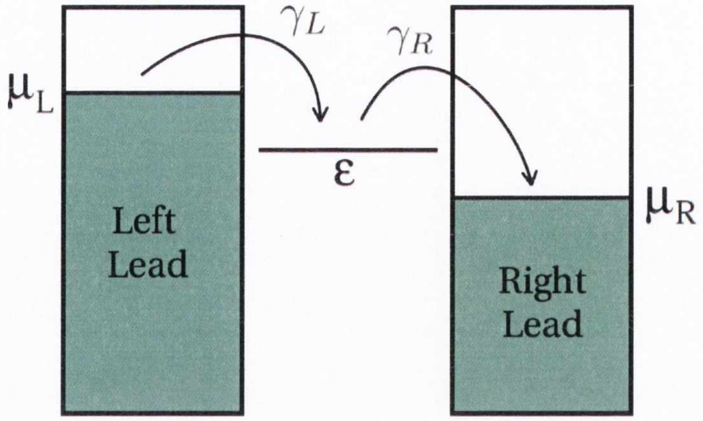

Figure 2.3: Schematic representation of the toy model. The left and right contacts are kept at two different chemical potentials, μ_L and μ_R. The coupling of the single molecular orbital, ε, to the left lead (right lead) is γ_L (γ_R).

level given by

$$f_{L,R} = \frac{1}{1 + e^{(\varepsilon - \mu_{L,R})/k_B T}} \, .$$

For $V \neq 0$, however, equilibrium cannot be established. In this case, if $\mu_L > \mu_R$, the left lead will pump electrons into the molecule energy level, while the right lead will take electrons from it. As such, the occupation of the energy state in non-equilibrium conditions will be between that of f_L and f_R and the resulting imbalance drives a current flow.

The net flux of charge from the left lead into the energy level, I_L, is proportional to the difference between the actual occupation of the orbital, N, and the equilibrium occupation, f_L

$$I_L = e\frac{\gamma_L}{\hbar}(f_L - N). \tag{2.6}$$

Similarly, the charge flux I_R from the right lead into the energy level is given by

$$I_R = e\frac{\gamma_R}{\hbar}(N - f_R), \tag{2.7}$$

where $\frac{\gamma_{L,R}}{\hbar}$ is the transmission rate from the left/right contact to the energy level. Here, $\gamma_{L,R}$ depends on the strength of the coupling between the lead and the energy level. At the steady state, the charge occupation of the energy level is constant. This is because there is no net flux into or out of the energy level, i.e., $I_L + I_R = 0$. The average charge on the energy level can then be derived using Eqns. (2.6) and (2.7) and the condition that $I_L = -I_R$

$$N = \frac{\gamma_L f_L + \gamma_R f_R}{\gamma_L + \gamma_R}.$$

Similarly, the steady state current can be also calculated using the condition that $I_L = -I_R$

$$I = I_L = -I_R = \frac{e}{\hbar}\frac{\gamma_L\gamma_R}{\gamma_L+\gamma_R}[f_L(\varepsilon,\mu_R) - f_R(\varepsilon,\mu_R)].$$

In order to take into account the broadening of the molecular energy level due to its interaction with the infinite leads the discrete energy level is replaced by a Lorentzian density of states centered around $E = \varepsilon$, with a width determined by γ

$$D_\varepsilon(E) = \frac{\gamma/2\pi}{(E-\varepsilon)^2 + (\gamma/2)^2},$$

where $\gamma = \gamma_L + \gamma_R$. The occupation of the broadened energy level is now given as

$$N = \int_{-\infty}^{\infty} D_\varepsilon(E)\frac{\gamma_L f_L + \gamma_R f_R}{\gamma},$$

and the steady state current as

$$I = \frac{e}{\hbar}\int_{-\infty}^{\infty} D_\varepsilon(E)\frac{\gamma_L\gamma_R}{\gamma}[f_L(E) - f_R(E)], \qquad (2.8)$$

$$= \frac{e}{\hbar}\int_{-\infty}^{\infty} T(E)[f_L(E) - f_R(E)], \qquad (2.9)$$

where $T(E) = D_\varepsilon(E)\frac{\gamma_L\gamma_R}{\gamma}$ is the total transmission probability (the transmission coefficient). The current integrand is non-zero only in the region $f_L - f_R \neq 0$ and so the integral only needs to be evaluated over an energy window between μ_L and μ_R known as the 'bias window'.

2.3.2 Green's Functions

The toy model of transport introduced in the previous section, while capturing many of the basic concepts involved, needs to be extended to include the real electronic structure of the electrodes and the scattering region. A full quantum mechanical description is now required. Several schemes for achieving goal this exist and include many-body and time-dependent DFT methods [65, 66]. One of the most popular methods, and the one used in this thesis, is the non-equilibrium Green's function formalism (NEGF) combined with DFT [67]. The transport calculations in this work are performed by using the SMEAGOL platform [68, 69], which interfaces a NEGF routine with the DFT code SIESTA.

The NEGF method allows one to calculate the non-equilibrium state of a system consisting of a scattering region attached to semi-infinite electron current/voltage probes (electrodes). These electrodes are assumed to be in equilibrium so all states are filled up to the Fermi level while the occupation of the states in the scattering region has to be determined. A detailed theoretical description of the NEGF equations and formalism can be found in the literature [67, 70, 71, 72, 73]. Here, we initially present some general properties of the Green's functions in relation to electronic transport calculations followed by an outline of the SMEAGOL algorithm.

Introduction to green's functions

The Green's function for an operator $\hat{O}$ is defined as

$$\hat{O}\,G = \hat{I},$$

where $\hat{I}$ is the identity matrix. The scattering region can be described by the single particle Hamiltonian H such that $H\psi_n = E_n S\psi_n$, where ψ_n are the single particle wavefunctions with eigenvalues E and S is the overlap matrix. The retarded Green's function can then be defined as

$$G(E) = [(E + \imath\delta)S - H]^{-1}$$

with $\delta \to 0^+$. The DOS and charge density can then be reformulated in terms of the Green's function and in particular in terms of a spectral function, $A(E)$. This is defined as the anti-Hermitian part of the Green's function [67]

$$A(E) = \imath[G(E) - G^\dagger].$$

The DOS can be written as

$$N(E) = \frac{1}{2\pi}Tr[A(E)S]$$

and the charge density matrix as

$$\rho = \frac{1}{2\pi}\int_{-\infty}^{\infty} f(E)A(E)dE,$$

where $f(E)$ is the Fermi-Dirac distribution.

Green's function for the scattering region

The NEGF formalism requires the device under investigation to be split into three separate subsystems: the left lead, the scattering region and the right lead. The leads are treated as semi-infinite and periodic in the direction of transport. The scattering region, however, breaks the translational symmetry so that the whole system must be described as infinite but yet non-periodic. As a result, Bloch's theorem cannot be used. The NEGF method solves this problem by mapping the infinite system onto an effective finite one. The general set-up is shown in Fig. 2.4.

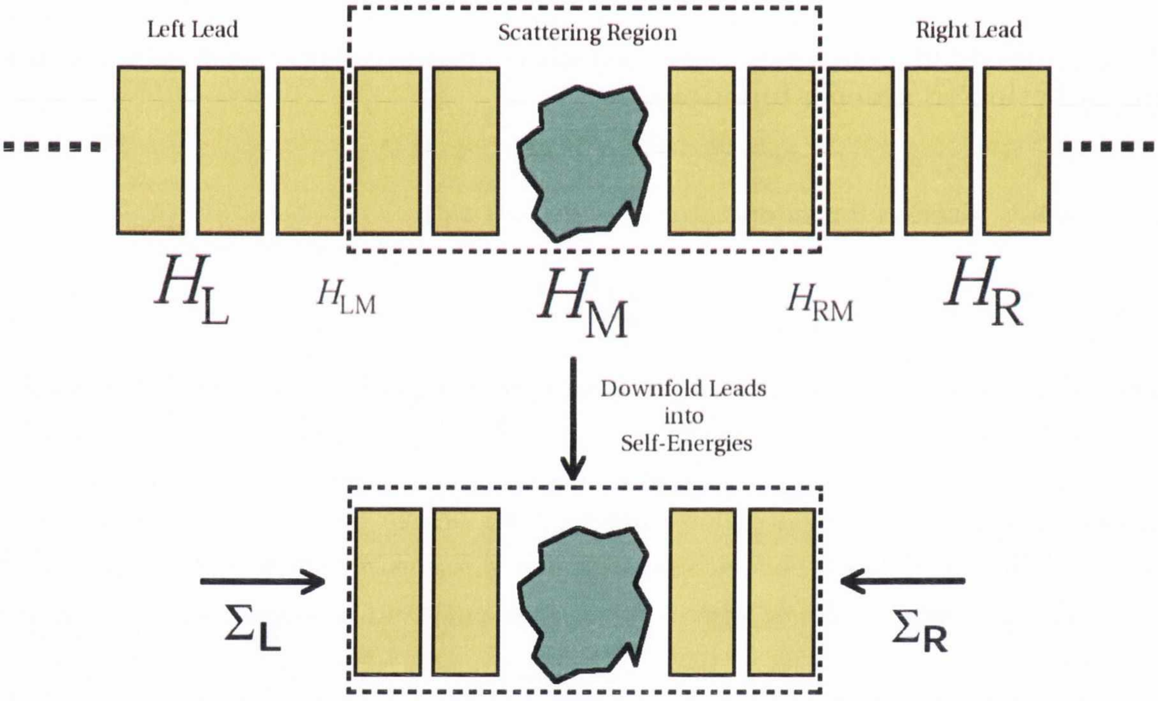

Figure 2.4: A schematic representation of the device set up in SMEAGOL. The device is partitioned into three distinct regions: the left lead, the scattering region and the right lead. The leads are subsequently replaced by effective self energies, Σ_L and Σ_R, that act on the finite Hamiltonian of the scattering region, H_M. These implement the open boundary conditions of the problem.

The central scattering region, also known as the 'extended molecule' (EM) is electronically coupled with both the left and right lead. The leads are assumed to interact with each other only via the EM. The leads are further subdivided into 'principle layers' (PLs), defined such that each PL only interacts with the two neighbouring PLs, one of either side of it. Several PLs are generally included in the scattering region in order to allow the charge density to converge to its bulk value. As a consequence, the electronic structure of the leads is assumed to be independent to that of the scattering region and so can be calculated independently.

The scattering region is described by a finite Hamiltonian, H_M, and the interaction between the scattering region and the left and right leads is described by H_{LM} and H_{RM} respectively, so that the full Hamiltonian of the infinite system is given by

$$H = \begin{pmatrix} . & . & . & . & . & . & . & . & . & . & . \\ . & 0 & H_{-1} & H_0 & H_1 & 0 & . & . & . & . & . \\ . & . & 0 & H_{-1} & H_0 & H_{LM} & 0 & . & . & . & . \\ . & . & . & 0 & H_{ML} & H_M & H_{MR} & 0 & . & . & . \\ . & . & . & . & 0 & H_{RM} & H_0 & H_1 & 0 & . & . \\ . & . & . & . & . & 0 & H_{-1} & H_0 & H_1 & 0 & . \\ . & . & . & . & . & . & . & . & . & . & . \end{pmatrix},$$

where $H_{-1,1}$ represent interactions between PLs. More simply,

$$H = \begin{pmatrix} \mathcal{H}_L & H_{LM} & 0 \\ H_{ML} & H_M & H_{MR} \\ 0 & H_{RM} & \mathcal{H}_R \end{pmatrix},$$

where $\mathcal{H}_L$ and $\mathcal{H}_R$ are the Hamiltonians of the left and right leads respectively (they have infinite dimension). The overlap matrix can be described with a similar matrix structure

$$S = \begin{pmatrix} \mathcal{S}_{\mathcal{L}} & S_{LM} & 0 \\ S_{ML} & S_M & S_{MR} \\ 0 & S_{RM} & \mathcal{S}_R \end{pmatrix}.$$

As the electronic structure of the leads far from the interface is not influenced by that of the scattering region, all the degrees of freedom associated with the leads can be eliminated using a re-normalisation procedure. This can be shown to be exact [74] and replaced by the lead *self energies*, Σ_L and Σ_R for the left and right leads respectively, which describe the electronic structure of the leads and their coupling to the scattering region. The effective Hamiltonian then becomes

$$H_{eff} = H_M + \Sigma_L + \Sigma_R$$

which is non-Hermitian (the number of electrons within the scattering region is not a conserved quantity).

The retarded Green's function for the scattering region is now defined as

$$G_M(E) = [\lim_{\delta \to 0^+} (E + \imath\delta)S_M - H_M - \Sigma_L - \Sigma_R]^{-1}$$

and it contains all the information about the EM attached to the leads.

The 'broadening matrix', Γ, defines the rate at which electrons enter and leave the scattering region

$$\Gamma_{L/R} = \imath[\Sigma_{L/R} - \Sigma^{\dagger}_{L/R}].$$

The application of an external bias, V, affects only the Hamiltonian of the EM while the Hamiltonian of the leads changes only by a simple rigid shift of the on-site energies (because of the efficient electron screening in the metal) so that the Hamiltonian becomes

$$H = \begin{pmatrix} H_L + S_L\frac{eV}{2} & H_{LM} & 0 \\ H_{ML} & H_M & H_{MR} \\ 0 & H_{RM} & H_R + S_L\frac{eV}{2} \end{pmatrix}.$$

By a similar reasoning the self energy and broadening matrices at a bias V can be calculated by determining them at zero bias and by applying a shift of $\mp\frac{eV}{2}$ to the electronic structure

$$\Sigma_{L/R}(E,V) = \Sigma_{L/R}(E \mp \frac{eV}{2}, V = 0),$$
$$\Gamma_{L/R}(E,V) = \Gamma_{L/R}(E \mp \frac{eV}{2}, V = 0).$$

2.3.3 Transmission and Current

Using the Green's function of the EM, the lesser Green's function can then be calculated

$$G^{<}(E) = \imath G_M(\Gamma_L f_L + \Gamma_R f_R)G^{\dagger}_M,$$

where $f_{L/R} = f(E - \mu_{L/R})$ is the Fermi distribution and $\mu_{L/R}$ is the chemical potential of the left/right lead. The density matrix can then be obtained from $G^{<}(E)$ as

$$\rho = \frac{1}{2\pi\imath}\int_{-\infty}^{\infty} G^{<}(E)dE. \tag{2.10}$$

This is the fundamental equation of the NEGF formalism.

Once the converged solution for the charge density is achieved (discussed in the next section) the transmission coefficients and current can be calculated. The two-terminal current can be defined as [75]

$$I = \frac{e}{h}\int_{-\infty}^{\infty} Tr[\Gamma_L G^{\dagger}_M \Gamma_R G_M](f_L - f_R).$$

By comparing this equation to Eqn. (2.8) we can see that the transmission coefficient becomes

$$T(E,V) = Tr[\Gamma_L G_M^\dagger \Gamma_R G_M],$$

where $V = \mu_L - \mu_R$ is the potential bias applied to the system.

2.3.4 Smeagol Code

SMEAGOL (Spin and Molecular Electronics in Atomically-Generated Orbital Landscapes) is a DFT implementation of the non-equilibrium Green's function method, specifically designed for magnetic materials, including non-collinear spin. It is capable of calculating currents and transmission coefficients with a high degree of accuracy and can facilitate large scale simulations. SMEAGOL has been successfully used to describe transport in heterostructures [76], tunnel junctions [77], molecules [78] (including DNA [50]), point contacts [79], nanowires [80] and nanotubes [81], among others.

The only input required by the NEGF formalism is the Hamiltonian of the system. Although in principle any DFT code that outputs a Hamiltonian in a tight-binding-like form can be used, in this case SMEAGOL is interfaced with the DFT code SIESTA (described in Section 2.2.7). As such, it can capitalise on the advantages offered by SIESTA, in particular in relation to the efficient (linear) scaling achieved for large systems. Several aspects of the implementation of the SMEAGOL code will be discussed briefly here. A more thorough description is given in Refs. [68, 69].

The Kohn-Sham Hamiltonian is constructed in SIESTA using a trial initial density matrix. The self energies are determined from a previous calculation for a bulk infinite system corresponding to the leads. By using all this information the effective NEGF Hamiltonian, H_{eff}, can be constructed and it is used to generate the retarded Green's function for the scattering region. The new NEGF density matrix can be determined with Eqn. (2.10) which is then used as the new input density for SIESTA. This process is then iterated until self-consistently is achieved.

With the application of an applied bias, the Hartree potential at the left and right boundaries of the scattering region must match that of the electrodes. This is now shifted by $\pm\frac{V}{2}$ due to the external potential so that $V_H(z_L) = V_H(z_R) + eV$. This can be achieved by simply adding a term $V_{ramp}(z) = eV(z - \frac{z_L - z_R}{2})/(z_R - z_L)$ to the potential calculated within SIESTA for the periodic scattering region (using the fast fourier transform (FFT) method). A schematic of this method is shown in Fig. 2.5. Note also, that due to the FFT method of solving the Poisson equation within SIESTA, the DFT potential is defined only up to a constant. This is problematic

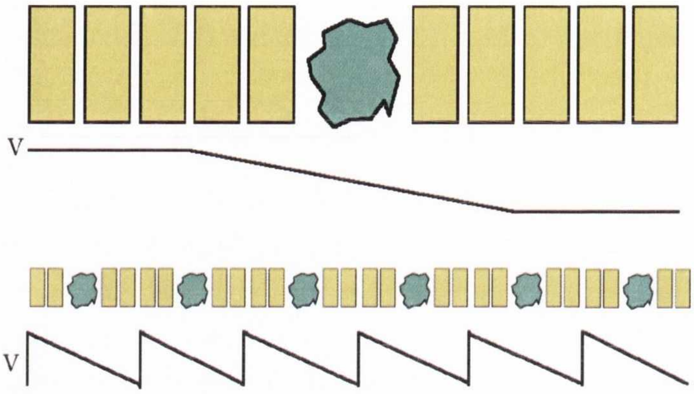

Figure 2.5: The top panel shows the system we wish to study, an extended molecule sandwiched between two leads, together with its potential profile. The bottom panel shows the periodic system obtained by repeating the extended molecule in the direction of the transport and the potential profile ramp, V_{ramp}, that will be added to the potential calculated within SIESTA.

as the potential at the edges of the scattering region must match that of the bulk electrodes. A simple solution is to rigidly shift the Hartee potential of the entire cell in order to enforce the matching of the potential at the boundary. The exact value is chosen by examining the bulk electrode potential at a certain plane and by comparing it to the potential at an equivalent plane in the EM structure.

2.3.5 Limitations of the DFT-NEGF formalism

We end this section with a brief discussion of the limitations of the DFT-NEGF method. Many of these limitations originate in those already discussed for DFT. For example, the identification of the Kohn-Sham orbitals as the system removal energies can generate errors if the exchange-correlation potentials give incorrect results. This in particular can be a problem in the calculation of transport across molecules. Furthermore, the assumption that the equilibrium Kohn-Sham Hamiltonian is valid when the system is not in equilibrium has been questioned [82]. The DFT-NEGF method does not produce the correct the I-V characteristics for systems with strong electronic interactions or where Coulomb blockade effects dominate. Systems with weak coupling are similarly poorly described due, in part, to the absence of the derivative discontinuity of the potential [83]. In saying this however, the DFT-NEGF approach is a powerful method to determine the transport properties of realistic systems at the atomic level where the full problem is treated in an *ab initio* manner.

2.4 Conclusion

In this chapter we have presented the theoretical formalism of both density functional theory and the NEGF method for transport calculations. Density functional theory has emerged as one of the most powerful methods for computing the ground state properties of many-electron systems with a wide range of applications in physics, chemistry and material science. The theory is, in principle, exact and it is limited only by the approximation of the exchange-correlation energy functional. The implementation of DFT in the *ab initio* code SIESTA was described. The NEGF formalism can calculate the quantum mechanical transport properties of nanoscale devices at finite bias. Within the SMEAGOL code the NEGF method is interfaced with the SIESTA code. The current can then be calculated as a function of bias by integrating the transmission coefficient over the relevant energy region. The implementation of the SMEAGOL code was briefly discussed. Finally, some limitations of the DFT-NEGF method were outlined.

CHAPTER 3

Bulk $SrRuO_3$ and $BaTiO_3$

3.1 Introduction to ABO_3 perovskite oxides

The term perovskite is given to the family of materials with general chemical formula ABX_3, where A and B are cations and X is an anion. Perovskite oxides, where X is oxygen, exhibit an exceptional range of properties. They range from insulators to semiconductors to metals, and can possess properties such as ferromagnetism, anti-ferromagnetism, ferroelectricity, high dielectric constant, highly correlated electron behaviour, colossal magnetoresistivity, high-T_C superconductivity and many more. Such electronically rich behaviour can be attributed to the subtle interplay between charge, spin and orbital ordering. Both fundamental and device-orientated research have striven to master these interactions by way of doping, applying strain and applying external magnetic or electric fields. As such, these materials show considerable promise for future technical applications, even more so due to the tremendous progress made in recent years in the thin film oxide growth.

Single-crystalline films of various thicknesses can now be routinely grown on a wide variety of substrates without defects and with a high degree of control of the structural and electronic properties of the film. This was achieved by an advancement in growth techniques, in particular by the techniques of physical vapor deposition such as sputtering, pulsed laser deposition and molecular beam epitaxy. The maturation of these methods has resulted in sub-monolayer control over deposition to the extent that oxide lattices can be grown with a similar quality to semiconductor lattices. Indeed, perovskite oxides can now be deposited on silicon substrates with atomically sharp interfaces.

Along with a desire to understand the fundamental properties of oxide materials, interest is also driven by the prospect of creating new devices. In particular, oxides are playing an ever increasing role the in the enhancement of spintronic effects such as in CMOS-based and emergent logic and memory devices.

3.1.1 ABO_3 structure

The perfect perovskite structure has ABO_3 stoichiometry, where A is a mono- or divalent metal and B is a tetra- or prevalent atom. In its cubic allotrope, which in general exists at high temperatures, it can be described as a cube with the A cations located at the cube corners, the B cation at the body centre and the oxygen anions located at the face centres forming an octrahedra around the B ion as shown in Fig. 3.1(a). It can be alternatively be seen as a cubic network of corner-sharing BO_6 octahedra, where the A-site cation is located at the center of a cube defined by eight BO_6 units giving it twelve-fold coordination.

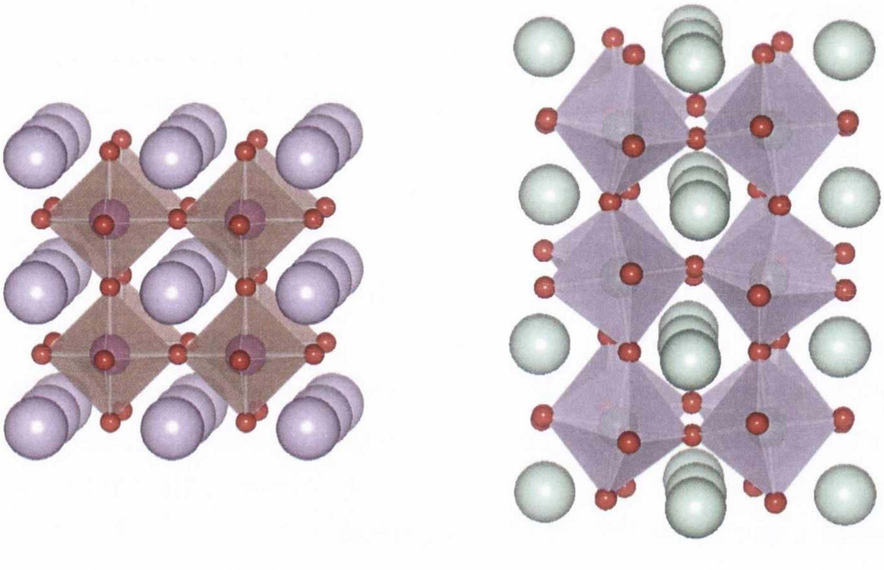

(a) $Pm\bar{3}m$ space group (b) $Pbnm$ space group

Figure 3.1: Schematic representation of the ABO_3 perovskite.

The ideal perovskite is cubic (space group $Pm\bar{3}m$), however it readily undergoes structural transitions, involving only small distortions from the ideal geometry, owing to the range of cation sizes that can be accommodated in the structure. Deviations from the ideal cubic structure are defined by the Goldschmidt tolerance factor

$$t' = \frac{R_A + R_O}{\sqrt{2}(R_B + R_O)} \quad ,$$

where R_i is the radius of atom i, and can be attributed to the requirement to optimize the anion coordination about the A-site cation [84]. The cubic perovskite structure is formed when $t' \approx 1$. When $t' > 1$ the A cation is too large for its interstitial position and the structure can develop a small polar distortion. When $t' < 1$, the A cation is now too small and so cannot bond effectively with the oxygen ions surrounding it. If t' is only slightly less than 1 (between 0.71 and 0.9) then small rotations and tiltings of the oxygen octahedra will be sufficient to stabilize it [resulting in, for example, the orthorhombically distrorted structure in Fig. 3.1(b)]. If the A and B cations are of similar size ($t' < 0.71$) a more strongly distorted structure will be required to stabilise it, for example the ilmenite or the corundum structure.

In this chapter we will focus on the bulk properties of two very different perovskite oxides that form the basis for much of the work in later chapters. Firstly, we will discuss the $4d$ itinerant ferromagnet $SrRuO_3$ and in particular the effect of electronic correlation on its electronic properties. We then describe the prototypical ferroelectric material $BaTiO_3$ by using two different exchange correlation functionals with the intention of finding the best description of its transport properties when incorporated in a tunnel junction.

3.2 Structural and Electronic Properties of SrRuO$_3$

3.2.1 Introduction

Conductive oxides are essential components in composite heterostructures where they are often used as electrode materials in thin film applications [85, 86, 87]. In the perovskite crystal family, the itinerant ferromagnetic SrRuO$_3$ (SRO) is a popular choice since it is one of the more conductive metallic oxides with good thermal properties [88]. In thin films, SrRuO$_3$ is intensely investigated as a possible route to the realization of novel field-effect devices [89, 90]. In addition, it is of particular interest to the spintronic [91, 92] and multiferroic [21, 93] communities, which have been recently energised by the possible device applications available from engineering interface phenomenon [94, 95, 96, 97, 98, 99, 100]. However, one limitation in the design of thin film oxide devices is the observation of increased resistivity in metal oxides as the film thickness decreases. Such behavior is clearly present in ultra-thin films of SrRuO$_3$, where a metal-to-insulator (MI) transition [101] occurs at four monolayers. This substantial change in the electrical conductivity presents a serious challenge for device miniaturization. This thin film MI-transition has generally assumed to be attributable to electron-electron correlation effects and so here we explore the effect of electron correlations on the electronic properties of SrRuO$_3$.

The $3d$ transition metal oxides (TMOs) are known to possess strong electron-electron correlations that can drive a system that should be metallic, within a simple band picture, into an insulating state. Due to the large spatial extent of the $4d$-orbitals in the ruthenates, correlation effects are anticipated to be less important as stronger hybridization provides more effective screening and a reduced Hubbard U Coulombic repulsion energy. Many experimental studies have already addressed the degree of electron-electron correlation in SrRuO$_3$ including X-ray and ultraviolet photoemission spectroscopy [102, 103, 101, 104], specific heat measurements [105], conductivity measurements [106], and transport experiments [107]. For example, Kim and coworkers [102] use X-ray photoemission spectroscopy (XPS) to identify how such correlations change within the ruthenate family, and Toyota *et al.* [101] use photoemission spectroscopy (PES) to detail the metal-insulator transition in SrRuO$_3$ as a function of film thickness concomitant with the onset of magnetism. In all of these studies, the general consensus is that electron correlation effects *do* play an important role in determining the electronic structure of this itinerant ferromagnet, but to what degree remains unclear. Furthermore, some theoretical investigations have begun examining covalency [108], correlation [109] and orbital ordering [110] effects in bulk $SrRuO_3$. The magnetic properties of $SrRuO_3$ under epitaxial strain have also been investigated with first-principles techniques [111].

Here, first-principles density functional theory (DFT) calculations are performed to identify the degree of correlation in bulk $SrRuO_3$. Correlation effects are introduced into the conventional band theory (local spin density) approach to treat the Ru d-orbitals and their hybridization with O $2p$-orbitals via the pseudopotential self-interaction corrected (ASIC) local spin density method. Two structural variants are considered - the ideal cubic perovskite structure and the experimentally observed orthorhombic structure, which includes tiltings and rotations of the RuO_6 octrahedra.

3.2.2 Crystal Structure & Magnetism

Due to the small size of the Sr^{2+} cation, $SrRuO_3$ undergoes a series of structural transformations with temperature, from high symmetry cubic ($Pm\bar{3}m$, stable above 950 K) to tetragonal ($I4/mcm$, stable above 820 K) to distorted orthorhombic structure ($Pbnm$) at low temperatures. The deviation in the structure from the high symmetry cubic state is described by the tilting angle $(180° - \phi)/2$ and the rotation angle $(90° - \theta)/2$ of the oxygen octahedra. The RuO_6 octahedra tilt in alternate directions away from the c axis and rotate around the b axis. Adjacent octahedra distort in opposite directions (see Fig. 3.2).

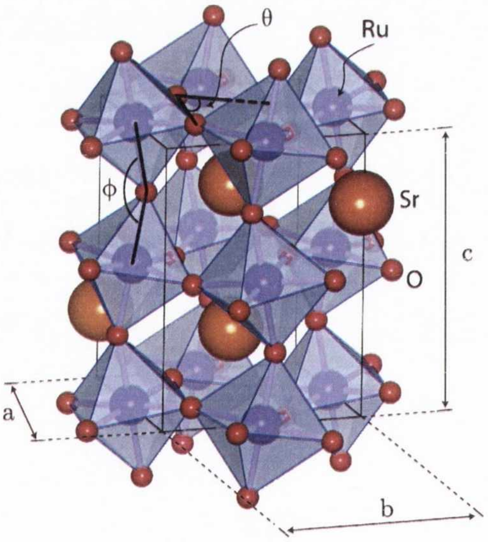

Figure 3.2: The $Pbnm$ crystal structure of $SrRuO_3$.

By using the Shannon-Prewitt radii for this compound a predicted Goldschmidt tolerance factor of t'=0.908 is found, which is far from the the ideal case of t'=1, suggesting that distortions should indeed occur. A rotation angle of 7.99° and a tilting angle of 10.56° (corresponding to a Ru-O-Ru angle of 158.89°) are found for *Pbnm* $SrRuO_3$. Such distortions reduce the hybridization between the Ru $4d$ states and the O $2p$ states narrowing the band width and thereby increasing the degree of correlation.

Below approximately 160 K, $SrRuO_3$ exhibits strong ferromagnetic behavior, and has a measured Rhodes-Wohlfarth ratio [112] (μ_{eff}/μ_{ord}) of 1.3 suggesting that its magnetism can be well described by a localized d-electron model similar to the elemental ferromagnetic metals. Within this model and under an octahedral crystal field, the $4d$-manifold splits into a threefold degenerate t_{2g} subband that is lower in energy than the twofold degenerate e_g states. Neglecting covalency in the undistorted cubic structure, the spin-only magnetic moment for $SrRuO_3$ is 2 μ_B and corresponds to a low-spin state for Ru^{4+} ions ($d^4 : t^3_{2g\uparrow}, t^1_{2g\downarrow}$). Experimentally, however the magnetic moment is measured to be closer to 1.1 μ_B/f.u., although values ranging from 0.9 μ_B/f.u. and 1.6 μ_B/f.u. have been reported [113]. (The spread in values is attributed to the large magnetocrystalline anisotropy of the material, and the difficulty in making large single-domain samples.) First-principles calculations also report a magnetic moment ranging from 0.9 μ_B/f.u. to 2.0 μ_B/f.u. [114, 105, 115, 116] depending on the details of the exchange and correlation functional and the treatment of the core and valence electrons. The reduced calculated magnetic moment in the solid compared to that in the free ion is due in part to the large spatial extent of the $4d$ orbitals, which results in a significant overlap (hybridization) with the oxygen $2p$ orbitals. Furthermore, due to the metallic character of $SrRuO_3$, an overlap of the majority and minority Ru $4d$ bands occurs at the Fermi level; as a result partial occupation of the minority bands also leads to the magnetic moment reduction.

In this work, we examine both the electronic and magnetic structure of the *Pbnm* and $Pm\bar{3}m$ crystal variants. Metallicity and magnetism are both related to the d bandwidth, which in turn depends on both correlations and structural properties such as tiltings and rotations of the oxygen octahedra. Our goal is to identify the relative contributions of electron-electron correlation effects and structural distortions to the electronic properties of $SrRuO_3$.

3.2.3 Theoretical Methods

LSDA

Our initial electronic band structure calculations were performed within the local spin density approximation [117] (LSDA) using the SIESTA [118, 119, 120] density functional theory (DFT) package. We used the Perdew-Zunger [44] parametrization of the Ceperley-Alder data [121] for the exchange and correlation (XC) functional.

The core and valence electrons were treated with norm-conserving fully separable [122] Troullier-Martin [123] pseudopotentials.[1] The localized atomic orbitals for each atom used a single-ζ basis set for the semicore states and a double-ζ for the valence states. Total energies were computed in a uniform real space grid, corresponding to an equivalent plane-wave cutoff of 800 Ry. The Brillioun zone for the cubic structure was sampled with a $26\times26\times26$ k-point Monkhorst-Pack mesh, and with a $15\times15\times12$ k-point mesh for the *Pbnm* structure. Integrations were performed with a Gaussian broadening of 0.10 eV in all calculations.

The equilibrium lattice parameter for the cubic structure was found by fitting the total energy as a function of volume to the Murnaghan equation of state. The theoretical equilibrium volume is 59.75Å^3, about 4.7% smaller than the experimental volume of 62.736Å^3 as is to be expected from an LSDA calculation. The cell parameters and atomic positions of the orthorhombic structure (Table 3.1) were optimized by starting from the theoretical positions reported in Ref. [111] and the ionic coordinates were relaxed until the Hellmann-Feynman forces on the atoms were less than 4 meV Å^{-1}.

Atom	Site	x	y	z
Sr	$4c$	-0.0050	0.02948	0.25
Ru	$4a$	0.5	0.0	0.0
O(1)	$4c$	0.0653	0.4939	0.25
O(2)	$8d$	0.71419	0.28569	0.03439

Table 3.1: Calculated structural parameters for SrRuO$_3$ with the *Pbnm* symmetry. The orthorhombic lattice constants are given as a = 5.5031, b = 5.4828, and c = 7.7459 Å.

Investigations of the electronic structure of $Pm\bar{3}m$ SrRuO$_3$ have been described by several different groups [114, 105, 111] within the LSDA; and here we briefly summarize those conclusions and remark that our results are consistent with the earlier calculations. A metallic ferromagnetic ground state is found to be stable, with strong Ru 4d character at the Fermi level. Substantial hybridization occurs between the O 2p states and the Ru 4d states and no energy gaps are observed in the density of states (DOS). The calculated magnetic moment is also always reduced from the fully ionic limit of 2 μ_B.

---

[1] The electronic configurations for each atom is: Sr $4s^2 4p^6 4d^0 4f^0$ (1.50, 1.50, 2.00, 2.00), Ru $4s^2 4p^6 4d^7 4f^0$ (1.30, 1.30, 1.40, 1.30), and O $2s^2 2p^4 3d^0 4f^0$ (1.15, 1.15, 1.15, 1.50), where the cutoff radii (Bohr) for each orbital is given in parentheses.

In Section 3.2.4, we will discuss in detail the electronic structure of orthorhombic $SrRuO_3$, where the need for the 'beyond-LSDA" approaches becomes more transparent. The method to examine electron-electron correlation effects is described in more detail in the remainder of this section.

Self-interaction corrected (SIC) methods

It is well known that the LSDA and other approximate local and semi-local XC-functionals are affected by spurious self-interaction (SI). This unphysical self interaction error is not a problem for materials with delocalized electronic states, e.g. simple metals or semiconductors with mostly covalent interactions. However, it can make a significant contribution to the total energy in systems characterized by spatially localized electronic states. The self-interaction in itinerant-correlated systems, such as $SrRuO_3$ has not yet been previously evaluated and therefore $SrRuO_3$ is an excellent testing ground for the SIC methods.

Many different methods have been proposed to remove SI in DFT calculations since there is no unique way to define SIC for a solid. The first was made by Perdew and Zunger [44], where they directly removed the self-XC energy of all the occupied Kohn-Sham orbitals from the LDA XC-functional. The approach we use here incorporates part of the SIC into the pseudopotential (ASIC) by a nonlocal, atomic-like contribution, which reduces many of the computational overheads [46, 47, 45]. This procedure allows the SIC to be separated into contributions from both the core and the valence electrons. In this work, we use the method described in Ref. [47]. The atomic SIC is then rescaled by the self-consistent occupation numbers of the orbitals within the crystal. In this scheme, only the valence bands are corrected since the empty conduction bands, coming from orbitals where the occupation numbers are close to zero make no contribution. In comparison to LSDA+U, ASIC does not require external parameters, it can be applied to both magnetic and non-magnetic systems, and does not require a choice of which orbitals to correct [124].

3.2.4 Results & Discussions

As we have mentioned before, the electronic structure of $SrRuO_3$ has been investigated previously using the LSDA [114, 105, 111]. Here we verify our own LSDA calculations, with an emphasis on the discrepancies between the experimental measured photoemission results [102, 101] and our calculated electronic structure of the orthorhombic material. We then extend our study to a "beyond LSDA" approach to examine effects of the correlation on the electronic structure.

3.2.5 LSDA Results

Cubic structure

The total energies were calculated for the cubic ferromagnetically ordered $SrRuO_3$ and the non-magnetic state using the optimized lattice parameters. The ferromagnetic groundstate is found to be lower in energy by 31.6 meV with respect to the constrained paramagnetic (non-spin-polarised) solution.

The density of states of cubic $SrRuO_3$ is shown in Fig. 3.3.

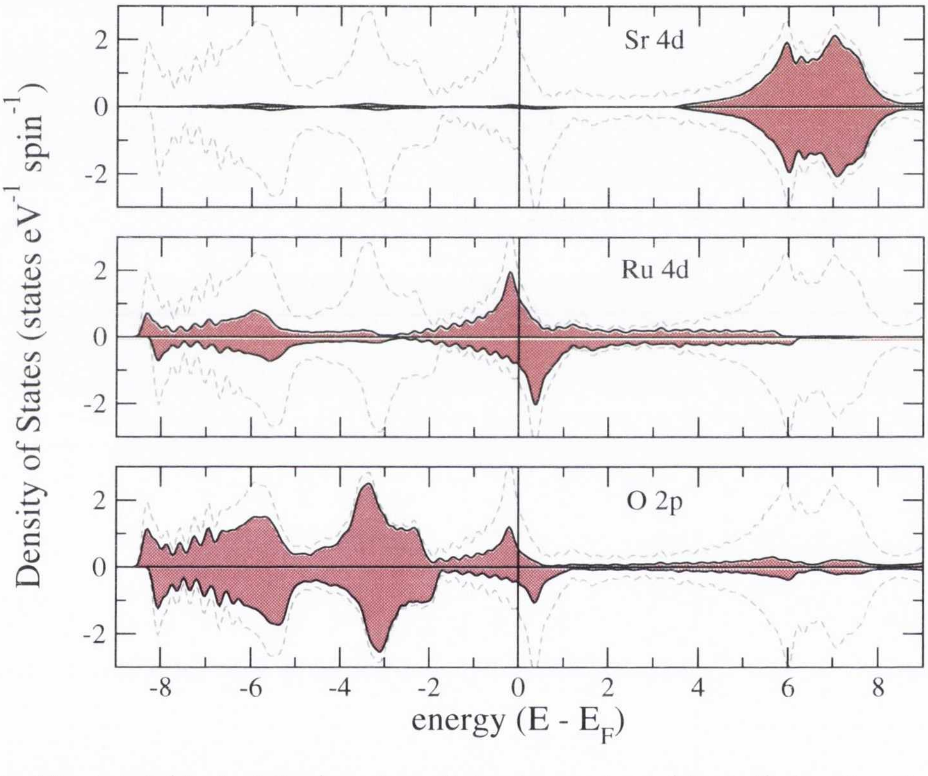

Figure 3.3: The total (dashed line) and partial spin-resolved (shaded) density of states for cubic $SrRuO_3$ calculated within the LSDA. (UPPER) Sr $4d$ states, (MIDDLE) Ru d states and (LOWER) O $2p$ states.

The valence band is composed largely of O $2p$ states hybridized with Ru $4d$ states, with the oxygen contribution predominately found in lower regions of the valence band and the Ru one dominating at the Fermi energy. The large peak in the DOS near the Fermi level is caused by the fairly flat Ru t_{2g} bands while the strongly hybridized e_g orbitals form broader bands at the bottom of the valence and conduction bands. The Sr $4d$ states are found around 5 eV above the Fermi energy (E_F).

The exchange splitting causes an energy shift between the majority and minority spin states; at the Γ point a splitting of $\approx$0.60 eV is observed in the Ru $4d$ states while a split of $\approx$0.30 eV in found in the O $2p$ states. The calculated magnetic moment per formula unit was found to be 1.26 μ_B [2]. Approximately 70% of the moment is found on the Ru atoms, with the remaining distributed over the oxygen octrahedron.

Orthorhombic structure

By using the optimized LSDA lattice parameters for the *Pbnm* structure, we find that the ferromagnetic ground state is 6.34 meV/f.u. lower in energy than the constrained nonspin-polarised structure, and additionally it is 150 meV/f.u. lower in energy than the ferromagnetic cubic phase. This energy stabilization can be associated with the oxygen octahedral tiltings and rotations, and agrees well with previous first-principles studies that used experimental lattice parameters [114, 111] (the LSDA underestimates the lattice parameters by only about 1%). Also it is consistent with the experimental observation of ferromagnetic $SrRuO_3$ in the distorted $GdFeO_3$ structure [126].

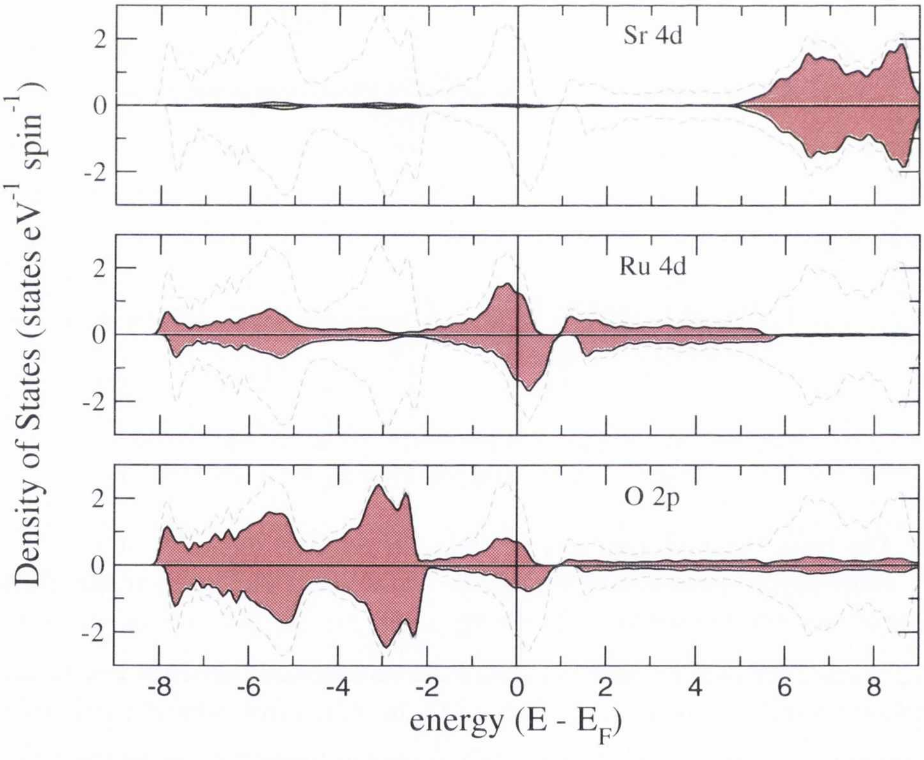

Figure 3.4: The total (dashed line) and partial spin-resolved (shaded) density of states for *Pbnm* $SrRuO_3$ calculated within the LSDA. (UPPER) Sr 4*d* states, (MIDDLE) Ru *d* states and (LOWER) O 2*p* states.

The (P)DOSs for the orthorhombic structure are shown in Fig. 3.4. This can be seen to be similar to those of the cubic structure discussed earlier (Fig. 3.3). Con-

---

[2] Local magnetic moments are determined, here and elsewhere, using standard Mulliken population analysis [125].

sistent with the reduction in Ru 4*d* - O 2*p* overlap resulting from the tiltings and rotations, the bandwidths are slightly narrower in the orthorhombic structure. This results in gaps appearing in both the majority and minority states at about 0.9 eV above the Fermi level. Interestingly, the Ru 4*d* exchange splitting is reduced slightly at Γ. This is accompanied by a reduction in the magnetic moment compared with the cubic structure to 0.92 μ_B/f.u. Turning now to the magnetic properties of the orthorhombic structure, there is yet another discrepancy between the LSDA calculations and the experimental results. For the orthorhombic structure, a moment of 0.92 μ_B/f.u. was found with the relaxed atomic positions. As noted, the spontaneous magnetization in the bulk (films) has been reported to be near 1.6 μ_B ($1.4\mu_B$). Some of the underestimate in the magnetic moment compared to experiment can be attributed to the LSDA in which it is known that solids are typically overbound, leading to greater bond strengths and enhanced hybridization between the Ru 4*d* states and the O 2*p* states.

Finally for the LSDA section, we compare our first principles LSDA results with recent PES data [103, 127, 128] with the goal of identifying which features are driven by correlation. In an ideal single-electron picture, the measured PES would consist of narrow peaks corresponding to the energies required to excite noninteracting electrons from the valence band into the continuum. However, the photoemission energies are more accurately interpreted as differences between two many-body N-electron states: the ground state, and the excited state with a photoelectron and hole. The effect of the many-body interactions is to broaden the one-electron peaks and shift spectral weight into so-called quasiparticle peaks. The strongest reduction in spectral weight from correlation effects occurs from so-called coherent peaks near E_{F}, and it is accompanied by transfer of the spectral weight to higher energy features (incoherent peaks). The redistribution of the incoherent spectral weight into a well-defined satellite structure is indicative of strong correlations, whereas a redistribution into the background spectral distribution with a renormalization of the bandwidth indicates weak correlations.

In Fig. 3.5, we compare the measured spectra (cf. Refs. [101] and [129] for further information on the experimental sample preparation) with our LSDA-calculated band structure. Before commenting on the discrepancies between the bulk polycrystalline spectrum and that of the thin film, we point out that both spectra are dominated by three principle features (with the caveat that the bulk spectrum is highly broadened), which are assigned to different electronic states by a comparison to our calculated densities of states. In order to make this comparison, we convolute an energy-dependent Lorentzian function [full width at half maximum (FWHM) = $0.1\,|\epsilon - \epsilon_F|$ eV)] with the calculated DOS to account for lifetime broadening. A Gaussian function with a

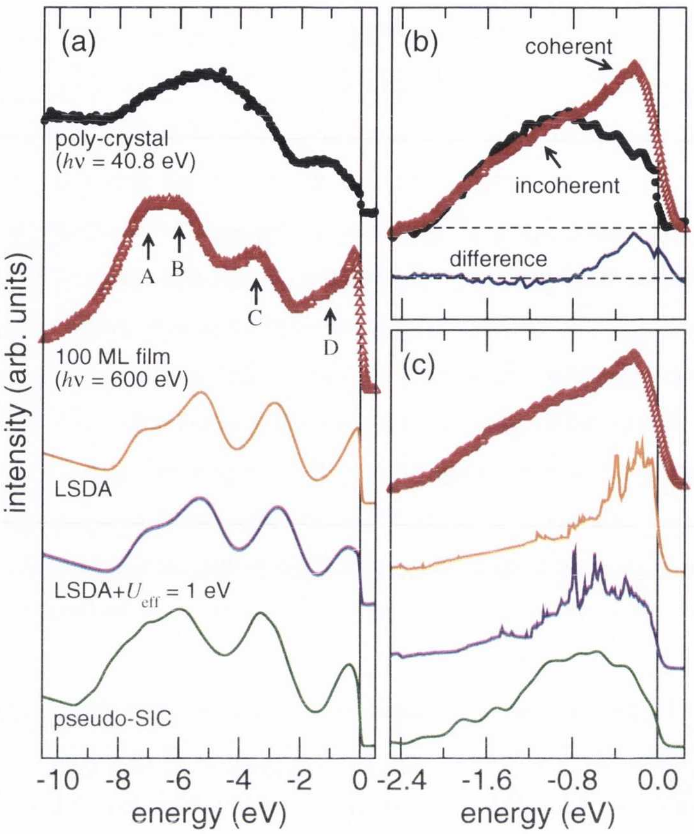

Figure 3.5: The experimental PES spectra for bulk polycrystalline [129] $SrRuO_3$ (filled circles) and 100 monolayer $SrRuO_3$ film [130] (triangles) grown on $SrTiO_3$ are compared to the calculated LSDA(+U) and ASIC densities of states. The calculated DOS are broadened with an energy dependent Lorentzian (FWHM = $0.1\,|\epsilon - \epsilon_F|$ eV) and a Gaussian function (0.34 eV FWHM). An energy dependent parabolic background has also been added.

FWHM=0.34 eV is also used to account for the instrumental resolution, and an energy dependent parabolic background is added. The O $2p$ bonding states are located between 8 and 5 eV (A and B), while the O $2p$ nonbonding states are found at around 3.5 eV (C). In the range between 8 eV up to the Fermi level there are the occupied Ru $4d$ states, with the t_{2g} state lying across the Fermi energy beginning at 3 eV and with a broad shoulder (D) between 2.4 and 0.7 eV.

In Fig. 3.5(b), we show more clearly the Ru $4d$ states around the Fermi level by removing the background intensity and the contribution of the O $2p$ states by fitting a Gaussian function to the experimental spectral distribution. In the thin film sample, the sharp coherent feature located below the Fermi level is broadened by the many-body effects already described; however an additional shoulder appears between 2.4 and 0.7 eV. This subtle spectral feature is a signature of correlation and is primarily due to spectral weight transfer from the coherent to the incoherent feature. In contrast, the bulk polycrystalline sample shows only a single broad feature centered at 0.8 eV, with reduced spectral weight below the Fermi level. The question that one needs to answer before proceeding is whether or not this broad feature is due to intrinsic correlations or due to sample preparation techniques. Based on previous experimental comparisons between $SrRuO_3$ films and polycrystals [131, 132], this shift in the spectral weight to the incoherent peak is attributed to the creation of near surface states induced during *in situ* scraping and not due to intrinsic correlation effects. Additionally the presence of grain boundaries and compositional defects are also known to yield reduced coherent peak features in polycrystalline samples. We therefore restrict our comparison of the PES data to the 100 monolayer film for the remainder of this study, since it more accurately describes the intrinsic electronic structure.

Some important discrepancies exist between our LSDA results and the spectroscopic data: the Sr $4d$ states are positioned approximately 1.5 eV lower in energy than is expected from the experimental spectra as determined in the bremsstrahlung isochromat spectroscopy (BIS) and x-ray absorption spectroscopy (XAS) spectra (not shown) [103, 127]. The spread of the O $2p$ states is also underestimated. The most drastic difference, and one examined many times in the literature, occurs in the Ru $4d$ states, where indications of correlations are found. In Fig. 3.5(c), we show only the Ru $4d$ states near E_{F} compared to our calculated densities of states (without broadening). As mentioned, the signature of strong correlations as observed in the PES data is the strong renormalization (or even absence) of the quasiparticle peak near E_{F} or large satellite peaks. In the thin films, the weak coherent t_{2g} peak centered about 0.5 eV below the Fermi level has a substantial incoherent feature near 1.2 eV and is good evidence for localized electronic states from strong correlation effects. Experimentally the Ru $4d$ spectrum shows a coherent peak that is approximately 0.40 eV broader than what the LSDA predicts. Furthermore, the incoherent feature in the experimental PES is 1.0 eV broader than in the LSDA calculation, where it is suppressed. The long tail in the t_{2g} states is likely due to hybridization with the nonbonding O $2p$ states.

More recent ultraviolet photoemission spectroscopy (UPS) data [104] suggest that the Ru stoichiometry plays a significant role in determining the spectral weight and intensity of the t_{2g} peak at the Fermi level. For stoichiometric $SrRuO_3$ films, the spectral intensity near the Fermi level is in much better agreement with the calculated PDOS, while Ru deficient samples have a reduced intensity. These facts suggest that previous comparisons may have been made with nonstoichiometric Ru samples, which may be caused by a high partial pressure of oxygen during growth. Although the Ru cation deficiency appears to explain the discrepancy with experimentally measured spectra, it is difficult to fully remove correlation effects that implicitly result from changes in stoichiometry, e.g., the *d* bandwidth can be varied by changing the volume of the unit cell via changes in O-Ru-O bond angles which occurs upon Ru vacancy formation. For example, Siemons and co-workers [104] found the enhancement of an incoherent peak at approximately 1.5 eV below the Fermi level in ruthenium poor samples measured with ultraviolet photoemission spectroscopy. Future first-principles calculations may be able to identify the role of these defects. It is clear that the LSDA incompletely describes the electronic and magnetic structure of bulk SrRuO3, and this suggests that some underlying physics may be missing in the local spin-density approximation. We next explore an extension of that description to address whether the incoherent feature missing in the LSDA calculations, as well as the reduced magnetization, could be due to correlated electron - electron interactions, and whether these can be captured by a static on-site correction.

3.2.6 "Beyond LSDA" Results

We now explicitly add correlation effects into our electronic structure calculations for $SrRuO_3$ using the ASIC method outlined above.

Orthorhombic structure

Fig. 3.6 shows the densities of states calculated with the ASIC method for both *Pbnm* and $Pm\bar{3}m$ $SrRuO_3$. When compared to the LSDA, the correlated bands are narrower, with energy gaps appearing in both spin channels for the orthorhombic structure (left panel). The inclusion of correlations causes a 70% drop in the total DOS at the Fermi level compared with LSDA, with the result that the contribution to the Ru 4*d* states is almost entirely derived from the minority spin channel, and the material is close to half-metallicity. This significantly enhances the magnetic properties compared to the LSDA, increasing the magnetic moment per formula unit to around 1.9 μ_B (Table 3.2). In addition, the peak positions of the correlation-included densities of states are in better agreement with the experimental spectra (Fig. 3.5), although the intensity of the O 2*p* peak at $\approx$7 eV is still low compared with that of the Ru t_{2g} peak.

We note that the ASIC method gives very similar results to LSDA+U when a U_{eff}=1.0 eV is used. (For larger U_{eff} values they are still consistent, however they differ in a few of the finer details). The main difference between the electronic structures calculated with U_{eff} = 1 eV and the ASIC methods is a larger bandwidth of the

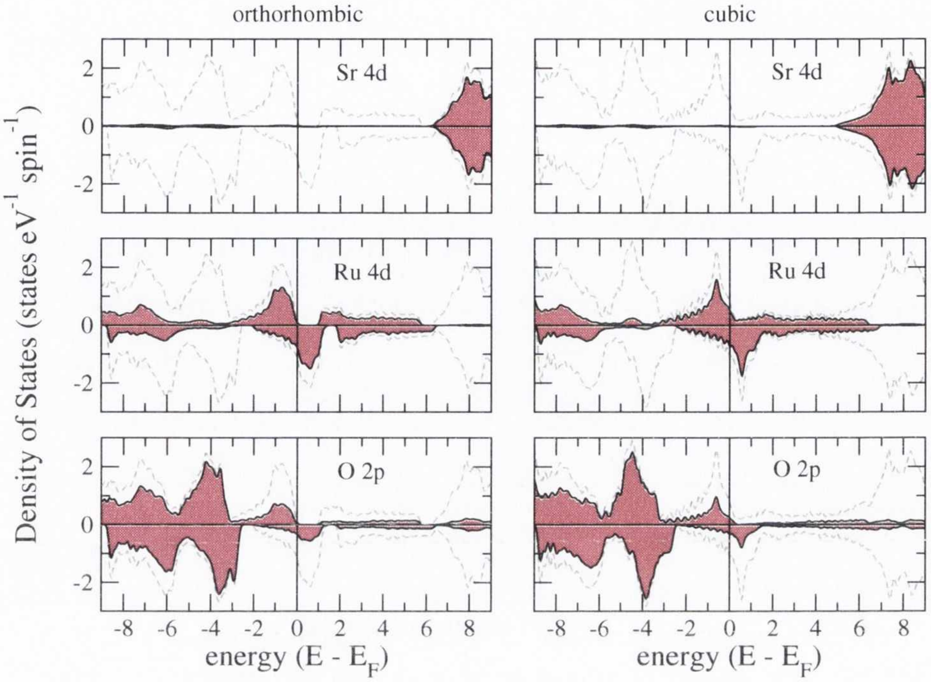

Figure 3.6: The total (dashed line) and partial spin-resolved (shaded) density of states for cubic (left) and orthorhombic (right) $SrRuO_3$ calculated with ASIC are shown in each panel. (UPPER) Sr 4d states, (MIDDLE) Ru d states, and (LOWER) O 2p states.

	Orthorhombic	Cubic
Experimental	0.90-1.60	n/a
LSDA	0.92	1.26
ASIC	1.99	1.77
LSDA+U_{eff}=1eV	1.97	1.64

Table 3.2: Summary of the calculated magnetic moments given in μ_B compared to the available experimental data.

occupied orbitals, by ≈1.7 eV, in the ASIC calculation (Fig. 3.7). This has the greatest effect on the Ru 4d bands and the O 2p bands near 8.0 eV. As a result, the ASIC shows better agreement with the PES in the bandwidth for the O 2p states between 8 and 4 eV, and as a result reproduces more closely the correct ratio of the higher energy features to the Ru t_{2g} peak. In Fig. 3.5(c) it is clear that both the LSDA+U method and the ASIC suppress the t_{2g} states at the Fermi level and shift the center to higher energy (near 0.6 eV). However, the ASIC more accurately reproduces the incoherent feature found experimentally at 1.2 eV when compared to the LSDA+U result, while still maintaining a defined coherent peak.

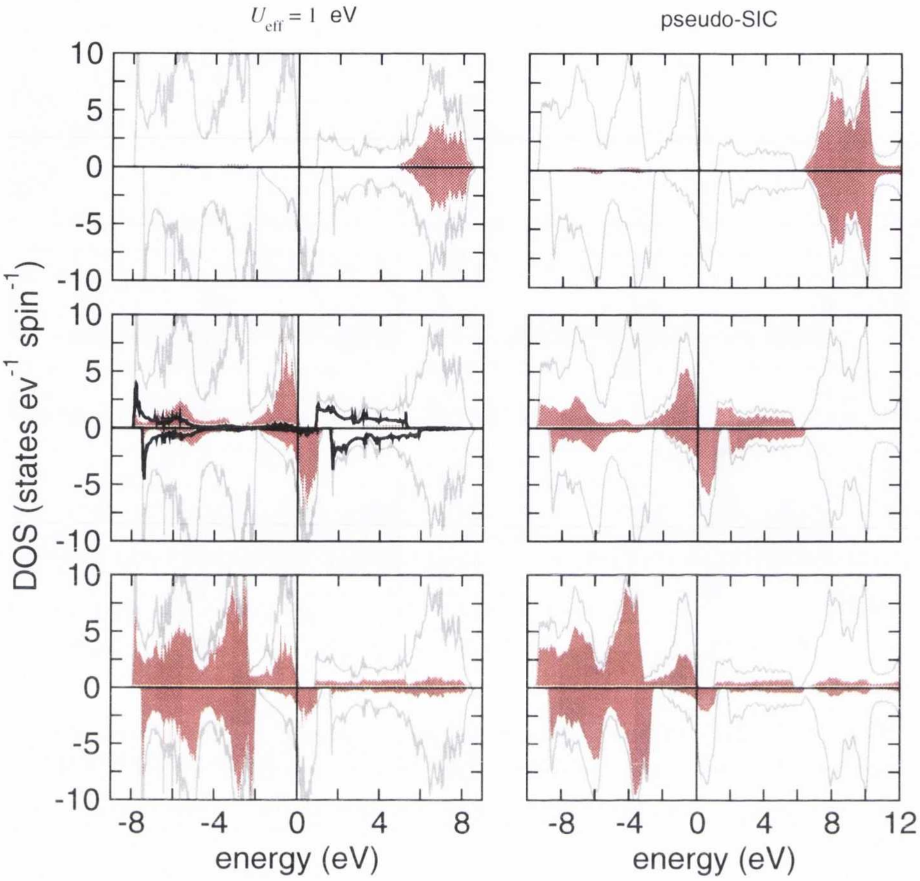

Figure 3.7: The total (gray line) and partial spin-resolved (shaded) density of states for orthorhombic $SrRuO_3$ calculated with U_{eff} = 1 eV (left) and ASIC (right) are shown in each panel. (Upper) Sr 4*d* states, (middle) Ru 4*d* states, and (lower) O 2*p* states.

Cubic structure

We complete this discussion by describing the differences in the calculated bulk cubic electronic structure with the addition of correlation effects. This will help to isolate the contribution of the octahedral distortions in the orthorhombic structure to the bandwidth narrowing. Overall the weight and shape of the total density of states calculated by including correlations are consistent with that calculated by the LSDA, with the exception that the large densities of states at the Fermi level (majority t_{2g} states) are pushed lower in energy (Fig. 3.6). The observed exchange splittings for the various states are overall larger for the cubic structure, and this is consistent with the electronic structures calculated with the LSDA. The magnetic moment is found to be $\approx 1.77\ \mu_B$ and a fully metallic ground state is always maintained.

To summarize the bulk $SrRuO_3$ results, ASIC improves the description of the electronic and magnetic structure. However, the precise experimental spectra are not fully reproduced although correct peak assignments can be made. By correcting the SI error in LSDA, the Ru t$_{2g}$ bandwidths are improved with respect to the experiments [109]. The total width of the O 2p band structure is also increased to approximately 7 eV in agreement with the spectral weights. We therefore suggest that SrRuO$_3$ can best be described as a moderately correlated material. Finally, as stated earlier, the intensity at E_F has been decreased in comparison to LSDA, although it is still larger than experimentally observed.

3.2.7 Spin Polarisation & Transport Properties

SrRuO$_3$ has been experimentally reported [133] to belong to the class of negatively spin-polarized materials characterized by a greater number of minority spins at the Fermi surface which are aligned antiparallel to the bulk magnetization. However, the magnitude of the spin polarisation at the Fermi level remains controversial within the experimental community, due in part to the different definitions of the spin polarisation (resulting from the different experimental techniques used to probe this quantity), as well as to difficulties in performing the experiments. Furthermore, the theoretical community has also not converged on the magnitude of the spin polarisation, due to the sensitivity of the Ru t$_{2g}$ states near E_F on the choice of exchange-correlation functional. In this section, we perform first-principles transport calculations on orthorhombic and cubic SrRuO$_3$, and compare our results to the available data in the literature. We also describe the various definitions of the spin polarisation commonly used in the literature, and relate them to calculated *ab initio* quantities.

The spin polarisation at the Fermi level $\mathrm{P}_0^{E_F}$ can be calculated from the density of states at the Fermi level (N_{E_F}) by the following ratio:

$$P_0^{E_F} = \frac{N_{E_F}^{\uparrow} - N_{E_F}^{\downarrow}}{N_{E_F}^{\uparrow} + N_{E_F}^{\downarrow}} \quad . \tag{3.1}$$

By using this definition with the LSDA, the sign of the spin polarisation for orthorhombic SrRuO$_3$ is ambiguous: we find that with a plane-wave (VASP) code $P_0^{E_F} = -2.95\%$ while the local orbital code (SIESTA) gives a positive spin polarisation of +2.00%. In contrast, for the cubic structure we find a positive spin polarisation $P_0^{E_F}$ for both first-principles calculations, +1.3% (VASP) and +8.8% (SIESTA). The reason for this discrepancy is attributed to the sensitivity of the exchange splitting of the Ru 4d bands near the Fermi level to the structure. The majority t$_{2g}$ band is positioned very close to the band edge, and its precise location is sensitive to the finer details of the DFT calculation. As a result, the large spread in the calculated spin polarisation is not surprising, and since the magnitudes of the spin polarisations are small, changes of a few percent can give a change in sign.

When correlations are introduced, $P_0^{E_F}$ increases in magnitude significantly and is negative in all cases. The spin polarisation calculated for the orthorhombic structure with the ASIC method is -85.7%, compared with a value of +2.00% when the SI error is not corrected. This value agrees with that obtained by the LSDA+U when U_{eff}=1.4 eV. We previously found that smaller U_{eff} values improve the agreement between ASIC and LSDA+U band structures and magnetic properties, suggesting that the ASIC transport results should be regarded as providing an upper bound on the magnitudes of the spin polarisation.

Despite being the most natural definition of spin polarisation at the Fermi level, determining $P_0^{E_F}$ as defined in Eqn. (3.1) is a nontrivial experimental process, since the spectroscopic measurements required typically have poor energy resolution. As knowledge of the degree of spin polarisation in a ferromagnet is crucial for its use in spintronics, several different experimental methods have been developed in order to determine this quantity.

The *transport* spin polarisation can be defined as

$$P = \frac{I^{\uparrow} - I^{\downarrow}}{I^{\uparrow} + I^{\downarrow}} \quad , \tag{3.2}$$

where I^{σ} is the spin-dependent current. However I^{σ} is not directly observable and must be determined indirectly. The transport spin polarisation now depends on the experiment in question, and in particular on whether the transport is in the ballistic or diffusive regime. In the ballistic limit the current is proportional to $N_{E_F}\nu_F$, while for diffusive transport it is proportional to $N_{E_F}\nu_F^2$ (assuming that both spin species have the same relaxation time), where ν_F^{σ} are the spin dependent Fermi velocities.

Therefore the transport spin polarisation at the Fermi level can be redefined as

$$P_n = \frac{N^{\uparrow}_{\epsilon_F}\nu_F^{n\uparrow} - N^{\downarrow}_{\epsilon_F}\nu_F^{n\downarrow}}{N^{\uparrow}_{\epsilon_F}\nu_F^{n\uparrow} + N^{\downarrow}_{\epsilon_F}\nu_F^{n\downarrow}} \tag{3.3}$$

where $n = 1$ for ballistic transport or $n = 2$ for diffusive transport [134, 135]. If $n = 0$, this definition reduces to that of the spectroscopic polarisation, P_0. An additional definition of polarisation is used in Meservey-Tedrow style tunneling experiments. Here the spin-dependent DOSs are weighted by their corresponding tunneling matrix elements. Such an experiment has been performed for $SrRuO_3$ and report approximately a -10% spin polarisation [133]. Inverse tunnel magnetoresistance measurements also suggest that $SrRuO_3$ is negatively spin polarized [86]. This is in agreement with the majority of the calculations which find that $SrRuO_3$ is a negatively spin-polarized material at the Fermi level.

The point-contact Andreev reflection (PCAR) technique, which is based on the process of Andreev reflection [136] and developed as an experimental method in the work of Soulen et al. [137] and Upadhyay et al. [138] has been used successfully to determine the magnitude of the transport spin polarisation, although it cannot determine its sign. Experimental results [139, 140, 141] using this method report values ranging between 51% and 60%. It should be noted that in the Andreev experiment the polarisation is not uniquely defined, in that it must be extracted from the data through a fitting procedure and involve terms that describe the transmittivity of the interface between the ferromagnet and the superconductor. These parameters are typically difficult to determine precisely and consequently introduce further uncertainty in the experimental spin polarisation. Furthermore, it is important to note that in all PCAR experiments, it is necessary to establish whether the transport is in the ballistic, diffusive or intermediate regime (noninteger n) which ultimately depends on the transmittivity of the interface. The experimental results for $SrRuO_3$ are further complicated by the fact that the transport in the system has been measured in both regimes.

In order to allow for a direct comparison with the PCAR experiments, the transport spin polarisation in both the ballistic and diffusive limit was determined by using the *ab initio* electronic transport code SMEAGOL [142]. Here we calculated the transport at zero bias through both the orthorhombic and cubic structures[3], and present the results in Table 3.3 and Fig. 3.8.

	P_n % (LSDA, ASIC)	
	Orthorhombic	Cubic
$n = 0$	+2.00, -85.7	+8.80, -16.1
$n = 1$	-1.44, -92.9	-8.99, -50.9
$n = 2$	-15.1, -98.0	-32.9, -79.5

Table 3.3: Transport spin polarisations, according to the definition of Eqn. (3.3) and calculated with the LDSA and ASIC. Results for both the orthorhombic and cubic $SrRuO_3$ crystals are included.

The shortcomings of the LSDA in describing the spin polarisation at the Fermi level in $SrRuO_3$ are again apparent. The highest spin polarisation obtained with

---

[3] The Brillioun zone was sampled in these cases with a 20 × 20 × 1 Monkhorst-Pack mesh for the orthorhombic structure and a 40 × 40 × 1 mesh for the cubic structure.

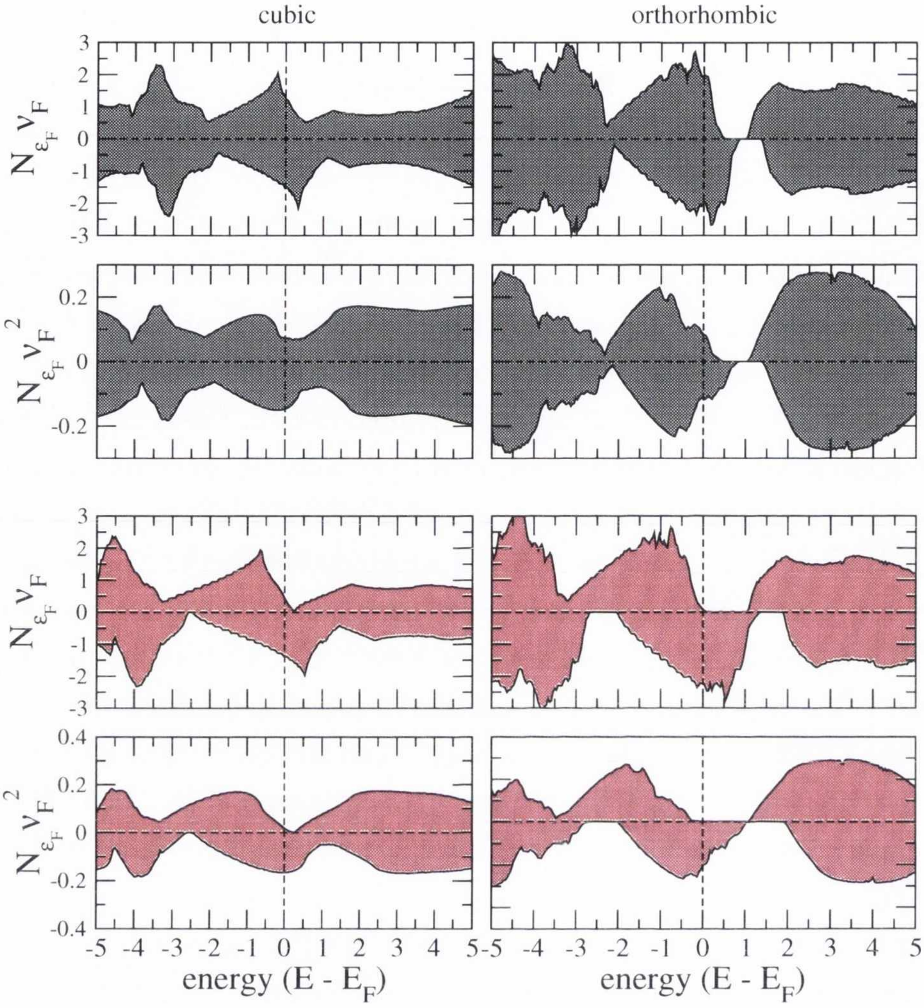

Figure 3.8: Spin dependent transport coefficients, $N_{\epsilon_F}\nu_F$ and $N_{\epsilon_F}\nu_F^2$, calculated with ASIC.

the LSDA for the orthorhombic structure is 15% and it is obtained in the diffusive limit. This is notably smaller than the experimental PCAR results measuring the same quantity, P_2. As shown in Fig. 3.8, on changing from P_0 to P_2 the polarisation increases and becomes more negative. Since the group velocity tends to zero at the band edge, and it is maximized at the band center, higher powers of n in P_n suppress the contribution of the Ru 4*d* states at the band edge and enhance those at the band center. From Fig. 3.8 it is then clear that the large negative polarisation is a consequence of the center of the *majority* Ru 4*d* band being positioned approximately 1 eV below the Fermi level, while the *minority* Ru 4*d* band center is aligned across the Fermi level.

Further enhancement is seen by introducing correlation; for example, by correcting for the SI error, the spin polarisation increases due to the reduction in the number of majority Ru t_{2g} states at the Fermi level. The correlated *ab initio* calculations now give a very high spin polarisation, ranging between 85.7% and 98.0%, whereas the highest value achieved experimentally is just 60%. Qualitatively similar results are found for the cubic structure, although the SIC in general has a smaller influence on the spin polarisation. For example, P_1 goes from 8.99% (LSDA) to 50.9% (ASIC), while P_2 goes from 32.9% to 79.5%.

It is also useful to note the strong dependence of spin polarisation on distance from the Fermi level. In Fig. 3.9 we show for the orthorhombic structure that if the Fermi level is moved just 100 meV into the valence band, P_1 is decreased to 81.4%, while moving E_F by 200 meV decreases it further to 59.8%, bringing it within the experimental range of values. In practice this shift in the Fermi level can be realized by off-stoichiometric compounds such as those investigated by Siemons et al. [104]. The discrepancy between the computational and experimental results could be then due to a number of factors: for example, there are several known limitations with PCAR including spin-flip scattering events which could drastically reduce the measured value of P_2, as well as the possible ambiguous fit of PCAR measurements to a multiparameter model [143]. We also note that spin-orbit coupling, which we did not account for in our transport calculations, could reduce the spin polarisation at the Fermi level.

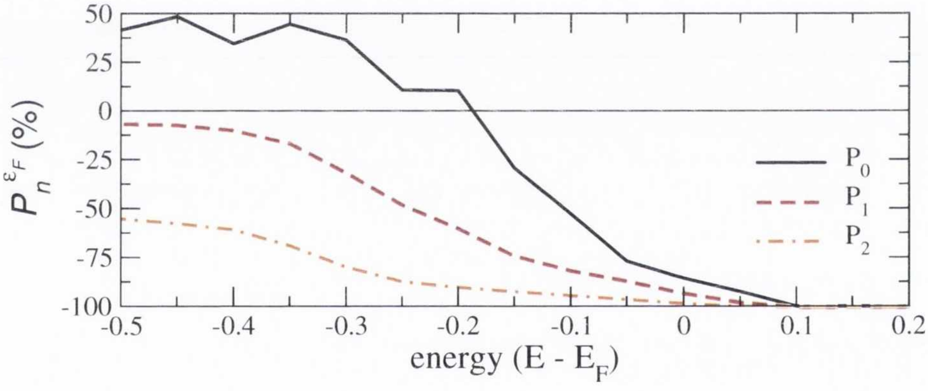

Figure 3.9: Spin polarisation, according to the definition of Eqn. (3.3), as a function of distance from the Fermi energy (set to 0 eV) and calculated with the ASIC for the orthorhombic structure.

Despite these disparities, both ab initio calculations and experiment show $SrRuO_3$ with a high negative spin polarisation. As expected, LSDA underestimates the spin polarisation at the Fermi level, whereas the inclusion of correlation through the correction of the SI error results in much better agreement between theory and experiment.

3.2.8 Conclusions

We have examined the effects of the structural distortions and the correlation effects on the electronic and magnetic properties of $SrRuO_3$ with first-principles calculations. We find that including weak strong correlations via the correction of the self-interaction error gives good agreement with the experimental spectroscopic data for bulk orthorhombic $SrRuO_3$. The addition of the octahedral distortions leads to a narrowing of the majority spin Ru t_{2g} and the O $2p$ states. However, the exchange splitting is small with respect to these bandwidths and consequently a fully insulating ground state is not obtained.

3.3 Structural and Electronic Properties of $BaTiO_3$

3.3.1 Introduction to Ferroelectric Materials

In order to be classified as ferroelectric, a material must exhibit a spontaneous electric polarization that can be switched between two states with the application of an electric field. These two states, which are both stable at zero electric field, are equivalent and differ only in the orientation of the electric polarization vector [144]. The analogy with ferromagnetic materials, namely the hysteresis effect in the applied field-polarization curve, the existence of a Curie temperature T_c and the fact that the dipole moments align in the same direction, lead to the prefix *ferro-* being used. The first such material to be experimentally confirmed was the Rochelle Salt in the 1920s by Valasek. For decades it remained the only known ferroelectric crystal and the microscopic mechanism leading to its polarization was poorly understood, mainly due to its complicated crystal structure. Little progress was made until the discovery in 1945 of a material exhibiting a dielectric constant of the order of several thousands at room temperature, barium titanate ($BaTiO_3$). Shortly after, it was also revealed to be ferroelectric [145]. It was the first of a family of ferroelectric perovskites, which also includes $PbTiO_3$, $KNbO_3$ and $Pb(Zr,Ti)O_3$ (PZT), to be reported. Due to the relative structural simplicity, (the unit cell has only five atoms per unit cell and exists in a structure with high symmetry) both theory and experiment now progressed rapidly.

In conventional ferroelectrics, a category including many of these perovskites, ferroelectricity is driven by the atomic arrangement of atoms within the crystal. In particular, they undergo a rich variety of structural phase transitions with temperature which are inextricably linked with the ferroelectric phase transitions. The cubic (centrosymmetric) phase is most stable at higher temperatures but, as the temperature is lowered, the symmetry is lowered into various ferroelectric structures. Such ferroelectrics, depending on the displacement of the internal atomic coordinates, are called the conventional or displacive ferroelectrics.

Electronic ferroelectrics do not rely on physical displacements of atoms; instead the electric polarization and ferroelectric transition is due to purely electronic degrees of freedom and electronic interactions. The result is a symmetry-breaking transition that will occur even if the atoms are held in their high symmetry positions. One example of such behaviour is the triangular mixed valence oxide, $LuFe_2O_4$, where frustration on a triangular lattice leads to the ordering of Fe^{2+} and Fe^{3+} ions in an arrangement of polar symmetry.

Ferroelectric materials are classified as "improper" when the polarization is no longer the primary order parameter but rather is coupled to a non-polar lattice distortion or a magnetic order parameter. Examples include the multiferroic $HoMnO_3$ where the electronic ordering results in a structure lacking inversion symmetry. In such materials, ferroelectricity is induced only as a result of some electronic phase transition and as such can be described by a secondary order parameter.

Some ferroelectrics have also been classified as "order - disorder" type (e.g. $NaNO_2$). Such a classification distinguishes between materials that are macroscopically or microscopically non-polar above T_c. That is, in an order-disorder ferroelectric, symmetry breaking distortions are present above T_c but are randomly orientated such that there is no net electric polarization. This is in contrast to the so-called "displacive" ferroelectrics where high symmetry is microscopically restored above T_c. Real materials generally fall between these two classifications.

Initial attempts to theoretically describe ferroelectricity at the microscopic level were slow and hindered by seemingly different mechanisms in each of the ferroelectric materials discovered. For a long time hydrogen bonding was thought essential for the creation of a polar instability. It wasn't until 1960 that Anderson and Cochran established that the ferroelectric phenomenon could be described by the theory of lattice dynamics. In this model, the ferroelectric transition is associated with the softening of a phonon mode which freezes in below T_c generating the ferroelectric structure. In the case of centrosymmetric $BaTiO_3$, two transverse optic modes are unstable at the Γ point. These are associated with the displacement of the Ti atom against the oxygen octrahedra cage [146].

Landau theory

Landau theory [147] has been used successfully to describe the phenomenological behaviour of phase transitions in superconductors and ferromagnets. Such a theory assumes that any thermodynamic equilibrium state can be completely expressed as a polynominal expansion of the thermodynamic potential with respect to a number of variables, for example the stress σ, the strain s, the temperature T, the entropy S and the electric field E (only the symmetry compatible terms are retained). Devonshire extended the theory to ferroelectric materials by including the polarization variable P [148, 149]. The free energy can be written as a function of these variables (usually the three components of polarization, the six components of the stress tensor and the temperature). The free energy can then be minimized with respect to the order parameter, in the case of ferroelectrics the polarization P. Other important thermodynamic quantities can then be found by a suitable differentiation of the free energy. The free energy density of a ferroelectric material as a function of a single-component polarization can be written to the 6^{th} power as

$$\mathcal{F}_P = \frac{1}{2}aP^2 + \frac{1}{4}bP^4 + \frac{1}{6}bP^6 - EP,$$

where a, b and c are coefficients generally to be fitted from experiment. The equilibrium configuration can then be determined by taken the derivative with respect to the order parameter P. For example the electric field as a function of the polarization will then be given by

$$E = aP + bP^3 + cP^4.$$

If a, b and c are positive then $\mathcal{F}_P$ has a minimum at the origin. If $a < 0$, and $b, c > 0$, then the free energy will instead have the double-well profile characteristic of a ferroelectric ground state. Examples of these two energy profiles are shown in Fig. 3.10. The ferroelectric transition can then be described by assuming $a = a_0(T - T_0)$ so that:

$$\mathcal{F}_P = \frac{1}{2}a_0(T - T_0)P^2 + \frac{1}{4}bP^4 + \frac{1}{6}bP^6 - EP,$$

where a_0 is positive for all known ferroelectrics and the sign of b determines the nature of the ferroelectric transition. If $b > 0$ then the transition from paraelectric to ferroelectric with the decrease in temperature will take place at $T = T_0$ and the

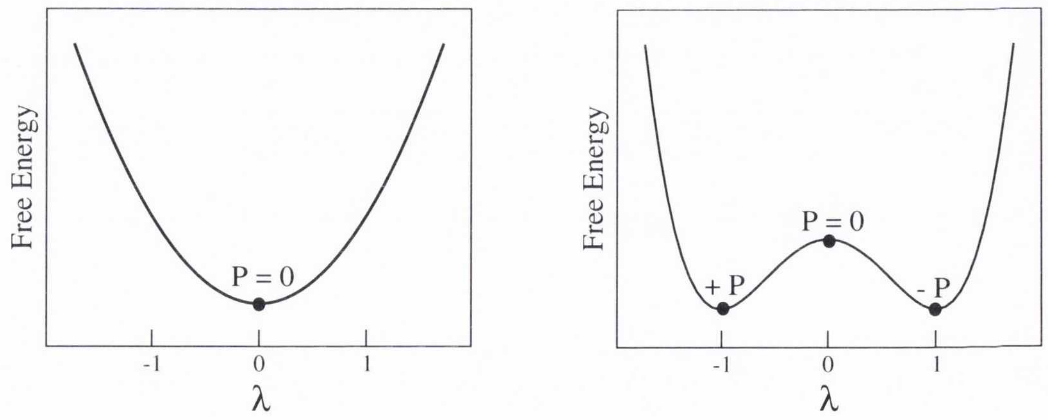

(a) (b)

Figure 3.10: Schematic representation of the potential energy with respect to the displacement pattern (λ) in a (a) centrosymmetric material and (b) ferroelectric material.

transition will be continuous indicating a second order transition. The spontaneous polarization, P_0, is given by the two minima of the double well and can be estimated by taking the appropriate derivatives of the free energy, i.e. when $\frac{\partial F}{\partial P} = 0$ and $\frac{\partial^2 F}{\partial P^2} < 0$:

$$P_0 = \pm\sqrt{\frac{a}{b}(T_0 - T)}.$$

P_0 decreases as T decreases and vanishes when $T > T_0$. If $b < 0$, the order parameter jumps discontinuously to zero at T_c indicating a second order phase transition.

Experimental and theoretical measurement of the electric polarization

The polarization can be related to the integrated macroscopic current flowing through the system via $\frac{dP(t)}{dt} = j(t)$, where $j(t)$ is the current density. A typical experimental measurement of the spontaneous polarization is shown schematically in Fig. 3.11. The transition between ferroelectric states is driven by an applied electric field. The maximum polarization achieved with such a field is called the saturated polarization. When this field is removed the remnant polarization, P_r, is left. Applying a field in the opposite direction to the original polarising field reduces the polarization until it reaches zero at $E = E_C$. This is the coercive field. It is important to note that it is not possible to measure either P nor $-P$ directly, but only their difference. Thus, the spontaneous polarization is given by $\frac{1}{2}$ the difference between P and $-P$, where symmetry considerations determine the factor $\frac{1}{2}$. In this way the spontaneous polarization of $BaTiO_3$ has been measured to be $26\mu C/cm^2$ [150].

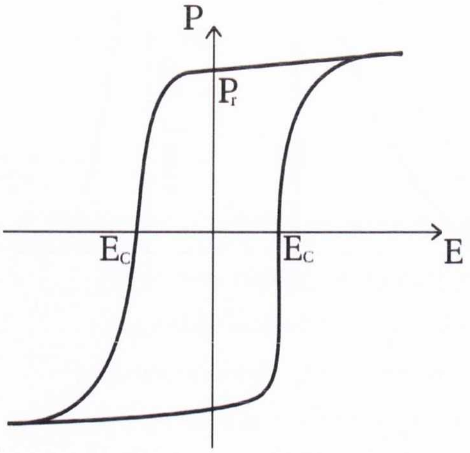

Figure 3.11: Polarization versus Electric Field (P-E) hysteresis loop for a typical ferroelectric crystal.

Despite being the most important quantity in any description of ferroelectric materials, an *ab initio* method for determining the spontaneous polarization was not available until the Berry Phase formalism was developed in 1993. This so-called 'modern theory of polarization' allows one to calculate the macroscopic polarization of a crystal as a Berry phase of the electronic Bloch wavefunctions [151, 152].

The total macroscopic polarization, $\boldsymbol{P}$, is given as a sum of an ionic and an electronic contribution

$$\boldsymbol{P} = \boldsymbol{P_e} + \tfrac{1}{2}\sum_{i=0}^{N} Z_i \boldsymbol{r}_i,$$

where N is the number of atoms in the unit cell, $\boldsymbol{r}_i$ are the positions of the ions and Z_i are their charges. $\boldsymbol{P_e}$ is calculated by using a discretized version of the formula

$$\boldsymbol{P}_{e,||} = \tfrac{ifq_e}{8\pi^3} \int_A d\boldsymbol{k}_\perp \sum_{n=1}^{M} \int_0^{|G_{||}|} d\boldsymbol{k}_{||} \langle u_{\boldsymbol{k}n} | \tfrac{\delta}{\delta k_{||}} | u_{\boldsymbol{k}n} \rangle,$$

where f is the occupation, q_e is the electron charge, M is the number of occupied bands, and u_{kn} are the Bloch functions. $\boldsymbol{G}_k$ is the shortest reciprocal vector along the chosen direction. (Note: The macroscopic polarization is only defined modulo $fq_e\boldsymbol{R}$, where $\boldsymbol{R}$ is an arbitrary lattice vector).

The nominal static charges for ABO_3 perovskites are 1 or 2 for the A cation, 4 or 5 for the B cation and -2 for the oxygen. If an ion is displaced, the electron charge is carried by that ion as it moves and can be described by the Born Effective Charge (BEC) tensor. As such, the BEC tensor describes the electric polarization induced in zero field upon ionic displacements. It can be equivalently described as the force exerted on undisplaced ions by a field. In some materials, the charge carried by the displaced ion is much larger than is expected from the formal ionic charges. Such BECs are anomalous. BECs are found to be highly anomalous in many (though not all) ferroelectric compounds, in particular in the family of ferroelectric perovskites. The magnitude of the spontaneous polarization can be estimated by studying the BECs and displacements for the centrosymmetric reference configuration. The BECs are defined by

$$Z^*_{i,\alpha,\beta} = \frac{\Omega_0}{e} \frac{\partial P_\alpha}{\partial u_{i,\beta}}\Big|_{q=0},$$

where Ω_0 is the unit cell volume, α refers to the direction of polarization and β refers to the direction the atom is displaced to.

Exchange-correlation functionals

In recent years, and in particular since the development of the modern theory of polarization, DFT calculations have become increasingly indispensable in the analysis of experimental work on ferroelectric materials and even in the prediction of new materials. LDA and GGA are the most commonly used functionals but these are not without their problems - indeed their limitations with respect to ferroelectric materials have been well documented. As for most materials, LDA calculations generally underestimate the lattice constants of ferroelectrics by about 1 or 2%. This is problematic when we consider the strong interplay between the polar structural distortion and the volume. In some cases the polarization can be significantly suppressed by such an underestimation of the equilibrium volume. For this reason many authors use the experimental lattice constants but such an approach is not always feasible (for instance, when predicting new materials) or desirable (it would be preferable to conduct all calculations without introducing any adjustable parameters). GGA tends to overestimate lattice constants, leading to the so-called 'super-tetragonal' structure. We note that several exchange correlation functionals have been developed in recent years with the intention of overcoming these deficiencies. The modified GGA functional of Wu and Cohen [153] predicts highly accurate volumes and displacements for $BaTiO_3$ and $PbTiO_3$. Hybrid functionals such as B3LYP have also recently been applied to ferroelectrics [154] and multiferroics [155]. Another well known limitation of both LDA and GGA is the underestimation of the bandgap. This is a considerable problem when dealing with metal/ferroelectric interfaces when an underestimation of the bandgap can have pathological results if charge is nonphysically exchanged with the ferroelectric material.

For these reasons, a thorough investigation of the structural and electronic properties of $BaTiO_3$ is necessary and this will be the focus of the rest of the section.

3.3.2 Crystal Structure and Polarization

Unstrained structure

The cubic perovskite structure, containing five atoms per unit cell, is stable at high temperatures. Its space group symmetry is the non-polar $Pm\bar{3}m$ and it is the usual 'reference' structure to which the ferroelectric configuration can been seen as a perturbation. The experimental lattice constant is 4.00Å. As the temperature is lowered $BaTiO_3$ exhibits three structural phase transitions:

- A transition from cubic to tetragonal ($P4mm$) occurs at 405K with a polarization pointing along [001],
- A transition from tetragonal to orthorhombic ($Pmm2$) occurs at 278K with a polarization along [011],

- Finally, an rhombohedral structure ($P3m1$) becomes stable at 183K with P pointing along [111].

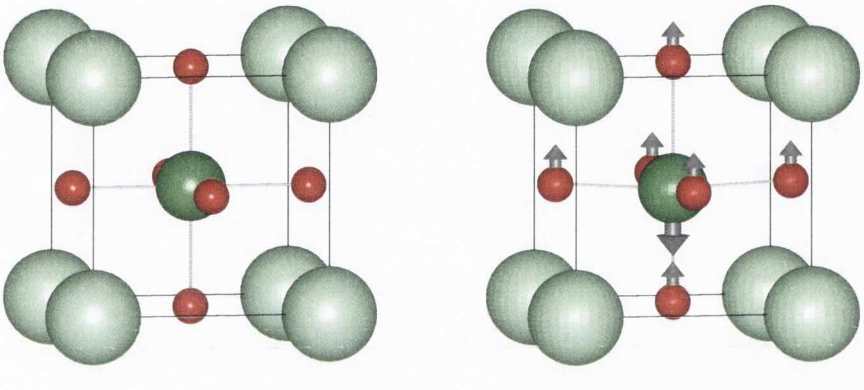

(a) Centrosymmetric (b) Ferroelectric

Figure 3.12: (a) Schematic representation of the ideal cubic $BaTiO_3$ perovskite. (b) Schematic representation of the pattern of displacements related to the ferroelectric configuration of $BaTiO_3$.

It is the symmetry lowering from $Pm\bar{3}m$ to $P4mm$ that allows the relative displacements (Δ) of the atoms along the z-axis. The Ba ion occupies the Wyckoff position $1a$ (0, 0, 0), the Ti cation occupies the $1b$ $(\frac{1}{2}, \frac{1}{2}, \frac{1}{2} + \Delta\ _{Ti})$ while the two in-equivalent oxygens (O_I and O_{II}) occupy the $1b$ and $2c$ with positions $(\frac{1}{2}, \frac{1}{2}, \Delta_{O_I})$ and $(\frac{1}{2}, 0, \frac{1}{2} + \Delta_{O_{II}})$ respectively. It is these displacements that result in a nonzero polarization along [001].

The equilibrium lattice constant for the cubic structure is 3.9465Å within the LDA. This is similar to that reported for other LDA calculations [156] but it is a slight underestimation of the experimental value (4.000Å). The GGA results in a slightly overestimated lattice constant of 4.026Å.

Relaxation of a ferroelectric tetragonal phase requires the simultaneous relaxation of both lattice constants and internal atomic coordinates which are no longer defined by symmetry considerations. The results of our structural optimizations are shown in Table 3.4.[4] The position of the Ba ion was chosen to be a reference in the unit cell and so it remains fixed at $(0, 0, 0)$. The displacements of the other atoms are given relative to the corresponding centrosymmetric structure in units of the out-of-plane lattice constant, c.

---

[4] Relaxations were carried out with a k-mesh of at least 6x6x6 and a mesh cut-off of 800Ry. Although an insulator, a denser k-mesh than normal is necessary for ferroelectric materials in order to properly describe the mixed ionic-covalent character of the bonding.

Phase (%)	a (Å)	c (Å)	c/a	V (Å^3)	Δ_{Ti}	Δ_{O_I}	$\Delta_{O_{II}}$	$\boldsymbol{P_s}$
Cubic LDA	3.9465	3.9465	1.00	61.47	0.00	0.00	0.00	0.00
Cubic GGA	4.0263	4.0263	1.00	65.27	0.0	0.00	0.00	0.00
Tetragonal LDA	3.9354	4.002	1.02	61.98	0.016	-0.022	-0.015	31.05
Tetragonal GGA	3.9899	4.199	1.05	66.85	0.020	-0.046	-0.028	46.58
Experimental	3.9860	4.026	1.01	63.95	0.015	-0.022	-0.015	26.0

Table 3.4: Structural parameters of $BaTiO_3$. Displacements (Δ) are given relative to the centrosymmetrically-strained structure in units of the out-of-plane lattice constant, c. $\boldsymbol{P_s}$ is the Berry-phase polarization in μC/cm^2.

While the use of LDA results in a reasonable good agreement with experiments, the so-called 'super-tetragonality' of the GGA structure is evident. For instance, the c/a ratio is much larger than that observed experimentally. The polarization, as calculated with the GGA, is very high: 46.6 μC/cm^2. This is significantly higher than the experimental value of 26.0 μC/cm^2 and it is due to the 'supertetragonal' structure. The relaxed GGA c lattice is longer than that experimentally found by $\approx$ 0.2Å, with the result that the oxygen displacements are larger than expected. A possible method to avoid the problem of a 'supertetragonal' structure is to use the experimental volume. However, for consistency with the rest of our calculations, and similar to other multilayer calculations [157, 158], we will use the relaxed GGA structure.

Strained structure

Anisotropic strains can be routinely applied to ferroelectric thin films as they are deposited on an underlying substrate due to differences in crystal lattice parameters (See Fig. 3.13). As a result, the thin films can display greatly improved properties compared to the properties of the corresponding unstrained bulk materials. By ensuring that the misfit strain is not too large and the films are sufficiently thin, strains of several per cent can be tolerated before misfit dislocations appear and the quality of the film properties are degraded. Thus, by using strain one can enhance the intrinsic properties of a chosen material in a process known as 'strain-engineering'. For example, the transition temperature (T_c) can be increased by several hundred degrees [159] as well as large increases in the remnant polarization can be achieved [160, 161]. Strain can also induce a polarization in $SrTiO_3$, a non-ferroelectric material in its bulk state [162]. Breakthroughs in materials processing has meant that is now possible to grow heterostructures that are epitaxially matched to the substrate for large thicknesses and accommodate very large strains, up to 2-3%. In some cases it is possible to drive a system through a number of phase changes, for example alternating layers of $BaTiO_3$ with $SrTiO_3$ can drastically change its properties [163].

The Landau free energy density, extended to include strain, predicts that the polarization-strain coupling is quadratic in nature. Such a strong coupling portends a highly sensitive relationship between ferroelectricity and mechanical constraints and results in the rich structural phase diagrams that are found for some of the perovskite oxides. A detailed review of the strain tuning of ferroelectric properties can be found in Ref. [164].

For perovskites, the most commonly used substrates have orthogonal and equal in-plane lattice constants. The misfit strain can then be defined as $\frac{a-a_0}{a_0}$, where a is the in-plane lattice parameter of the substrate and a_0 is the bulk equilibrium lattice constant of the thin film material.

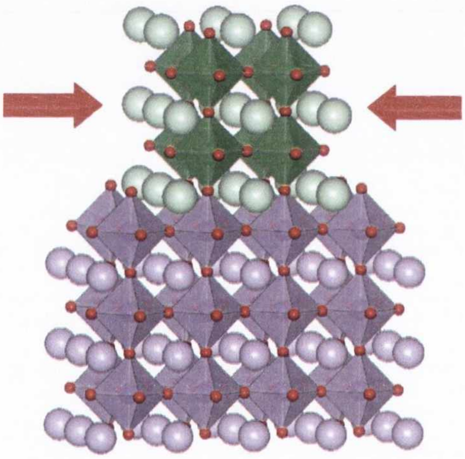

Figure 3.13: Schematic of a fully coherent epitaxial ferroelectric film bi-axially strained to match an underlying substrate.

Although the in-plane lattice constant of a ferroelectric material grown on a substate is constrained, the out-of-plane lattice constant is free to relax. In general, a large compressive in-plane strain will result in the increase of the out-of-plane lattice constant such that the polarization will increase in magnitude and point along the z-direction. A large tensile plane will reduce the out-of-plane lattice constant and the polarization will have an in-plane orientation. Intermediate values of strain can result in the polarization having both an in-plane and out-of-plane component. Strain engineering of this sort is used to artificially manipulate the magnitude and direction of the polarization. Fig. 3.14 shows the resulting phase diagram of a theoretical cal-

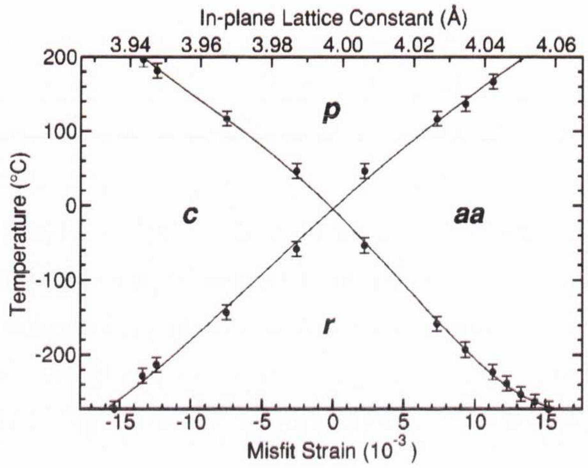

Figure 3.14: Phase diagram of $BaTiO_3$ in terms of epitaxial misfit strain and temperature (from [165]). The labels are: p= paraelectric phase, c= tetragonal phase with polarization oriented in the out-of-plane direction, aa= orthorhombic phase with polarization oriented in the in-plane direction and r= monoclinic phase with polarization oriented in the three directions

culation concerning $BaTiO_3$. One can see that by manipulating $BaTiO_3$ with both strain and temperature it should be possible to drive the structure from tetragonal to orthorhombic or even to monoclinic.

The effect of strain on these materials can be effectively described with DFT by considering the behaviour of the bulk material under the same mechanical boundary conditions. The effect of strain across a wide range has been thoroughly studied within DFT elsewhere [166, 167, 168].

Fig. 3.15 shows how the length of the c-axis varies as a function of lattice mismatch. We see that when the lattice is clamped in the ab-plane to the experimental lattice parameters, the GGA functional tends to overestimate the distortion along c. The LDA functional on the other hand underestimates this ferroelectric distortion. If the compressive strain is increased the c lattice increases, in accordance with the Poisson effect whereby a compressive strain in one direction in accompanied with an expansion of the unit cell in the perpendicular direction. Similarly, increasing tensile strain results in a reduced c axis.

Here, we consider in more detail the effect of a $SrTiO_3$ substrate on $BaTiO_3$. The in-plane compression reduces the rhombohedral distortion of the bulk state, but it does not eliminate it completely. However, the energy difference between it and the optimised tetragonal structure is 1.86 meV and for this reason we consider only the tetragonal structure. The GGA lattice constant of $SrTiO_3$ is 3.95Å. A compressive strain of 1% is therefore applied to $BaTiO_3$. The structural results are shown in Table 3.5. The c/a ratio is now 1.08 with a corresponding increase of polarization to

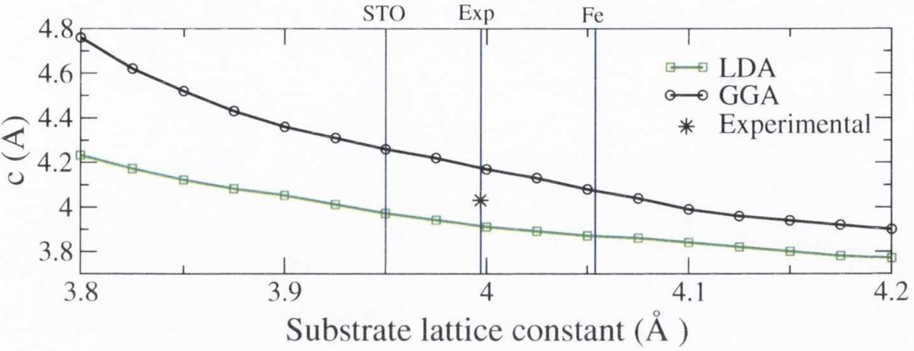

Figure 3.15: The out-of-plane lattice constant of $BaTiO_3$ as calculated for the bulk clamped to different substrate lattice constants. Experimental data taken from Ref. [169, 170]

almost 52 μC/cm^2, an increase of over 10% compared to unstrained $BaTiO_3$. Thus it is possible to enhance the polarization of $BaTiO_3$ compared to its bulk value. Such a result is invaluable when $BaTiO_3$ is combined as part of a heterostructure that might otherwise reduce the polarization to a useless value. The effect of a range of other strains on the stability of the various structures of $BaTiO_3$ is shown in Fig. 3.16 where the unit cell energy for the the centrosymmetric ($Pm\bar{3}m$), tetragonal ($P4mm$) and trigonal ($R3m$) phases are plotted. As already noted, when $BaTiO_3$ is constrained to the lattice parameter of $SrTiO_3$ there is no significant difference in energy between the trigonal and tetragonal structures, i.e. the ferroelectric distortion will be along the c-direction. However when $BaTiO_3$ is subject to a tensile strain, for example when grown on a Fe substrate, there is a significant energy difference (50 meV/f.u.) between the trigonal and tetragonal structures. Here we expect the trigonal phase to be dominant, allowing the polarization to have a significant non-zero component in the ab-plane.

Strain (%)	a (Å)	c (Å)	c/a	V (Å^3)	Δ_{Ti}	Δ_{O_I}	$\Delta_{O_{II}}$	$\boldsymbol{P_s}$
Unstrained (0%)	3.9899	4.199	1.05	66.85	0.020	-0.046	-0.028	46.58
Strained (-1%)	3.9500	4.263	1.08	66.51	0.021	-0.053	-0.033	51.899

Table 3.5: The misfit strain (%) is defined as $(a - a_0)/a_0$ where a_0 is the unstrained lattice parameter of the tetragonal phase. Structural parameters of strained $BaTiO_3$ compared to unstrained $BaTiO_3$. Displacements (Δ) are given relative to the centrosymmetrically-strained structure in units of the out-of-plane lattice constant, c. P_S is the Berry-phase polarization in μC/cm^2.

Next, we look at the how such structural changes effects the electronic structure of $BaTiO_3$ and in particular we discuss which exchange-correlation functional can best

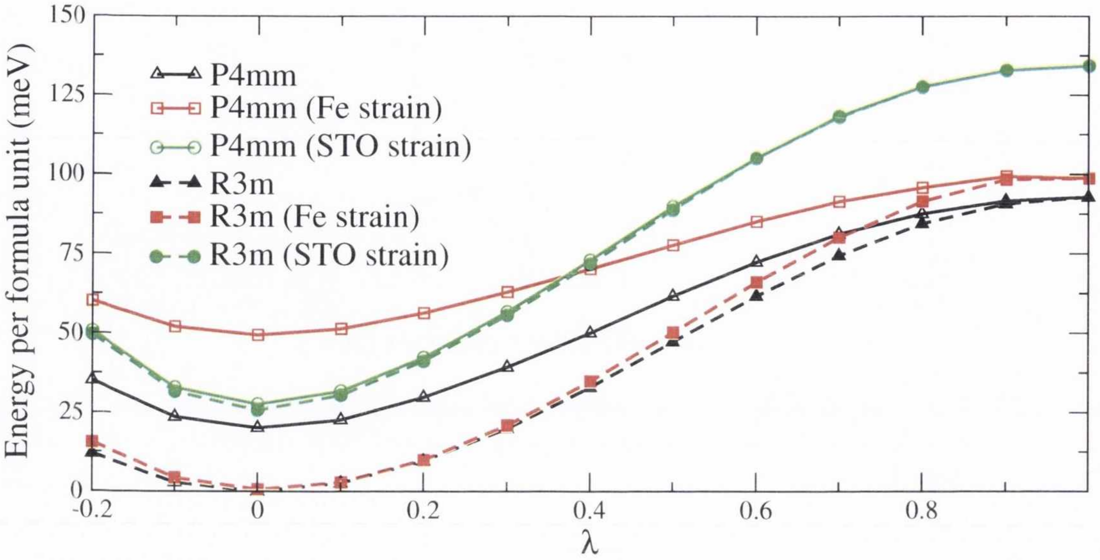

Figure 3.16: GGA total energy as a function of the ferroelectric distortion for bulk $BaTiO_3$ in the tetragonal (*P4mm*) or trigonal (*R3m*) structure, either unstrained, strained to the in-plane lattice constant of $SrTiO_3$ or to the in-plane lattice constant of Fe. λ=0 refers to the ferroelectric ground state, λ=1 refers to a reference centrosymmetric structure.

describe both the structural and electronic properties.

3.3.3 Electronic Structure

In Fig. 3.17 the calculated total and partial density of states of unstrained tetragonal $BaTiO_3$ are shown for both the reference centrosymmetric structure and the relaxed ferroelectric one. The general characteristics of the (P)DOS close to the Fermi level are as follows: the conduction band is largely of Ti 3*d* character and it is placed between +1.5 eV and +7.5 eV (energies are taken from the top of the valence band, which is set to zero). Mostly O 2*p* character is found between 0.6 and 8.0 eV. Hybridisation between the Ti 3*d* and O 2*p* states drive the system to a ferroelectric (FE) state via off-centering atomic displacements [171]. The PDOS shows that some *p*-*d* hybridisation is present, in particular between Ti 3*d* and the top oxygen (O_I) between -2.5 eV and -6.0 eV.

Born effective charges were calculated with GGA for the unstrained structure (see Table 3.6) and our results compare well with other first principles calculations [172]. Highly anomalous charges are found, in particular for the ions involved in the ferroelectric transition. Ti, for instance, carries a charge of +7.24, significantly higher than its purely ionic charge of +4. The decrease of Z^*_{zz} compared to Z^*_{xx} and Z^*_{yy} is expected. In the tetragonal phase, along the ferroelectric direction, a short Ti-O bond

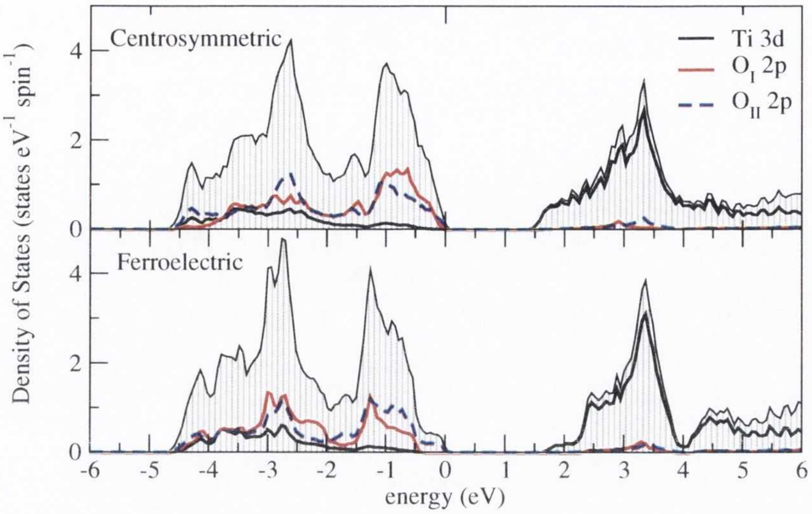

Figure 3.17: Density of States of unstrained BaTiO$_3$ as calculated with the GGA. Shown are the total DOS (grey, shaded), the Ti 3*d* states (black solid line), the O$_I$ 2*p* states (red solid line) and the O$_{II}$ 2*p* states (blue dashed line).

length is followed by a longer one. This breaks the Ti-O chain along this direction, with the result that the current flow associated with the effective charge is reduced. The band structure (Fig. 3.18) shows an indirect band gap of 1.65 eV between R in the valence band to Γ in the conduction band. The low-lying O 2*s* bands lie at -16.8 eV while the Ba 5*p* states are at -11.2 eV. The O 2*p* which contribute to the ferroelectric instability, are spread over 4.7 eV. These values, and in particular that of the band gap, do not agree well with experimental results. The experimental band gap is given as 3.2 eV. Furthermore, the spread of the O 2*p* manifold is much larger at 5.5 eV, while the Ba 5*p* and O 2*s* are approximately 0.5 eV and 1.3 eV deeper in energy than GGA predicts, respectively. An accurate description of the structural and electronic properties of BaTiO$_3$ is vital if we wish to correctly analyze its behavior as part of a junction. We find, however, that the behavior of bulk BaTiO$_3$ depends

	GGA			ASIC			Ghosez et al. [172]		
Atom	Z^*_{xx}	Z^*_{yy}	Z^*_{zz}	Z^*_{xx}	Z^*_{yy}	Z^*_{zz}	Z^*_{xx}	Z^*_{yy}	Z^*_{zz}
Ba	2.56	2.56	2.76	2.53	2.53	2.68	2.72	2.72	2.83
Ti	7.24	7.24	4.97	6.42	6.42	4.93	6.94	6.94	5.81
O$_I$	-1.88	-1.88	-4.02	-1.89	-1.89	-3.84	-1.99	-1.99	-4.73
O$_{II}$	-2.14	-5.79	-1.80	-2.05	-5.03	-1.88	-2.14	-5.53	-1.95

Table 3.6: Born effective charges (Z^*_{ii} for i = x, y, and z) calculated within the GGA and ASIC for tetragonal BaTiO$_3$ at the GGA relaxed coordinates. O$_I$ and O$_{II}$ label oxygen atoms on top of Ti and planar with Ti, respectively.

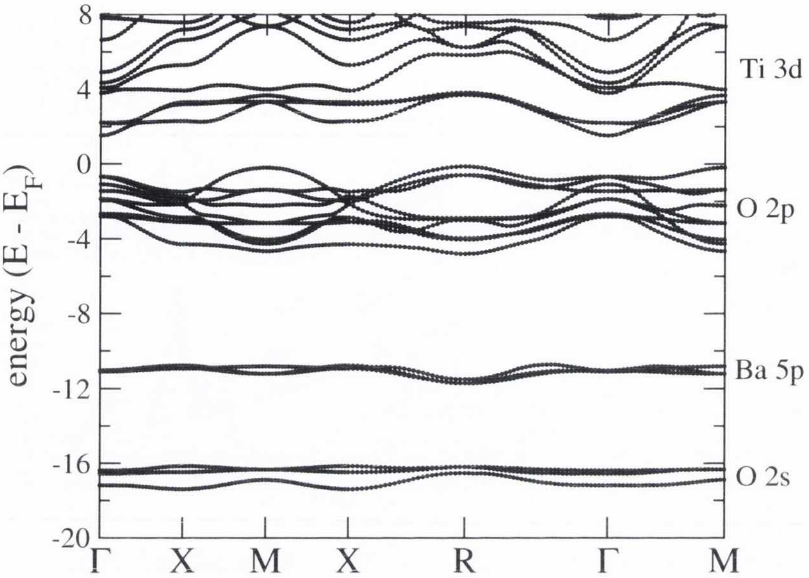

Figure 3.18: GGA Band Structure of unstrained BaTiO$_3$.

in a critical way on the exchange-correlation functional used.

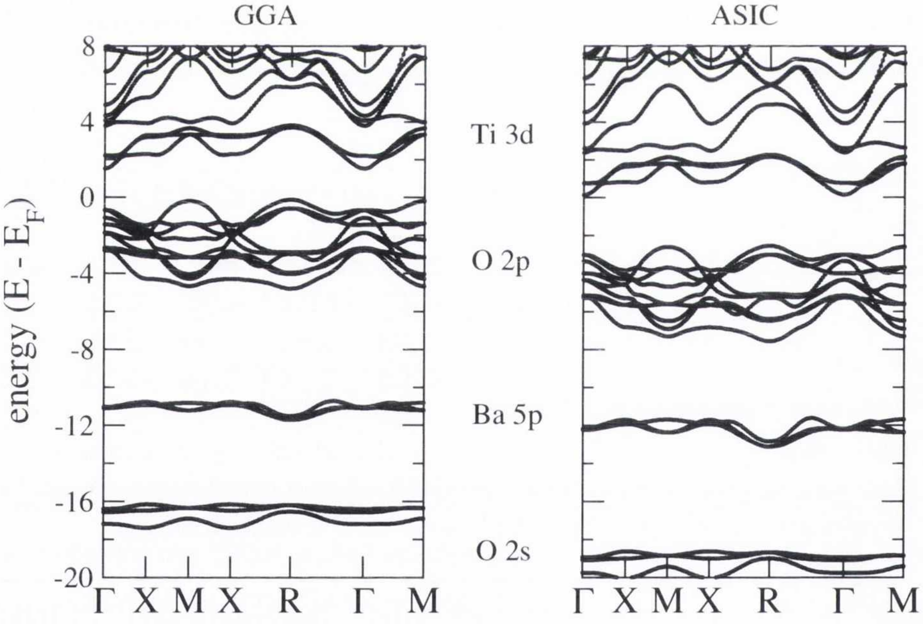

Figure 3.19: ASIC band structure of BaTiO$_3$ for the ferroelectric GGA structure.

ASIC has been found to correctly describe the electronic properties of oxides [173]. With this in mind, we calculate the ASIC band energies of BaTiO$_3$ in the right panel of Fig. 3.19. The band gap is now 2.70 eV, the O 2*p* manifold has a width of 5.07 eV and the Ba 5*p* and O 2*s* states are now at energies of -12.1 eV and -18.6 eV, respectively, in much better agreement with experiments. ASIC corrects, to a large extent, the electronic properties of BaTiO$_3$ with its most significant contribution being the increase of the Kohn-Sham bandgap.

In Table 3.6 the ASIC Born effective charges are shown, calculated at the GGA relaxed coordinates. There is a large decrease of the BECs for both Ti and O_I, when calculated with ASIC. They are still much larger than the formal ionic charges, but much reduced with respect to the GGA. This is due to the ASIC induced orbital localisation which reduces the *p-d* hybridisation and hence the BECs.

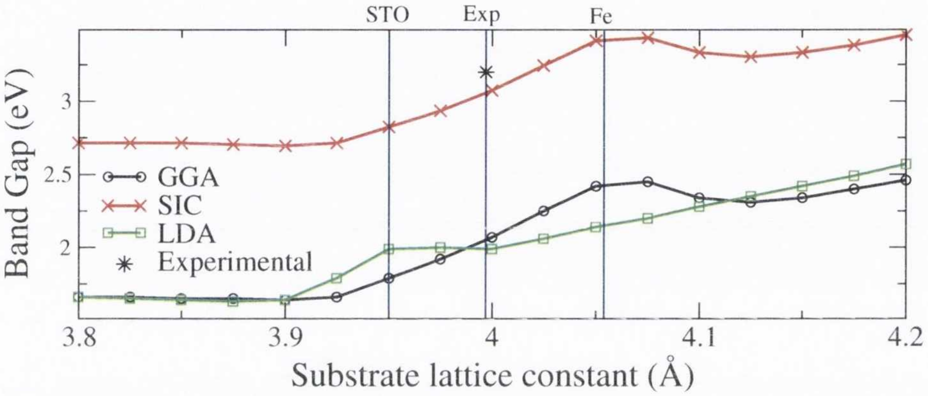

Figure 3.20: Band gap calculated for bulk $BaTiO_3$ clamped to different substrate lattice constants. The structure of LDA and GGA were relaxed, the ASIC band gap was calculated with the GGA structure. Experimental data taken from Ref. [169, 170]

We already found that straining $BaTiO_3$ can have a profound affect on the ground state atomic structure. Strain can also modify the electronic structure. In Fig. 3.20 we see that for all the three functionals studied (GGA, LDA and ASIC) the band gap increases as we apply compressive strain to $BaTiO_3$. For all distortions the LDA and GGA band gaps are similar, with the ASIC band gap significantly bigger and matching experiment well at the experimental lattice constant of $BaTiO_3$.

As the ferroelectric distortion is very sensitive to the exchange correlation functional used it is necessary, when attempting to correct the electronic structure to assess the affect this has upon the structure. Although ASIC provides a significant improvement to the electronic structure, we found that the atomic structure suffered as a consequence. By performing relaxations with the ASIC functional we found that it is unable to provide the correct structure. The relaxation destroys the ferroic phase and the material reverts to the cubic centrosymmetric phase. To analyze the ASIC forces for $BaTiO_3$ we linearly distort the structure from the LDA centrosymmetric ($\lambda = 1$) to the LDA tetragonal phase ($\lambda = 0$) as shown in Fig. 3.21. This calculation was performed for a set of ASIC scaling parameters (α), where $\alpha = 0$ is LDA and $\alpha = 0.5$ is the typical scaling for a majority of bulk insulating materials, in particular oxides. We see that the forces in the ASIC promote the non-ferroic centrosymmetric phase.

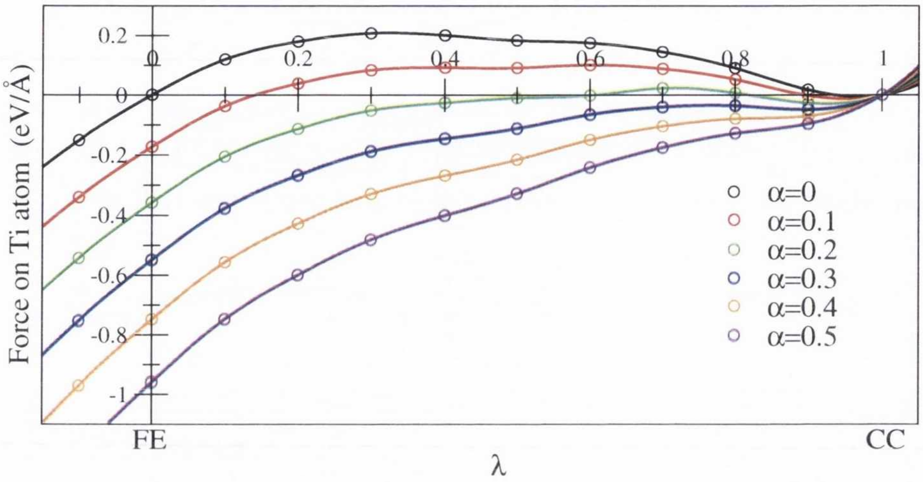

Figure 3.21: Force on the Ti atom through the centrosymmetric - ferroelectric phase transition.

The inability of the ASIC functional to describe the ferroic structure is on two fronts. Firstly, the ASIC method does not provide a full energy functional, i.e., it is not strictly variational. As such the definition of the forces is somewhat arbitrary as we take the ASIC force to be the LDA force calculated at the ASIC density. Secondly, the ASIC functional tends to localize atomic orbitals. This is not in itself a failure since the localization of the orbitals is directly linked to the band dispersion, which has already been shown to improve. It does however reduce the O $2p$ - Ti $3d$ hybridization which is responsible for the ferroic distortion [21, 174]. This is demonstrated in Fig. 3.22 where we plot the local density of states (LDOS) for the top 2 eV of the valance band in the tetragonal phase for both the GGA and ASIC ($\alpha = 0.5$) functionals.

3.3.4 Conclusions

We have examined the structural and electronic properties of $BaTiO_3$ in an effort to find an exchange-correlation functional capable of simultaneously describing both. We found that the local functionals are capable of describing the ferroelectric transition adaquately but fail to describe the electronic structure accurately. The underestimation of the band gap, in particular, would prove problematic if $BaTiO_3$ is included as a barrier material in a tunnel junction. In an effort to improve on this shortcoming, we found that by correcting for the self-interaction error a much better agreement was found with experiments. This improvement in the electronic structure was at the expense of the structural properties however as ASIC does not stablilise a ferro-

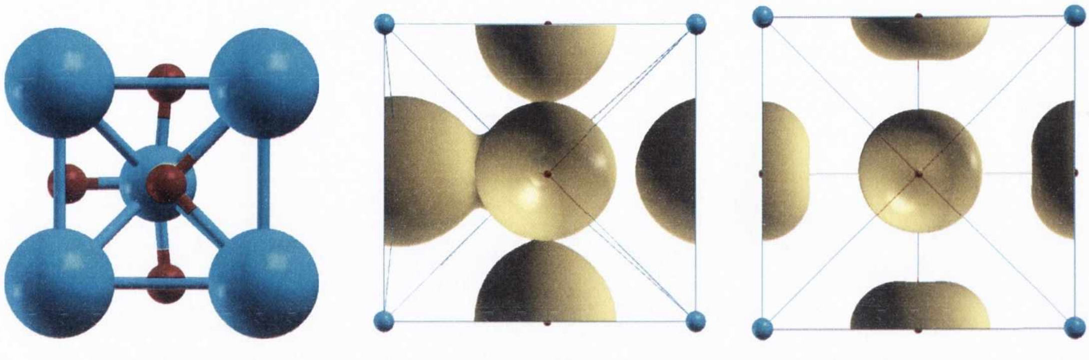

(a) $BaTiO_3$ cell (b) GGA (c) ASIC

Figure 3.22: Local Density of States plotted in an energy range between -2 eV and the Fermi level. GGA (a) shows increased hybridization in comparison to ASIC (b) over this energy range. This is due to the increased localization of SIC orbitals.

electric ground state. We found that the best description of $BaTiO_3$ was to relax the structure by using the GGA functional and then to calculate the electronic properties with the ASIC functional.

CHAPTER 4

Spin Dependent Tunnelling: The TMR effect

4.1 Introduction

The emerging field of spintronics aims at utilising the spin of an electron to create novel devices that go beyond simply enhancing the performance of conventional electronic devices. One particular area where spintronics has made a critical contribution is that of magnetic tunnel junctions (MTJs), consisting of two magnetic layers separated by an ultra-thin insulating film. The current through such a film is strongly dependent on the relative magnetisation of the magnetic layers; switching between parallel (P) and anti-parallel (AP) alignment causes a change in the device resistance. The interest in MTJs is driven by their potential for commercial applications, including magnetoresistive read heads for hard-disk drives, modern magnetic sensors and magnetoresistive random access memory (MRAM).

The figure of merit for MTJs is the tunnelling magnetoresistance (TMR). It is defined as TMR=$[I_P-I_{AP}]/I_{AP}$, where I_P is the current through the junction with parallel alignment and I_{AP} is the current through the junction with anti-parallel alignment. Very high TMR values of up to 1010% have been reported in CoFeB/MgO/CoFeB tunnel junctions at 5K [12]. However, in order to achieve such high TMR values, very high quality interfaces with very few defects are required [77]. The progress in producing magnetic tunnel junctions (MTJs) with large TMR was initially limited by the use of amorphous tunnel barriers. The situation however changed after the prediction [23, 24] and subsequently the experimental realisation [175, 176] of epitaxial MTJs. Since then, room temperature TMR in excess of 600% has been demonstrated in MgO-based devices [177]. In general, for amorphous barriers the spin polarisation of the tunnelling current and hence the TMR magnitude, depends solely on the electrodes' density of states (DOS) at the Fermi level, E_F [10]. In contrast, perfectly crystalline tunnel barriers are wave-function symmetry selective and make the tunnelling process sensitive to their electronic structure. As a result the amplitude and even sign of the TMR may depend on the barrier itself. The understanding of such a concept suggests that one can engineer the TMR by carefully selecting the insulating barriers to be epitaxially grown on magnetic electrodes. Ferromagnets [178] and ferroelectrics [179, 180] are of particular interest as functional barriers.

The introduction of active barriers, in particular incorporating ferroelectric or even multiferroic materials into the tunnel junctions has attracted considerable interest and its influence on electronic tunnelling has only recently been explored. Multiferroics have been formally defined as materials that exhibit more than one primary ferroic order parameter simultaneously (i.e. in a single phase). There are four primary ferroic orders; ferromagnetism (FM), ferroelectricity (FE), ferroelasticity and ferrotorroidicity. The formal definition of multiferroics is quite restrictive and for that reason it is common practice to also include the non-primary ferroic orders such as antiferromagnetism. Here we are primarily concerned with multiferroics that have FM and FE ordering.

The coexistence of ferroelectricity and ferromagnetism in one material was long thought to be impossible. The conventional mechanism for ferroelectricity requires empty d orbitals (d^0), while partially filled d orbitals are generally necessary for magnetism. It was not until the 2003 discovery of a large ferroelectric polarisation in epitaxially grown thin films of antiferromagnetic $BiFeO_3$ [181] and the discovery of strong magnetoelectric coupling in orthorhombic $TbMnO_3$ [182] and $TbMn_2O_3$ [183] that renewed interest in the field of multiferroics began. $BiFeO_3$ is one of the most extensively studied single-phase magnetoelectric multiferroics. The Bi $6s$ lone-pair electrons are responsible for the ferroelectricity while the partially filled Fe d orbitals result in AFM ordering [184]. $BiFiO_3$ is unique in that its FM and FE ordering temperatures are well above room temperature ($T_C \approx 640K$ and 1080K, respectively). In general transition temperatures above 50K for both the magnetic and electric phase transition are rarely found simultaneously and the magnitude of the ME coupling is usually also small. For these reasons, the penetration of such single-phase multiferroics into practical devices has been slow.

Since a prototypical single-phase multiferroic suitable for room temperature industrial devices has not yet emerged, an alternative must be found. Such an alternative could be the so-called 'double-phase' multiferroics. These are heterostructures or superlattices composed of individual ferromagnetic and ferroelectric layers. The advantages of this approach are numerous. Firstly, it is possible to choose the FM and FE materials with high phase transition temperatures. Secondly, these materials could be optimized to ensure they have large spontaneous magnetisations and polarisations, respectively.

4.1.1 Complex Oxide Multilayers

Breakthroughs in materials processing has meant that it is now possible to grow heterostructures comprised of perovskite oxides with thicknesses of only one or two unit cells. These can be grown with atomically smooth and flat interfaces over hundreds of square microns [185]. The growth is usually achieved by thin-film vapour deposition techniques, including pulsed laser deposition, chemical vapour deposition, molecular beam epitaxy and sputtering. A common technique is to combine high-pressure reflection high-energy electron diffraction (RHEED) with pulsed laser deposition in order to control growth at the atomic level. With such a high level of control over the growth it is possible to design artificial materials with specific properties by atomic-scale tailoring their composition. For instance it has been shown, both experimentally and theoretically, that the functionality of thin-film oxides can be engineered by controlling strain [159, 186]. This can be achieved by optimising the lattice mismatch between the oxide and its substrate. With careful choice of substrate and film it is possible to tune the required properties. Importantly, a methodology to deposit oxides on silicon has already been developed with the result that their successful incorporation into standard microelectronic devices is now possible [187].

Since the development of epitaxial growth techniques, and driven by the interest in complex thin oxides, a variety of combinations of different materials has been investigated experimentally. For instance, the ferroelectric PZT, Pb(Zr, Ti)O_3 has been experimentally combined in a thick film laminate geometry with ferromagnetic Terfenol-D ($Tb_{1-x}Dy_xFe_2$) [188] and also $CoFe_2O_4$ [189]. Thin-film geometries have also been investigated, by combining FE materials such as $BaTiO_3$ with FM ones usch as (Pr, Ca)MnO_3. Another popular experimental geometry consists of embedding vertical pillar nanostructures in a matrix of another material in order to fabricate composite materials with high magnetoelectric coefficients [190].

Due to the long-range nature of the ferroelectric interaction, early theoretical work suggested that ferroelectric materials should have a critical thickness (t_c), i.e., a thickness below which the ferroelectric state become energetically or thermodynamically unfavourable [144]. It was thought that this thickness could be of the order of a few μm, with the result that the incorporation of ferroelectric materials in nan-

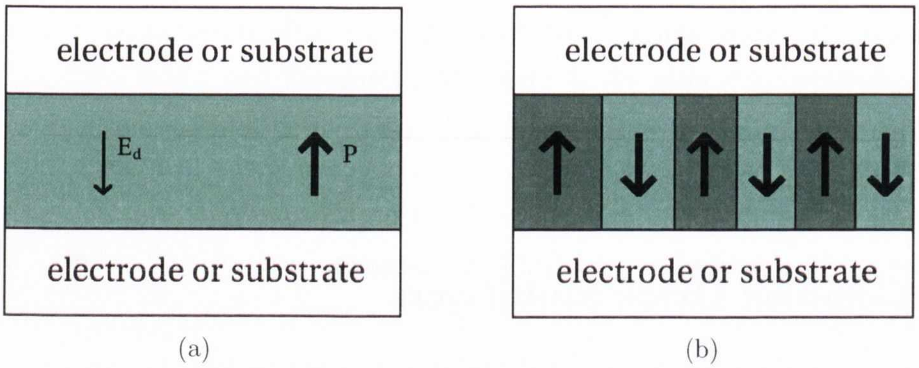

(a) (b)

Figure 4.1: Left panel: Electrode is comprised of a metallic material resulting in a depolarisation field, $\vec{E}_d$, in the ferroelectric barrier. Right panel: Electrode is insulting resulting in the creation of parallel polarisation domains.

odevices would be impossible. However, experimental work showed that t_c could be much smaller, at least by an order of magnitude. It was discovered that this critical thickness was not an intrinsic property of the ferroelectric material, but rather it depends on extrinsic electrical and mechanical boundary conditions and indeed on the ability to grow high quality samples at extremely low thicknesses. An effect of such boundary conditions is the so-called depolarisation field, $\vec{E}_d$. Assuming a polarisation normal to the interface, we expect a build-up of charge at either boundary of equal and opposite charge. This will result, if uncompensated, in a depolarising electric field and the spontaneous polarisation will be reduced (Fig. 4.1) [191]. The depolarisation field increases with the thickness reduction of the FE material. If the substrate is an insulator or a semiconductor, parallel polarisation domains will usually form so that the overall charge build-up will cancel. Metallic electrodes can provide charge compensation at the FE boundaries in order to reduce the depolarisation effects. Ideal electrodes can achieve complete charge compensation and thus result in zero depolarisation field. However, in realistic electrodes, the screening charge is located at a non-zero distance from the interface. The result is a small voltage drop across the electrodes and the appearance of a depolarisation field that will suppress a ferroelectric polarisation. For that reason, a careful choice of electrodes is critical to maintaining a ferroelectric state in ultra-thin films. Sample preparation can also have a huge effect on the critical thickness. It was reported [192, 193] that at small ferroelectric thicknesses a *passive* layer could be formed at the interface between the FE material and the electrodes. This resulted in a much reduced polarisation and was a factor leading to fatigue failures [194] in some FE memory devices. Lattice mismatch, and in particular strain relaxation, diffusion across the interface and other defects can all result in the formation of a passive layer.

In a significant theoretical advancement, Junquera and Ghosez reported a first-principles calculation on a fully strained $SrRuO_3/BaTiO_3/SrRuO_3$ film [157]. Such *ab initio* calculations mean that it is possible to take the effect of interfacial chemistry and atomic relaxations into account explicitly. They showed that the polarisation decreases with the thickness of the BTO layer (t_{BTO}) and that the film finally becomes paraelectric for thicknesses smaller than 6 unit cells, i.e., at 2.4 nm (Fig. 4.2). Such promising results were found across a range of multiferroic multilayers. $PbTiO_3$ was theoretically found to maintain a switchable spontaneous polarisation below three unit cells as long as the depolarisation field is fully compensated [195]. It was then experimentally found that PZT films can maintain a switchable polarisation down to thicknesses of a few nm [196].

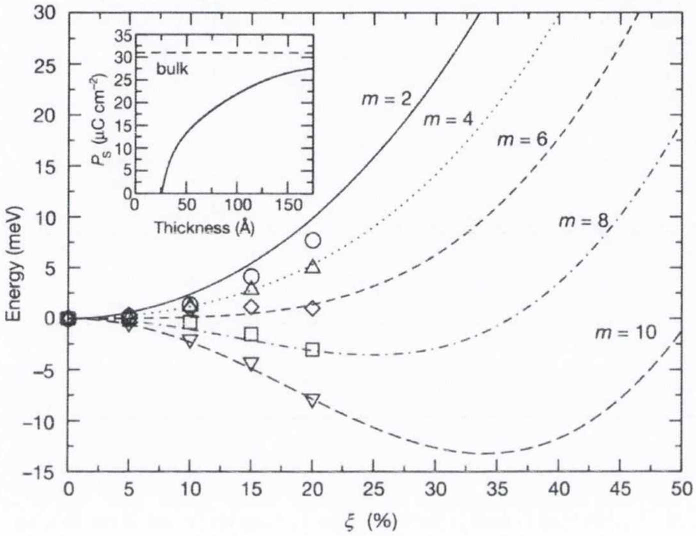

Figure 4.2: Total energy calculations for different thicknesses of BTO as a percentage of the bulk soft-mode displacements, Inset, evolution of the spontaneous polarisation, P_s, with thickness. Figure taken from Ref. [157].

In 2005 and 2006 Noh et al. [197, 198, 199] published a series of seminal experimental studies on ultrathin $BaTiO_3$ in a fully strained SRO/BTO/SRO/STO (001) geometry. This was the first experimental verification of the *ab initio* calculations by Junquera and Ghosez. High-quality epitaxial layers were grown on the $SrTiO_3$ substrate by using pulsed laser deposition. *In-situ* reflection high-energy electron diffraction (RHEED) measurements were carried out to control the thickness of the $BaTiO_3$ layer and also to monitor the quality of the interfaces. X-ray reciprocal space mapping (X-RSM) showed that the in-place lattice constant was the same in all the deposited layers; i.e. it was epitaxially matched to the $SrTiO_3$ substrate. The epitaxial growth was, in this case, possible up to t_{BTO} = 30nm. Most importantly, they found that their samples remained ferroelectric down to a thickness of at least 5nm without the formation of any passive layer. Encouragingly, as can be seen in Fig. 4.3, their structure also showed negligible effects of fatigue failure after 10^9 polarisation cycles.

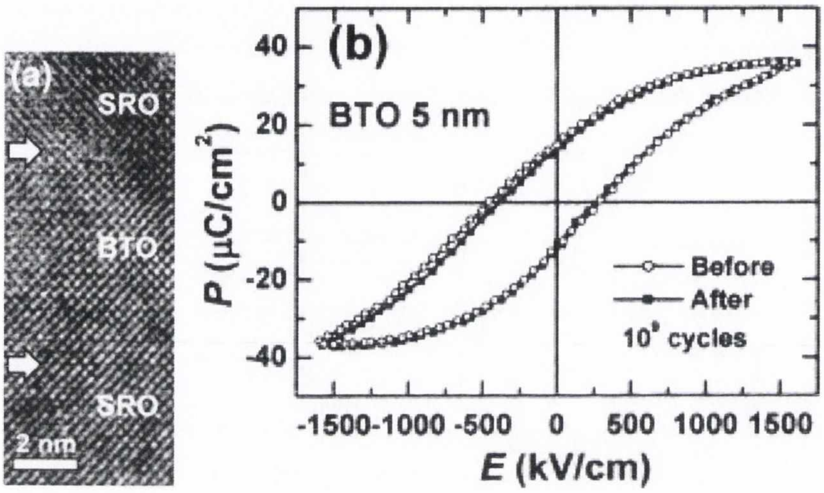

Figure 4.3: (a) TEM image of SRO/BTO (6.8 nm)/SRO capacitor structure. Arrows indicate interfaces between SRO and BTO layers and (b)P-E hysteresis loops for the 5 nm thick BTO structure showing negligible changes after 10^9 polarisation cycles. Figures taken from Ref. [199].

4.1.2 Jullière Model

The first model of the TMR effect was introduced by Jullière in his groundbreaking paper [10] from 1975. In this work the first measurements of the TMR were displayed, in an amorphous Fe/Ge/Co tunnel junction. A maximum TMR of 14% was found at zero applied bias which rapidly decreases with the application of a bias voltage (Fig. 4.4) and a model was developed to interpret the experimental results. This is still widely used to describe spin-dependent tunnelling. The model is based on two assumptions. The first is the so-called ‘two current’ model. This assumes that the conduction processes of the spin-up and spin-down electrons are completely independent [1]. Thus, for the parallel alignment of the magnetic electrodes, spin-up electrons moving in the left-hand side electrode remain spin up on the right-hand side one after tunnelling through the barrier. Similarly, spin down electrons on the left are still spin down on the right. The two current model neglects any effects arising from the spin-orbit interaction or any exchange interactions at the interface that could cause the spin magnetic moments to locally deviate from their bulk alignment. The second assumption is that the tunnelling matrix elements are independent of the energy and the spin direction of the tunnelling electrons. The result of these two assumptions is

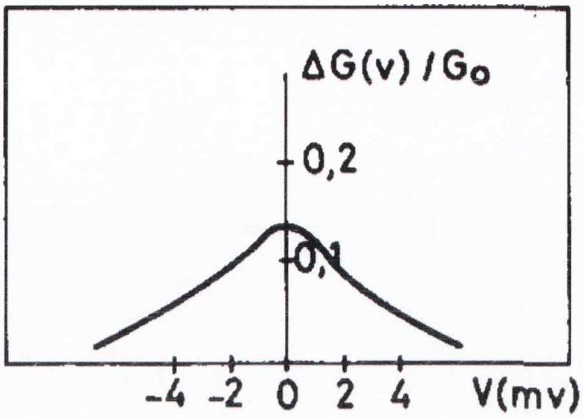

Figure 4.4: Original results from Jullière's 1975 experiment (Ref. [10]). Relative conduction (ΔG/G) as a function of applied bias to Fe/Ge/Co tunnel junction at 4.2K. ΔG is the difference in conduction between parallel and antiparallel magnetisation alignment of the two ferromagnetic electrodes. The maximum TMR effect of about 14% is found at zero bias but decreases dramatically with increasing bias, vanishing around 6mV.

that the tunnelling current is proportional to the density of states of the ferromagnetic electrodes

$$G^{\uparrow\uparrow} \propto N_L^{\uparrow} N_R^{\uparrow} \qquad G^{\downarrow\downarrow} \propto N_L^{\downarrow} N_R^{\downarrow}$$

$$G^{\uparrow\downarrow} \propto N_L^{\uparrow} N_R^{\downarrow} \qquad G^{\downarrow\uparrow} \propto N_L^{\downarrow} N_R^{\uparrow}$$

where $G^{\uparrow\uparrow(\uparrow\downarrow)}$ is the device conductance for parallel (antiparallel) magnetisation alignment and $N_L^{\uparrow(\downarrow)}$ and $N_R^{\uparrow(\downarrow)}$ are the density of states of the two ferromagnetic electrodes at the Fermi level. By defining the TMR as

$$TMR = \frac{G_P - G_{AP}}{G_{AP}}$$

and the spin polarisation as

$$P_{L,R} = \frac{N_{L,R}^{\uparrow} - N_{L,R}^{\downarrow}}{N_{L,R}^{\uparrow} + N_{L,R}^{\downarrow}}, \tag{4.1}$$

we have that

$$TMR = \frac{2P_L P_R}{1 - P_L P_R}.$$

(A discussion of the various definitions of spin polarisation can be found in Chapter 3, Section 3.2.7). The Jullière model achieved good agreement with experiment for the case of amorphous Al_2O_4 barriers. However, in some cases it does not work. For instance, the values of P measured for Fe, Co and Ni indicates that transport is dominated by majority electrons. The Jullière model would suggest the opposite based on the mainly minority Fermi level density of states in these materials (note that both Co and Ni are strong magnets). In order to apply the Jullière model more generally, the DOS entering in Eqn. (4.1) must represent an 'effective' tunnelling DOS, characterising the interfaces as well as the electrodes.

4.1.3 Free electron model

The Jullière model was extended by Slonczewski in 1989 [200] within the free electron framework. The free electron model considers a rectangular potential barrier (see Fig. 4.5) of height V_B separating two exchange split ferromagnetic electrodes described by potentials V_1^σ and V_2^σ. Here 1 and 2 refer to the left-hand and right-hand electrodes, respectively and σ is the spin index. The transverse component of the wave vector, $\vec{k}_{||}$, is assumed to be conserved. On the left-hand side of the barrier the longitudinal wavevector is given by $k_1 = \sqrt{\frac{2m}{\hbar^2}(E_F - V_1 - k_{||}^2)}$ while on the right side it is given by $k_2 = \sqrt{\frac{2m}{\hbar^2}(E_F - V_2 - k_{||}^2)}$. Within the barrier it is purely imaginary and given by $\kappa = \sqrt{\frac{2m}{\hbar^2}(V_B - E_F + k_{||}^2)}$. By assuming a sufficiently thick barrier, the transmission coefficient can be written as

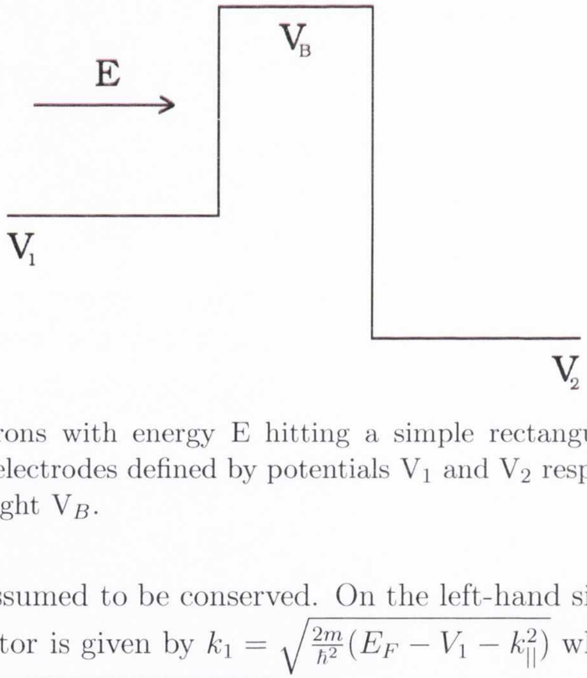

Figure 4.5: Free electrons with energy E hitting a simple rectangular barrier, with left and right electrodes defined by potentials V_1 and V_2 respectively and potential barrier height V_B.

$$T_\sigma(\vec{k}_{||}) = 16\kappa^2 \frac{k_L^\sigma}{(\kappa^2 + k_L^{\sigma 2})} \frac{k_R^\sigma}{(\kappa^2 + k_R^{\sigma 2})} e^{-2\kappa d}.$$

We can define two interface transmission functions $T_L^\sigma(\vec{k}_{||})$ and $T_L^\sigma(\vec{k}_{||})$ as

$$T_n^\sigma(\vec{k}_{||}) = \frac{4\kappa k_n^\sigma}{\kappa^2 + k_n^{\sigma 2}}$$

so as to decouple the transmission coefficient into contributions from the left and right electrodes interfaces

$$T^{\sigma}(\vec{k}_{||}) = T^{\sigma}_{L}(\vec{k}_{||})e^{-2\kappa d}T^{\sigma}_{R}(\vec{k}_{||}).$$

If we assume that the primary contribution to the tunnelling conductance occurs at $\vec{k}_{||} = 0$ (valid for thick junctions) the total conductance is proportional to the product of $T^{\sigma}_{L}(\vec{k}_{||} = 0)$ and $T^{\sigma}_{R}(\vec{k}_{||} = 0)$. We can then define an 'effective' spin polarisation of the electrodes to be

$$P_n = \frac{T^{\uparrow}_{n}(\vec{k}_{||} = 0) - T^{\downarrow}_{n}(\vec{k}_{||} = 0)}{T^{\uparrow}_{n}(\vec{k}_{||} = 0) + T^{\downarrow}_{n}(\vec{k}_{||} = 0)},$$

which becomes

$$P_n = \frac{k^{\uparrow}_{n} - k^{\downarrow}_{n}}{k^{\uparrow}_{n} + k^{\downarrow}_{n}}\frac{\kappa^2 - k^{\uparrow}_{n}k^{\downarrow}_{n}}{\kappa^2 + k^{\uparrow}_{n}k^{\downarrow}_{n}}. \tag{4.2}$$

as found by Slonczewski [200]. Thus the spin polarisation depends not only on the electrodes but also contains a factor that depends on the barrier height. In the limit of infinite barrier height, Eqn. (4.2) reduces to the Jullière model.

Although such free electron models are physically intuitive and in many cases can give good qualitative descriptions of the tunnelling process, they are not capable of quantitative predictions. They do not take into account the band structure of the electrodes, the complex band structure of the barrier or the details of the interface that can include resonant states and chemical bonding effects.

4.1.4 Complex Band Structure

Density functional theory provides a powerful method to calculate TMR by taking into account the multiband description of the electronic structure. The Bloch condition of propagating states with wavevector $\vec{k}$ can be written as

$$\psi_k(\vec{r} \ + \ \vec{a}) = e^{\iota\vec{k}.\vec{a}}\psi_k(\vec{r}).$$

Within the bulk crystal, periodicity demands that $\vec{k} \in \mathbb{R}$. However, at an interface or a surface, complex wavevectors are required to ensure that the wavefunction and its derivative are continuous. This theory of complex band structures was first developed by Heine [201] in 1963 and its importance in relation to tunnelling through an insulating barrier was noted by Mavropoulos et al. [202] and Butler et al. [23] Although such evanescent or complex states only exist at the boundary, it is possible to derive them from the bulk band structure by formally allowing $\vec{k} \in \mathbb{C}$ solutions to the Schrödinger equation.

Within a perfectly epitaxial tunnel junction (meaning that there is perfect translational symmetry in the direction orthogonal to the transport), periodicity in the xy-plane requires that the transverse component of the wavevector, $\vec{k}_{||}$, is real and conserved. However, the z component of wavevector, k_z, can be complex. The wavevector can be then written as

$$\begin{aligned} \vec{k} &= \vec{k}_{||} + k_z \\ &= \vec{k}_{||} + q + \iota\kappa, \end{aligned}$$

where κ is the decay constant. The imaginary part of the wavevector, κ, dominates the transport properties of an insulating barrier as it determines the wavefunction decay. This is given as $\sim e^{-\kappa z}$ where z is the barrier thickness. In order to determine the complex band structure it is usual to solve the the 'inverse' band structure problem, i.e., instead of fixing the wavevector and solving for the eigenstates, one fixes the energy and solves for both the real and complex wavevectors. As the wavefunction decay is determined by these complex bands, it is clear that the state with minimum κ, κ_{min}, will dominate the transport properties. A general strategy for determining κ_{min} is a follows

1. For given values of $\vec{k}_{||}$ and E_F find the smallest κ,
2. Vary $\vec{k}_{||}$ and search for absolute min κ_{min}.

Of primary importance is the character of κ_{min}, i.e., its symmetry and $\vec{k}_{||}$ value. In general, κ_{min} will be found at $\vec{k}_{||} = 0$. This is true for a wide variety of insulators, in particular for materials with a direct band gap at Γ. However, finding κ_{min} at some $\vec{k}_{||} \neq 0$ is also possible, especially for materials with an indirect band gap, e.g. Si [202]. The complex bands inherit the symmetry properties of the real bands they are connected to. In order for an electron to tunnel through a junction, a state with a particular symmetry in the electrode must couple effectively with an evanescent state of the same symmetry in the insulator. The important role of such symmetry matching between metal and insulator wavefunctions has been recently investigated by several *ab initio* calculations [23, 203, 204, 205, 206]. One of the first systems studied was the Fe/MgO/Fe tunnel junction. Electron wavefunctions in Fe with Δ_1 symmetry decay much slower across the MgO barrier than states with any other symmetry. States with Δ_1 symmetry in Fe are filled for majority spins and empty for the minority ones. The result is that the Fe/MgO system acts as an half-metal and the TMR is expected to be very large [23, 24]. This was later confirmed by experiment

[207].

In the rest of this Chapter we will focus on an all-oxide tunnel junction with a ferroelectric barrier, namely $SrRuO_3/BaTiO_3/SrRuO_3$.

Firstly, we will discuss the structural and electronic properties of the junction, concentrating on several properties in particular: the effect of the metallic electrodes on the ferroelectric distortion, the influence of the insulating barrier on the magnetic properties of the ferromagnetic electrodes and the band alignment between the two materials. The effect of two different exchange correlation functionals on some of these properties is also discussed.

We then describe the transport properties of such a junction, looking at both an artificial centrosymmetric structure and the relaxed ferroelectric one. We demonstrate theoretically a huge TMR and more importantly we will show that the TMR sign can be reversed with bias. Our results are rationalized in terms the band-structure match between the ferroelectric insulator and the ferromagnetic electrodes [208].

4.2 $SrRuO_3$/$BaTiO_3$/$SrRuO_3$ - structural and electronic properties

Theory and modeling of tunnelling junctions incorporating functional materials are in their infancy. Most models proposed to date are based on simplified band structures [178, 209, 210], while DFT has been limited to the evaluation of the local atomic structure [211], the electrostatic profile [212] or the zero-bias conductance [213]. First principles calculations of insulating junctions are complicated as the interfacial properties are strongly influenced by the band alignment which cannot be correct if the band gap is severely underestimated. As was discussed in Chapter 3, the band gap of $BaTiO_3$ is underestimated when determined by local exchange and correlation functionals. In this work we have chosen to use the approximate self interaction correction scheme (ASIC) [45], which has been shown to produce an increased band gap for $BaTiO_3$ as well as accurate band energies for $SrRuO_3$.

Calculations were performed using density functional theory (DFT) as implemented in the SIESTA code [118]. For reasons that shall be explained in the following sections, the GGA functional was used to perform structural relaxations while the ASIC functional was used in the calculation of the transport properties. An optimized double-ζ basis set is defined in a split valence manner, where the radial part of the wavefunction smoothly goes to zero beyond a cut-off radius [118]. Core electrons were removed from the calculations and described by norm-conserving Troullier-Martins' pseudopotentials [60] with non-linear core corrections [214]. Basis parameters for $BaTiO_3$ and $SrRuO_3$ were previously used in the study by Junquera et al. [215]. Real-space integration was performed on a regular grid with grid spacing equivalent to a plane-wave cut-off of 800 Ry. A k-point grid with an equivalent spacing of 15 Å was used throughout the work for structural relaxations. Relaxations were preformed so that the forces were less than 0.01 eV/Å.

In this section we concentrate on the structural and electronic properties of a $SrRuO_3/BaTiO_3/SrRuO_3$ tunnel junction while the transport and the TMR are discussed in the following section. We first look at the factors that can influence the electrical polarisation of the $BaTiO_3$ layer, we show how the ferroic phase can manipulate the interfacial magnetic properties and finally discuss in detail the band alignment of the heterostructure.

4.2.1 Structure

We perform an initial relaxation of bulk $BaTiO_3$ and $SrRuO_3$ under an in-plane compressive strain, emulating the common epitaxial growth on $SrTiO_3$, to find the relaxed out-of-plane lattice constant. The relaxed cells are then used to construct the transport supercell. The $SrRuO_3/BaTiO_3$ interface was chosen to be SrO/TiO_2, due to the experimentally observed volatility of the RuO_2 termination [157, 216]. We consider two structures. In the first non-ferroic (NFE) structure the atoms are frozen artificially in their centro-symmetric positions with the interfacial distance given by an average between the $BaTiO_3$ and $SrRuO_3$ *c*-lattice constant. In the second all positions in the supercell are completely relaxed out-of-plane until the forces are less than 10 meV/ Å, resulting in a stable ferroelectric ground state (FE structure) as shown in Fig. 4.6.

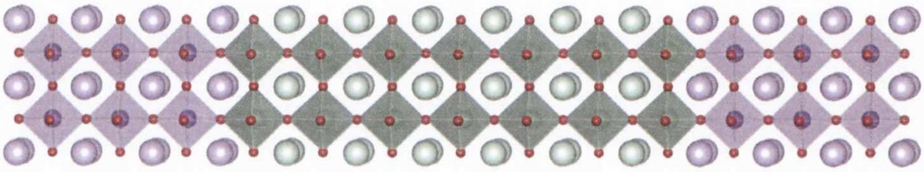

Figure 4.6: $SrRuO_3/BaTiO_3/SrRuO_3$ heterostructure. Periodic boundary conditions are applied in all directions.

The basic unit cell, periodically repeated in space, corresponds to

$$(\mathrm{SrO}-\mathrm{RuO_2})_3-\mathrm{SrO}\ /\ \mathrm{TiO_2}-(\mathrm{BaO}-\mathrm{TiO_2})_\mathrm{n}\ /\ (\mathrm{SrO}-\mathrm{RuO_2})_3$$

where we considered n = 3, 4 and 6. Starting from the above structure we performed a full relaxation with respect to the atomic coordinates to find the ferroelectric ground state. Fig. 4.7 shows the layer by layer displacement between oxygens and cations along the stack direction for n = 6. The displacements can be related to the magnitude of the ferroelectric distortion in the layers. Indeed, an approximation to the polarisation is $P = \Sigma Z^* d$, where Z^* are the Born effective charges of each ion and d is the magnitude of the displacement of the ion from the centrosymmetric reference configuration. Here, displacements are defined for each atomic plane as $\delta = (z_{cation} - z_O)$ where z_{cation} and z_O denote the cation and oxygen positions in a particular plane. At the center of the $BaTiO_3$ slab Ti is displaced by 0.14 Å, which is significantly smaller than the value of 0.23 Å of bulk $BaTiO_3$ experiencing the same strain. In agreement with calculations for the bulk the tetragonal phase is stabilized by the constraint of the substrate and only polarisation along the direction perpendicular to the interface is observed. In Fig. 4.7 the displacements within the centre of the $BaTiO_3$ are almost uniform right up to the interface with $SrRuO_3$. Such a quick recovery distance for the polarisation, where the polarisation is suppressed only in the layer or two immediately close the interface has already been shown [217]. Ionic displacements are also evident extending into the $SrRuO_3$ electrodes. Such displacements in the electrode were predicted to provide a lattice contribution to the screening ability of the metal along with the electronic screening [218] and have been experimentally found in Ref. [219]. Indeed, the value of critical thickness given by Junquera and Ghosez in Ref. [157] is likely to be underestimated as their calculation was carried out under the constraint that the ions of the electrode are held in their fixed bulk positions and the displacements within the ferroelectric are homogeneous throughout the material. The quantitative effect of the ionic contribution to the screening is shown in Fig. 4.8. Here, two possibilities are considered. In the first, all the atoms of $SrRuO_3$ are held fixed as the $BaTiO_3$ layer is allowing to relax (black squares). The maximum Ti - O displacement for this configuration is 0.12 Å. In the second configuration, the unit cell of $SrRuO_3$ closest to the interface is also allowed to relax along with $BaTiO_3$. A dramatic increase in polarisation is achieved with a maximum displacement of the Ti atoms now of 0.14 Å. Allowing the electrodes, and in particular perovskite metal oxide electrodes, to share the ionic displacements reduces the critical thickness for ferroelectricity in $BaTiO_3$ in such heterostructure due to the increased possible screening.

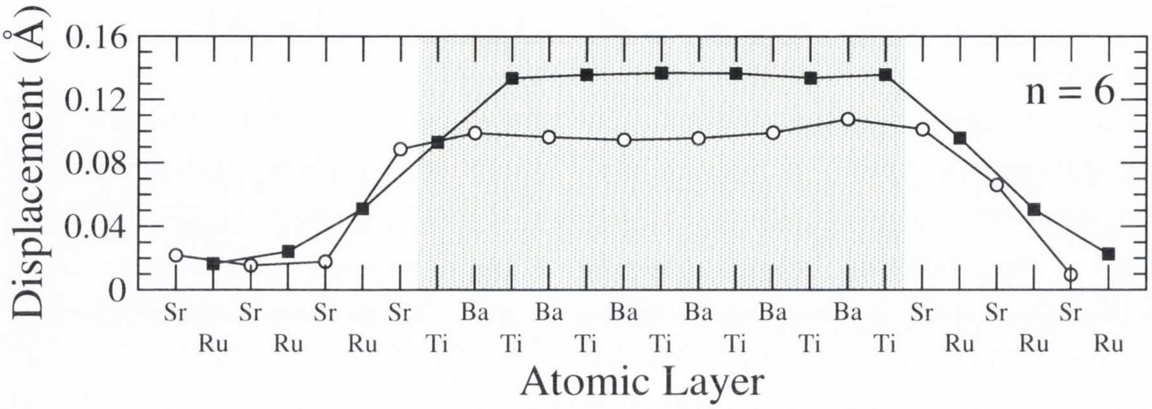

Figure 4.7: Relative atomic displacement for Sr, Ba (open circle) and Ru, Ti (filled circle) in the relaxed $SrRuO_3/BaTiO_3/SrRuO_3$ MTJ investigated. The displacements are with respect of the O atoms in the same plane, $\delta = (z_{\text{cation}} - z_{\text{O}})$, with z being stack direction.

Fig. 4.9 shows the displacements associated with the relaxed ferroelectric state for $n = 3$ and $n = 4$. As expected, the reduction of t_{BTO} results in a decrease of the

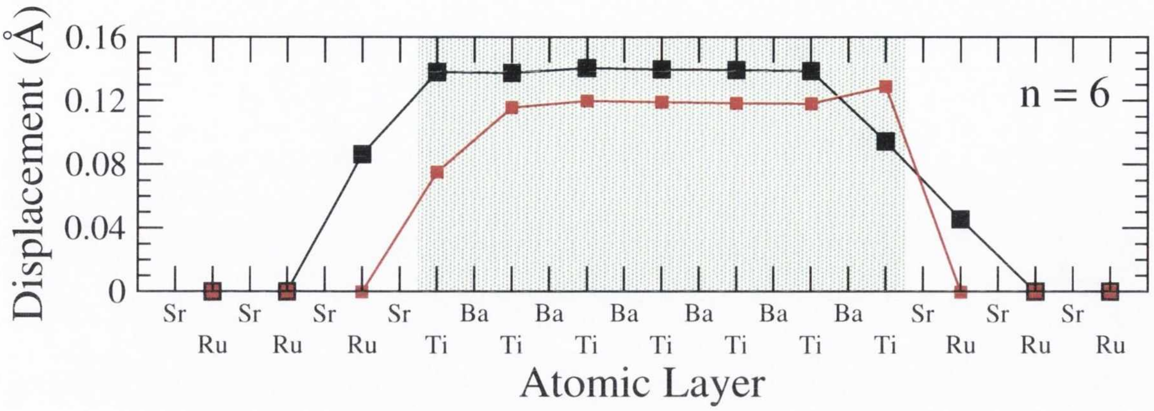

Figure 4.8: Relative atomic displacement for Sr, Ba (open circle) and Ru, Ti (filled circle) in the relaxed $SrRuO_3/BaTiO_3/SrRuO_3$ MTJ investigated for the case where only the interfacial $SrRuO_3$ layer is allowed to relax (black curve) and where all of the $SrRuO_3$ atoms are held fixed (red curve).

spontaneous polarisation. This can be seen from the decreased atomic displacement for the $n = 3$ case as compared to the $n = 4$ case. A further increase in polarisation can also be seen for $n = 6$ (Fig. 4.7). In all of these cases, the total $SrRuO_3$ layer was also allowed to relax.

Finally, we discuss the effect of ASIC on the structural relaxations. As we saw in Chapter 3 when dealing with bulk $BaTiO_3$, ASIC is incapable of describing simultaneously both the structural and the electronic properties. The result is that the ferroic ground state of the heterostructure becomes unstable, namely the relaxation with the ASIC functional results in a non-ferroic ground state as shown in Fig. 4.10. Clearly at the centre of the $BaTiO_3$ layer, the displacements are zero. Here, the structure has reverted to a centrosymmetric ground state. Close to the interfaces some displacements occur but these are approximately equal and opposite at the two edges of the $BaTiO_3$ layer so that the overall polarisation remains zero.

In the rest of this Chapter we will consider the n = 6 structure only.

4.2.2 Magnetic Properties

Magnetoelectric coupling can be mediated in a multiferroic multilayer via interfacial bonding. The atomic displacements at the interface driven by a ferroelectric distortion alters the overlap between the interfacial atomic orbitals which in turn alter the local magnetisation. Thus, by reversing the direction of the electrical polarisation of the ferroelectric barrier - by applying an external electric field - it is possible to manipulate the magnetic properties of the heterostructure. Such an approach to enhancing magnetoelectric coupling has been investigated [220, 221] previously for a

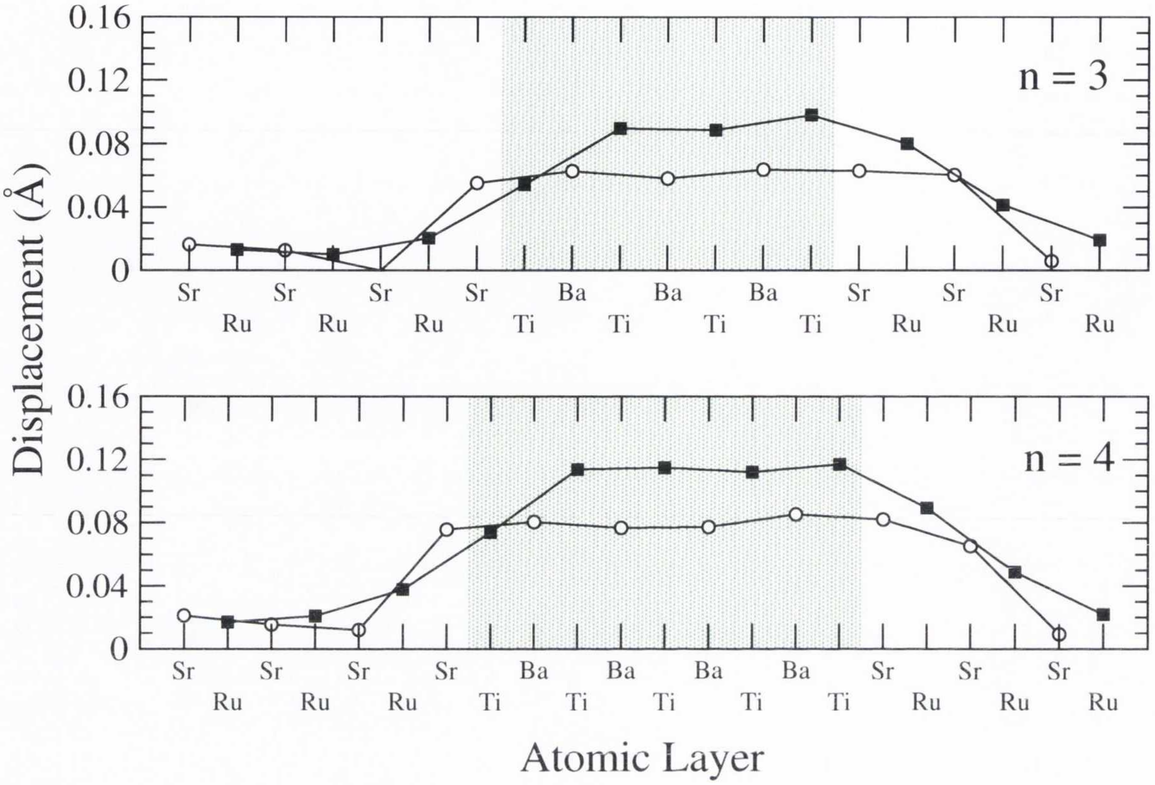

Figure 4.9: Displacements of A (=Sr, Ba) and B (=Ru, Ti) atoms with respect to the O atoms in the same plane (calculated with the GGA) for the n=3 and n=4 structures. Solid symbols denote displacements of Ru and Ti. Open symbols denote displacements of Sr and Ba. The shaded area shows the $BaTiO_3$ region between the two interfaces.

number of junctions. Here we consider only how the interfacial magnetic moments are modified when the system changes from a centrosymmetric configuration (NFE) to the ground state ferroelectric (FE) structure.

Symmetry demands that in the NFE case, the magnetic moments of the atoms at left and right interfaces are identical. These are shown in Fig. 4.11 for the ASIC functional. Previous studies of magnetoelectric effects in multilayers containing $BaTiO_3$ have found induced magnetic moments on the interfacial Ti and O atoms and modified moments on the atoms in the magnetic electrodes. Here we see that the magnetic moment on the interfacial Ru atom is slightly depressed compared to its bulk value (at the same strain): $1.34\mu_B$ compared to $1.356\mu_B$. This can be attributed to bonding effects at the interface. A small moment ($0.02\mu_B$) is induced on the interfacial Ti atom in the opposite direction.

The FE ordering breaks the mirror symmetry about the median plane through the $BaTiO_3$ layer so that now the magnitude of the induced magnetisation depends of the direction of polarisation. In this case, the polarisation is pointing towards the

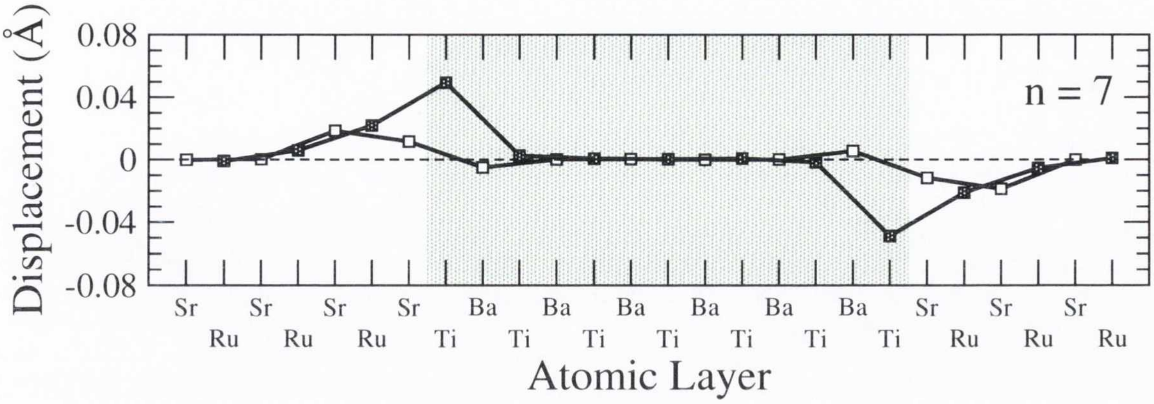

Figure 4.10: Displacement of Sr, Ba (open circle) and Ru, Ti (filled circle) in the $SrRuO_3/BaTiO_3/SrRuO_3$ MTJ investigated when relaxed by using the ASIC forces. Note the complete suppression of the FE state in $BaTiO_3$.

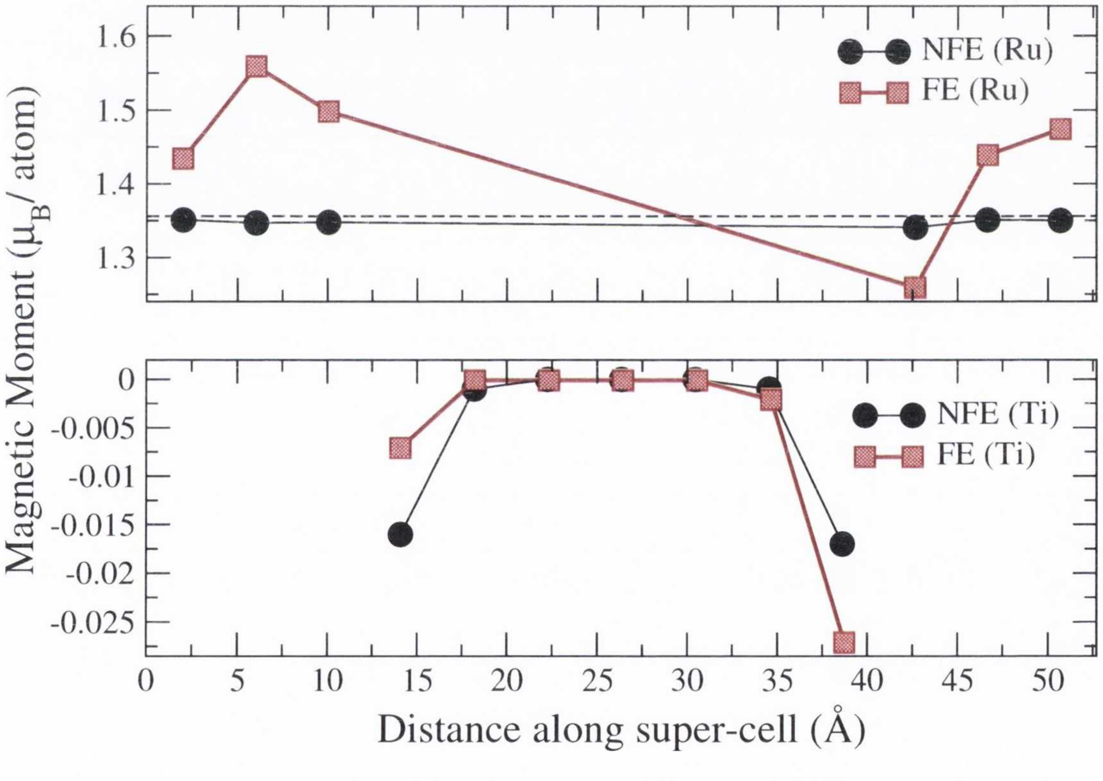

Figure 4.11: Magnetic moments of the Ru ions (top graph) and Ti ions (bottom graph) for the NFE structure (black circles) and the FE structure (red squares) calculated with the ASIC.

right interface (Interface 2). Here, the magnetic moment on the interfacial atom is increased to $1.50\mu_B$. In contrast, at the left interface it is reduced to $1.28\mu_B$. The difference in Ru magnetic moments at the two interfaces for the ASIC functional is then $\Delta\mu_{Ru} = 0.22\mu_B$. A similar trend is found for the GGA functional although the magnitude of the changes is smaller ($\Delta\mu_{Ru} = 0.10\mu_B$).

Table. 4.1 presents the magnetic moments of the interfacial Ti, O and Ru atoms in the FE structure for both the GGA and the ASIC functionals.

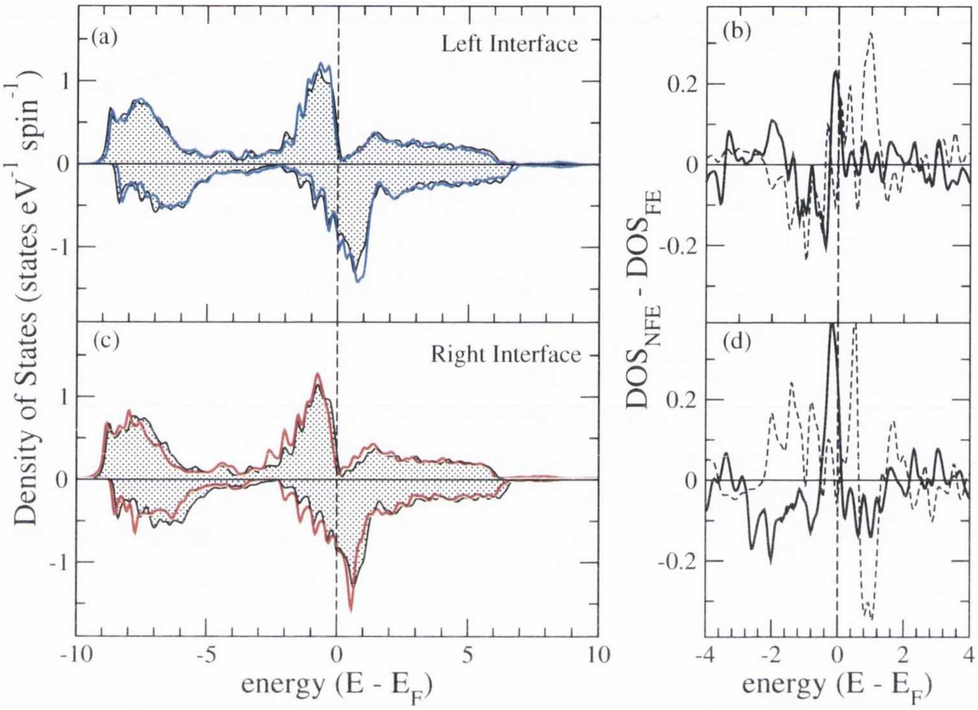

Figure 4.12: Electronic structure at the left-hand and right-hand side interfaces of a $SrRuO_3$ / $BaTiO_3$ / $SrRuO_3$ junction. The left panel shows the density of states projected onto the Ru 4*d* states at either interface for the NFE structure (black curves) and the FE structure (blue and red curves). The right panel gives the difference between the DOS for the NFE and FE states at either interface for spin up (solid line) and spin down (dashed line).

In order to achieve insight into the mechanism that alters the interfacial magnetic moment, we plot the projected density of states (PDOS) for the Ru and Ti atoms. The DOS projected onto the Ru 4*d* orbitals at the left and right interfaces are shown in the left panels of Fig. 4.12. The larger change in spin splitting for the right interface compared to the left interface which can be seen in the right panel of Fig. 4.12, leads to the increased magnetic moment at that interface.

The origin of this change in spin splitting depending on the interface has been attributed [221] to different screening effects at either interface. In Fig. 4.13 the density of states projected onto the Ti orbitals are shown. The Ti 3*d* orbitals hybridize with the exchange split O 2*p* states (not shown) which results in an induced spin splitting. Since Ti is closer to the electrodes at the right interface than it is at the left one, hybridisation is stronger here. This is evident in the increased magnitude of induced magnetic moment at such an interface. In particular, it appears that the Ti atom is anti-ferromagnetically coupled to Ru. However the induced moment decays very quickly and is reduced to zero by the third layer.

		Interface 1	Interface 2	Bulk
	Atom	μ_B	μ_B	μ_B
GGA	Ti	-0.03	-0.01	0.00
	Ru	1.30	1.40	1.49
ASIC	Ti	-0.02	-0.01	0.00
	Ru	1.28	1.50	1.45

Table 4.1: Magnetic moments of the Ti and Ru atoms at left and right interfaces for the electrical polarisation pointing from left to right. Bulk values are taken as the average value in the centre of the BTO and SRO layers.

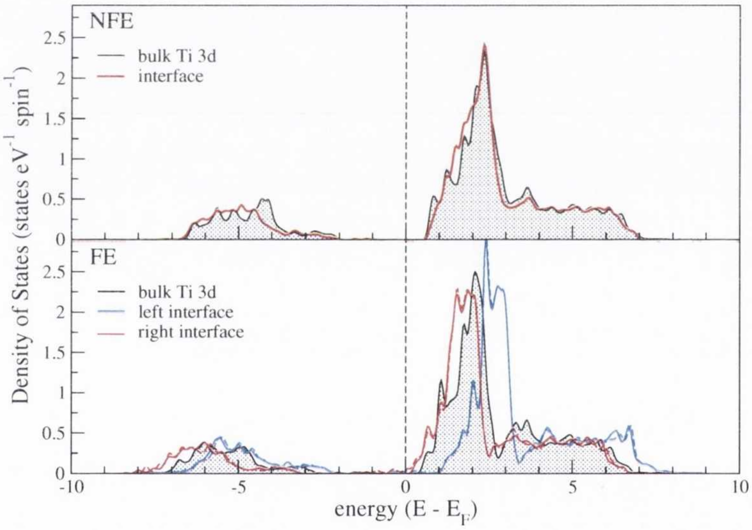

Figure 4.13: Density of states projected onto the Ti 3*d* states for the NFE and FE structures at the left (blue) and right (red) interfaces. The bulk values are taken from the central Ti ion in the $BaTiO_3$ layer.

4.2.3 Band Alignment

For a tunnelling junction to function, the Fermi level of the ferromagnetic electrodes must lie in the gap of the insulator. If this does not happen, charge can spill out from the metal to the insulator, resulting in changes to the electronic and structural properties of the interface. The band gap problem associated with the use of local exchange and correlation functionals can artificially lead to this effect. An underestimated band gap can result in the Fermi level of the metal being unphysically aligned with the conduction band of the insulator. Charge can then spill into the

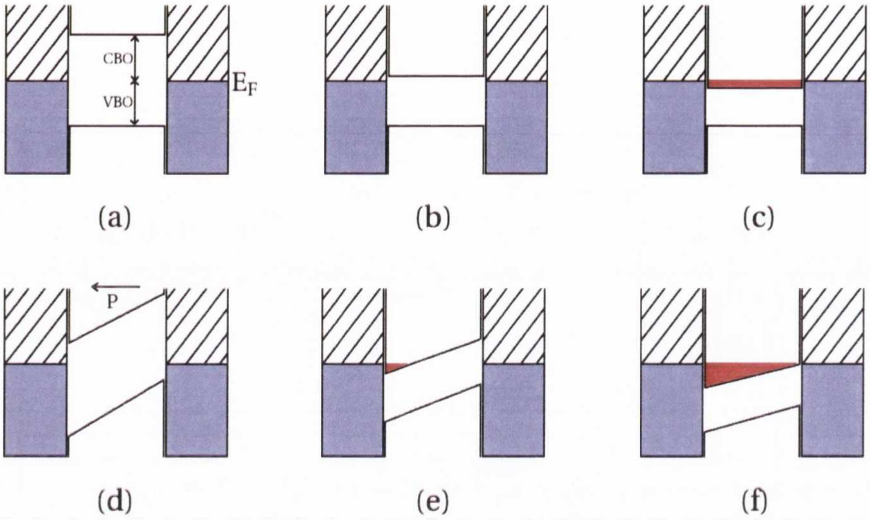

Figure 4.14: Schematic band alignment in a typical FM/FE/FM tunnel junction. The paraelectric (PE) case is shown in (a)-(c) while the ferroelectric case is shown in (d)-(f). (a) and (d) show the ideal case where the Fermi level sits within the bandgap of the insulator and remains so, even for the FE case. (b) and (e) shows the typical outcome of the DFT band gap problem, where in the PE case (b) the CBO is positive but small and for the FE case some charge spillage (red) occurs at the layers close to the interface. (c) and (f) show the pathological case where even for the PE case the Fermi level is aligned with the conduction band of the barrier.

barrier resulting in unphysical metallicity of at least the first few interfacial layers. The situation becomes more complicated when ferroelectric barriers are considered. This is because the depolarising field induces an electrostatic potential drop across the barrier. Several possible alignments are then possible depending on the materials involved and even on the exact layer terminations at the interface. A schematic diagram of the various possibilities is shown in Fig. 4.14. A detailed discussion of this problematic situation can be found in Ref. [222]. Here, it is noted that the effects of such a band alignment problem are subtle to detect and in many cases have been overlooked or attributed in the literature to other causes.

Determining the band alignment from first principles

The band alignment cannot be determined from simply looking at the band edges of the two bulk materials in question; it can only be obtained from a self-consistent calculation of a supercell containing both the materials. There are two methods to extract the band alignment from a first principles calculation. The first one involves the local density of states. Firstly, one computes the density of states in the supercell at a point in the barrier far from either interface and projected onto a deep semicore state. Such a state should be insensitive to the chemical environment. Secondly, we need to extract the atomic coordinates for a unit cell located at this position and build a periodic bulk calculation based on them. The PDOS for this unit cell is then calculated as before. Then we align the two PDOSs by using the sharp semicore state that was chosen as the reference energy. If there is a finite DOS at the Fermi level it is likely that charge has spilled from the metal to the insulator. If not, then the exact alignment can be determined by using the electrostatic potential profile. Following the procedure in Ref. [215], the band offset can be split into two terms, the valence band offset (VBO) and the conduction band offset (CBO)

$$\begin{aligned} VBO =& \Delta E_V + \Delta V, \\ CBO =& \Delta E_C + \Delta V. \end{aligned}$$

$\Delta E_V (\Delta E_V)$ is the 'band structure' term and is it defined as the difference between the top of the valence band (bottom of the conduction band) and the Fermi level as obtained from two independent bulk calculations and $\Delta \mathrm{E}_C = \Delta \mathrm{E}_V + \Delta \mathrm{E}_{gap}$ where $\Delta \mathrm{E}_{gap}$ is the band gap of the barrier. ΔV is the line-up of the average of the electrostatic potential[1] in a supercell calculation. The resulting macroscopic average should be smooth far from the interface. ΔV is then defined as the difference between the two 'bulk-like' regions. Due to structural problems in the description of $BaTiO_3$ with ASIC and problems with the electronic structure with LDA and GGA functionals we have opted to relax the heterostructure with the GGA functional and used this relaxed structure to calculate the electronic density with all the functionals. The band alignment for the $SrRuO_3/BaTiO_3$ heterostructure, calculated by the method described in Junquera et al [223], is shown schematically in Fig. 4.15. The Fermi level of $SrRuO_3$ lies within the $BaTiO_3$ band gap in all cases and the ASIC provides an improvement to the band alignment. In the paraelectric case there is a 0.45 eV gap between the Fermi level and the bottom of the conduction band in GGA; this increases to 0.78 eV with the ASIC. Furthermore, the GGA 0.18 eV gap at one interface of the ferroelectric phase is increased to 0.35 eV with the ASIC. Currently no experimental band alignment information exists we therefore predict that the valance band offset for the $SrRuO_3/BaTiO_3$ junction is 2.6 eV.

In conclusion, the description of a heterostructure is not straightforward with DFT. It requires a good description of the atomic and electronic structure simultane-

---

[1] To obtain the macroscopic average [223] of the electrostatic potential, the total microscopic electrostatic potential is averaged with two step-like filter functions whose lengths are given as the distance between the AO and BO_2 planes in SRO and BTO.

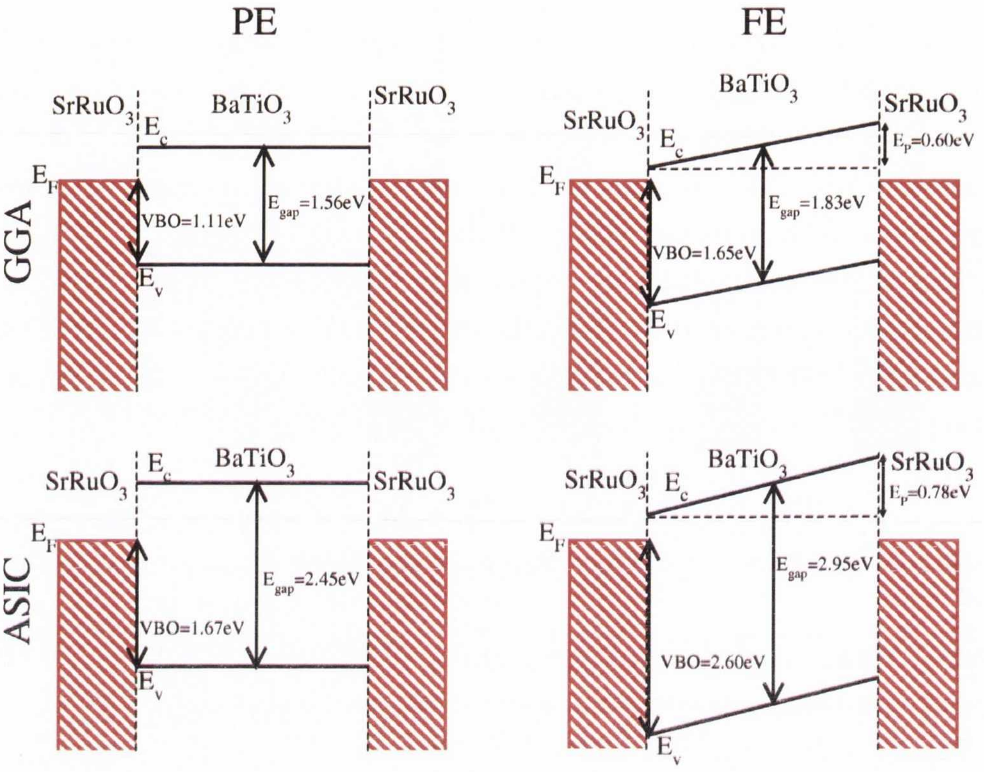

Figure 4.15: Schematic of the valence and conduction band offsets (VBO and CBO, respectively) for $SrRuO_3/BaTiO_3/SrRuO_3$ interfaces.

ously but none of the functionals studied here can provide this. GGA and LDA offer a reasonable description of the atomic structure of $BaTiO_3$ and $SrRuO_3$, however the band dispersion and the band gap of $BaTiO_3$ are incorrectly reproduced. ASIC corrects the electronic structure of both $BaTiO_3$ and $SrRuO_3$ and we find that the valance band offset in the $SrRuO_3/BaTiO_3$ should be 2.6 eV. However, as noted in Chapter 3, ASIC is incapable of describing the ferroic phase of bulk $BaTiO_3$. This remains true when $BaTiO_3$ is included as barrier material in a tunnel junction. We found that the strategy of using the GGA atomic structure and the ASIC charge density provides the most realistic junction description of the electronic structure to be used in a transport calculation. The transport properties of the $SrRuO_3/BaTiO_3/SrRuO_3$ heterostructure are discussed in the following section.

4.3 $SrRuO_3/BaTiO_3/SrRuO_3$ - transport properties

4.3.1 Introduction

In this section we demonstrate theoretically a huge TMR and more importantly we show that the TMR sign can be reversed with bias, at a critical bias which depends on the ferroic state of the barrier. Our results are rationalized in terms the band-structure match between the ferroelectric insulator and the ferromagnetic electrodes.

Density functional theory (DFT) calculations are performed with the local basis set code SIESTA [118]. Structural relaxation is obtained with the generalized gradient approximation (GGA) of the exchange and correlation functional [38]. This gives a satisfactory device geometry, but it produces a rather shallow band alignment mainly because of the DFT-GGA gap problem. As was discussed in Section 4.2.3, this is problematic when applying a bias across the junction as the conduction band will quickly become populated leading to an underestimation of the break-down electric field [224]. In order to make up for this shortfall the electronic structure used for the transport calculations is that obtained with the atomic self-interaction correction (ASIC) scheme [45], which improves drastically the electronic properties of both bulk $BaTiO_3$ [225] and $SrRuO_3$ [226] while increasing the electric field at which the device will break-down. As we saw, the approximate ASIC energy functional is not sufficient to produce good structural parameters and in particular the $BaTiO_3$ ferroelectric state cannot be stabilized. This is a current limitation of the method, which otherwise has been successful in predicting the electronic properties of oxides [227]. For this reason we perform ASIC transport calculations at the GGA relaxed structural parameters to provide the most realistic junction description. For all the calculations we use a $6\times6\times1$ k-point Monkhorst-Pack mesh to converge the density matrix to a tolerance of 1×10^{-5} and a grid spacing equivalent to a plane-wave cutoff of 800 eV.

Electron transport is computed with the SMEAGOL code [142, 228], which combines the non-equilibrium Green's function scheme with DFT. Since SMEAGOL interfaces SIESTA as the DFT platform, we employ here the same parameters used for the total energies calculations. A detailed discussion of the SMEAGOL code and transport theory in general is given in Chapter 2. The spin-dependent transmission coefficient, $T^\sigma(E,V)$, is evaluated on a $100\times100\times1$ k-point Monkhorst-Pack mesh for the 0-bias calculations and on a $24\times24\times1$ k-point mesh at finite bias. No sensible changes in $T^\sigma(E,V)$ were found when enlarging these k-point meshes.

4.3.2 Results and Discussions

Band structure and symmetries

The symmetries of the electronic bands of both the ferromagnetic electrodes and the insulating spacer dictates the transport properties. As discussed in Section 4.1.4, a wavefunction, whether propagating or evanescent, is described in terms of irreducible representations of the crystal's symmetry group. For a cubic space group, the Δ_1 symmetry transforms as a linear combination of 1, z and $2z^2-x^2-y^2$ functions, while the Δ_5 as a linear combination of zx and zy (e.g. p_x, p_y, d_{xz} and d_{yz}). Finally the $d_{x^2-y^2}$ and d_{xy} states have Δ_2 and $\Delta_{2'}$ symmetry respectively. The orbital components of each of these symmetries are drawn in Fig. 4.16. Importantly an incident Bloch state in the electrodes can couple to a given evanescent state in the insulator, and then sustain a tunnelling current, only if the two share the same symmetry. Fig. 4.17 shows the $SrRuO_3$ band-structure close to E_F along the direction of the transport. At E_F only a doubly-degenerate minority Δ_5 state is available, in contrast to previous DFT calculations, where both minority (↓) Δ_5 and majority (↑) Δ_1 bands were found [158]. Such a discrepancy is due to the use of the GGA functional in Ref. [158], which underestimates the Ru d manifold exchange splitting [226]. Note that a large spin splitting is expected based on point contact Andreev reflection experiments [140].

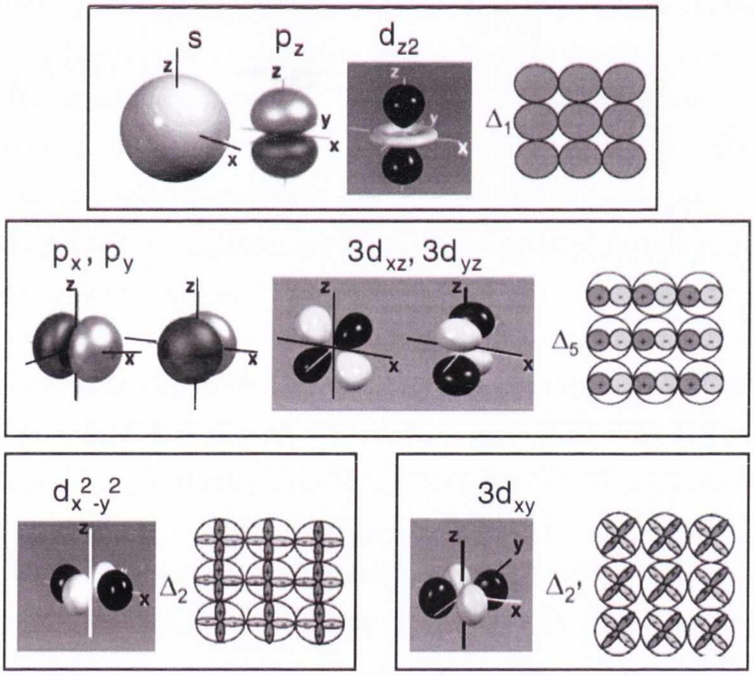

Figure 4.16: Orbitals grouped by symmetry properties. From Ref. [229]

In Fig. 4.18 we plot the $BaTiO_3$ real and complex band-structure. In contrast to MgO, where states with Δ_5 symmetry decay significantly faster than those with Δ_1 [23], in NFE $BaTiO_3$ the Δ_1 and Δ_5 symmetries have comparable decay rates. However, the magnitude and slope of κ depends on the energy. In particular close to the valence band top the slower decay rate is for Δ_1, while the situation is reversed at the conduction band minimum. The enlargement of the bandgap associated with the FE order results in an increased decay rate for all the symmetries. The effect is more pronounced for Δ_5 close to the top of the valence band where now the Δ_1 symmetry primarily contributes to the tunnel conductance.

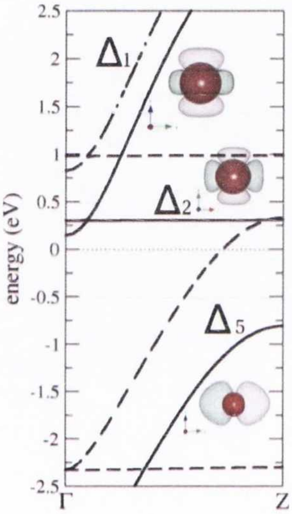

Figure 4.17: ASIC-calculated band-structure along the transport direction ($\Gamma \rightarrow Z$) for centro-symmetric tetragonal $SrRuO_3$. The wavefunction symmetries of the bands close to E_F are indicated.

4.3.3 Zero-bias Transport Properties

We begin our analysis of the transport properties from the NFE structure by showing $T(E)$ at zero bias for the NFE and FE structure and for the parallel magnetic alignment of the electrodes (Fig. 4.19). The band gap of $BaTiO_3$ can be seen in the vanishing transmission around the Fermi level. This suggests a band gap of ~ 2.6 eV, close to the calculated one of 2.7 eV. The total transmission for the FE structure is smaller than that for the NFE structure; the reason for this decrease will be discussed later. In Fig. 4.20, the spin resolved transmission coefficient is plotted again, this time on a logarithmic scale over a smaller energy range around E_F.

In the parallel (PA) configuration, $T(E)$ close to E_F is dominated by the minority spin channel. This is expected from the band-structure of $SrRuO_3$, which presents only a Δ_5 minority band along the transport direction for energies comprised between

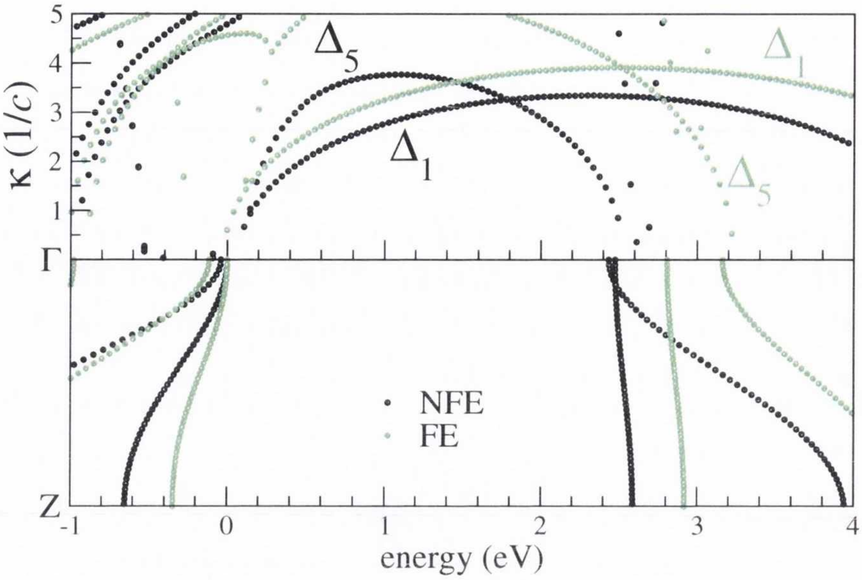

Figure 4.18: ASIC-calculated band-structure along the transport direction ($\Gamma \rightarrow Z$) for tetragonal $BaTiO_3$ both in the NFE (black) and FE (green) configuration. The top panel reports the complex band-structure for $BaTiO_3$. The wavefunction symmetries of the bands close to E_F are indicated. Zero energy marks the top of the valence band.

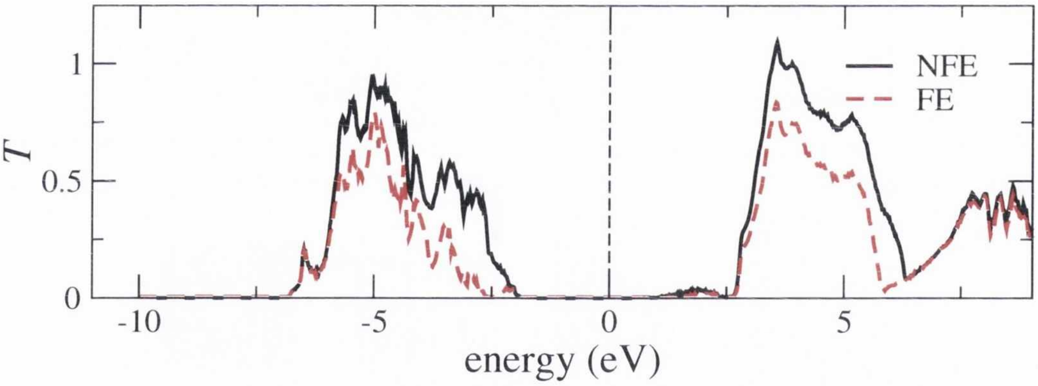

Figure 4.19: Total transmission coefficient for the NFE and FE structures as a function of energy. The dashed line at 0 eV denotes E_F.

-0.8 eV and $+0.1$ eV. The minority conductance in this energy range is five orders of magnitude larger ($T^{\downarrow} \sim 10^{-7}$) than that for the majority spins. For $E > 0.1$ eV there is a sharp rise in $T^{\uparrow}$, due to the Δ_1 majority band now contributing to the conductance. In the energy window 0.3 eV $< E <$ 0.8 eV there are no minority states available and $T^{\downarrow}$ drastically drops. A similar drop, due to the lack of minority $SrRuO_3$ bands is found at -2.5 eV. In the antiparallel (AP) configuration the electron transmission occurs between majority (minority) states in the left-hand side electrode and minority (majority) in the right-hand side one, so that $T(E)$ for both the spins

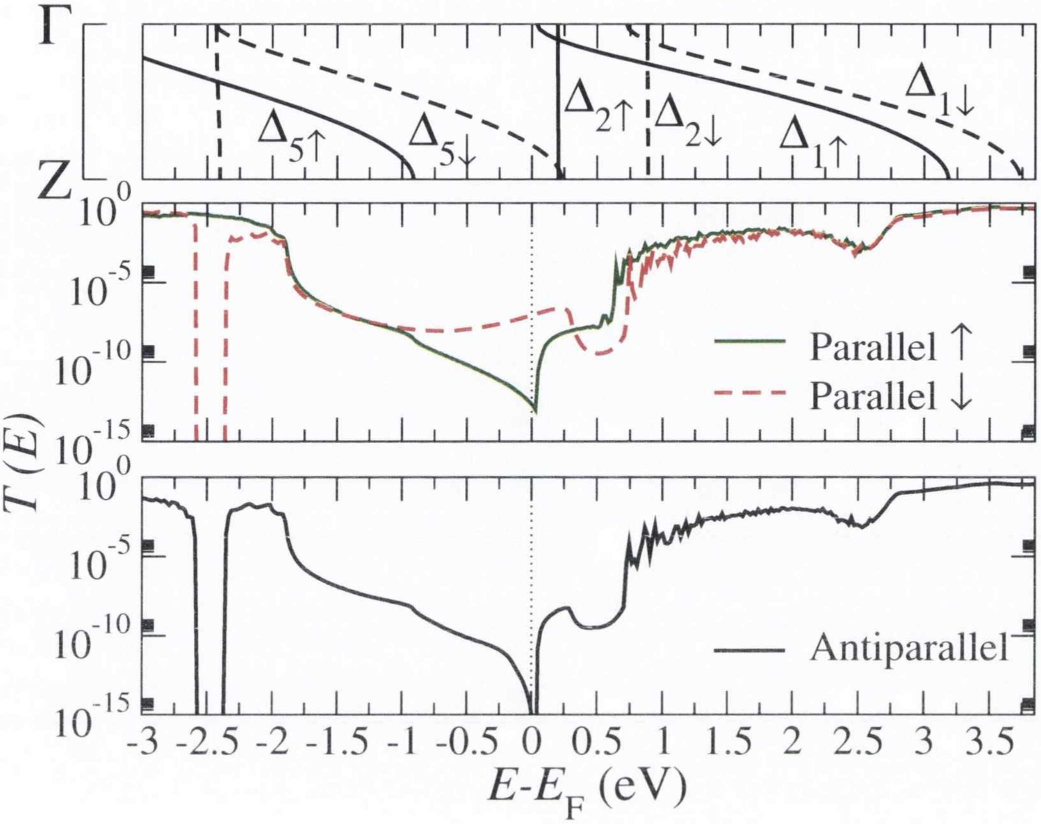

Figure 4.20: Transmission coefficients, $T(E)$, as a function of energy for the NFE structure. The middle panel is for the parallel magnetic configuration, while the lower one is for the antiparallel. At the top we report again the $SrRuO_3$ band-structure at the Γ point of the 2D transverse BZ. The dotted line at 0 eV denotes E_F.

(identical) is essentially a convolution of those for the majority and minority spin channels of the PA state. As a consequence there is a drastic suppression of $T(E)$ in the regions -0.8 eV $< E <$ 0.1 eV and 0.3 eV $< E <$ 0.8 eV, where respectively the Δ_5 minority and Δ_1 majority bands in one electrode are not paired in the other. In particular $T(E_F)$ for the AP configuration is orders of magnitude smaller than in the PA one.

In order to clarify the dominance of the band symmetry matching of the $SrRuO_3$ electrodes, in Fig. 4.21 the transmission coefficient is calculated at the $\bar{\Gamma}$ point alone. Here the requirement that a band of a particular symmetry in one electrode must match a band of the same symmetry in the second electrode in order for tunnelling to occur is valid. A comparison of Fig. 4.21 and Fig. 4.20 shows that although transmission through the $\bar{\Gamma}$ point comprises the dominant contribution to the total transmission coefficient, Bloch states with larger transverse wave-vector contribute to the transport and produce a residual transmission.

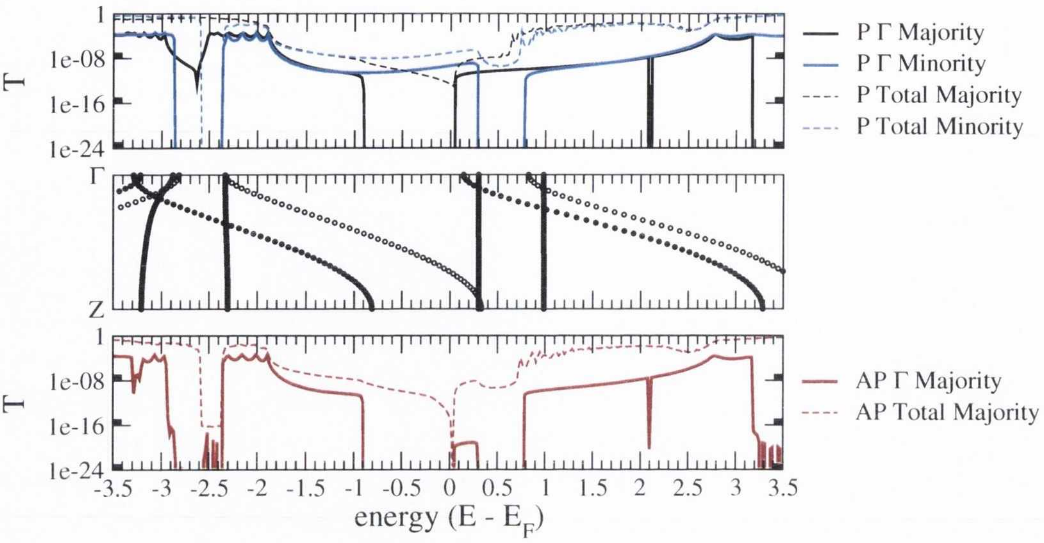

Figure 4.21: Transmission coefficients, $T(E)$, as a function of energy for the NFE structure. The top panel is for the parallel magnetic configuration, while the bottom one is for the antiparallel. The solid lines show the transmission coefficient calculated at the Γ point alone, while the dashed lines indicate the total transmission coefficient. In the middle we report again the $SrRuO_3$ band-structure at the Γ point of the 2D transverse BZ where the filled (open) symbols denote majority (minority) spin.

4.3.4 *I-V* Curves and bias-dependent TMR

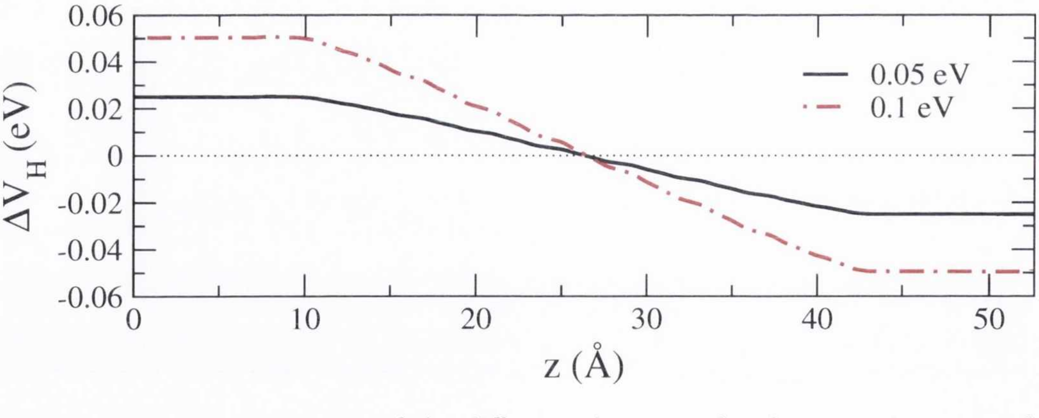

Figure 4.22: Macroscopic average of the difference between the electrostatic potential at a finite bias voltage and the one at zero bias (ΔV_H), as function of position z, for two different bias voltages.

The planar average along x and y of the difference between the electrostatic potential at a finite bias and at zero bias, ΔV_H, is shown in Fig. 4.22 for two different biases, as a function of position in the supercell. ΔV_H is approximately flat inside the $SrRuO_3$ electrodes and decays approximately linearly in the $BaTiO_3$ insulator as expected.

In order to apply a voltage across an interface there are two possibilities. One is the self-consistent approach at each bias step. This however leads to very intensive calculations taking large amounts of time and computational resources. The second possibility is a rigid-shift approximation where the Hamiltonian is calculated self-consistently at zero bias but for bias calculations the electrode chemical potentials are simply shifted by the appropriate energies. This approximation assumes a linear potential drop across the barrier. Such a calculation is significantly lighter than a full self-consistent calculation. The linear potential drop that was calculated in Fig. 4.22 suggests that the rigid shift approximation is justified to calculate the bias properties in this tunnel junction. In order to confirm such a hypothesis, a comparison of the I-V curves calculated by using both the self-consistent method (black curve) and the rigid shift method (red curve) is shown in Fig. 4.23. The agreement is good at least up to 0.6 V. Thus, for the remainder of this Chapter, all bias calculations are calculated using the simpler rigid-shift approximation.

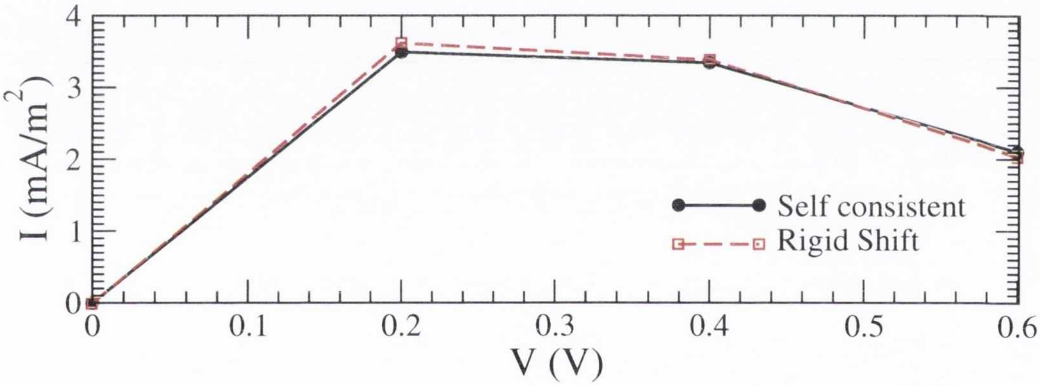

Figure 4.23: Total current per unit area, I, as a function of voltage, V, as calculated using the self-consistent method (black curve) and the rigid shift method (red curve).

The spin-polarized current for both the PA and AP configurations and for both the NFE (top panel) and FE (middle panel) structures are shown in Fig. 4.24, where we focus on the low voltage region in which the current is due entirely to tunnelling (the broader I-V are displayed in the insets). The most distinctive feature emerging from the I-V curves is the presence of negative differential resistances (NDR) for the PA alignment, originating from the movement of the Δ_1 majority band-edge with V. Because of the NDR the relative magnitude of the current for the parallel (I^{PA}) and antiparallel alignment (I^{AP}) can be reversed, i.e. the TMR changes sign with V. This is demonstrated in the lower panel of Fig. 4.24, where we present the "pessimistic" TMR ratio, TMR$=(I^{\mathrm{PA}}-I^{\mathrm{AP}})/(I^{\mathrm{PA}}+I^{\mathrm{AP}})$, as a function of bias. Clearly TMR sign inversion is observed for both the NFE and the FE junctions for voltages in the range

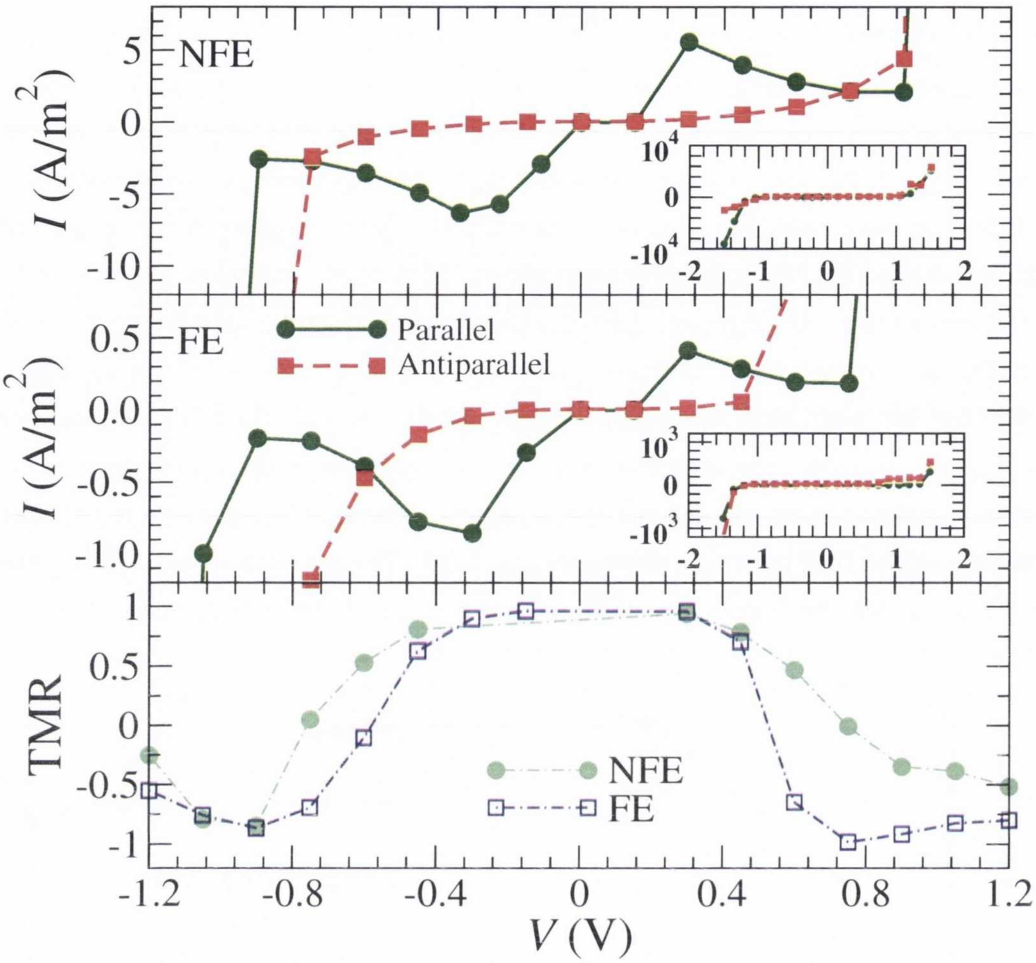

Figure 4.24: Total current per unit area, I, as function of voltage, V, for the NFE (top panel) and FE (middle panel) structures. In the bottom panel we present the TMR as a function of voltage for both the geometries. In the insets the I-V is presented over a larger current range (the units are the same as in the main figure). Note that at the on-set of the $BaTiO_3$ conduction and valence bands the current increases by three orders of magnitude over its low bias value.

0.7-0.9 V. Furthermore for $V \sim 0.7$ V the TMR for the NFE junction is positive, while that of the FE one is negative, meaning that subtle changes in the barrier electronic structure, such as those induced by ferroelectricity, are sufficient to change the sign of the TMR. Note also that the TMR values reported here are actually extremely large. For instance for both the NFE and FE junctions and voltages $|V| < 0.4$ V the optimistic TMR $[(I^{\mathrm{PA}} - I^{\mathrm{AP}})/I^{\mathrm{AP}}]$ is around 5,000%. The I-V curves can be rationalised by looking at the dependence of $T(E)$ on the bias, which is presented in Fig. 4.25 for the NFE structure. This is mainly determined by the shift of the electrodes' Δ_1 and Δ_5 band-edges with V. For positive voltage the band-structure of the left electrode is shifted by $+eV/2$ and that of the right one by $-eV/2$. At a given energy a large T is found only if a band of the same symmetry and spin is found in both electrodes at that energy. For PA alignment at $V = 0$, the minority spins dominate the transmission up to 0.3 eV, after which one encounters the Δ_5 minority upper band-edge and $T^{\downarrow}$ is drastically reduced. As V is applied, the Δ_5 minority band edge is shifted to lower energies in the right electrode (for $V > 0$), so that for $V = 0.6$ V the high transmission region extends only up to E_{F}, and for $V = 1.2$ V it extends only up to $E_{\mathrm{F}} - 0.3$ eV. This is the origin of the NDR found for the PA alignment. In contrast for the AP configuration T is small for energies below 0.1 eV after which it drastically increases because of the Δ_1 conduction bands (see Fig. 4.20). With increasing V the Δ_1 band in the right electrode is shifted to lower energies, so that there is a rather large transmission inside the bias window and eventually the AP current becomes larger than the PA one. This results in the TMR sign change at about 0.7-0.9 V.

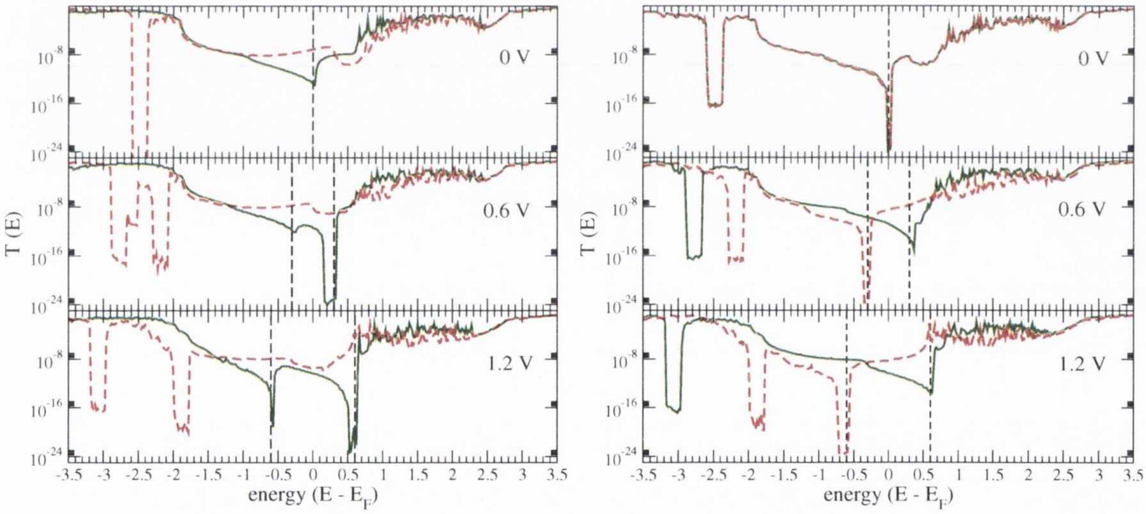

Figure 4.25: Transmission coefficient T(E;V) as a function of energy and for different biases V for the NFE structure. The vertical lines are placed at $E_F \pm \frac{eV}{2}$ and enclose the bias window.

4.3.5 Effect of Ferroelectric Ordering

The main effect of the ferroelectric order on the transport is an increase of the $BaTiO_3$ band-gap, i.e. an increase of the Δ_1 and Δ_5 decay coefficients (see Fig. 4.18). In particular, states with Δ_5 symmetry decay significantly faster in the FE MTJ with respect to the NFE one. This results in a global reduction of the transmission although other general features remain rather similar in the two cases. The comparison between $T(E;V)$ for the FE and NFE junctions is presented in Fig. 4.26. Below E_{F} one may

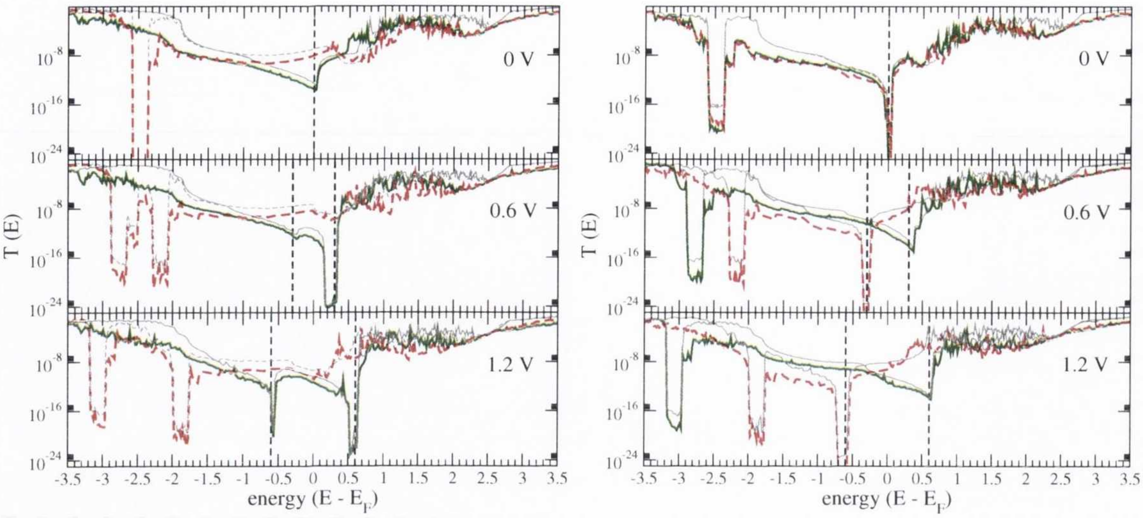

Figure 4.26: A comparison of transmission coefficient T(E;V) for the NFE (thin grey lines) and FE (majority green and minority red) structure.

note a substantial reduction of the transmission when going from NFE to FE for both PA and AP alignment as a consequence of the increased Δ_5 decay rate.

In Fig. 4.27 the k-resolved transmission coefficient is plotted over the full 2D Brillioun Zone perpendicular to the transport direction for different energies close to the Fermi level. Contributions to majority transmission between -0.50 eV and the Fermi level is mainly from the band edges. This is most obvious at the Fermi level, where transmission is minimised. Above the Fermi level, the transmission has a maximum at the $\bar{\Gamma}$ point. In contrast, transmission through the minority spin is broadly the same for a range of energies between -0.50 eV and +0.25 eV and is centred around the $\bar{\Gamma}$ point, with the region between Γ and X also contributing, reflecting the d-state symmetry available at E_F. At +0.50 eV the contribution from the $\bar{\Gamma}$ point becomes negligible compared to that of the Brillioun zone edge. For both majority and minority spin, the highest transmission is associated with the $\bar{\Gamma}$ point as expected. Transmission from the Brillouin zone edge is between 1 and 4 orders of magnitude smaller. Fig. 4.28 shows the k-resolved transmission for the antiparallel case. At +0.50 eV there is very high transmission but from a very limited region of the Brillioun zone away from the $\bar{\Gamma}$ point. Finally, the ferroelectric ordering does not change the symmetry of the tunnelling transmission in the k_x-k_y plane.

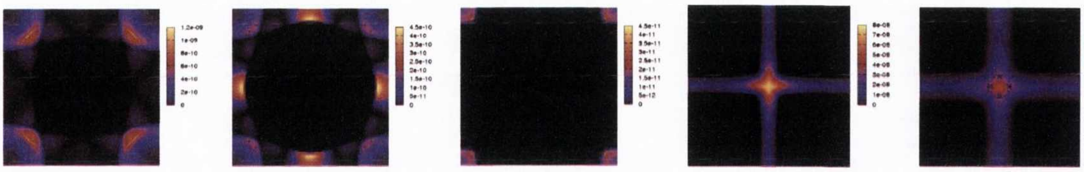

(a) -0.50 eV (b) -0.25 eV (c) E_F (d) +0.25 eV (e) +0.50 eV

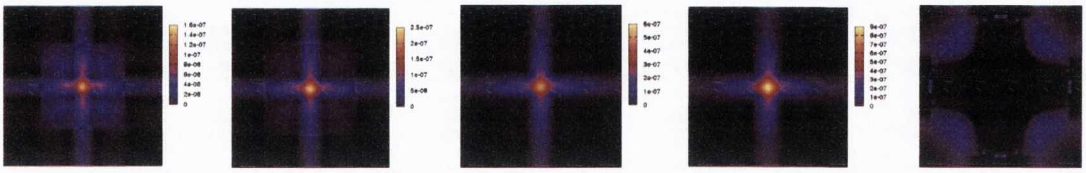

(f) -0.50 eV (g) -0.25 eV (h) E_F (i) +0.25 eV (j) +0.50 eV

Figure 4.27: k-resolved transmission coefficients over a range of energy close to the Fermi level for a parallel magnetic configuration of the electrodes. (a) - (e) are for the majority spin. (f) - (j) label minority spin.

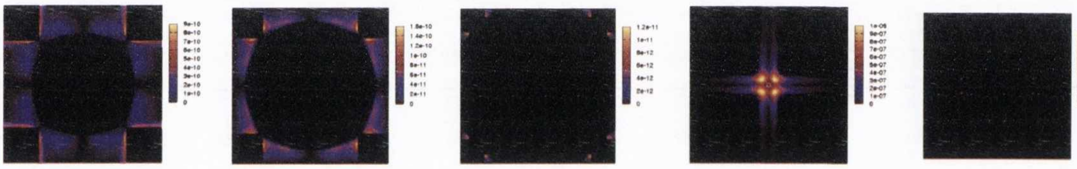

(a) -0.50 eV (b) -0.25 eV (c) E_F (d) +0.25 eV (e) +0.50 eV

Figure 4.28: k-resolved transmission coefficients over a range of energy close to the Fermi level for an antiparallel magnetic configuration of the electrodes.

4.4 Conclusion

In this Chapter we investigated the transport properties of a multifunctional, epitaxial $SrRuO_3/BaTiO_3/SrRuO_3$ tunnel junction from first principles. We first analyzed several exchange and correlation functionals and the approximate self-interaction correction to assess their applicability to describe the interface between the two ferroic materials. We found that although the GGA functional provides an adequate description of the structural properties of the hetrostructure, it underestimates the band gap of the ferroelectric barrier and so it is unsuitable for describing the electronic and thus the transport properties. The ASIC functional has previously been found to correct somewhat the band gap problem of local functionals. However, as a non-variational functional, it is insufficient to calculate the relaxed structure; the structure always relaxes to a non-ferroic state. We found that using the structure determined by the GGA functional along with the ASIC electronic structure provides the most realistic junction description for the transport work. Changes can also be seen in the band alignment of the heterostructure between the GGA and the ASIC functionals. The valance band offset between $SrRuO_3$ and $BaTiO_3$ is found to be 2.6 eV within ASIC compared to 1.65 eV with the GGA functional.

We found that the transport properties at zero bias are dominated by the tunnelling of minority carriers due to the doubly-degenerate minority state alone that is available at the $SrRuO_3$ Fermi level. The complex band structure of $BaTiO_3$, which determines the decay rate of the tunnelling electrons, has similar decay rates for both Δ_1 and Δ_5 states. We found that the main effect of ferroelectric ordering on the electronic properties of $BaTiO_3$ is to increase the band gap. This in turn, modifies the complex band structure so that the decay rate for states with Δ_5 symmetry is faster than for states with Δ_1 symmetry. This is evident in the transmission coefficient at zero bias.

We then investigated the bias dependence of the current and TMR. We have demonstrated that in such an all-oxide ferroelectric MTJ not only can the tunnelling magnetoresistance reach enormous values but the sign of which can be inverted as the applied bias increases. Furthermore the sign inversion occurs at different voltages by altering the barrier electric state from the NFE structure to the FE structure. Again, our finite-bias results are explained in terms of the electrodes and the barrier band-structures. The possibility to control the TMR by manipulating the ferroic state of the barrier in an MTJ opens a potential avenue for the electrical control of magnetic devices.

CHAPTER 5

Spin Dependent Tunnelling: The TER effect

5.1 Introduction

The phenomenon detected in a magnetic tunnel junction (MTJ) whereby the tunnelling current depends on the relative magnetisation orientation of the ferromagnetic electrodes has been known since the 1970s. MTJs are now vital components in hard disk reading heads, magnetic sensors and more recently in non-volatile magnetic memories (MRAM). For a long time, it was believed that in these tunnel junctions, the barrier material plays no role other than generating the potential barrier through which the electrons tunnel. However, as we saw in the Chapter 4, the nature of the barrier can in some cases dictate the behaviour of the junction via its electronic band structure, both real and complex. From there it was a short step to realise that it might be possible to manipulate the tunnelling current by using a functional material as tunnelling barrier. In fact, this idea was first formulated by Esaki et al. in 1971 [230], when he postulated that by integrating an ultrathin ferroelectric film as the barrier it would be possible to influence the tunnelling current. However, several challenges had to be overcome in order to create the first ferroelectric junction (FTJ). The most difficult of these was the ability to grow single crystalline films that are thin enough so that tunnelling can occur and yet thick enough that they remain ferroelectric.

5.1.1 Ferroelectric Memory

Progress in this area has been driven in some part by the possibility of employing FTJs in the data storage industry. A ferroelectric random access memory (FeRAM) is a type of non-volatile memory that uses a ferroelectric thin film as a capacitor to store data. It offers high speed writing times (150ns compared to 10μs for flash memory), low power consumption and a long rewriting endurance (ten billion cycles compared to ten thousand for flash memory) [231]. In order to read the memory a voltage is applied that, depending on the initial orientation of the ferroelectric polarization, will either reverse it or leave it unchanged. If it reverses it, a pulse of current will be registered and in this way the orientation can be determined. However, such a readout method is destructive so that a write cycle is required with every read. For this and other reasons, FeRAMs are used only in certain niche applications such as smart cards and video game consoles but have never achieved the widespread use that was originally conjectured. Alternative non-volatile ferroelectric memories are now being explored, one of which is the ferroresistive memory. Here the conducting tip of an atomic force microscope (AFM) is used to create domains in a ferroelectric thin film by applying a poling voltage large enough to switch the polarisation direction. In order to read the orientation of each domain a smaller voltage is applied between the tip and the conducting bottom electrode. The subsequent 'leakage' current that flows is measured. Within each domain, the resistance is approximately constant. However, when crossing a domain wall a dramatic change in resistance will be registered. Thus, the direction of polarisation can be easily determined. While experimentally such currents can be attributed to channels created by crystalline defects or localised conducting channels at the domain walls, ideally the primary mechanism responsible for the flow of current is again quantum mechanical tunnelling across the insulating barrier.

5.1.2 Tunnelling through ferroelectric barriers

The key quantity in a ferroelectric tunnel junction is the tunnelling electroresistance (TER). Analogously to the TMR effect in a magnetic tunnel junction, the TER effect is the change in resistance of an FTJ that occurs when reversing the ferroelectric polarisation. In order to observe the tunneling electroresistance (TER) effect simply introducing a ferroelectric material as the insulating barrier is not sufficient. In such a case the potential barriers generated by the two polarizations are mirror images of one another and therefore the tunneling current for both states will be identical. In other words, the two ferroelectric states are connected by inversion symmetry. There are several ways to introduce asymmetry into the system. These are shown in Fig. 5.1. Sufficient asymmetry may be achieved by simply creating different concentrations of defects at either interface. This was found experimentally in a LSMO/BiFeO$_3$/LSMO tunnel junction where no deliberate effort was made to introduce asymmetry and the TER effect was attributed to the two interfaces being different from each other [232]. However, the control over such a structure is minimal. Insuring two different terminations of the barrier material at either interface is also predicted to generate a TER effect [158]. Another strategy involves the inclusion of a second insulating material at one interface. Finally two different electrode materials may be used [233].

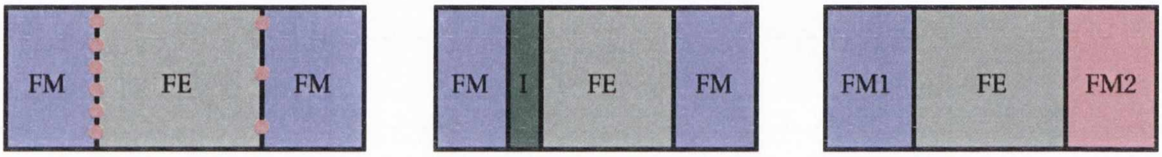

(a) Different Defect Density (b) Interfacial Insulating Layer (c) Different Electrodes

Figure 5.1: Schematic of different methods to introduce a spatial asymmetry into a ferroelectric tunnel junction: (1) Different defect concentrations at either interface or different interface terminations. (2) Introducing a composite barrier including a non-polar dielectric layer (I). (3) Using dissimilar electrode materials.

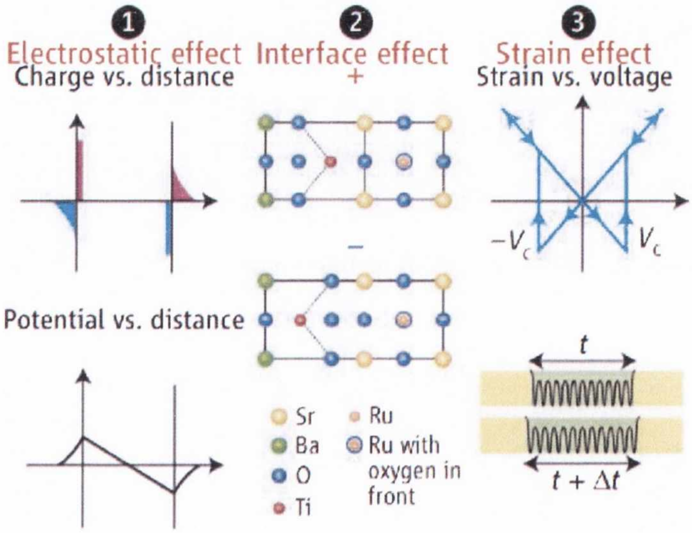

Figure 5.2: Three possible mechanisms by which the ferroelectric polarisation can modify the tunnelling current. Taken from Ref.[234]. V$_C$ is the coercive voltage, t is the barrier thickness and Δt is the thickness variation under an applied field.

Tsymbal and Kohlstedt proposed three likely mechanisms by which the tunnelling current could be modified by the reversal of the electric polarisation direction [234]. These are summarised in Fig. 5.2. The first of these is the so-called electrostatic effect and it is possibly the most important. As the electrodes are not ideal, the charge that is accumulated at the metal/FE interface is screening over a finite distance. The actual screening distance depends on the Thomas-Fermi screening lengths of the electrodes. If, for some reason, the screening lengths at either interface are different there will be an asymmetric deformation of the electrostatic potential when the direction of the polarisation is reversed. The tunnelling electrons will then see a different potential profile depending on the polarisation direction and so experience a different resistance.

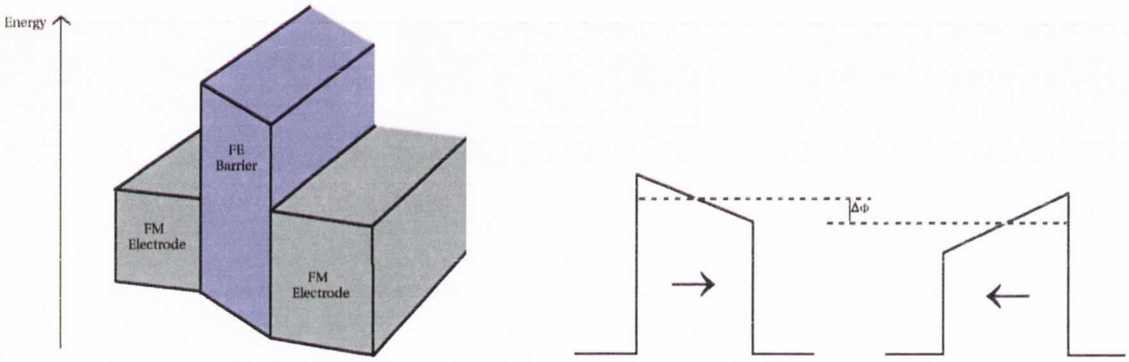

(a) (b)

Figure 5.3: (a) Schematic of a ferroelectric tunnel junction. (b) Schematic potential energy profiles for opposite orientations of ferroelectric polarisation in an asymmetric tunnel junction. The shift in average barrier height (dashed line) is indicated as $\Delta\phi$.

A schematic of a ferroelectric tunnel junction is shown in Fig. 5.3 including the average barrier height for polarisations pointing in either direction. When the direction of polarisation is flipped the average barrier height is shifted by $\Delta\phi$. This can be calculated as

$$\Delta\phi = \frac{dP(\delta_1 - \delta_2)}{2\varepsilon_0\varepsilon(\delta_1 + \delta_2)},$$

where P is the remnant polarisation, $\delta_{1,2}$ are the Thomas-Fermi screening lengths of the two electrodes, ε_0 is the vacuum permittivity and ε is the dielectric constant of the barrier material.

A second possible mechanism that could generate the TER effect is the change in interfacial atomic positions with the polarisation reversal [(2) in Fig. 5.2]. Assuming that the displacements are asymmetric upon flipping the polarisation, the transmission probability will be altered. This is due to the altered atomic orbital hybridisations at either interface which modifies the electronic band structure of the junction and can thus significantly modify the tunnelling properties.

A final possibility [(3) in Fig. 5.2] relies on the piezoelectric effect, and in particular on the converse effect, whereby there is an internal mechanical strain generated in the barrier upon reversal of the polarisation direction. As the decay of the tunnelling electrons depends exponentially on the barrier thickness it is likely that this mechanism, if present, could provide an appreciable contribution to the TER effect.

5.1.3 Recent Progress

One of the first experimental indications of a modulation of the tunnelling current with the ferroelectric polarisation came in 2009 with the work of Garcia et al. [235] [Fig. 5.4 (a) to (c)]. Here, the prototypical ferroelectric $BaTiO_3$ was grown highly strained on a half metallic $La_{0.67}Sr_{0.33}MnO_3$ (LSMO) substrate. Scanning probe microscopy was then used to write ferroelectric domains and subsequently read them by mapping the resistance changes across the sample. The tunnelling electroresistance was found to reach massive values; 200% and 75,000% for 1- and 3-nm thick $BaTiO_3$ films respectively. They also found that the electroresistance scales exponentially with ferroelectric film thickness, a result previously predicted by electrostatic models [209]. A similar study using a $SrRuO_3$ electrode with a $BaTiO_3$ ferroelectric also reported polarisation dependent resistive switching of ultrathin films at room

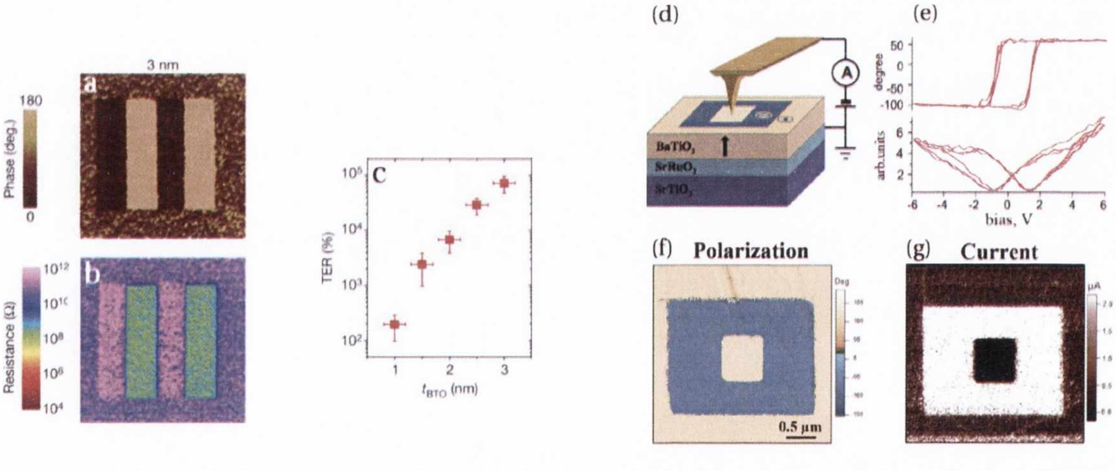

Figure 5.4: Parallel piezoresponse force microscopy (PFM) phase image (a) and conductive-tip atomic force microscopy (CFAFM) resistance map (b) of written 3nm thick ferroelectric stripes of $BaTiO_3$ on an LSMO substrate. The TER is shown as a function of thickness of the ferroelectric layer, t_{BTO}. (d) Sketch illustrating the structure geometry. (e) Local PFM hysteresis loops measured in a 4.8nm thick $BaTiO_3$ film. (f) PFM phase image. (g) Tunnelling current map aquired in the same region as (f). Figures (a) to (c) are adapted from Ref. [235]. Figures (d) to (g) are adapted from Ref. [236].

temperature [Fig. 5.4 (d) to (g)], with a resistance change of almost two orders of magnitude between ferroelectric films [236]. The effect is not confined to barriers comprising of $BaTiO_3$. Several experiments have been also preformed on $PbTiO_3$ [237], $Pb(Zr_{0.2}Ti_{0.8})O_3$ [238] and $BiFeO_3$ [232].

Several theoretical works have now begun to describe the TER effect in ferroelectric heterostructures in order to determine its origin. The majority of these are restricted to simple free electron model calculations. One of the first studies [209] found a conductance change of a few orders of magnitude for metallic electrodes with significantly different screening lengths and attribute it to the two different potential profiles seen by the transport electrons for the opposite polarisation directions. This model was extended a few years later to account for magnetic electrodes and the subsequent spin-dependent screening [239].

However, to date there have been very few first principles calculations showing the effect of ferroelectricity on electron transport. In Ref. [213] Velev et al. calculate the difference in conductance in a $Pt/BaTiO_3/Pt$ tunnel junction between the paraelectric state and the ferroelectric state and attribute the difference to changes in the decay rates of the evanescent states in the barrier. In this case, however, the junction studied is symmetric and so no TER effect is found.

Asymmetry is introduced in Ref. [158] through different interface terminations of $BaTiO_3$: BaO at one interface and TiO_2 at the other. As magnetic $SrRuO_3$ electrodes are used, the coexistence of the tunnelling magnetoresistance and tunnelling electroresistance effects in one device are predicted. A TER effect of 52% and a TMR effect of 64% is found for $BaTiO_3$ thickness of six unit cells. Again, it was suggested that the dominant source of TER in this junction is the change in complex band structure induced by the asymmetry of the displacements in the barrier.

Zhuravlev et al. [240] first suggested that the TER effect could be greatly enhanced by using a composite barrier that combines a functional ferroelectric film and a thin layer of a nonpolar dielectric. Free-energy calculations showed that the dielectric layers acts as a 'switch'; changing the barrier height from a low to a high value when the direction of polarization is reversed. The authors also find that the TER ratio increases exponentially with the dielectric layer thickness. This study assumed a uniform polarisation distribution in the ferroelectric. Wu et al. [241] extended the model to allow a gradual change in the polarisation magnitude within the ferroelectric material and some ferroelectric distortion in the dielectric due to induced screening charges. They found that the TER depends sensitively on the choice of electrode as well as the dielectric thickness and that allowing a ferroelectric-like distortion in the dielectric material reduces the TER significantly. To date however, there have been no experimental work or no first principles calculations carried out on this type of structure.

In this Chapter, we report a first-principles study of the transport properties of a ferroelectric tunnel junction comprising of $BaTiO_3$ sandwiched between two $SrRuO_3$ electrodes and incorporating a thin layer of $SrTiO_3$ (< 8 Å) at one $SrRuO_3$ / $BaTiO_3$ interface. The rest of the chapter is organised as follows: in Section 5.2 we detail the junction structure, the interfaces and the computational methodology used for both the structural relaxations and the tunneling transport calculations. In Section 5.3 we report on the electronic properties of the junction including both the real and complex band structures as well as the bands alignment. The transport properties of the junction are discussed in Section 5.4, including the thickness dependence of the TER effect. All calculations are performed with parallel alignment of the magnetic electrodes. Finally in Section 5.5, the coexistence of the TER and TMR effect is discussed in relation to the prospect of realising a four state memory cell.

5.2 Methology and Structural Properties

Density functional calculations were performed using the localized basis DFT code SIESTA [118, 119, 120]. Structural relaxations were obtained within the Perdew, Burke and Ernzerhof (PBE) generalized gradient approximation (GGA) [38]. A 6×6×1 k-point Monkhorst-Pack mesh [242] and a grid spacing equivalent to a plane-wave cut-off of 800 eV are sufficient to converge the charge density. The electronic structure of all supercells was calculated with the atomic self-interaction correction (ASIC) [45] to the LSDA exchange and correlation potential. ASIC has previously been found to improve the electronic properties of bulk $BaTiO_3$ [225] and $SrRuO_3$ [226] and is vital in transport calculations to ensure a good band alignment between the two materials [225]. The transport properties are determined using the *ab initio* electronic transport code SMEAGOL [142].

We use a 6 unit cell thick $BaTiO_3$ layer ($\approx$ 2.5nm) while 3 unit cells of $SrRuO_3$ describe the left and right electrodes respectively. The basic supercell, periodically repeated in space, is $(SrO - RuO_2)_3/(SrO - TiO_2)_n/(BaO - TiO_2)_6/(SrO - RuO_2)_3$, where $n = 0, 1, 2$. When $n = 0$ the structure is symmetric and no TER effect is expected as switching the direction of the $BaTiO_3$ electrical polarisation produces a mirror image of the tunnelling barrier with opposite polarisation direction. That is, time inversion symmetry forbids a change in the tunnelling conductance [243].

Experimentally such thin-film perovskite heterostructure can be grown with sharp interfaces and minimum defect concentration. Here we assume perfectly sharp interfaces, epitaxial growth and no defects. As in Chapter 4, the in-plane lattice parameter was set to that of bulk $SrTiO_3$ (3.95Å). This is to mimic the effect of an $SrTiO_3$ substrate which, by applying an in-plane compression, tends to increase the polarization of $BaTiO_3$. While the polarization of bulk $BaTiO_3$, calculated by the Berry phase method with GGA, is $43.8\mu C/cm^2$ ($c/a = 1.05$), this is increased to 48.1μ C/cm^2 ($c/a = 1.08$) when subjected to such a compressive strain (+1.6%). In order to find both ferroelectric ground states, two structures were initialized with the polarization pointing in opposite directions. Relaxations were performed until the maximum force on the atoms was less than 40 meV/Å (less than 4 meV/Å for the $n = 0$ case). As a result of the depolarising field created by the incomplete screening of the induced charges by the metallic electrodes, the displacements at the centre of a typical cell correspond to a polarization of $35.5\mu C/cm^2$; much reduced from the bulk value ($43.8\mu C/cm^2$). We note that the GGA functional is known to routinely overestimate the polarization of ferroelectric oxides but this is not expected to qualitatively affect our conclusions.

Fig. 5.5 shows the layer by layer displacements of oxygens and cations along the stack direction. These can be related to the magnitude of the ferroelectric distortion in the layers. Here the displacements are defined for each atomic plane as $\delta = (z_{cation} - z_O)$ where z_{cation} and z_O denote the cation and oxygen positions in a particular plane. As such, $\delta > 0$ defines a structure with the polarization pointing parallel to the substrate normal ($P_{\rightarrow}$), while $\delta < 0$ define a structure with the polarization pointing in the opposite direction ($P_{\leftarrow}$).

The displacements within the centre of the $BaTiO_3$ are almost uniform right up to the interface with $SrRuO_3$ for the symmetric structure (n = 0). Such a fast recovery distance for the polarization, where the polarization is suppressed only in the first layer or two immediately close the interface has already been shown [217]. Ionic displacements are also evident in $SrTiO_3$ and extend into the $SrRuO_3$ electrodes. Such atomic displacements in the electrodes were predicted to provide a lattice contribution to the screening ability of the metal along with the electronic screening [244] and have

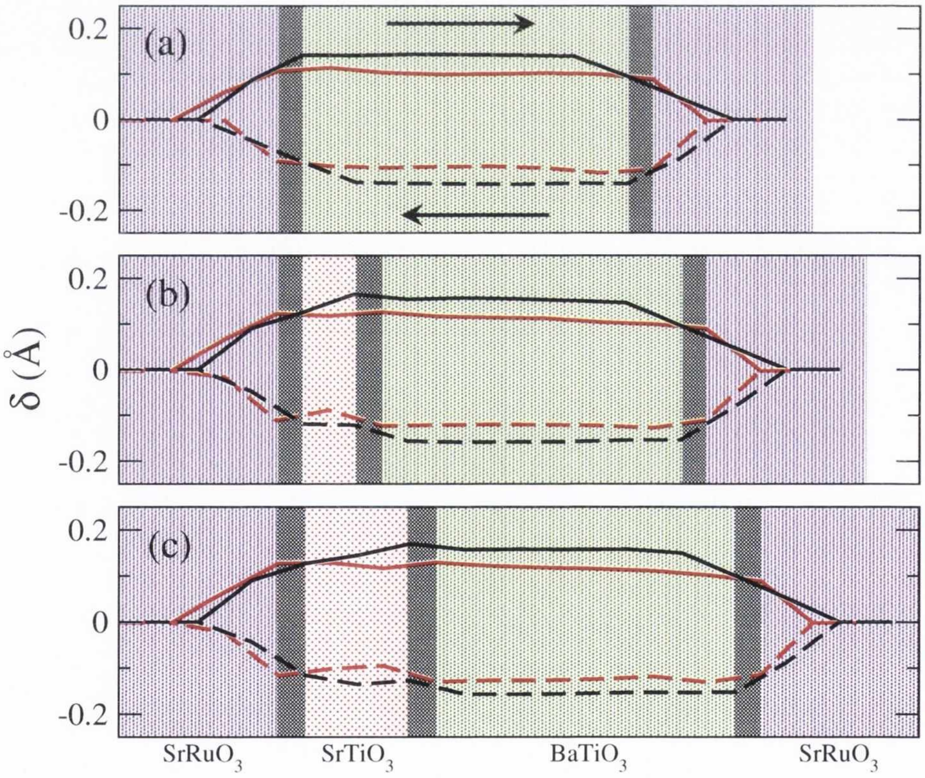

Figure 5.5: Relative cation-oxygen displacements along the z-axis direction for the fully relaxed configuration for n=0 (a), n=1 (b) and n=3 (c). The black lines corresponds to displacements in the B-O_2 layer. The red lines correspond to displacements in the A-O. The solid lines indicate $P_{\rightarrow}$ while the dashed lines indicate $P_{\leftarrow}$.

been experimentally found [219]. Structurally it is clear that there is not a significant difference between $SrTiO_3$ and $BaTiO_3$, with the thin section of $SrTiO_3$ taking on the ferroelectric polarization of the $BaTiO_3$. We would, of course, only expect this distortion to be a surface effect in thicker $SrTiO_3$ layers.

5.3 Electronic Properties

Bulk $SrTiO_3$

Bulk $SrTiO_3$ is an incipient ferroelectric, meaning that in its pure state it remains paraelectric down to 0 K. It was suggested that the ferroelectric transition is suppressed due to quantum fluctations [245] but the paraelectric state is sensitive to small perturbations and a ferroelectric state can be stabilised. Small levels of impurities [246] and mechanical stress [247] have been found to induce ferroelectricity. $SrTiO_3$ is a commonly used substrate for ferroelectric oxides due to its ground state cubic perovskite structure and high dielectric permittivity. As such it is an important material for both fundamental research and technological applications. The lattice constant is 3.905Å experimentally providing biaxial compressive strain for some of the most commonly studied ferroelectrics, namely $BaTiO_3$ and $PbTiO_3$.

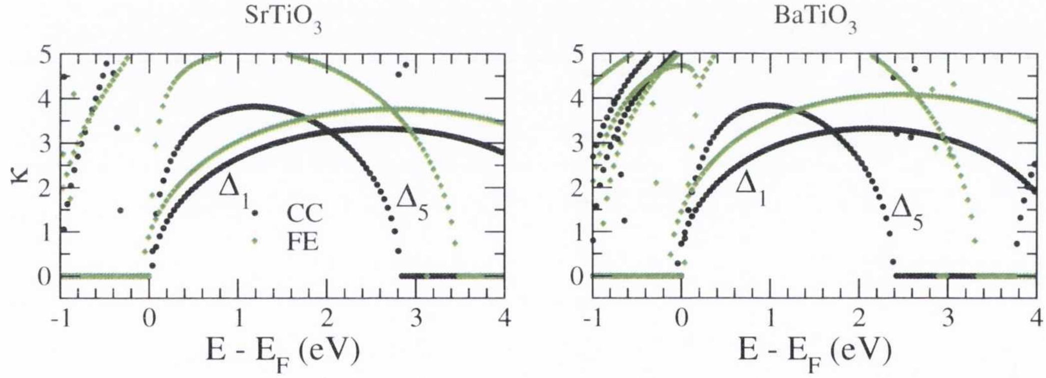

Figure 5.6: Complex band structure of bulk $SrTiO_3$ (left panel) and bulk $BaTiO_3$ (right panel) at the same in-plane lattice constant as the supercell for both a centrosymmetric (CC) configuration and a representative ferroelectric configuration (FE).

Some of the mechanisms put forward to account for the TER effect in asymmetric tunnel junctions assume that the magnitude of the displacements at the center of the ferroelectric barrier is sufficiently different for $P_{\rightarrow}$ and $P_{\leftarrow}$ to influence the tunnel current via the complex band structure (and hence the decay constant). Here we find that for this relatively weakly asymmetric case, this does not contribute to the TER. The difference in displacements between $P_{\rightarrow}$ and $P_{\leftarrow}$ at the center of the $BaTiO_3$ is only ~0.005Å (Fig. 5.5) with the result that the complex band structure between the two is negligibly different. This does not preclude changes in the complex band structure close to the interface where changes in the chemical and structural environment may have a major influence. It is also possible that if the symmetry of the complex band structure of the dielectric is different to that of the ferroelectric it could add a

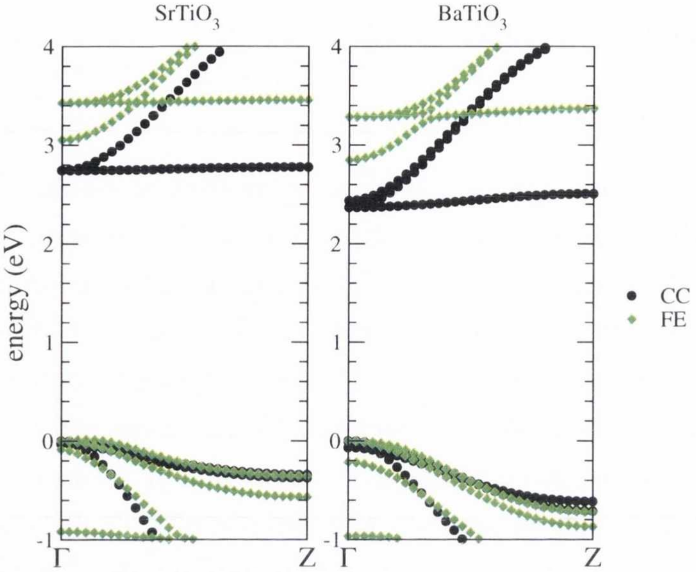

Figure 5.7: Real band structure of bulk $SrTiO_3$ (left panel) and bulk $BaTiO_3$ (right panel) at the same in-plane lattice constant as the supercell for both a centrosymmetric (CC) configuration and a representative ferroelectric configuration (FE).

second selection criteria for tunnelling electrons. However, in the case of $SrTiO_3$ the decay rates for the various orbital symmetries are very similar to those of $BaTiO_3$. This is due to the O $2p$ and Ti $3d$ states that fill the top of the conduction band and bottom of the valence band, respectively, for both $SrTiO_3$ and $BaTiO_3$. $SrTiO_3$ has a larger band gap than that of $BaTiO_3$ which is reflected in the slightly larger decay constant for states with Δ_5 symmetry. However, states with Δ_1 symmetry in ferroelectric $BaTiO_3$ decay faster over a wide energy range (these states are involved in the ferroelectric distortion). The real band structures of $BaTiO_3$ and $SrTiO_3$ are shown in Fig. 5.7 for the centrosymmetric and the ferroelectric structure and we can see that, at least close to the Fermi level, they are almost identical. The Sr $5s$ states are located far above the Fermi level at about +10 eV and the Sr $4p$ states are located approximately 19 eV below the Fermi level with some small hybridisation with the Ti d and O p states just below E_F. Therefore, from the bulk properties alone we would not expect any significant change due to the introduction of a layer of $SrTiO_3$ into the $SrRuO_3/BaTiO_3/SrRuO_3$ junction.

In Fig. 5.8, the difference in the macroscopic total charge density (ionic + electronic) between the ferroelectric state and a reference state where all the atoms are in a centrosymmetric configuration are shown. The polarisation in the $BaTiO_3$ thin film induces surface charges of opposite sign at either interface. At the $BaTiO_3/SrRuO_3$ interface, electrons in the metal tend to screen these surface charges. For $P_{\rightarrow}$, these

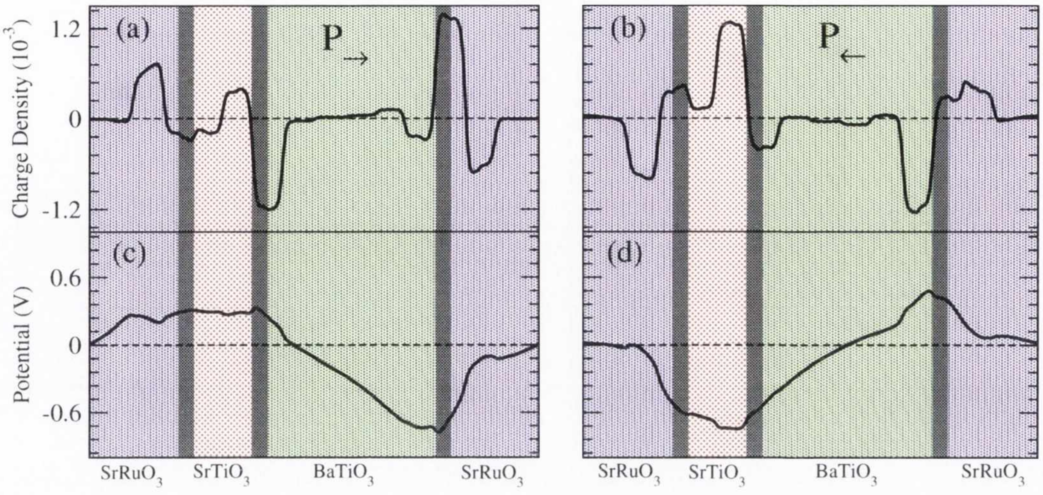

Figure 5.8: The difference in charge distribution and potential profile through the n=2 junction between the centrosymmetric and ferroelectric structures. The left panel shows $P_{\rightarrow}$ and the right $P_{\leftarrow}$.

can be seen as a build up of positive charge density in $SrRuO_3$ just at the interface. At the $SrTiO_3/BaTiO_3$ interface some space charges build up in order to compensate the induced charge but due to the lack of sufficient charge carriers in the dielectric the surface charge is not totally screened. Instead, the remaining charge is screened in the metallic electrode. The result is that the potential in the $SrTiO_3$ layer is pinned to the potential at the interface with $BaTiO_3$. The formation of these localised screening charges at each interface generates dipoles that must be cancelled in order to preserve the short-circuit boundary conditions. The result is the creation of a depo-

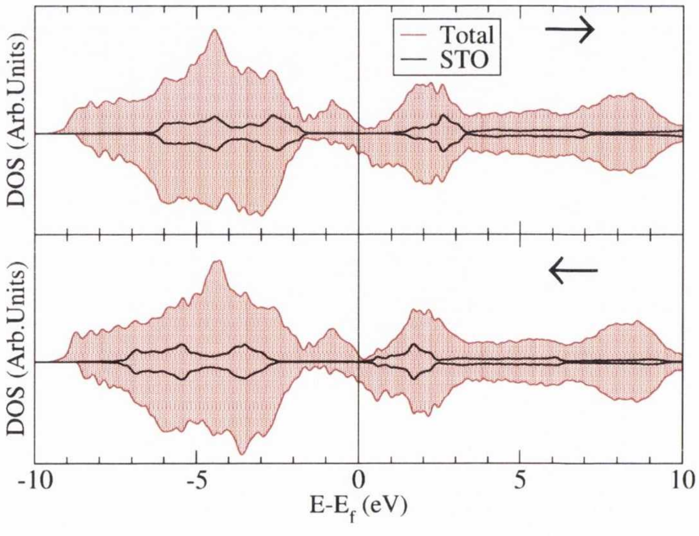

Figure 5.9: Density of states for each polarization of the ferroelectric barrier $P_{\rightarrow}$ (top) and $P_{\leftarrow}$ (bottom) showing the rigid shift in the $SrTiO_3$ potential.

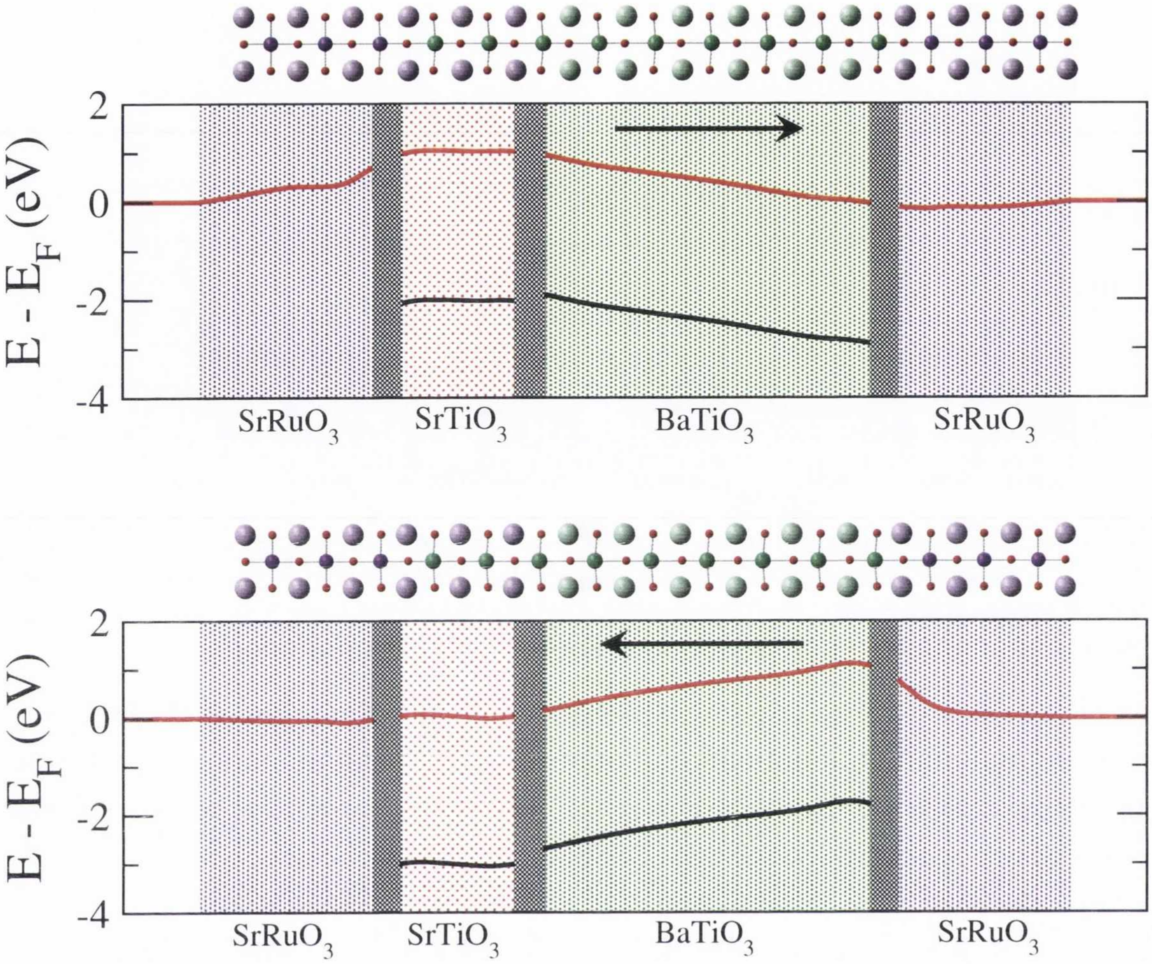

Figure 5.10: Schematic representation of the band offset for the n=2 structure for $P_{\rightarrow}$ (top) and $P_{\leftarrow}$ (bottom). The red line represents the LUMO (conduction band) while the black line represents the HOMO (valence band). 0 eV corresponds to the Fermi level of the $SrRuO_3$ electrodes. The shaded regions correspond to various interfaces where the calculation of the band alignment is not valid.

larising electric field in $BaTiO_3$. This can be seen as a gradient in the difference of the macroscopic average of the potential [Fig. 5.8 (c) and (d)]. As a result of the $SrTiO_3$ potential being pinned to the level of the $BaTiO_3$ potential at the interface, if we change the direction of polarisation in the ferroelectric we can observe a simple rigid shift in the potential of the $SrTiO_3$ layer. This shift can be readily seen if we plot the density of states projected onto the atoms of the $SrTiO_3$ layer alone. This is shown in Fig. 5.9 where we present both the total DOS of the entire supercell and the $SrTiO_3$ PDOS. It is clear that the difference in the $SrTiO_3$ DOS between $P_{\rightarrow}$ and $P\leftarrow$ is just a rigid shift, in this case by approximately 0.9 eV. By using the methods outlines in Section 4, we can determine the position of the conduction band minimum and

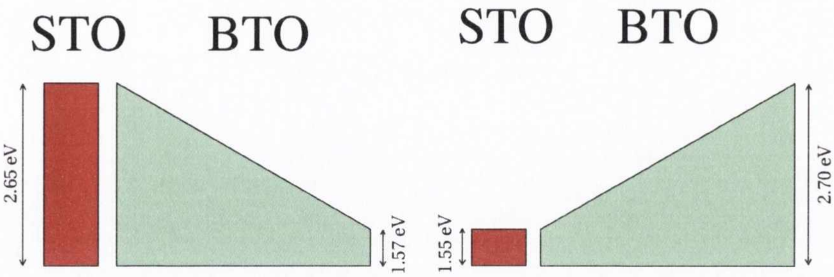

Figure 5.11: Schematic representation of the tunneling barrier for $P_{\rightarrow}$ (left) and $P_{\leftarrow}$ (right) respectively. The numerical values of the various band offsets are for $n = 2$.

valance band maximum throughout the junction. This is shown in Fig. 5.10 where the band alignment across the junction is plotted for the n = 2 case. An electrostatic drop can be seen across the ferroelectric barrier as expected. We can see that both the $SrTiO_3$ and $BaTiO_3$ layers remain insulating, although the electrode Fermi level is very close to the bottom of the $SrTiO_3$ conduction band. We can now see clearly the rigid shift in potential of the $SrTiO_3$ layer which can be modulated depending on the direction of polarization in the ferroelectric. When the polarization is switched, the barrier height seen by the tunneling electrons can be increased or decreased resulting in two different conductances being measured.

By considering the band alignment in Fig. 5.10 we can see that the mechanism for the TER effect may be modelled by considering a simple tunneling barrier as shown in Fig. 5.11. The $BaTiO_3$ region is considered as a potential barrier with a constant gradient while the $SrTiO_3$ region can be viewed as a square potential with a height to match the potential of the $BaTiO_3$ interface. Clearly, tunnelling through the $BaTiO_3$ barrier is going to be the same regardless of the direction of ferroelectric polarisation. The TER effect is then dominated by the height of the potential barrier in the $SrTiO_3$ region.

5.4 Transport Properties

Fig. 5.12 shows the transmission coefficient for both the $P_{\rightarrow}$ and $P_{\leftarrow}$ structure and the TER ratio as a function of the thickness of the dielectric layer [panel (d)]. The

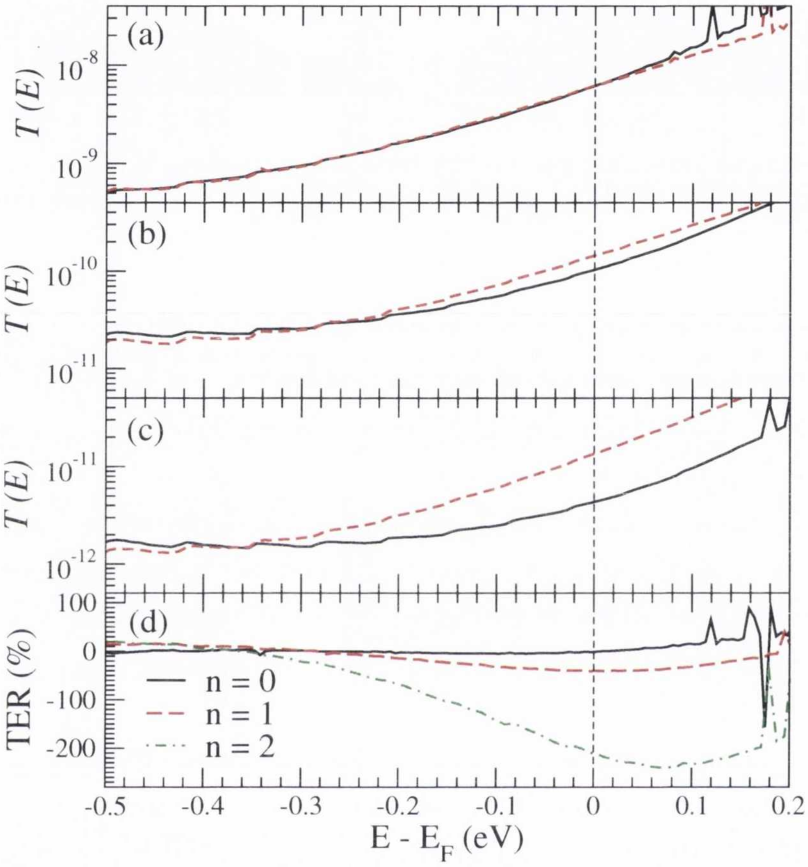

Figure 5.12: Transmission coefficient for the (a) n=0, (b) n=1 and (c) n=2 structures. The solid black lines corresponds to $P_{\rightarrow}$ while the dashed red line corresponds to $P_{\leftarrow}$ structure. (d) TER values for n=0 (solid black line), n=1 (dashed red line) and n=3 (dot-dashed green line).

TER is defined as follows:

$$TER = \frac{G_{\leftarrow} - G_{\rightarrow}}{G_{\rightarrow}} \tag{5.1}$$

where $G_{\rightarrow}$ ($G_{\leftarrow}$) is the conductance of the tunnel junction for the $P_{\rightarrow}$ ($P_{\leftarrow}$) structure. When $n = 0$ there is no $SrTiO_3$ layer, i.e., the structure has symmetric interfaces between $SrRuO_3$ and $BaTiO_3$. If the structure was identically symmetric we would expect the TER to be zero. However, small unavoidable differences in the exact atomic positions result in a non-zero TER of 0.31%. This number, although small, is quite sensitive and it is possible to produce a change of 13.8% in TER by displacing by less than 0.02Å one interfacial $SrRuO_3$ unit cell alone. We note that a TER effect in a symmetric junction is very likely to be observed experimentally due to the difficulty in creating defect-free structures, namely there will be always a degree of asymmetry between the interfaces which will result in a measurable TER effect [232]. Despite this, such defect-driven TER effects are not desirable for device applications due to lack of reproducibility.

Due to the switching behaviour of the $SrTiO_3$ barrier height, the tunnelling conductance through the $P_{\rightarrow}$ and $P_{\leftarrow}$ decreases at different rates for increasing interfacial dielectric thickness. For one unit cell of $SrTiO_3$ the TER increases from 0.31% to 39.1% and for two unit cells it increases again to 210.36%. This data is tabulated in Table 5.1 and graphed on a logarithmic scale in Fig. 5.13. The general trend of exponentially increasing TER with increasing $SrTiO_3$ thickness agrees with what was predicted by a simple model approach [241].

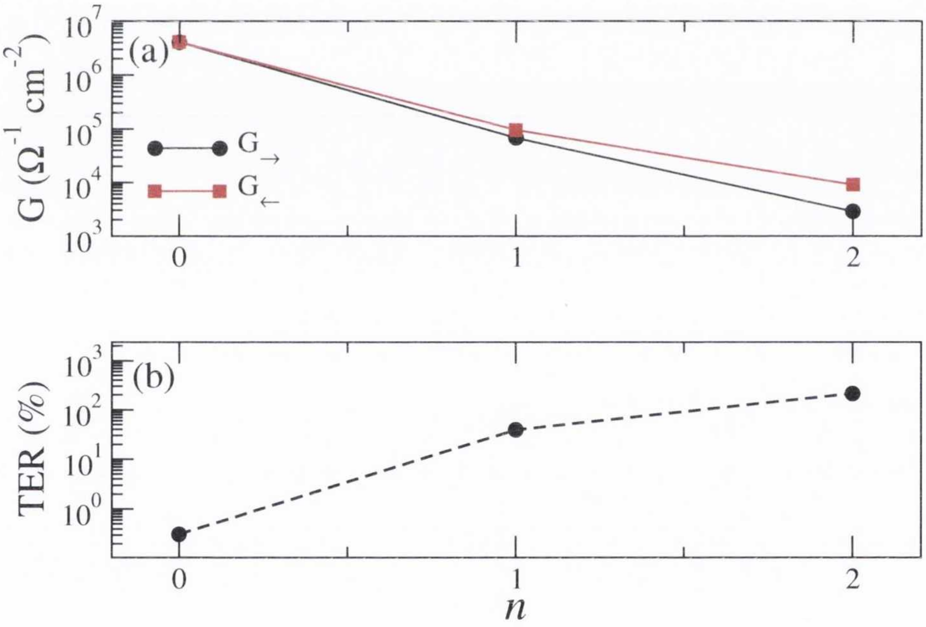

Figure 5.13: (a) Conductance as a function of n for the $P_{\rightarrow}$ (black curve) and $P_{\leftarrow}$ (red curve) ($G_{\rightarrow}$ and $G_{\leftarrow}$ respectively). (b) TER as a function of n on a logarithmic scale.

	$G_{\rightarrow}$ (Ω^{-1}cm^{-2})	$G_{\leftarrow}$ (Ω^{-1}cm^{-2})	TER (%)
n = 0	4.05x10^6	4.06x10^6	0.31
n = 1	6.82x10^4	9.49x10^4	39.07
n = 2	2.80x10^3	8.69x10^3	210.36

Table 5.1: Conductance of the n=0, n=1 and n=2 tunnel junctions for both the $P_{\rightarrow}$ and $P_{\leftarrow}$ structures ($G_{\rightarrow}$ and $G_{\leftarrow}$ respectively). The TER ratio is defined according to Equation 5.1.

In Fig. 5.14 the k-resolved transmission coefficient is plotted over the full 2D Brillioun Zone perpendicular to the transport direction at the Fermi level. The top row (a - d) shows the transmission for the $n = 0$ structure for both polarisation orientations while the bottom row shows the same information for $n = 2$. For both structures, the contribution to majority transmission at the Fermi level is mainly from the band edges. In contrast, the transmission through the minority spin is centered around the $\bar{\Gamma}$ point, with a broad region between Γ and X also contributing, reflecting the d-like symmetry available at E_{F}. The large increase in transmission coefficient for the $\mathrm{P}_{\rightarrow}$ structure compared to the $\mathrm{P}_{\leftarrow}$ one is evident, in particular for tunnelling through the dominant minority states.

Until now, we have only discussed the total tunnelling transmission. However, as expected when the electrodes are ferromagnetic, it is also possible for the junction to exhibit tunnel magnetoresistance (TMR). This will be discussed in the next section.

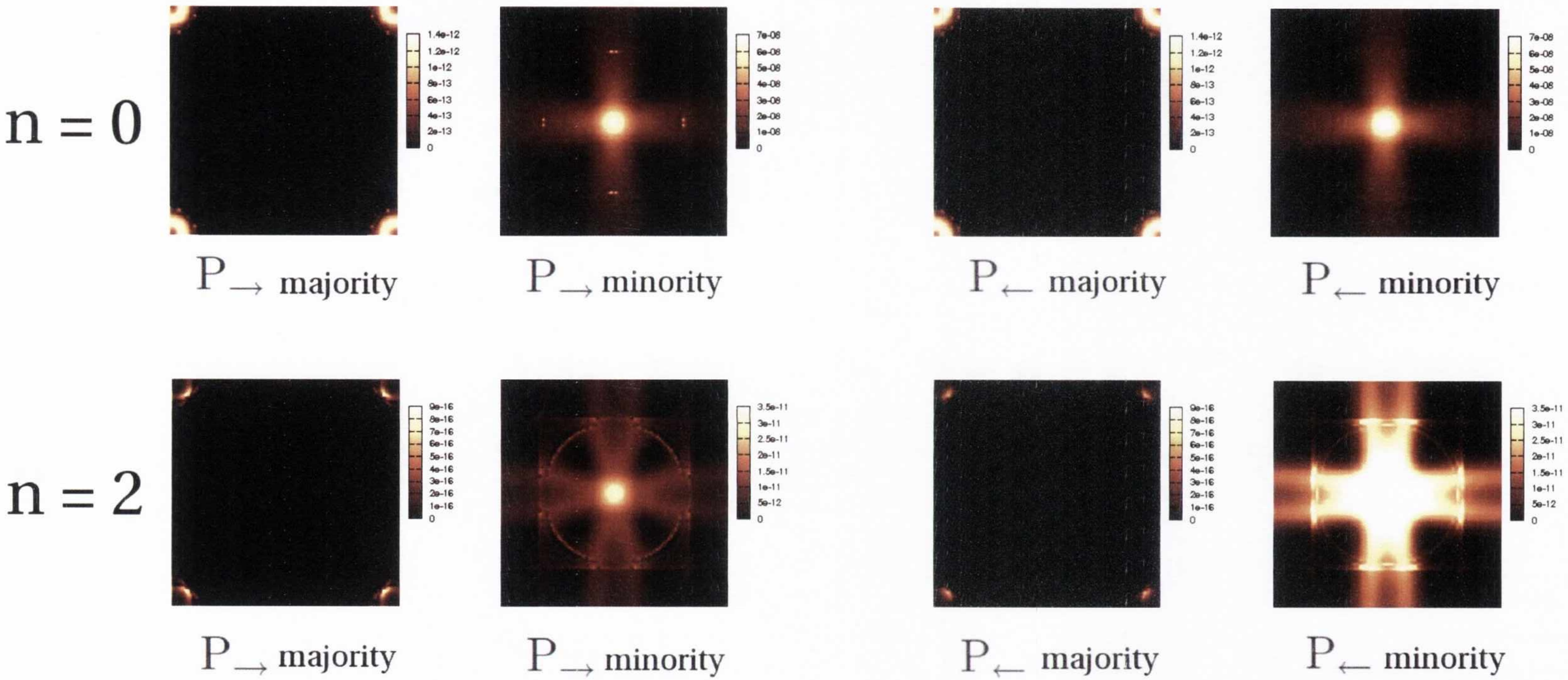

Figure 5.14: k-resolved transmission coefficients calculated at the Fermi level for a parallel magnetic configuration of the electrodes, for the $n = 0$ structure (top row) and $n = 2$ structure (bottom row).

5.5 Four State Memory

If the electrodes used in a ferroelectric tunnel junction are ferromagnetic a TMR effect will be generated upon the reversal of the magnetisation direction of the electrodes. It is also possible that the TMR effect will be modified by the switching of the ferroelectric polarisation. This was found in the experimental work of Garcia et al. [248, 249] for a LSMO/$BaTiO_3$/Fe structure. They found that the TMR depends strongly on the direction of the $BaTiO_3$ polarisation. When the polarisation is orientated towards the Fe electrode, the TMR value is more than twice as large as when it is pointing towards the LSMO layer. They thereby demonstrate the electrical control of the TMR effect in a tunnel junction with dissimilar electrodes. In order to quantify the sensitivity of the TMR with the ferroelectric polarisation, they define a new figure of merit, the tunnel electromagnetoresistance (TEMR), as

$$TEMR = \frac{TMR_{\rightarrow} - TMR_{\leftarrow}}{TMR_{\leftarrow}},$$

where TMR is defined as

$$TMR_{\rightarrow(\leftarrow)} = \frac{G_{\uparrow\uparrow} - G_{\uparrow\downarrow}}{G_{\uparrow\downarrow}}$$

for the $P_{\rightarrow(\leftarrow)}$ structure. A description of the TMR effect, and its dependence on the electronic structure of a symmetric $SrRuO_3$/$BaTiO_3$/$SrRuO_3$ junction was discussed in Chapter 4. For the junction containing two unit cells of $SrTiO_3$ at one interface (n = 2) we find a large value of TEMR (426.32%). Such a value is comparable to those reported experimentally for the Fe/BTO/LSMO thin film structure where TEMR values of 140% and 450% were found [248], depending on the exact structure used.

Thus, we find a change in resistance of a $SrRuO_3$/$SrTiO_3$/$BaTiO_3$/$SrRuO_3$ heterostructure when either the electric polarisation of the barrier is reversed *or* when the relative magnetisation of the electrodes is switched from parallel to antiparallel. A similar result was found in Ref. [158], where asymmetric terminations of $BaTiO_3$ were used to introduce asymmetry, although the TEMR effect was smaller at ~17%.

Due to the coexistence of the TMR and TER effect, it is possible that such a barrier maybe be used as a four-state memory. In such a memory, the ferromagnetic and ferroelectric order parameters can independently encode information, the result of which will be a massively increased storage density. The four states must be independent with minimal multiferroic coupling. The states formed by the electric polarisation P and magnetisation M are shown in Fig. 5.15 and are (P→, ↑↑), (P→, ↑↓), (P←, ↑↑) and (P←, ↑↓).

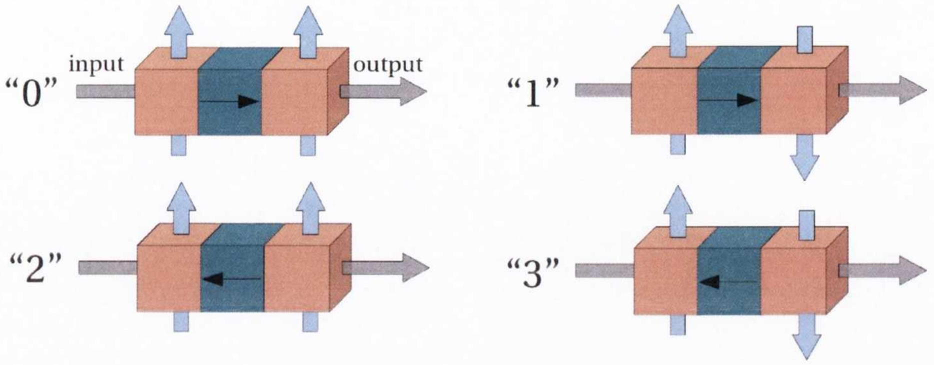

Figure 5.15: A four resistance state system achieved by the combination of the TER and TMR effects. The sketch indicates the magnetic (thick blue arrows) and electric (thin black arrows) configurations.

G	↑↑	↑↓	TMR (%)
→	$2.80\text{x}10^{3}$	$1.12\text{x}10^{-4}$	$2.50\text{x}10^{9}$
←	$8.69\text{x}10^{3}$	$1.83\text{x}10^{-3}$	$4.75\text{x}10^{8}$
TER (%)	210.36	1533.93	

Table 5.2: Conductance for the $n = 2$ tunnel junction for both parallel and antiparallel magnetisation alignment of the electrodes and for both the $P_{\rightarrow}$ and $P_{\leftarrow}$ structures. The subsequent values of TMR and TER are presented. The TER ratio is defined according to Eqn. (5.1).

Such a memory would be non-volatile as both $\boldsymbol{P}$ and $\boldsymbol{M}$ do not need to be powered up. Information can be read be measuring the source - drain current and so would not require the more complicated and destructive read-out process used in FeRAM. The destructive read-out and subsequent re-write of each bit causes memory fatigue in FeRAM due to the repetitive cycling and so places a limit on its reliability. This resistive memory eliminates such a drawback.

5.6 Conclusions

For a tunnel junction with a composite barrier combining a ferroelectric material and a dielectric one and symmetric ferromagnetic electrodes, we demonstrate a sizable TER effect that increases exponentially with the thickness of the dielectric layer. We find that the TER effect is generated somewhat indirectly by the ferroelectric material through its influence on the barrier height of $SrTiO_3$. In an attempt to screen the interfacial charge induced by the ferroelectric polarisation, the dielectric electrostatic potential becomes pinned to the $BaTiO_3$ barrier height at that interface. Thus the magnitude of the barrier height varies dramatically when the direction of polarisation is reversed. We predict that by modifying the thickness of the ferroelectric layer (which will modify the barrier height) or by changing the thickness of the $SrTiO_3$ layer it is possible to tune the TER effect. In this way, a very large effect can be generated, in contrast to any contribution from interfacial defects, which offers little control. Finally, the use of ferromagnetic electrodes allows the TMR effect to be manipulated with the ferroelectric polarisation. We find a TEMR effect of over 400%, in line with recent experimental observations. Due to the coexistence of the TMR and TER effects we believe that such a tunnel junction may become the basis of a new player in the family of future resistive based memories.

CHAPTER 6

Electronic Transport through Fe/MgO/Ge (001) tunnel junctions

6.1 Introduction

One of the most important outstanding challenges in spintronics is that of achieving spin polarised electron injection and detection in semiconductors. The technological implications of such an accomplishment would be immense - allowing the integration of spintronics with existing logic solid-state devices. The detection of information stored in a magnetic memory within a semiconductor heterostructure would be possible. There are two requirements for an efficient spin injection device:

1. A long spin relaxation time in the semiconductor,
2. A high spin injection efficiency from the metal to the semiconductor.

Slow spin relaxation in semiconductors has been already demonstrated - Kikkaw and Awschalom [250] showed that the spin diffusion length in semiconductors can reach values comparable to device lengths. For example, in GaAs spin lifetimes of 100ns have been measured at 1.6K although this decreases at higher temperatures. Efficient spin injection from a ferromagnetic source into a semiconductor remains challenging due to the fundamental conductivity mismatch between metal and semiconductor [251, 252]. Two possible methods to overcome this problem have been put forth. One way is to use a magnetic semiconductor as spin injector, for example (Ga,Mn)As. Such materials, however, usually have a very low T_c and so are unsuitable for device applications. A second method is to introduce an interfacial spin dependent tunnel barrier at the interface between the ferromagnet and semiconductor [253]. For instance, a spin injection efficiency of 9% was found in a GaAs light-emitting diode

(LED) system by introducing an amorphous Al_2O_3 tunnel barrier [254]. By using a crystalline barrier, such as MgO, one can increase the efficiency; a spin polarisation of 57% was found when injecting spins from CoFe to GaAs through MgO [255].

Until recently, the majority of optical and electronic studies have concentrated on the III-V direct gap materials such as GaAs. Relatively less attention has been given to the indirect band gap materials. However, the ultrafast carrier mobility of Germanium (Ge) has recently attracted renewed attention in using group IV semiconductors for spintronics. Ge has a substantially higher electron and hole mobility at low electric fields than silicon; as such it has the potential to become the basis for the next-generation complementary metal-oxide-semiconductor field effect transistor (CMOSFET). For this to happen, the control of the Schottky barrier height (SBH) at the metal/Ge interface is vital. However, it has been reported that the Fermi level of the metal are pinned close to the valence band edge (VBE) of Ge [256]. This has been attributed to either metal induced gaps states (MIGS) or defects / danging bonds at the Ge surface. One method to alleviate this problem is to introduce a thin layer of insulating material between Ge and the metallic contacts [257].

We can see, therefore, that the insertion of an insulating material at the interface may solve two problems simultaneously: it depins the Fermi level thereby reducing the Schottky barrier height, and also overcomes the conductivity mismatch problem for spin injection. The use of MgO as the tunneling barrier is particularly appealing. As we shall see later, the lattice mismatch with Ge is low ($\approx$5%) and MgO has been shown to be a good substrate material for the growth of functional oxides such as $BaTiO_3$ and ZnO as well as Co and Fe. Furthermore, as we have previously seen, MgO has been found to perform significantly better than the amorphous Al_2O_3 barrier [255] in increasing the tunnel magnetoresistance in tunnel junctions.

The use of photons as a method of both spin injection and detection was first suggested in the 1960s [258]. Such an approach, known as spin-optoelectronics, expoits the coupling between the angular moment of photons and the spin angular momentum of electrons. This coupling enables one to manipulate and read photon helicity by acting on the magnetic properties of ferromagnetic electrodes in integrated devices. The field of spin-optoelectronics is rapidly developing, driven by the potential for future spintronic devices [259]. It is particularly appealing in the technology sectors concerned with communication and information applications, such as data transmission cryptography, reconfigurable optical interconnects, optical switches and modulators [260, 261].

The development of the spin light emitting diode (spin-LED) was a significant milestone along the path of constructing integrated devices based on spin-optoelectronics. The spin-LED is used to optically analyse electrical spin injected into the semiconductor active zone of a light emitting diode with high sensitivity. Here the spin polarisation of the carriers injected in the conduction band of the semiconductor translates into the helicity of the photons emitted during recombination, via the dependence of the radiative recombination transition probabilities on the spin of the conduction band states and on the photon angular momentum [262]. The first injectors used dilute magnetic semiconductors (DMS) to inject spin polarised electrons directly into semiconductors [263, 264] but these devices only works at low temperatures unsuitable for device applications. The use of conducting ferromagnetic metals became possible when it was realised that the introduction of a resistive contact between the metal and the semiconductors removed the 'conductivity mismatch' problem. The use of Fe, Co, Ni and their alloys was then highly desirable due to their high Curie temperatures.

The spin polarised current is measured by studying the degree of circular polarisation of the electroluminescence emitted by the diode. Electroluminescence polarisations (ELP) of up to 40% at 4.5K [265] and 20% at 80K [266] were found for Fe/Al_2O_3/GaAs and FeCo/Al_2O_3/Al(GaAs) tunnel junctions, respectively. In these cases, the spin polarisation of the injected carriers was limited by the spin polarisation of the tunnelling process. As we have seen, introducing a crystalline MgO barrier in conjunction with Fe electrodes can increase dramatically the tunnelling polarisation. ELP of up to 52% has been found a CoFe/MgO/GaAs tunnel junction at 100K [255].

While spin-LEDs are now available, a critical step for developing spin optoelectronics into a viable technology is the fabrication of integrated detectors, i.e., detectors that do not require external optical elements. The spin-LED works on the principle that spin information is injected electrically and then detected using optical means - spin detection requires the reverse of this process, i.e., the information is created using optical means and subsequently detected electrically. In the last decade, many attempts have been made to accomplish integrated spin detection by essentially using the same structure of spin-LEDs. Spin polarised electrons are optically pumped into the conduction band of the semiconductor with circularly polarised photons resonant with the band gap. The electron spin polarisation is then converted into a modulation of the photocurrent. For this reason, and by analogy with the spin-LEDs, these devices are usually referred as spin-photodiodes (SPDs). Several variants of these SPDs have been investigated including direct FM/SC interfaces with Schottky barriers [267] and those including insulating barriers [268].

Most of these structures involve GaAs, the prototypical material for semiconductor spintronics. However, due to the positive results reported for Ge, including spin manipulation, efficient spin injection, spin transport and in particular a long spin relaxation time, it is now beginning to attract more attention. Epitaxial Fe|MgO|Ge(001) stacks have been recently been synthesised by several groups [269, 270, 271] but to date there has been no demonstration of SPDs based on Ge presenting a sizable and clear spin filtering effect at room temperature.

In Section 6.2, we examine the Fe|MgO|Ge heterostructure. The bulk properties of the three component materials are discussed with particular attention given to those properties that will dominate the transport properties. The Fe|MgO|Ge heterostructure is then discussed and compared to the experimentally found structure.

This has been recently proposed as an efficient and integrated method of detecting photon helicity. In Section 6.3, the room temperature integrated detection of the helicity of photons via spin photodiodes based on fully epitaxial Fe|MgO|Ge(001) hetrostructures is discussed. The experimental work was carried out by C. Rindali and co-workers from the group of R. Bertacco. In order to explain the experimental results, a careful analysis of the calculated electronic transmission through the MgO barrier is required. To this end, the spin transport properties of the junction are calculated from DFT and the NEGF method.

6.2 Structure

6.2.1 Bulk Materials

Ge

Ge is a semiconductor that crystallises in the diamond cubic structure (space group $Fd\bar{3}m$) with an experimental lattice constant of 5.6575 Å and an indirect band gap of 0.66 eV between Γ (valence band) and L (conduction band). The direct band gap has been found to be 0.8 eV. All the calculations in this chapter have been carried out within the generalized gradient approximation (GGA) using the parametrization of Perdew, Burke and Ernzerhof (PBE) [38] for the exchange and correlation functional. The core and valence electrons are treated with norm-conserving fully separable [122] Troullier-Martin [123] pseudopotentials. The predicted lattice constant within GGA is 5.778 Å, a slight overestimate of the experimental value. The band structure is shown in Fig. 6.1. The valence band maximum is doubly degenerate and occurs at the Γ-point. The conduction band minimum lies at the L-point, on the edge of the first Brillioun zone (Fig. 6.1(b)). We note that the usual GGA underestimation of the band gap reduces the gap of Ge to almost zero. We will discuss the implications of this on the transport properties in Section 6.3.

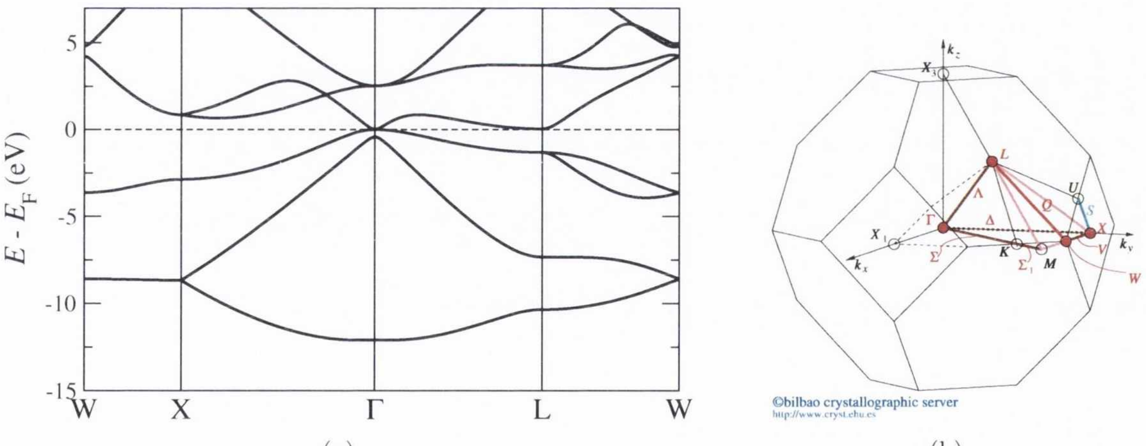

(a) (b)

Figure 6.1: (a) Calculated band structure of diamond cubic Ge obtained from GGA. The Fermi level is aligned to 0 eV. (b) The face centred cubic (fcc) Brillouin Zone.

Fe

Fe is a ferromagnetic metal that crystallises in the bcc structure (space group $Im\bar{3}m$). The experimental lattice constant is 2.87 Å. One of the more notable failures of the LDA functional is that it predicts a fcc ground state structure for Fe with an underestimated lattice constant. GGA, however, correctly predicts a bcc ground state structure that is ferromagnetically ordered and the predicted lattice constant is very close to that of experiment at 2.88 Å. The localized atomic orbitals for Fe is of double-ζ quality for the s states (cutoff radius 6 Å) and single-ζ for the p (cutoff radius 6 Å) and the d (cutoff radius 5.6 Å) symmetries. The band structure of Fe is shown in Fig. 6.2 for majority and minority spins. A spin split of $\approx$2 eV is evident in the d bands resulting in a magnetic moment of $2.27\mu_B$/Fe, which compares well with the experimental value of $2.2\mu_B$/Fe.

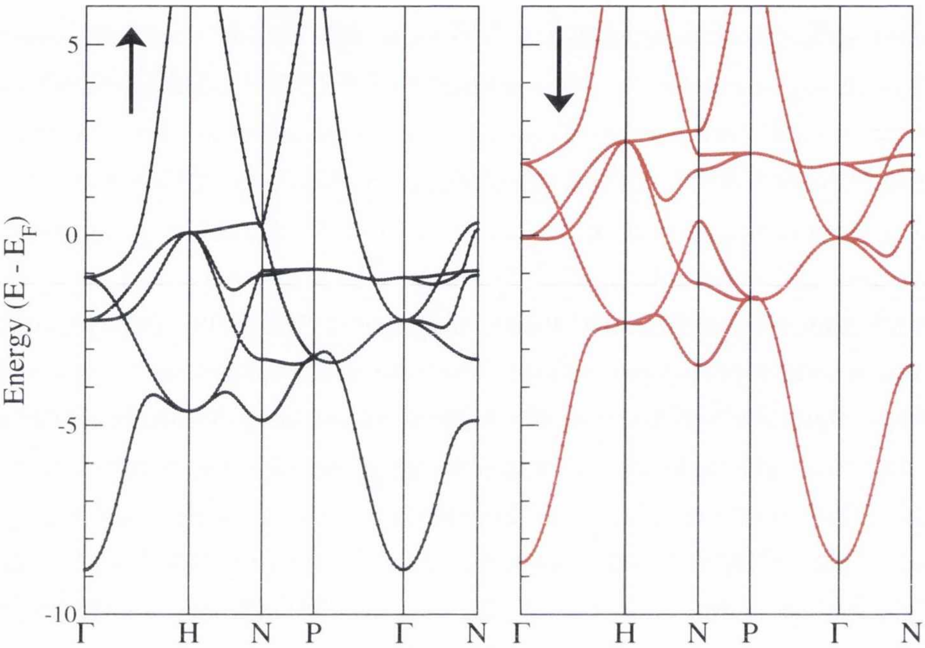

Figure 6.2: Fe band structure for majority and minority spins obtained from GGA.

MgO

MgO is a wide band-gap insulator that crystallises in the rock-salt structure (space group $Fm\bar{3}m$). Experimentally, the band gap has been found to be 7.8 eV while the lattice constant is 4.21 Å [272]. The localized atomic orbitals for each atom use a double-ζ basis set for the for the s and p states with cutoff radii for all the first ζs of 4 Å.[1].

---

[1] Although small, a cutoff radii of 4 Å is sufficient to accurately describe the electronic structure of MgO close to the Fermi level without introducing spurious flat bands in the complex band structure. A thorough description of the the influence of cutoff radii on the electronic properties of MgO can be found in Ref. [273]

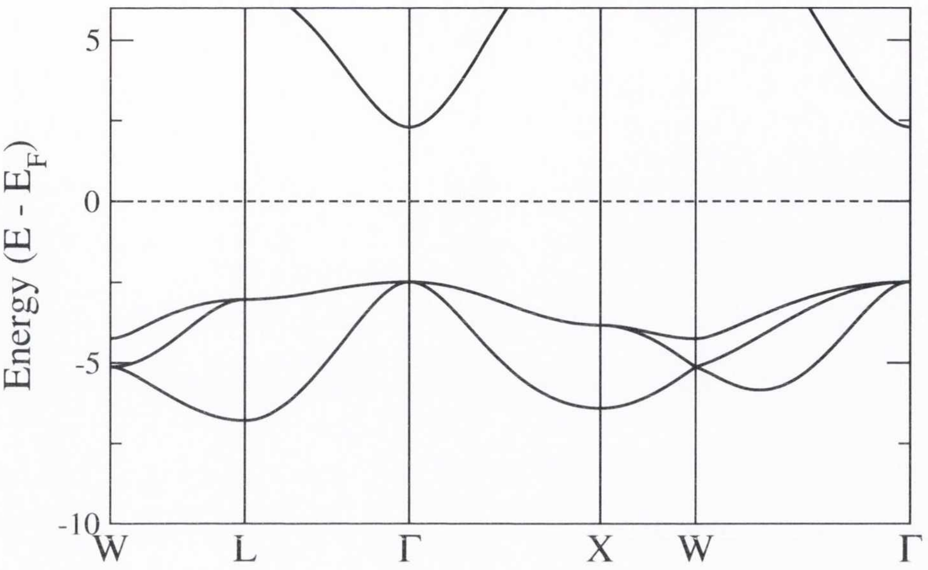

Figure 6.3: The calculated MgO band structure obtained from GGA.

The equilibrium lattice parameter for MgO within the GGA is found to be 4.27 Å, an overestimation of the experimental lattice constant by 1.4% as is to be expected from a GGA calculation. (Within the LDA the theoretical lattice constant is found to be slightly underestimated at 4.18 Å).

The band structure of MgO is shown in Fig. 6.3. The band gap is 4.78 eV and is direct at Γ. As usual, this is significantly smaller than the experimental band gap of 7.8 eV. Correcting for the self-interaction error via the ASIC functional has proved effective in opening the band gap of MgO to that experimentally observed [273]. However, in this case the GGA band gap is sufficiently large and should not impact on the conclusions of this chapter.

6.2.2 Fe/MgO/Ge heterostructure

As we discussed in Section 6.1, Fe/MgO/Ge(001) is a promising heterostructure for spin transport. The use of Ge as semiconductor is highly advantageous due to its high carrier mobility; the electron mobility is several times higher than that of Si while the hole mobility is the highest of all group IV and IIIV semiconductors. The introduction of a high resistive barrier with spin polarised resistance such as MgO has several effects: it solves the 'conductivity mismatch' problem between Ge and Fe and it allows the circumvention of the Schottky barrier, created due to the pinning of the Fe Fermi level to the valence band of Ge.

For this to happen, it is vital that the structure is epitaxial with well defined interfaces. The interface between Fe and MgO has been carefully studied but the growth of MgO on Ge has only recently been given attention.

Fe/MgO interface

Since the seminar theoretical work of Butler et al. [23], there have been numerous studies, both experimental and theoretical, of the growth of MgO on Fe and the electronic properties of the Fe/MgO interface [274, 275, 276, 277, 278, 279, 77]. It is generally found that for MgO deposited on Fe(001), the Fe[100] direction is parallel to MgO[110], i.e., the MgO crystal is rotated by 45° with respect to Fe. The lattice mismatch for this epitaxial arrangement is 3.8%. The Fe lattice constant along [100] is 2.87 Å compared to 2.98 Å for MgO along [110]. Low Energy Electron Diffraction (LEED) studies [280] have shown that the interface between Fe(100) and MgO(100) is such that the Fe atoms are positioned on top of the O atoms in the first MgO layer. However, the exact arrangement at the interface seems to depend on the experimental growth conditions. For example, several groups have found that one or more layers of FeO form at the interface [278, 281, 282]. Theoretical works have detailed the effect such an FeO layer can have on the transport properties [283, 284]. Other investigations, however, have found that no partial oxidation of Fe occurs [285, 286, 287] or that it is possible to control the level of oxidation depending on growth techniques and conditions [278, 288].

Ge/MgO interface

The growth of MgO on a Ge substrate has been studied much less than its growth on Fe. In particular, two possible epitaxial relationships between Ge and MgO have been proposed. The first one is the so-called cube-on-cube growth, that is observed for the growth of MgO on GaAs [289], i.e., [100] MgO is parallel to [100] GaAs. This would require an enormous lattice mismatch (defined as $a_{Ge} - a_{MgO}/a_{Ge}$) of 26.6%. For this reason, it has been suggested that such a cube-on-cube growth of MgO on GaAs is possible only because of the presence of an interfacial amorphous layer several nanometers thick. As a result, MgO need not be commensurate with the underlying GaAs crystal.

In contract, negligible oxidation has been found between MgO and Ge ($\approx$0.5 ML) [290]. Because of this and despite the similarity between the lattice constants of GaAs and Ge (5.65 Å compared to 5.66 Å), a second epitaxial relationship is possible, where [110]MgO is parallel to [100]Ge, i.e. MgO grows on Ge with a 45° rotation of the MgO lattice with respect to the Ge one. In this case, the lattice mismatch is much reduced to 5.1%, significantly lower than the misfit of cube-on-cube growth.

Fe/MgO/Ge heterostructure

Ge/MgO/Fe heterostructures have been grown in ultra-high vacuum by using Molecular Beam Epitaxy (MBE) [290, 269] and the structure has been determined by using Reflection High Energy Electron Diffration (RHEED). MgO has been deposited on Ge with a thickness ranging from ≈1 to 2.3nm. Optimal growth was achieved by growing MgO at room temperature on a *p*(2x1)-Ge(001) surface, as opposed to *p*(1x1)-Ge(001), as the former displays significantly lower oxidation of the Ge substrate after annealing (the formation of GeO_x is ≈0.5 mono-layers). The Ge/MgO structure was found to be crystalline after annealing at 773 K. As was expected, X-Ray Photoelectron Diffration (XPD) measurements show that MgO grows with orientation MgO[110] || Ge[100] [269]. This relationship has also been found by other authors [270, 271]. Using MBE, a 10 nm thick Fe layer is deposited on MgO and then annealed again resulting in an Fe film with good crystallographic quality with minimum interfacial oxidation of the Fe atoms. The Fe unit cell is found to be rotated by 45° with respect to the MgO layer, as is usual of epitaxial growth of Fe on MgO [291].

All heterostructure calculations are performed a 7x7x1 k-point Monkhorst-Pack mesh [242] and a grid spacing equivalent to a plane-wave cut-off of 600 eV is sufficient to converge the charge density. While in reality, the in-plane lattice constant varies throughout a heterostructure as it deforms in order to reduce the misfit strain, the application of periodic boundary conditions restricts us to constrain the in-plane lattice vectors of both electrodes, Ge and Fe, to be identical. The in-plane lattice constant of MgO must also adhere to this constraint.

The in-plane lattice parameter is set to that of bulk Ge (5.778 Å) in order to mimic the effect of a Ge substrate. The result of straining MgO to the lattice constant of Ge is that the band gap increases from 4.78 eV to 5.968 eV. MgO is then rotated by 45° with respect to the Ge lattice in order to minimize the strain (+4.53% compared to +5.12% experimentally) as sketched in Fig. 6.4. The agreement between experiment

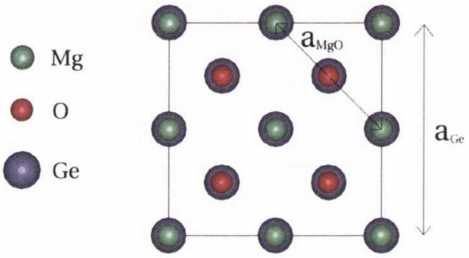

Figure 6.4: A schematic of the atomic arrangement for the [110] direction of MgO parallel to the [100] of Ge.

and theory with regard to epitaxial strain is quite good and is shown in Table 6.1. Within GGA the misfit strain between Ge and Fe is only 0.4%, assumming four Fe unit cells per one Ge in the xy-plane.

	Ge	MgO	(Strain)	MgO (45°)	(Strain)	Fe (Strain)
GGA	5.78 Å	4.27 Å	(26.08%)	6.04 Å	(4.34%)	2.88 Å(0.4%)
Experiment	5.66 Å	4.21 Å	(25.62%)	5.95 Å	(4.93%)	

Table 6.1: The lattice constants of Ge, MgO and Ge as obtained by GGA and compared to experiment [269]. The predicted stain is shown for both cube-on-cube growth of MgO on Ge and for MgO rotated by 45° on Ge.

In keeping with these experimental findings, we consider a tunnel junction formed by five MgO monolayers (<1.1 nm thick). The left-hand side electrode comprises of eleven Ge atomic layers, while the right-hand side one is made up of eight atomic layers of Fe. This is sufficient to converge to bulk properties. A layer of vacuum ~34 Å thick separates the two electrodes. In Fig. 6.5 the unit cell for the entire Ge/MgO/Fe heterostructure is shown. Periodic boundary conditions are applied in the plane perpendicular to the stacking direction (the xy-plane). The structure is then relaxed out-of-plane until the forces are less than 40 meV/Å. The relaxed Fe - O distance is 2.1 Å while the relaxed Mg - Ge distance is 2.73 Å. Rumpling of the interfacial MgO atoms is also evident.

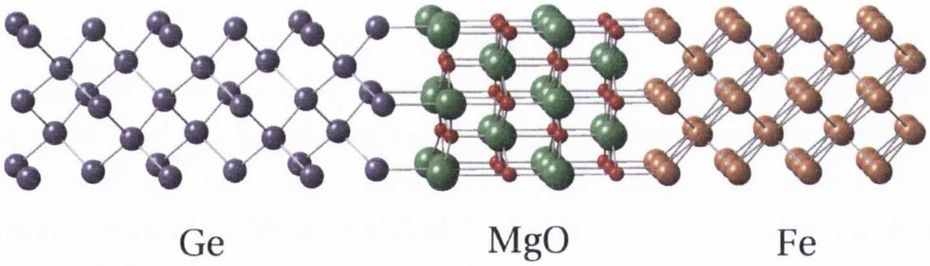

Figure 6.5: Unit cell used for the Fe/MgO/Fe(100) junction. Periodic boundary conditions are applied perpendicular to the stacking direction.

A detailed description of the spin filtering effect according to the symmetry of Bloch waves in crystalline tunnel junctions can be found in Chapter 4. Here, we briefly summarise the effect as we discuss the transport across the Fe/MgO interface. The huge TMR obtained using simple ferromagnetic electrodes together with epitaxial tunnelling barriers cannot be described using the Julliere model. It became evident that the transmission in a tunnel junction is determined not only by the DOS at the Fermi level of the electrodes and by their spin polarisation, but also by a spin filtering effect due to wave function matching across the barrier. This was first discussed by Butler and Mathon [23, 24] in relation to the Fe/MgO/Fe tunnel barrier.

The spin dependence of the tunnelling current can be deduced from the symmetry of the Bloch states in the electrodes and the evanescent states of the barrier. Although these states are a feature of a surface or an interface, their general properties can be derived from the bulk band structure of the constitutional materials once we consider both real and imaginary k-vector solutions to the Schrödinger equation for the periodic bulk potential [202]. The complex band structure of MgO is shown in Fig. 6.6 for $\boldsymbol{k}_{||} = 0$. States with $\boldsymbol{k}_{||} = 0$ have no momentum component in the plane perpendicular to the transport and, in general for materials with direct gaps at Γ, will have the slowest decay rate. As the complex bands inherit the symmetry properties of the real bands they are connected to, we can ascribe the lowest decay to states with Δ_1 symmetry (comparing to Fig. 6.3). States with Δ_1 symmetry are those that transform like a linear combination of functions with 1, z, $2z^2 - x^2 - y^2$ symmetry. States with Δ_5 symmetry transform as functions with zx and zy symmetry.

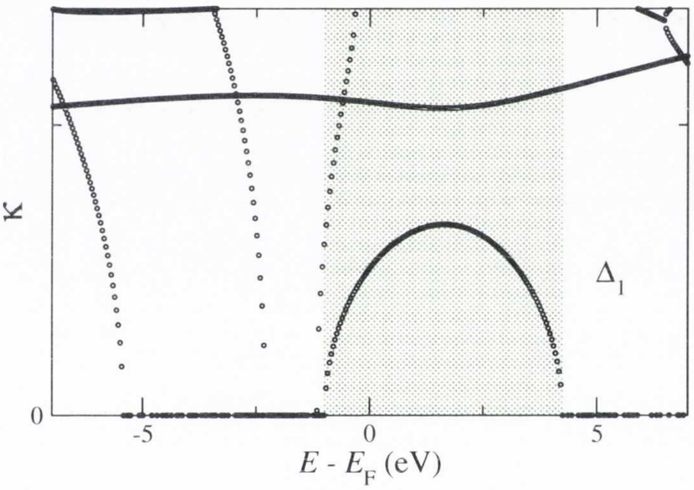

Figure 6.6: Complex Bands of the First Kind ($\boldsymbol{k}_{||} = 0$) for MgO. The shaded area marks the MgO band gap.

For an electron in Fe to tunnel across the MgO barrier it must belong to a state with the same Δ_1 symmetry so that it can couple effectively to that evanescent state. The real band structure of Fe along the Δ direction of the Brillioun zone (Γ - H) is shown in the left panel of Fig. 6.7. There is only one minority band at the Fermi level with Δ_1 symmetry whereas for the minority spins there are no wavefunctions with that symmetry. There are also both majority and minority Δ_5 states at the Fermi

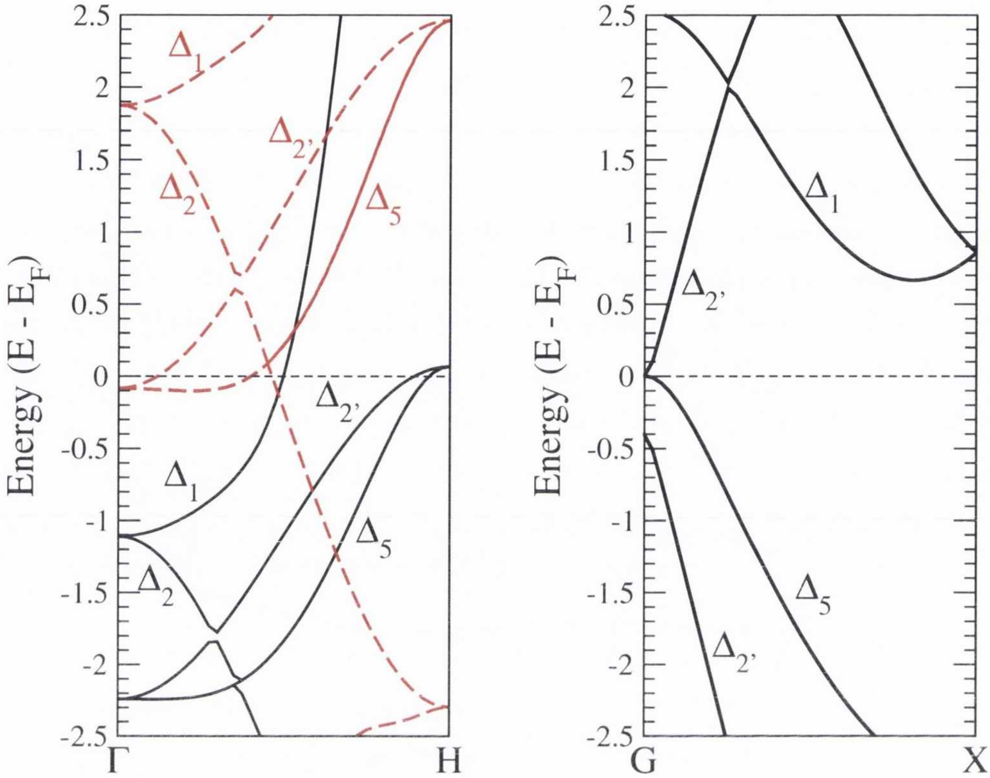

Figure 6.7: The left panel shows the Fe band structure for both majority (solid black) and minority (dashed red) bands along the Γ to H direction, i.e., the direction relevant to tranport. The right panel shows the Ge band structure along Γ to X. The symmetries associated with each band are marked.

level, but these decay significantly faster than those with Δ_1 symmetry in the MgO barrier. Thus, the Δ_1 majority states dominate the tunnelling current, such that the conductance across a Fe/MgO interface is close to 100% positively spin polarised, i.e. Fe(001)/MgO(001) acts like a half metal in this structure and the TMR is expected to be very large. In the case of the Fe/MgO/Ge structure, these states must then couple to appropriate states in the Ge layer.

In the next section, the consequences of this symmetry-matching to the transport properties of such a heterogeneous tunnel junction is discussed.

6.3 Transport

6.3.1 Experimental Method

Fe/MgO/Ge heterostructures have been prepared in-situ by Molecular Beam Epitaxy (MBE) in the group of R. Bertacco. The Ge substrate is lightly n-doped to maximize the spin diffusion length. Fig. 6.8 shows the epitaxial quality of the structure in a scanning transmission electron microscopy (STEM) image [290]. A cross section schematic of the entire SPD is shown in Fig. 6.9. An external magnetic field is used to direct the Fe magnetisation out-of-plane, overcoming the shape anisotropy. Circularly polarised light illuminates the front of the SPD, perpendicular to the surface. This means that the photons have to pass through both the Fe layer and the transparent MgO layer before it is absorbed in the Ge layer. The photo-current is then

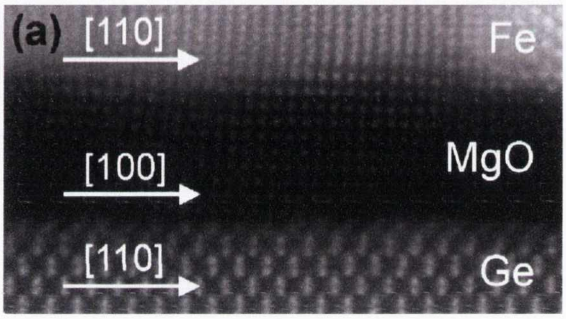

Figure 6.8: (a) STEM cross section of a Fe/MgO/Ge (001) heterojunction [269].

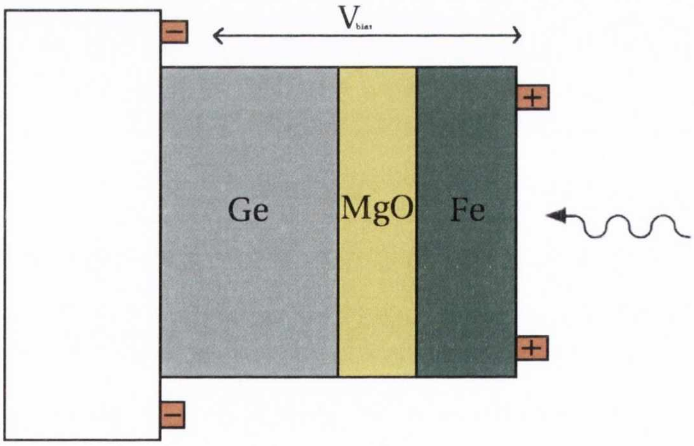

Figure 6.9: Schematical cross section of the SPD. The magnetic field (H) is applied perpendicular to the surface while the bias voltage (V_{bias}) is applied from the top to the bottom electrode. Circularly polarised light impinges the front of the stack, perpendicular to the surface.

measured as a function of bias for different combinations of the light polarisation and magnetization of the Fe layer. All measurements are performed at room temperature.

Fig. 6.10 illustrates how the device operated in forward bias. While MgO is transparent at the photon energy considered (1300nm), the intensity of light impinging on the device is attenuated in Fe due to Magnetic Circular Dichroism (MCD). Right and left circularly polarised light have different absorption coefficients in Fe so that one polarisation will be attenuated more than the other when the light arrives at the MgO/Ge interface. The intensity of light reaching the Ge layer is then given by

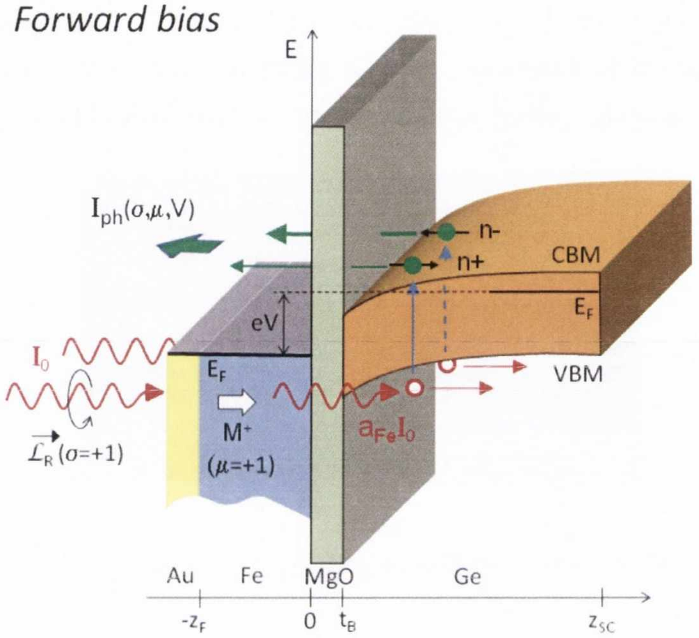

Figure 6.10: Sketch of the band diagram and SPD operation under forward bias. The convention used for the angular momentum of photons ($\mathcal{L}$) and for the unit vector representing the magnetization are illustrated for the case of right circular polarisation ($\sigma = +1$) and inward magnetization ($\mu = +1$).

$$I(z = 0) = I(z = t_B) = I_0 a_{Fe}(1 + \sigma\mu D),$$

where a_{Fe} is the attenuation for unpolarised light, D is the asymmetry of dichroic absorption, σ indicates the z-component of the photon angular momentum ($\mathcal{L}$) in units of $\hbar$ and μ indicates the z-component of the unit vector corresponding to the Fe magnetization so that $\mu = +1$, 0, -1 for positive out-of-plane, in-plane and negative out-of-plane magnetisation respectively. D was found to be 0.4%±0.05% by measuring the transmission of left and right polarised light thought a Fe layer grown on an MgO substate. The photo-generated electron - hole pairs are separated by the Ge band bending: an upward bending (as shown in Fig. 6.10 and Fig. 6.11) drives the electrons towards the interior of Ge where no spin-filtering action is encountered while the holes propagate towards the barrier and cross it into the Fe layer where they experience a spin dependent resistance. A downward bending (See Fig. 6.11) results in the opposite scenario where electrons are driven towards the Fe electrode.

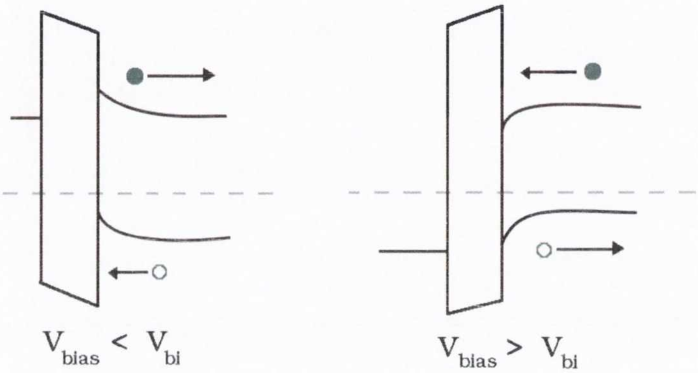

Figure 6.11: Sketch of the heterostructure band diagram as a function of the applied voltage. V_{bi} is the flat band bias, i.e., the applied bias required to counteract the built-in potential of Ge (measured to be 0.2 eV ± 0.1 eV).

The asymmetry in the spin-dependent transport, A_{SF}, is generated by both spin depolarisation during the carrier propagation and by the spin filtering action of the barrier. In order to eliminate spurious asymmetries introduced by the experimental method not related to spin-filtering or dichroism, is it necessary to take the difference of the following two quantities

$$\Delta I^{\sigma}_{+} = I_{ph}(+\sigma, +\mu, V) - I_{ph}(-\sigma, +\mu, V)$$

and

$$\Delta I^{\sigma}_{-} = I_{ph}(+\sigma, -\mu, V) - I_{ph}(-\sigma, -\mu, V),$$

obtaining, to first order,

$$\Delta I(V) = I_0.2a_{Fe}.\eta_c(V).(D + A_{SF}).\sigma\mu,$$

where $\eta_c(V)$ is a proportionality factor depending on the bias. That is, the difference of the photocurrent (I_{ph}) upon light polarisation reversal as a function of applied bias (V), for opposite out-of-plane Fe magnetisations was measured and then the semi-difference of those quantities taken. As

$$I_{photo}(V) = I_{ph}(\sigma = 0, \mu = 0, V) = I_0.a_{Fe}.\eta_c(V),$$

$$\Delta I(V) = 2I_{photo}.(D + A_{SF}).\sigma\mu$$

where $I_{photo}(V)$ is the photocurrent measured for incident linearly polarised light and in-plane magnetization.

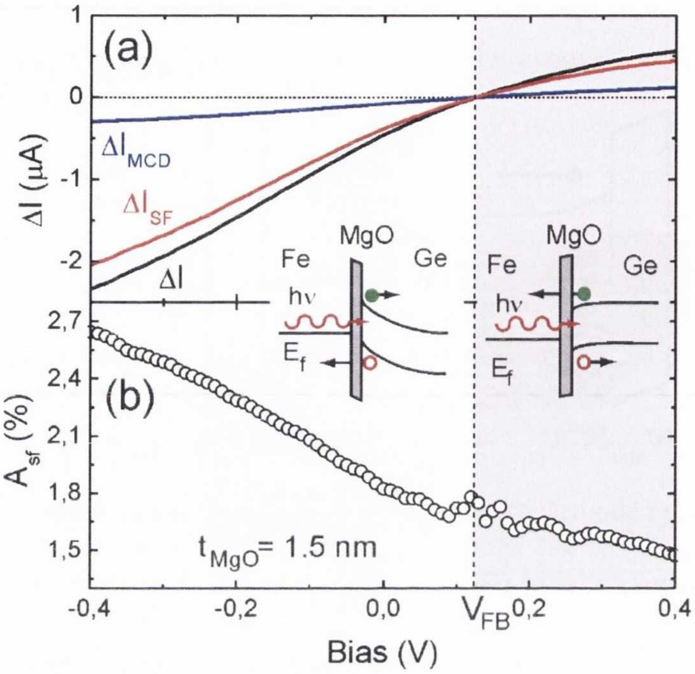

Figure 6.12: (a) Net photocurrent variation as a function the bias voltage due to full reversal of the circular polarisation of light (Δ_I, black curve), as well as its contributions from spin filtering (ΔI_{SF}, red curve) and from magnetic circular dichroism (ΔI_{MCD}, blue curve), for a Fe/MgO(1.5 nm)/Ge spin photodiode. (b) Spin filtering asymmetry (A_{SF}) deduced from data of panel (a). The sign of the photocurrent (to which ΔI_{MCD} is proportional) is coherent with the energy diagrams sketched in the two insets, for applied bias below and above the flat band voltage V_{bi}.

The result for a SPD with an MgO thickness of 1.5nm and an area of $5 \times 10^5 \mu m^2$ is shown in Fig. 6.12 as a function of the applied bias voltage. The black curve in Fig. 6.12(a) shows ΔI. The blue curve shows the contribution from magnetic circular dichroism (ΔI_{MCD}). Subtracting this from ΔI gives the true spin filtering term ΔI_{SF}, shown as the red curve in Fig. 6.12(a).

The spin filtering asymmetry, A_{SF}, is plotted in Fig. 6.12(b). The oscillations close to the flat band voltage, V_{bi} (an applied voltage corresponding to the that necessary to compensate for the internal voltage of Ge) are numerical artifacts due to the division of two vanishing quantities, ΔI_{SF} and I_{photo}.

We can see from the figure that there is a similar spin filtering effect for both forward and reverse bias, i.e., for both holes and electrons. This is surprising since the spin flip relaxation time for holes is much lower than that for electrons ($\tau_h \approx$ 100fs [292] compared to $\tau_e \approx$ 100ps [293]). For this reason, one would expect the spin filtering effect to be significantly higher for electrons than for holes.

In order to reconcile this information with the experimentally measured results we must carefully analyse the creation of the photo generated spin polarised carriers and in particular their subsequent transmission through the MgO barrier to the Fe electrode.

In Fig. 6.13 a schematic band structure of Ge close to the Γ point is shown, including the conduction band (CB), light (LH) and heavy (HH) hole valence bands and the split-off spin-orbit band (SO). Selection rules conserving angular momentum determine that the possible transition are those with j=±1 and are shown in the right panel of Fig. 6.13. The spin polarisation of the excited carriers depends then on the photon energy. Irradiation by photons at 1300nm ($h\nu = 0.96$ eV) excites interband transitions from $P_{3/2}$ and $P_{1/2}$ to $S_{1/2}$ at the Γ point. The circled numbers denote the relative transition intensities that apply for both these excitations. The maximum spin polarisation given by two simultaneous transitions from the top of the valence band is then 50% (P = (3 - 1) / (3 + 1)). After photogeneration, the spin-polarised electron-hole pairs that are created at the Γ point are then separated. The electrons relax, with a characteristic time $\tau_{\Gamma\rightarrow L} \sim$ 230fs [294], towards the conduction band minimum, which in the case of Ge, is at the L point [see the Brillioun Zone of Ge in Fig. 6.1(b)]. In contrast, holes remain in the valence band maximum at the Γ point. Because the electron spin-flip relaxation time (~100 ps) is much longer than $\tau_{\Gamma\rightarrow L}$ we can assume that the transport processes of electrons and holes take place at L and Γ respectively.

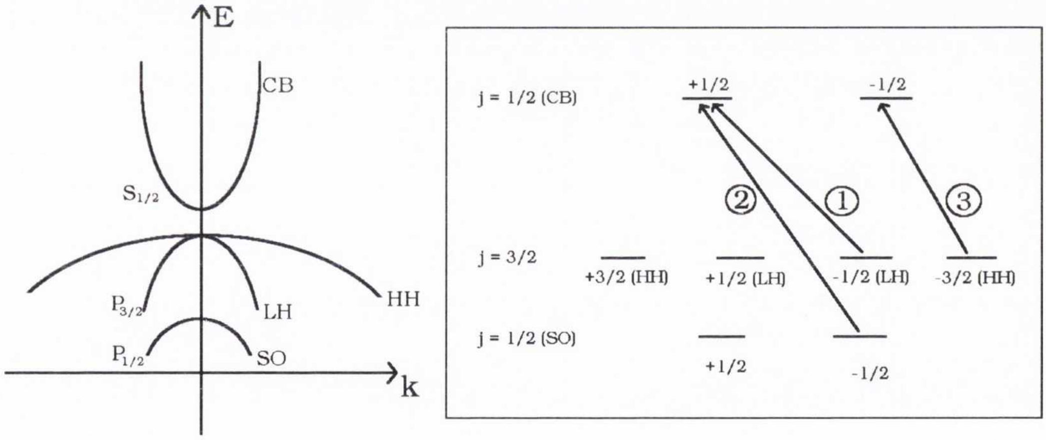

Figure 6.13: Left panel: Schematic band structure of Ge. Right panel: Optical transitions between the level j=3/2 (LH and HH), j=1/2 (SO) and j=1/2 (CB) for a right-circular polarised photon. The relative intensities of the transitions are given in circles.

6.3.2 Transport Properties

Fig. 6.14(a) shows the spin transport properties of a Fe/MgO/Ge tunnel junction by plotting the transmission of majority and minority spins as a function of energy. It is evident that the transmission is dominated by majority electrons throughout the MgO gap, with the minority transmission being at times three times lower in magnitude. Fig. 6.14(b) shows the spin asymmetry of the carrier transmission (A_T) as a function of energy. A_T is defined as

$$A_T = \frac{T_\uparrow - T_\downarrow}{T_\uparrow + T_\downarrow}, \tag{6.1}$$

where $T_\uparrow$ ($T_\downarrow$) is the tunnelling transmission coefficient for majority (minority) spins. For a wide range of energies around the Fermi level $A_T \simeq 1$, illustrating the fact that majority transmission is significantly higher than minority transmission across this range. In Fig 6.15 the average number of channels per $k_\perp$, n_c, is shown for both Ge and Fe electrodes. The massive drop in transmission close to the Fermi level can be attributed to the lack of Ge channels available in that electrode (the Ge energy gap calculated with GGA is essentially zero).

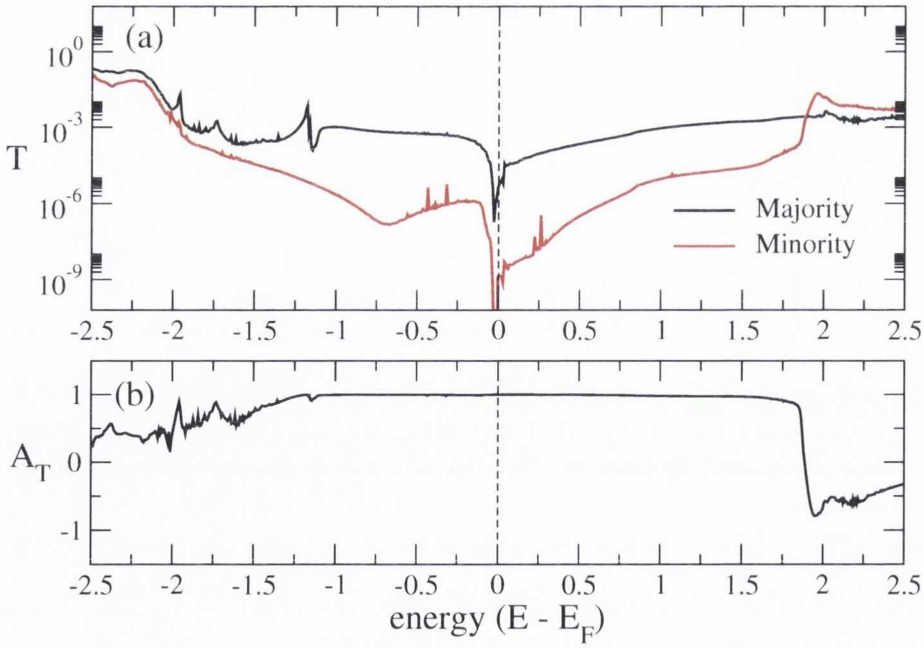

Figure 6.14: Calculated transport properties for a Fe/MgO/Ge heterojunction, where the MgO thickness is approximately 1.1 nm (five unit cells). (a) Total transmission coefficient for majority (black) and minority (red) spins as a function of energy. (b) Calculated spin polarisation as defined in Eq. 6.1 as function of energy. Note that the Fermi energy (E_F) sets the energy zero so that negative (positive) E corresponds to tunnelling of holes (electrons) respectively.

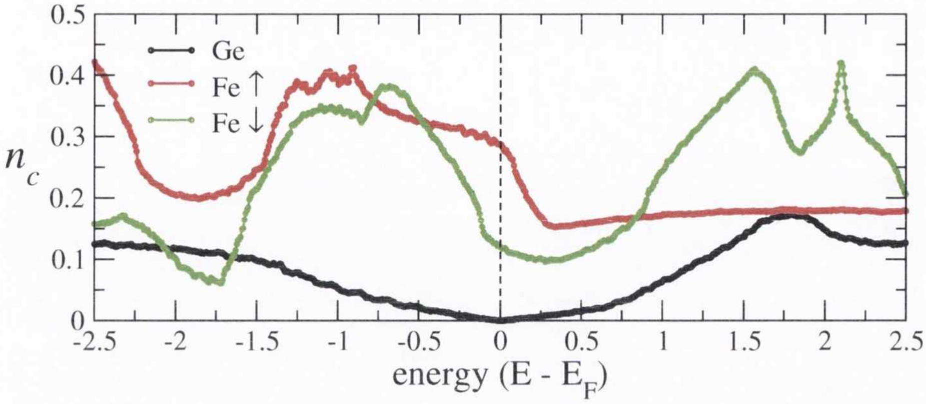

Figure 6.15: Average number of channels n_c for the Ge electrode (black), the Fe majority spin (red) and Fe minority spin (green).

In order to explain this transmission we need to consider the wave function matching at both the Ge/MgO and Fe/MgO interfaces. As this is exact only at the Γ point (0, 0, 0), in Fig. 6.16 we initially consider the transmission at this point alone for clarity. The relationship between the electronic band structure of the electrodes and the peaks in the transmission coefficient is then evident. The majority and minority Δ_1 Fe states are emphasised in particular as their influence on the transmission is striking. For instance, the high majority transmission between -1.1 eV and +2.8 eV can be attributed to the majority Δ_1 band in Fe. Electrons with this symmetry in Fe tunnel through the MgO barrier to states with a $\Delta_{2'}$ symmetry in Ge. The gap in the majority transmission between -0.4 eV and the Fermi level can also be attributed to the gap at those energies at Γ in Ge. Similarly, for the minority spins, the highest transmission can be associated with a Δ_1 state in the Fe electrode above +1.9 eV. Again, the transmission decreases at +2.8 eV corresponding to the band edge of the Ge $\Delta_{2'}$ band.

As discussed earlier, because the electrons relax to the L point in the Brillioun Zone in a characteristic time much shorter than the spin-flip relaxation time, we can assume that the transport process of electrons takes place at the L point predominantly. Holes remain at the top of the valence band at Γ and so by looking at the transport properties of the Γ point we can identify the primary contribution to reverse bias.

In order to ascertain the contribution of the spectral region around the Γ point we have integrated the k-dependent transmission coefficient over 7310 k-points of a disc centred at Γ with a radius corresponding to 17% of the total Brillouin Zone. A disc of the same radius centred at the L point has been used to determine the contribution of a region around L. The integration over this disc has been carried out with 4932 k-points. The chosen radius corresponds to the radius of the Fermi surface obtained by assuming that the Fermi level is within k$_B$T from the conduction band

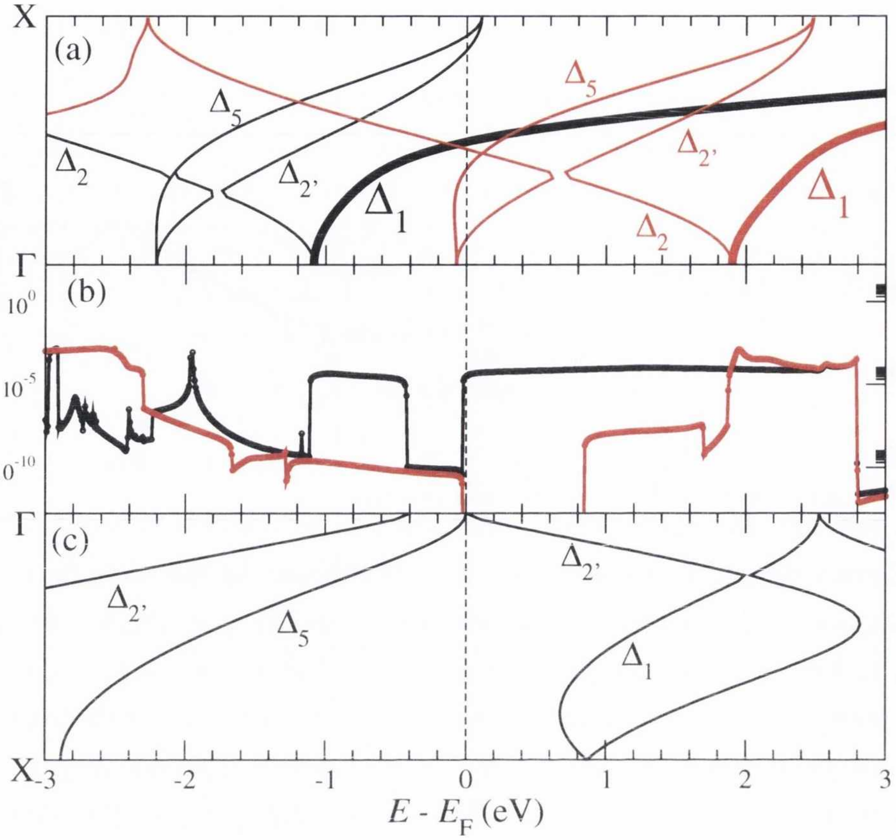

Figure 6.16: In the middle panel we present the Γ point transmission coefficients as a function of energy for majority (black) and minority (red) spin. Panel (a) shows the Fe band structure along the Γ to X direction, while Panel (c) shows the Ge band structure along the same direction.

minimum (k_B is the Boltzmann constant and T the temperature). Fig. 6.17 shows a simple schematic of the sampled points at both Γ and L. Fig. 6.18(b) is obtained

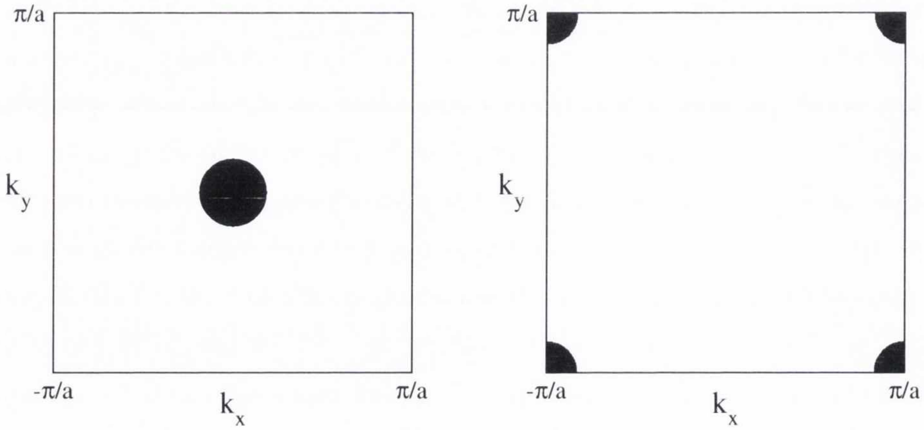

Figure 6.17: Left panel: Part of the total Brillioun Zone sampled close to the Γ point. Right panel: Part of the total Brillioun Zone sampled close to the L point.

by integrating the k-dependent transmission coefficients over the two-dimensional Brillioun Zone orthogonal to the device stack only around the Γ point, relevant for hole tunnelling. Also included in Fig. 6.18 are the Fe and Ge band structures along the relevant direction for transport, in this case along $\Gamma \rightarrow X$. In this case the Fe bandstructure along the direction stack (direction Γ to X) presents bands of Δ_1, Δ_2, $\Delta_{2'}$ and Δ_5 symmetry. The complex bandstructure of MgO (Fig. 6.6) reveals that wave-functions with Δ_1 symmetry have a considerably smaller imaginary wave-vector for energies in the MgO band-gap than those with any other symmetries. This means that the exponential decay of the wave-function is considerably slower for the Δ_1 bands. As in Fe there is only a majority band [black lines in panels (a)] with Δ_1 symmetry in the energy interval -1 eV to 2 eV around the Fermi level, one expects the tunnelling current to be completely dominated by majority electrons. Note that there is no Δ_1 symmetry in Ge along $\Gamma \rightarrow X$ except for (E - E_F) > 1 eV [see panel (c)], which means that electrons need to have a transverse component in the linear momentum to be absorbed by Ge. Note also that in our GGA calculations there is almost no bandgap for Ge at Γ. In contrast, Fig. 6.19 shows the transmission as

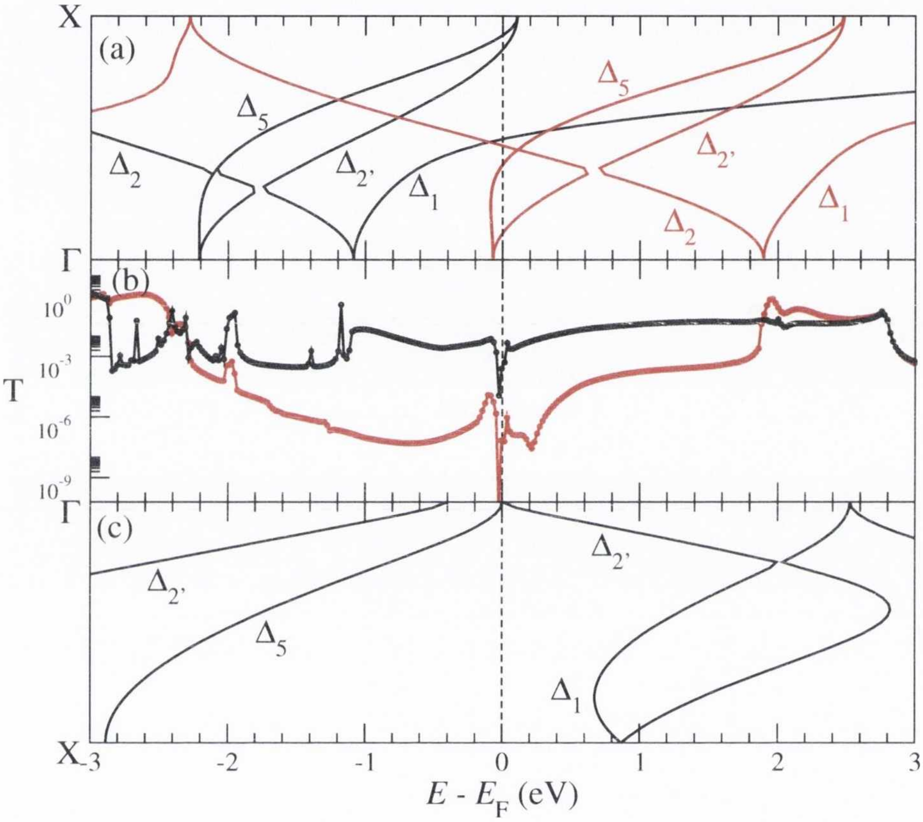

Figure 6.18: In the middle panel we present the carrier transmission for the section of the Brillouin Zone around Γ. Panel (a) and (c) show the real band structure of Fe and Ge, respectively along the direction relevant for transport.

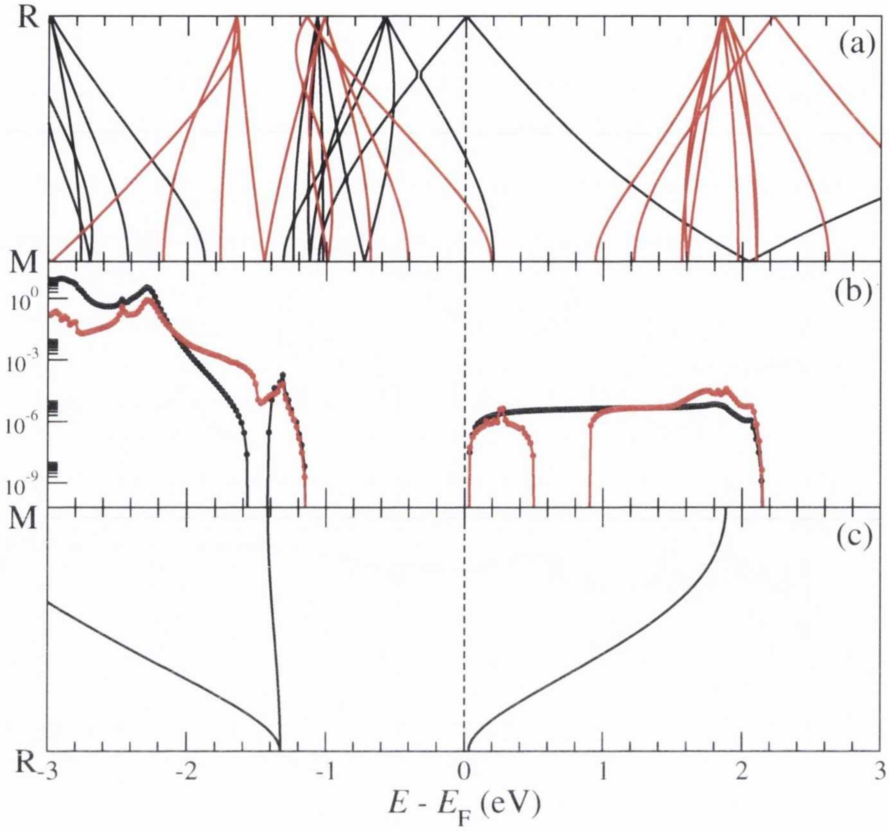

Figure 6.19: In the middle panel we present the carrier transmission for the section of the Brillouin Zone around L. Panel (a) and (c) show the real band structure of Fe and Ge, respectively, along the direction relevant for transport, in this case along the M to R direction of the cubic cell.

calculated by integrating around the L point, which is relevant for electrons in forward bias. The situation is now quite different; this time the transmission coefficient [panel (b)] has a gap in the interval [-1.5,0] eV around the Fermi level, reflecting the band-gap of Ge at that symmetry point. The Fe band-structure [panel (a)] is plotted along the device stack (R to M) of the cubic cell. It is now more complex to identify the various band symmetries but the drastic reduction in overall transmission (the transmission coefficient T changes from $\sim 10^{-3}$ at Γ to about $\sim 10^{-6}$ at L) indicates that the transport through the highly transmittance Δ_1 band is not efficient here.

For comparison with the experimental results, the central quantity of interest is the spin asymmetry of the carrier transmission (A_T) as a function of energy, which is shown in Fig. 6.20 for transport through both Γ and L. As noted above, the majority transmission thought Γ is significantly higher than the minority transmission. This generates the large value for the spin asymmetry A_T in that particular energy window. For transmission thought the L point, the Δ_1 transmission no longer dominates and as a result the spin-filtering is considerably less efficient and A_T is significantly smaller

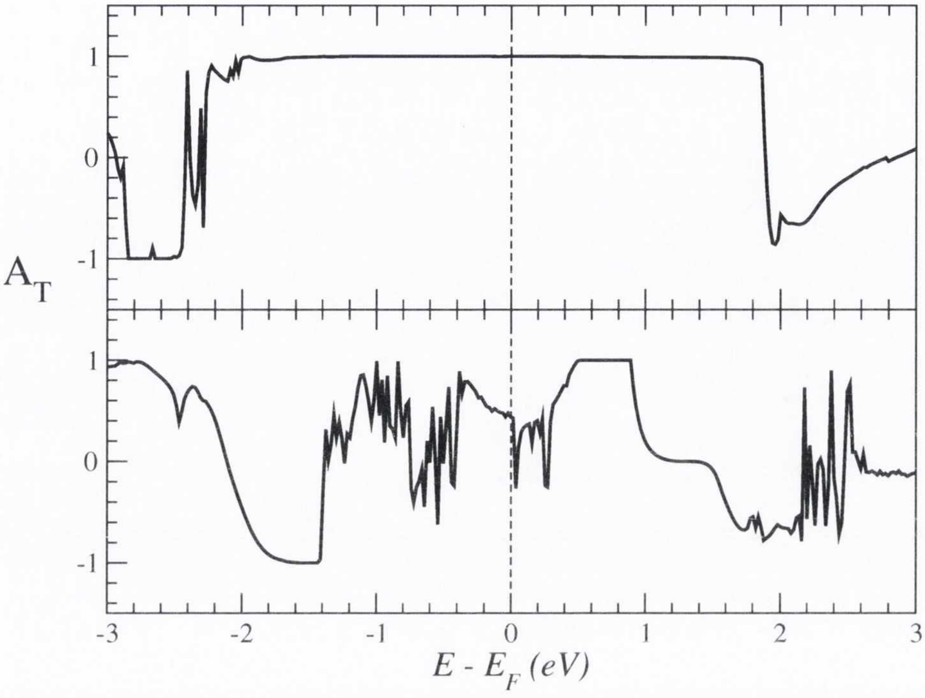

Figure 6.20: Calculated spin polarisation as defined in Eq. 6.1 as function of energy for the transmission around Γ (top panel) and L (bottom panel) as a function of energy.

(~0.5).

This means that while holes are essentially 100% spin-filtered by the Fe/MgO interface, the spin-polarisation of the tunnelling electrons is sensibly smaller. Note that such a large difference in A_T persists if one moves for at least ±1 eV within the valence band at Γ and ±0.5 eV into the conduction band at L. This means that our predicted larger asymmetry in the spin polarised transmission for holes as compared to electrons survives possible gap corrections (note that Ge is almost a metal in our DFT calculations) and finite voltages, like those applied in the experiment.

On the basis of our *ab initio* calculations of spin-dependent transmission we can then explain the reason for the similar maximum values of A_{SF} in forward and reverse bias: the lower spin flip relaxation time for holes is compensated by their much larger transmission spin polarisation, in force of the different points in the Brillioun zone where tunnelling takes place.

6.3.3 Conclusion

The experimentally measured variation of the spin polarised photocurrent induced in a Fe/MgO/Ge(001) heterojunction is of a similar magnitude for both electron and hole transport. This can be probed individually by measuring the photo generated current at forward and reverse bias, respectively. As the spin-flip relaxation time is significantly lower for holes than for electrons, one would expect the spin polarised current in forward bias to be higher than that for reverse bias.

In order to explain this unexpected behaviour, we preformed *ab initio* calculations of the spin-dependent transmission across the tunnelling junction. This allowed us to independently probe the transport process at Γ and L. We found that the transmission coefficient is significantly spin-polarised at Γ but much less so at L. As such, we can conclude that although the spin-polarisation of holes decays relatively quickly compared to electrons, this is compensated for by having a much higher initial polarisation. The result is that the experimentally measured asymmetry in spin dependent current are comparable for both forward and reverse bias.

CHAPTER 7

Influence of the Complex Band Structure on Electronic Transport

7.1 Introduction

In this Chapter we investigate the possible effects of an insulator's complex band structure on electron transport in magnetic tunnel junctions. Two different types of tunnel junctions are considered within which the complex band structure of the insulating material is predicted to have a considerable influence.

In the first we study the electronic structure of two insulating ferrimagnetic spinel ferrites, $CoFe_2O_4$ and $NiFe_2O_4$. The symmetry spin selection associated with the different decay rates in the band gap is predicted to resolve a discrepancy between theoretical calculations and experimental results for spin polarisation in these materials. We calculate the complex band structure of $CoFe_2O_4$ and $NiFe_2O_4$ and discuss how the disagreement between theory and experiment can be resolved.

We then continue our investigation of ferroelectric tunnel junctions by considering the effects of asymmetric electrodes on the structural and electronic properties of a ferroelectric material. The use of asymmetric electrodes can result in different polarisation magnitudes when the direction of polarisation is reversed. We consider how this will affect the complex band structure of $BaTiO_3$ in a $Fe/BaTiO_3/SrRuO_3$ tunnel junction.

7.2 The Spin Filter Effect

A source of highly spin polarised electron current is imperative for many spintronics applications. The class of materials known as half-metals provides candidates for such a source. Half-metals have only one spin channel available for conduction at the Fermi level, as the Fermi level falls into a gap for the other spin subband. Compounds exhibiting such half-metallic behaviour include the manganites [295, 296] and some of the double perovskites [297]. Another promising avenue to generate a highly spin polarised current is to ensure that the device resistance is much higher for one spin channel than for the other via the spin-filter effect. This can be achieved by using an ultrathin ferromagnetic insulating film as the tunnel barrier. The exchange-split electronic states of the magnetic barrier yield different tunnelling barrier heights for spin up and spin down electrons. As a result of the exponential dependence of the tunnel current on the barrier height, electrons entering the barrier material will then be transmitted differently depending on their spin (see Fig. 7.1). If the bottom of the conduction band is lower for spin up electrons than for spin down electrons a large positive spin polarisation will be found. A spin-filter is generally formed using one non-spin-polarised metallic electrode as a current source and one ferromagnetic metallic electrode as a detector with a ferro- (or ferri-) magnetic insulating barrier between them.

The spin filtering efficiency of the barrier is defined as:

$$P_F = \frac{J_\uparrow - J_\downarrow}{J_\uparrow + J_\downarrow}$$

where J_σ is the spin-resolved current density. For a given barrier thickness, d, and at low bias, the tunnelling current density depends exponentially on the barrier heights [298, 299]

$$\begin{aligned} J_\uparrow &= \sqrt{\phi_0 - \frac{\Delta\phi}{2}} exp\left(-A\sqrt{\phi_0 - \frac{\Delta\phi}{2}} d\right) \\ J_\downarrow &= \sqrt{\phi_0 + \frac{\Delta\phi}{2}} exp\left(-A\sqrt{\phi_0 + \frac{\Delta\phi}{2}} d\right), \end{aligned}$$

where ϕ is the averaged barrier height and $\Delta\phi$ is the spin-splitting of the bottom of the conduction bands. Due to the ferromagnetic nature of the detecting electrode, the tunnelling current will depend on the relative orientation of the barrier and electrode

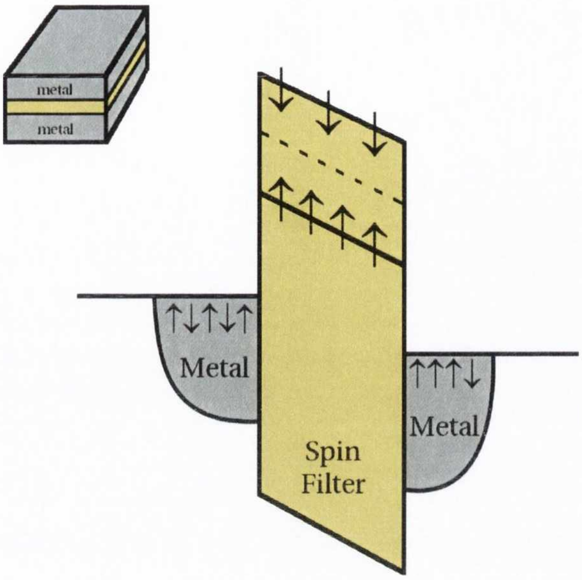

Figure 7.1: Schematic energy diagram for a spin filter consisting of a ferromagnetic barrier sandwiched between two metallic electrodes. The barrier height that an electron experiences upon tunneling is spin-dependent resulting in a spin polarised current. In principle, for thick junctions, this can lead to a 100% spin-polarized current.

magnetisations. The TMR of this spin filter can then be expressed as

$$TMR = \frac{2P_1 P_F}{1 - P_1 P_F},$$

in an extension of the Jullière model, where P_1 is the spin polarisation of the magnetic electrode. The spin filtering efficiency of a material is generally found experimentally in an indirect manner via a magnetoresistance measurement and the Jullière formula is then used to determine P_F. However, as we found in Chapter 4, the problem in reality is much more complex than what the Jullière model implies and the actual electronic structures of both the electrodes and barrier need to be taken into account.

A drawback to this approach of generating a highly spin polarised current is that ferromagnetic (or ferrimagnetic) insulators are rare, in particular at room temperature, and as such relatively little is known about them compared to ferromagnetic metals. An indication of the spin filter effect was first found in field emission experiments using tungsten tips coated with EuS [300, 301]. In this case, electrons tunnel from the Fermi level of tungsten into the exchange-split conduction band of EuS resulting in a spin polarisation of $\approx 90\%$ [302]. Subsequently, Moodera et al. measured the spin polarisation of the tunnelling current in a Au/EuS/Al tunnel junction using the Meservey-Tedrow technique [303]. Despite the lack of a magnetic source, a spin polarisation of approximately 80% is found. This is attributed to different barrier heights for the two spin directions. A tunnelling efficiency of $\approx 90\%$ was also found in a Al/EuS/Gd tunnel barrier [304]. The spin filter effect has also been found in EuSe [305] and in EuO [306]. As EuSe becomes ferromagnetic only under the application of a small applied magnetic field, the spin polarisation here displays an interesting field dependency: 0% at zero applied field and increasing to $\approx 100\%$ at 1T. The Eu chalcogenide group, including EuO, EuS and EuSe, suffers from the major disadvantage that magnetic ordering occurs at very low temperatures. The Curie temperature for EuS is 16.6K and 4.6K for EuSe. Although EuO offers a higher Curie temperature (69.3K) it is quite difficult to grow in high quality films. The Eu chalcogenide group is also poorly compatible with many of the commercially available electrode materials. This limits their potential to be incorporated into practical devices.

In contrast, much of the perovskite family can be simply incorporated into heterostructure devices. As a consequence, the search for high temperature ferromagnetic insulators was extended to the perovskites. $BiMnO_3$ is an insulating and ferromagnetic perovskite oxide, having an ordering temperature of ≈ 105K and a bulk magnetic moment of $3.6\mu_B$/f.u. [307], although this is much reduced when the material is in a thin film form. Gajek et al. [308] demonstrated a spin filtering efficiency of 22% using magneto-transport measurements in Au/$BiMnO_3$/LSMO junctions.

The spinel oxide family has also recently undergone intense study as a source of ferromagnetic insulators. Although they possess a complicated crystalline structure resulting in difficulties when creating high quality thin films, limited choice of ferromagnetic insulators has meant that the spinels are the best hope for creating room-temperature spin filters. Experiments have already shown significant spin filtering in $NiFe_2O_4$ and $CoFe_2O_4$. These two materials will be discussed in detail in this section, looking in particular at the disagreement between experimental measurements of their spin-filtering efficiency and that predicted by first principles calculations.

7.2.1 The Spinel Ferrites

$NiFe_2O_4$ has a high Curie temperature ($T_C \approx 850$K) and is insulating in its bulk form with a resistivity of 1kΩcm at room temperature [309]. $CoFe_2O_4$ is also a promising candidate for spin filtering applications due to a high Curie temperature of ≈ 793K along with high coercivity and good insulating properties. Thin films of $NiFe_2O_4$ and $CoFe_2O_4$ have been grown by sputtering [310], pulsed laser deposition [311] and molecular beam epitaxy [312]. Furthermore, epitaxial growth on MgO [313], $SrTiO_3$ [314, 315], $MgAl_2O_4$ [316] and Pt [315] have all been achieved.

The growth of the spinel ferrites as single crystals, avoiding dislocations and antiphase boundaries, presents many experimental difficulties. While a spinel substrate is available commercially, it has a large lattice mismatch with both $CoFe_2O_4$ and $NiFe_2O_4$. Epitaxial strain is known to lead to drastic changes in the magnetic and electrical properties of ferrite thin films; while $CoFe_2O_4$ is an inverse spinel in its bulk form, the degree of cationic inversion can be manipulated with strain [317].

Initial DFT studies of the spinel ferrites used the LDA or GGA as exchange-correlation functional. However, as we have seen, these approaches are not capable of describing the strongly correlated d-electrons in oxides and so erroneously describe the spinel ferrites as half metallic [318, 319, 320]. In order to correct this, LDA+U has been employed. Within this approximation both $CoFe_2O_4$ and $NiFe_2O_4$ are correctly described as insulators although $MnFe_2O_4$ remains half-metallic [321]. Hybrid density functionals have also being employed to good effect [322]. Szotek et al. used a Perdew-Zunger self-interaction corrected approach [323] to describe electronic correlations in these materials. They find $MnFe_2O_4$, Fe_3O_4, $CoFe_2O_4$ and $NiFe_2O_4$ to be all insulating in both their inverse and normal spinel structures [324].

Lüders et al. [325, 326] created an LSMO/$NiFe_2O_4$/Au spin filter and recorded a maximum TMR of about 50%. This corresponds to a spin filtering efficiency of 23%. This positive value of spin filtering was deemed to be surprising because the bottom of the conduction band in $NiFe_2O_4$ is predicted to be lower in energy for spin down than for spin up electrons [327, 324, 328]. They attributed the positive spin filtering polarity to wave function symmetry filtering effects: if the states at the top of the valence band and the bottom of the conduction band are comprised of different symmetries it is likely that certain electron wavefunctions will be transmitted with a higher probability than others. This symmetry selection process can either compete with or add to the filtering effect of the magnetic barrier and will depend on the materials involved and their band alignment. As such, it is very difficult to predict the resulting spin filtering efficiency based on simple effective mass models. Due to the discrepancy between the experimental results and theoretical predictions based on the the density of states, Lüders proposed that the symmetry selection filtering dominates over the influence of the barrier heights, at least for this particular combination of materials. However, at the time, no complex band structures were available for the spinel ferrites and so this explanation to date remains a hypothesis.

Structure

The unit cell of the spinel ferrites has a general formula AB_2O_4 and it is based on the face-centered cubic (fcc) unit cell with space group $Fd\bar{3}m$. The cations can be arranged over the A and B sites in two different ways. In the *normal* spinel structure divalent cations occupy the tetrahedrally coordinated (T_d) A sites, while the trivalent cations sit on the octrahedral (O_h) B sites. In the *inverse* spinel structure, the trivalent cations are equally distributed between the octrahedral and tetrahedral sites while the divalent cations occupy the remaining octrahedral ones. The choice of inverse or normal spinel structure depends on the ionic radii of the different species of the material in question. In practice, many materials adopt a mixture of both cationic arrangements depending on the growth conditions and film thicknesses. Considerable off-stoichiometry, disorder and defects are also common issues in the growth of spinels.

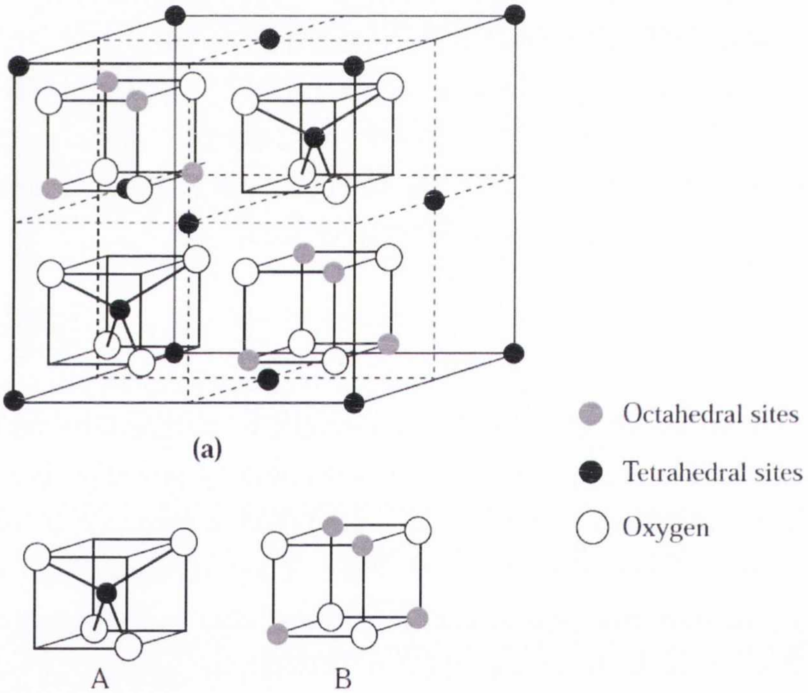

Figure 7.2: Schematic of the spinel unit cell structure showing the octrahedral and tetrahedral sites along with the A and B sub-cells. Figure taken from Ref. [329].

The $Fd\bar{3}m$ space group symmetry of the inverse spinels $NiFe_2O_4$ and $CoFe_2O_4$ requires that the divalent and trivalent cations are distributed randomly across the octrahedrally coordinated B sites. However, the use of periodic boundary conditions in our calculations would result in perfect long range cation order. One possibility to circumvent this problem is to use a very large unit cell so that a 'quasi-random' distribution could be modelled. Here, however, we choose to use the smallest possible unit cell that contains two spinel formula units. It was shown that this choice of unit cell and cation arrangement is sufficient to represent the true inverse spinel structure [330]. Two Fe cations are positioned on two of the B sites and the remaining two sites are filled with either Co or Ni, depending on the material under consideration. This artificial structure reduces the symmetry from space group $Fd\bar{3}m$ to $Imma$. In order to find the ground state lattice constants, while maintaining a good approximation to the $Fd\bar{3}m$ group symmetry, structural relaxations were carried out as follows:

- The lattice parameters, a, b and c, were constrained to be equal.
- All the A site cations are frozen in their ideal cubic positions with Wyckoff positions $4e$.
- Wyckoff positions $8i$ and $8h$ are allowed to relax.

The optimised lattice constants calculated using the GGA are shown in Table 7.1.

Lattice Constants (Å)	$NiFe_2O_4$	$CoFe_2O_4$
GGA	8.356	8.36
Expt. (Ref. [331])	8.339	8.392

Table 7.1: Optimised bulk lattice constants for $NiFe_2O_4$ and $CoFe_2O_4$ as calculated using the GGA in comparison with experimental data.

Magnetism

Using crystal field theory one can predict the spin arrangement of each of the cations. In octrahedral and tetrahedral environments, the Fe^{3+} and Co^{2+} cations can adopt either a high-spin or a low-spin configuration. However, experimentally only the high-spin states are observed. The ferrite spinels exhibit ferrimagnetic ordering consisting of two antiferromagnetically coupled sublattices (Néel-type ferrimagnetism): the first contains ferromagnetically ordered Fe^{3+} ($3d^3$) ions on the T_d A sites while the second contains ferromagnetically ordered Ni^{2+} ($3d^8$) or Co^{2+} ($3d^7$) and Fe^{3+} ($3d^3$) ions on the O_h B sites. The magnetic moments of the Fe^{3+} cations cancel so that the net magnetisation is a consequence of either the Ni^{2+} or Co^{2+} on the B sites. As a result, there is a net magnetic moment of $2\mu_B$/f.u. in $NiFe_2O_4$ and $3\mu_B$/f.u. in $CoFe_2O_4$.

7.2.2 Electronic Structure of $CoFe_2O_4$ and $NiFe_2O_4$

$NiFe_2O_4$

Fig. 7.3 shows the total and projected DOS for $NiFe_2O_4$ calculated using the GGA. It is immediately clear that, contrary to experimental evidence, $NiFe_2O_4$ is predicted to be metallic. This is due to the inaccurate description of the strongly correlated *d* electrons which are placed too high in energy close to the Fermi level. The shaded regions in Fig. 7.3 corresponds to the DOS projected onto the *d* orbitals of the three transition metal cations: $Ni(O_h)$, $Fe(T_d)$ and $Fe(O_h)$.

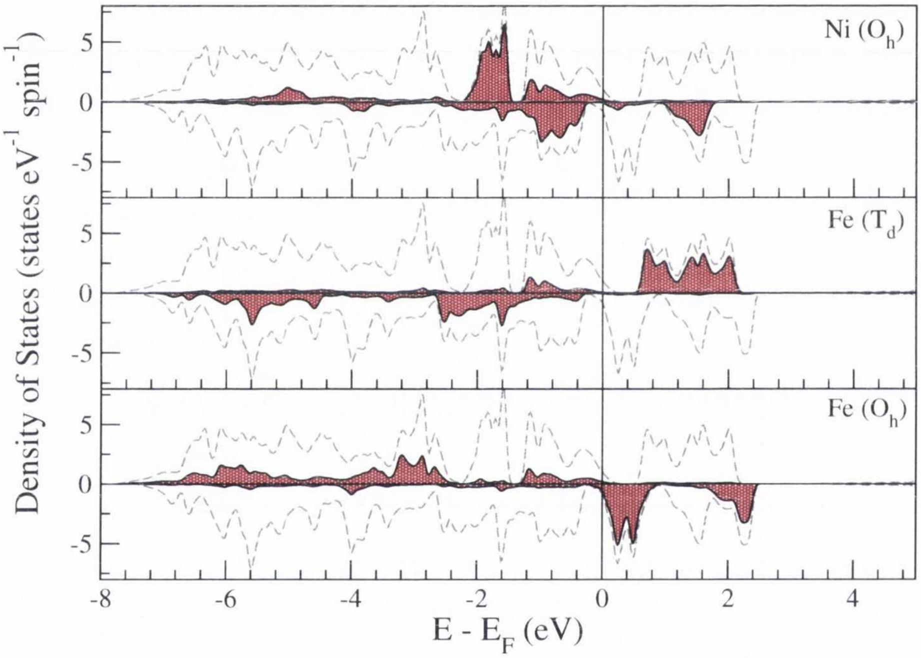

Figure 7.3: Total and projected DOS per formula unit for $NiFe_2O_4$ as calculated within the GGA. The total DOS is indicated by a dashed grey line in all panels. The Ni (O_h) states are shown in the top panel, the Fe (T_d) states are shown in the middle panel and the Fe (O_h) states are shown in the bottom panel.

Crystal field theory allows us to assign orbital information to the PDOS. The top panel shows that the majority $Ni(O_h)$ DOS is completely occupied while for the minority DOS, only the t_{2g} band is occupied with the e_g band located about ~1.5 eV above the Fermi level. This results in a magnetic moment of $1.596\mu_B$ on the Ni cations as expected from the d^8 configuration. The minority $Fe(T_d)$ DOS is completely occupied while the majority is completely unoccupied correlating well with a d^5 high-spin configuration. Comparing the middle and bottom panels, the antiferromagnetic ordering between the $Fe(T_d)$ and $Fe(O_h)$ sites is evident with the local majority spin direction on the $Fe(O_h)$ sites reversed relative to that on the

Fe(T$_d$) sites. In this case, the majority states are fully occupied and the minority t$_{2g}$ and e$_g$ states are empty. The result is that the magnetic moments of the Fe(T$_d$) and Fe(O$_h$) sites almost cancel (-4.251μ_B compared to +4.372μ_B) so that the major contribution to the net magnetic moment of 1.807μ_B is due to the Ni cation alone.

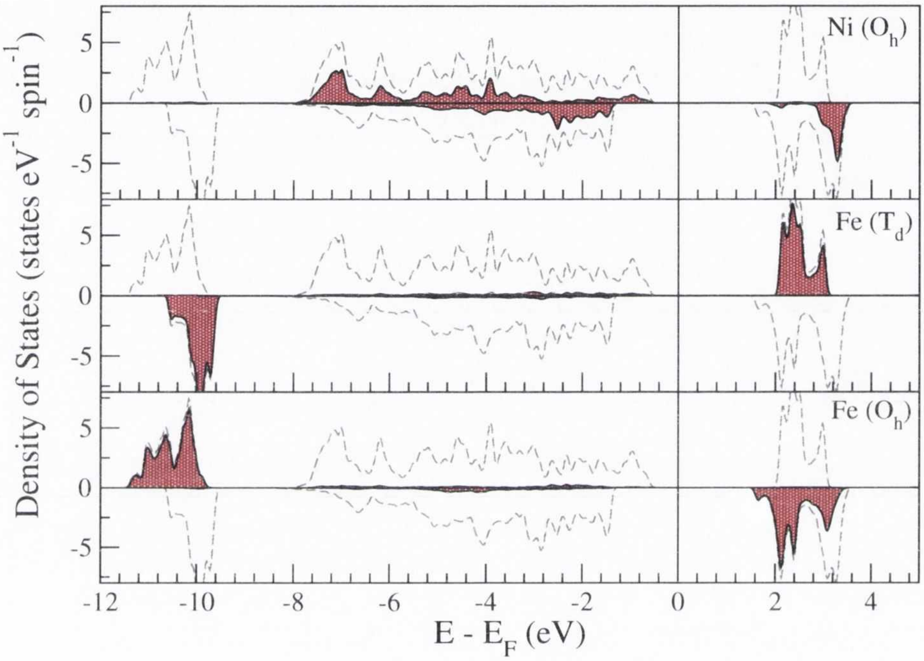

Figure 7.4: Total and projected DOS per formula unit for $NiFe_2O_4$as calculated within the ASIC approximation. The total DOS is indicated by a dashed line in all panels. The Ni (O$_h$) states are shown in the top panel, the Fe (T$_d$) states are shown in the middle panel and the Fe (O$_h$) states are shown in the bottom panel.

The use of the ASIC approximation opens a bandgap in $NiFe_2O_4$ so that is correctly described as an insulator. This can be seen in Fig. 7.4. The band gap of 1.97 eV is between a majority state at the top of the valence band and a minority state at the bottom of the conduction band. This gap is almost 1 eV bigger than that predicted by GGA+U (with U_{eff} = U - J = 3 eV) [330] and SIC-LSD [324]. We note however that experimental data on the bandgap is limited and the few available are spread over a wide energy range. Transmittance measurements found an energy gap of 3.78 eV at 78K in a 100nm $NiFe_2O_4$ thin film [332] whereas an optical band gap of 2.17 eV was found for nanocrystalline $NiFe_2O_4$ [333]. Also notable in the PDOS is the large energy gap between the filled Fe *d* states and the rest of the valence band which is comprised mostly of O 2*p* states. This gap between the Fe *d* and O *p* states is not seen with the GGA or GGA+U methods [330]. It can be seen however in other self interaction corrected methods [324]. In agreement with both the GGA+U [330] and SIC-LSD [324], the bottom of the conduction band is lower in energy for spin down than for spin up electrons. The local magnetic moments of the cations are shown in Table 7.2 as calculated with both the GGA and ASIC approach. The total magnetic moment of $NiFe_2O_4$ is $2\mu_B$ as expected. ASIC tends to increase the localisation of electrons on the magnetic cations resulting in an increased magnetic moment compared to GGA.

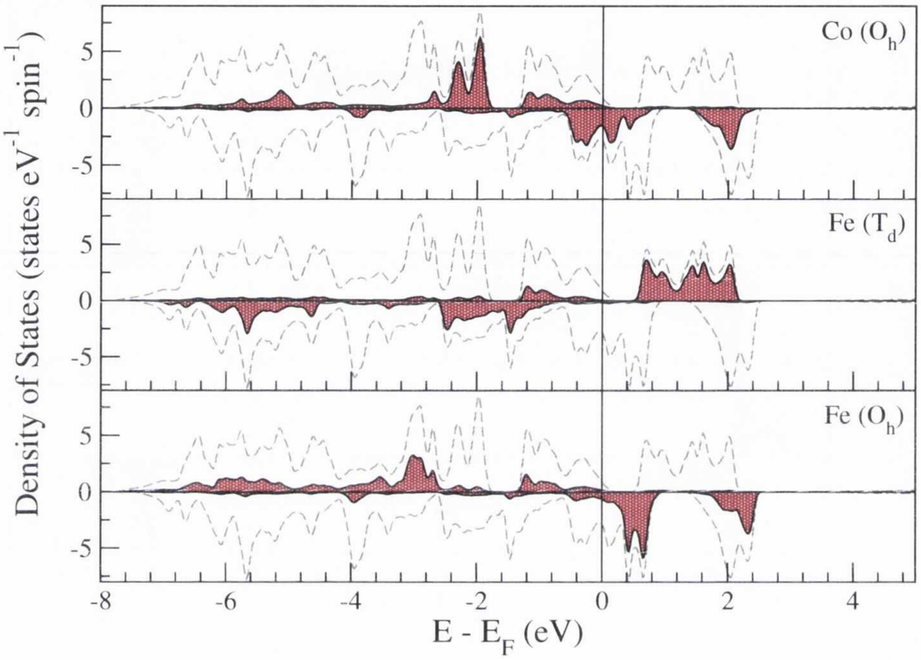

Figure 7.5: Total and projected DOS per formula unit for $CoFe_2O_4$ as calculated within the GGA. The total DOS is indicted by a dashed line in all panels. The Ni (O_h) states are shown in the top panel, the Fe (T_d) states are shown in the middle panel and the Fe (O_h) states are shown in the bottom panel.

$CoFe_2O_4$

The DOS of $CoFe_2O_4$ is presented in Fig. 7.5. Co^{2+} has formally one less electron compared to Ni^{2+} so that the minority t_{2g} orbitals are now only partially occupied. Within the GGA, $CoFe_2O_4$ is almost half-metallic with the minority Co $3d$ states positioned across the Fermi level and a gap of 0.3 eV in the majority states located just above it. The PDOS of the Fe cations is very similar to that in $NiFe_2O_4$.

The self-interaction corrected solution (Fig. 7.6) opens an energy gap between the occupied and unoccupied parts of the minority Co t_{2g} states resulting in an insulating ground state with a band gap of approximately 0.95 eV, similar to that predicted by GGA+U [330] and SIC-LSD [324] methods. Again, a wide range in bandgap energies has been found experimentally; a gap of 0.55 eV in $CoFe_2O_4$ was found by Jonker [334] using resistivity measurements, while Rai et al. [332] found a band gap of $\sim$ 1.53 eV.

The Fe $3d$ states are again separate from the O $2p$ states and are located at $\sim$ 11 eV below the Fermi level with a spin splitting of approximately 0.7 eV so that the bottom of the conduction band is lower in energy for spin down than for spin up electrons.

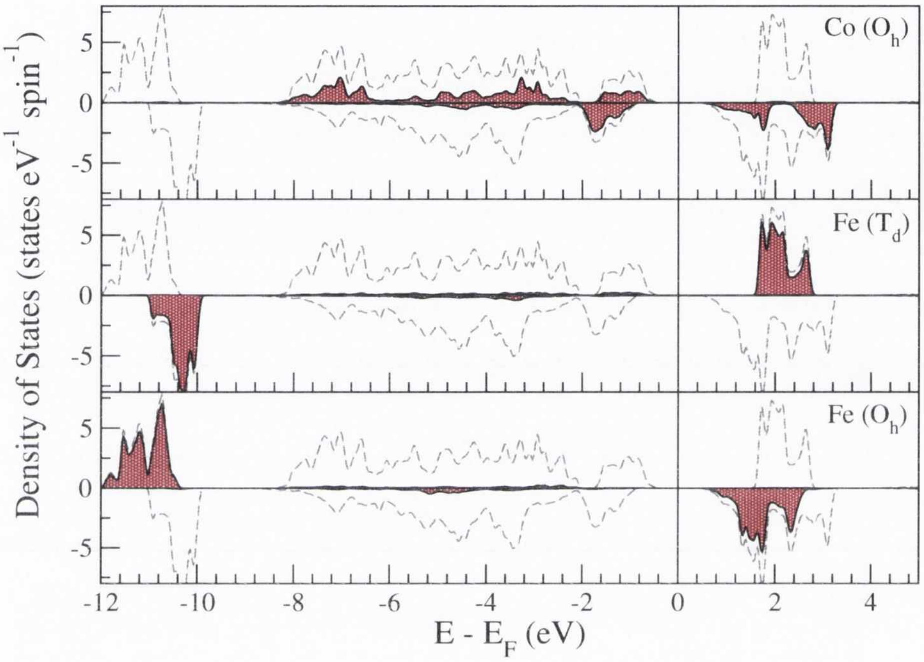

Figure 7.6: Total and projected DOS per formula unit for $CoFe_2O_4$as calculated within the ASIC approximation. The total DOS is indicated by a dashed line in all panels. The Ni (O$_h$) states are shown in the top panel, the Fe (T$_d$) states are shown in the middle panel and the Fe (O$_h$) states are shown in the bottom panel.

The total magnetic moment of $CoFe_2O_4$ is $3\mu_B$ within the ASIC approximation while GGA, yielding an incorrect metallic solution, results in a reduced magnetic moment of $2.894\mu_B$ (Table 7.2).

$NiFe_2O_4$	Ni (O_h)	Fe (O_h)	Fe (T_d)
GGA	1.258	3.635	-3.441
ASIC	1.596	4.372	-4.251

$CoFe_2O_4$	Co (O_h)	Fe (O_h)	Fe (T_d)
GGA	2.346	3.61	-3.396
ASIC	2.545	4.346	-4.22

Table 7.2: Calculated magnetic moments (in μ_B) for $NiFe_2O_4$ and $CoFe_2O_4$ using both the GGA and ASIC functionals.

We can thus conclude that the GGA is not sufficient to describe correctly the insulating ground state of either $NiFe_2O_4$ or $CoFe_2O_4$. ASIC succeeds in opening a band gap of almost 2 eV in $NiFe_2O_4$ and 0.95 eV in $CoFe_2O_4$. However, very few experiments have been carried out to determine the electronic structure of these spinel ferrites so that it is difficult to say which of the ASIC, GGA+U or SIC-LSD functionals offers the best electronic structure.

7.2.3 Complex Band Structure of $CoFe_2O_4$ and $NiFe_2O_4$

As we explained in the introduction, several experimental calculations of spin filtering efficiency in $NiFe_2O_4$ and $CoFe_2O_4$ have shown that the spin current density is higher for spin up electrons than for spin down electrons. This is not what one would expect from examining the DOS of these two materials which suggests that the energy barrier for tunnelling electrons is lower for spin down than for spin up electrons. It is clear that the detailed electronic structure of the insulating barrier of these experimental devices must play a role. Particularly important is their complex band structure which describes the energy dependence of the decay rates within the insulator.

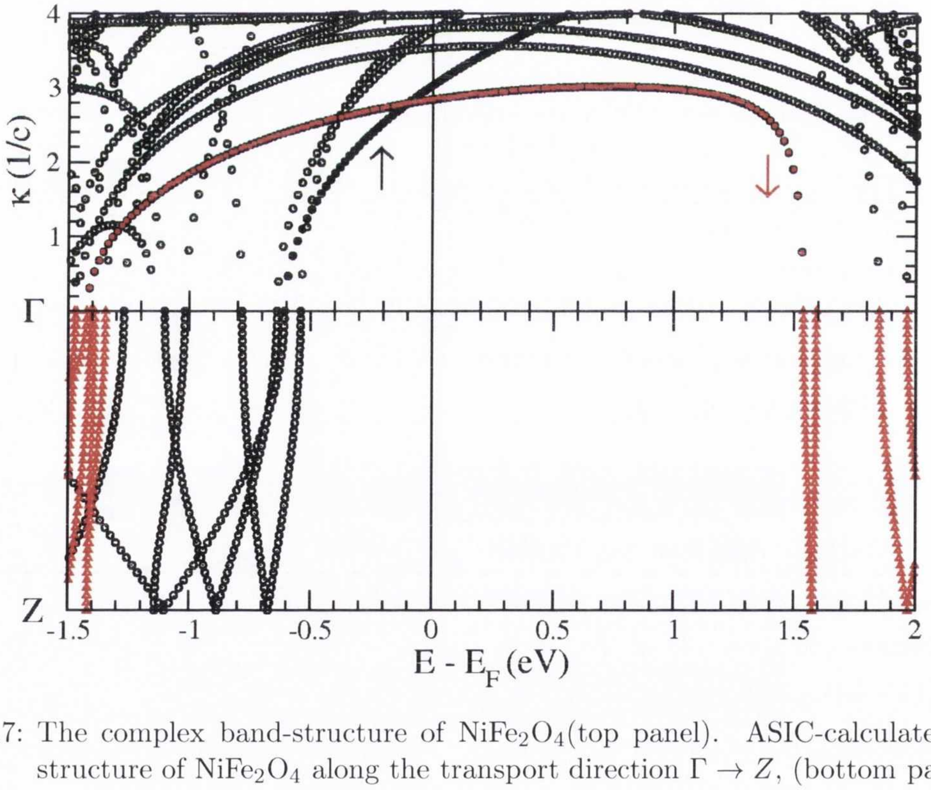

Figure 7.7: The complex band-structure of $NiFe_2O_4$(top panel). ASIC-calculated band-structure of $NiFe_2O_4$ along the transport direction $\Gamma \to Z$, (bottom panel).

In Fig. 7.7 we present the complex band structure of $NiFe_2O_4$ (top panel) along with the real band structure of the cubic unit cell (56 atoms) along the direction of transport, in this case (100). Close to the top of the valence band the slowest decay rate is given to majority electrons. This remains the case for approximately the next 0.5 eV into the band gap although the decay rate is increasing quickly with distance from the top of the valence band. At this stage however states with minority spin begin to decay at a slower rate. This decay rate remains almost constant for the remainder of the band gap.

Using this information, there are two possibilities for achieving the positive spin filtering efficiency found experimentally:

- If the Fermi level of the metallic electrodes is positioned within 0.5 eV of the top of the valence band the slowest decay rate will be for electrons with majority spin. The position of the Fermi level of the metal will depend on the band alignment between the two materials which can only be calculated with a full *ab initio* calculation of a heterostructure containing both materials.
- The electrode is half-metallic with only majority states available at the Fermi level. The result will be, despite the high decay rate for majority states, that transmission can only occur through these states.

This complex band structure is different to the one suggested in Ref. [335] where it was assumed that the top of the majority valence band was connected to the bottom of the majority conduction band via one complex band. This could occur if the states at the top of the valence band and the bottom of the conduction band had the same symmetry. However, in reality this is not the case.

The complex band structure for $CoFe_2O_4$ is shown in Fig. 7.8 along with the real band structure along the direction of transport. The smaller band gap of $CoFe_2O_4$ compared to that of $NiFe_2O_4$ results in slower decays within the band gap for both majority and minority spin. Similar to $NiFe_2O_4$, close to the top of the conduction band the slowest decay rate is for states with majority spin while close to the bottom of the conduction band the slowest decay rate is for states for minority spin.

Ramos et al. used a TMR measurement to reveal that $CoFe_2O_4$ was negatively spin polarised in a $Pt/CoFe_2O_4/\gamma\text{-}Al_2O_3/Co$ magnetic tunnel junction with a spin filter efficiency of -25% at low temperature [336]. This seems to agreed with *ab initio* calculations, including those presented here, predicting a lower tunnel barrier height for spin down electrons. However, the same group re-measured the spin filtering efficiency this time using the direct Meservey-Tedrow technique. They found the spin polarisation of $CoFe_2O_4$ in a $Pt/CoFe_2O_4/\gamma\text{-}Al_2O_3/Al$ tunnel junction [337] to vary from +6% to +26% depending on oxidation conditions during the growth of $CoFe_2O_4$. In an attempt to explain the discrepancy they noted two factors that differed between

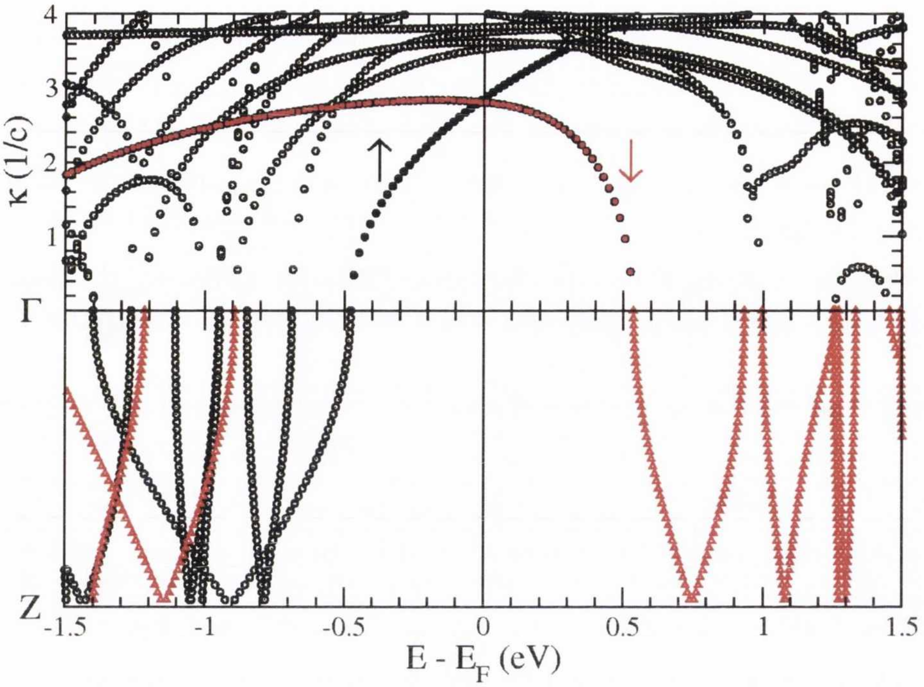

Figure 7.8: The complex band-structure of $CoFe_2O_4$(top panel). ASIC-calculated band-structure of $CoFe_2O_4$ along the transport direction $\Gamma \rightarrow Z$, (bottom panel).

the two experiments. The first is a difference in the applied bias voltage. It is much higher for the TMR experiment than for the Meservey-Tedrow experiment resulting in the transport there being governed by Fowler-Nordheim tunnelling [338]. The second is a change of detector electrode from Al to Co. They suggest that the Al detector electrode wave symmetry plays a dominant role, highlighting again the important role that the metallic electrodes play in these spin filter systems. Rigato et al. performed a point-contact Andreev refelection (PCAR) experiment by pressing a superconducting Nb tip on a $CoFe_2O_4/SrRuO_3$ thin-film bilayer [339]. They find, again, a positive spin filtering efficiency of $\approx$ 42% and suggest that the symmetry of the relevant wavefunctions may play a role. Finally, it is worth noting that magnetisation data acquired in thin films of $CoFe_2O_4$ and $NiFe_2O_4$ [340, 341] have shown that the cationic distribution may be very different to that found in the bulk crystal. This can have an important effect on the electronic structure of these materials which in turn will determine the sign of the spin polarisation. Szotek et al. showed that changing the cationic distribution in $CoFe_2O_4$ from the inverse spinel structure to the normal spinel structure can reduce the bandgap by approximately 75%.

7.2.4 Conclusions

We conclude that, contrary to expectation, the complex band structure does not resolve simply the discrepancies between the sign of the experimentally measured spin polarisation and that expected from *ab initio* density of states calculations. Both majority and minority states decay at different rates in $NiFe_2O_4$ and $CoFe_2O_4$, depending on the energies they are considered at. In order to completely elucidate the transport properties of tunnel junctions containing the spinel ferrites, it is not sufficient to examine the barrier material in isolation but rather in tandem with the electrode materials. The transport properties will be determined by the real and complex band structure of the electrodes and the insulating material and also by their band alignment in a heterostructure. Interface effects, such as interfacial bonding and defects, can also play an important role in the transport properties and cannot be neglected. A more detailed study should also consider the effects of thin film growth on the ferrite materials, as approximating it with the bulk structure may not be sufficient.

7.3 Influence of Asymmetric Electrodes on the Complex Band Structure of $BaTiO_3$

One of the most desirable properties of a ferroelectric tunnel junction is the substantial change in tunnelling transmission than can be achieved in response to minuscule changes in the ferroelectric tunnel barrier.

In Chapter 5 we discussed how the introduction of a thin dielectric layer at one interface can generate a large TER effect. In this section we consider whether such an effect could be created in an ferroelectric tunnel junction where asymmetry is introduced by using electrodes comprised of different materials. In particular, we investigate how the complex band structure of the ferroelectric material can be modified upon reversal of the electric polarisation.

In a ferroelectric tunnel junction, the electric field generated by the ferroelectric material is screened at the interface with the metallic electrodes. If the two electrodes have different screening lengths, the magnitude of polarisation pointing in one direction can differ significantly to that when the direction is reversed. If this occurs, the electronic properties of the barrier can be modified enough to elicit an appreciable tunnelling electroresistance effect.

Fe / $BaTiO_3$ / $SrRuO_3$ Tunnel Junction

We introduce asymmetry in the $SrRuO_3/BaTiO_3/SrRuO_3$ tunnel junction by replacing one of the electrodes with a different ferromagnetic material, in this case Fe. We

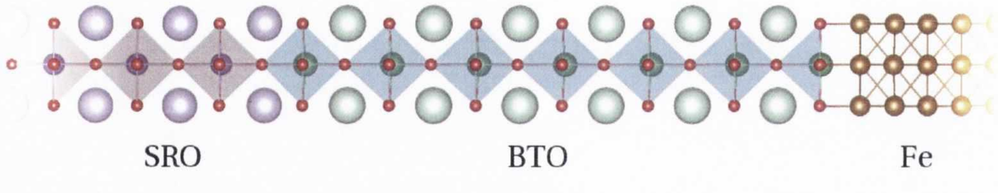

Figure 7.9: $SrRuO_3/BaTiO_3$/Fe heterostructure.

consider TiO_2 terminated $BaTiO_3$ so that the interfacial O atoms sit directly on top of the Fe atoms at one interface. The in-plane lattice constant is set to the calculated lattice constant of bulk $SrTiO_3$ (3.95Å). This results in a tetragonal distortion of both $SrRuO_3$ and Fe. A six unit cell thick $BaTiO_3$ layer is used while three unit cells of $SrRuO_3$ and six layers of Fe comprise the left and right electrodes respectively. The supercell used in our calculations is Fe_6 - TiO_2 - $(BaO - TiO_2)_6$ - $(SrO - RuO_2)_3$. A thick layer of vacuum is included between the two electrodes to isolate them from each other. In order to find both ferroelectronic ground states, two structures were initalised with the polarisation pointing in opposite directions. Both structures are then allowed to relax along the z-direction (i.e. along the stack direction) until the maximum force on the atoms was less than 10meV/Å. Fig. 7.9 shows the atomic structure of the asymmetric tunnel junction where the polarisation is pointing to the right (P$_\rightarrow$) into the Fe electrode.

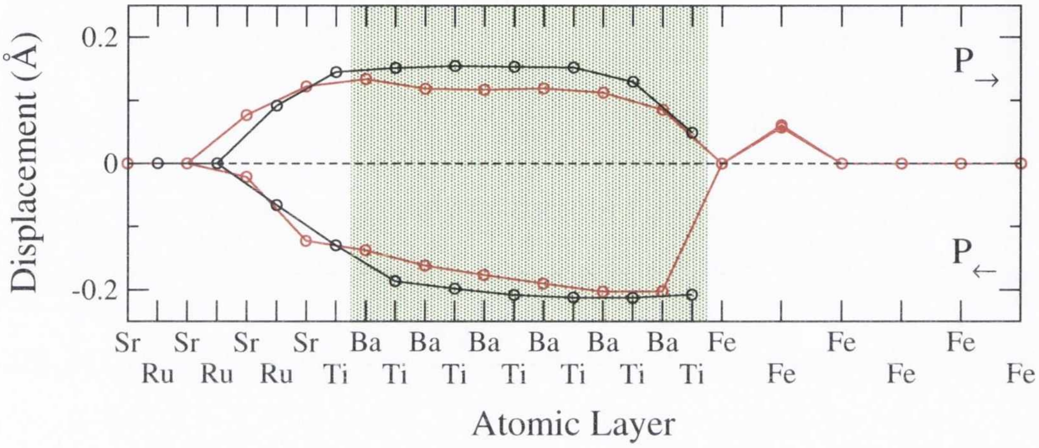

Figure 7.10: Displacements of A (=Sr, Ba), B (=Ru, Ti) and Fe atoms calculated with the GGA. Black symbols denote displacements of Ru and Ti. Open symbols denote displacements of Sr, Ba and Fe. The shaded area shows the BaTiO$_3$ region between the two interfaces.

Fig. 7.10 shows the layer by layer displacements between oxygens and cations along the supercell. The displacements in the perovskite materials are defined as $z_{cation} - z_O$ where z_{cation} and z_O denote the cation and oxygen positions in a particular plane. For the Fe layers, the displacement is defined as $z_{centre} - z_{corner}$, where z_{centre} and z_{corner} denote Fe atoms in the center and on the corner of the (001) unit cell, respectively.

Positive displacements refer to the P$_\rightarrow$ structure while negative displacements refer to the structure where the polarisation is pointing into the SrRuO$_3$ electrode (P$_\leftarrow$). It is evident that the magnitude of the displacements is much greater for P$_\leftarrow$ than for P$_\rightarrow$. For both structures, the polarisation achieves an approximately constant value at the centre of the ferroelectric layer. Using the displacements from such a central BaTiO$_3$ unit cell, we calculated a corresponding polarisation of 45.27μC/cm^2 for the P$_\leftarrow$ structure and 34.56μC/cm^2 for the P$_\rightarrow$ structure. Thus, when the polarisation points towards the SrRuO$_3$ electrode its magnitude is increased with respect to its bulk value (43.8μC/cm^2), while the polarisation is suppressed when the polarisation points towards the Fe electrode. The asymmetric structure results in an asymmetric double well potential profile (energy versus polarisation). It is more energetically favourable for the polarisation to point towards the SrRuO$_3$ electrode than towards the Fe electrode such that there is an energy difference of 0.36 eV between the two structures. The Ti displacements close to the BaTiO$_3$/Fe interface are dramatically suppressed for the $P_{\rightarrow}$ structure and slightly enhanced for the $P_{\leftarrow}$ structure. A suppression of the ferroelectric distortion is also predicted to occur in a Pt/PbTiO$_3$/SrRuO$_3$ heterostructure [217] when the polarisation points towards the Pt electrode although they did not consider the reverse polarisation.

Complex band structure

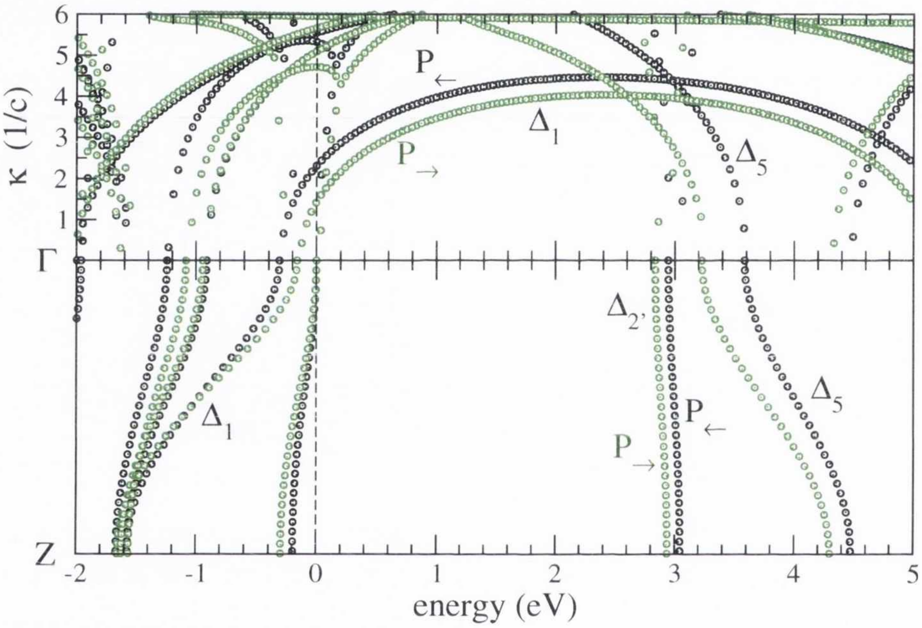

Figure 7.11: ASIC-calculated band-structure along the transport direction ($\Gamma \rightarrow Z$) for ferroelectric BaTiO$_3$ both in the $P_{\rightarrow}$ (green circles) and $P_{\leftarrow}$ (black circles) structure. The top panel reports the complex band-structure for BaTiO$_3$. Zero energy marks the top of the valence band.

Fig. 7.11 shows the slowest decay rates at E_F for both the $P_{\rightarrow}$ and $P_{\leftarrow}$ structures along with the corresponding real band structures along the direction of transport. Evanescent states with Δ_1 and Δ_5 symmetry have the slowest decay rates. In both cases states with $\Delta_{2'}$ symmetry make up the bottom of the conduction band although the decay rate for wavefunctions with this symmetry is extremely fast. In the cubic structure (space group $Pm\bar{3}m$) the $\Delta_{2'}$ state is degenerate with the Δ_5 state. The ferroelectric distortion splits the degeneracy so that states with Δ_5 symmetry (i.e., the d_{xz} and d_{yz} states) are pushed higher in energy. This increase in energy is proportional to the magnitude of the ferroelectric displacement. As a result of the increased energy gap between states with Δ_1 symmetry and Δ_5 symmetry the decay rate is significantly faster in the $P_{\leftarrow}$ structure.

As the decay of the wavefunction is given by $e^{-\kappa d}$, any change in κ can have an exponential influence on the transport properties. The thickness of the ferroelectric layer, d, can also impact on the tunnelling properties. An increase in the tetragonal distortion with increasing ferroelectric polarisation has been noted before. Here the thickness of the BaTiO$_3$ layer is larger for the $P_{\leftarrow}$ structure than for the $P_{\rightarrow}$ structure at 25.14Å and 24.84Å, respectively. The combination of the increased decay rate together with the increased barrier length should result in a smaller transmission when the polarisation points towards the SrRuO$_3$ layer than when it points towards the Fe electrode. As we saw in Chapter 5, any changes in the electrostatic potential and interfacial bonding is also likely to have a considerable influence on the transport.

In conclusion, we predict a large TER effect in such an asymmetric Fe / BaTiO$_3$ / SrRuO$_3$ tunnel junction. Due to the preferential polarisation direction, the ferroelectric displacements are noticeably different in both the $P_{\rightarrow}$ and $P_{\leftarrow}$ structures. As a result, the complex band structure changes depending on the direction of ferroelectric polarisation. It is predicted that this will have a big influence of the transport properties of such a device.

7.4 Conclusions

In this Chapter we considered how the complex band structure of a barrier material can influence the tunnelling properties of a junction.

We calculated the complex band structure of two spinel ferrites, $CoFe_2O_4$ and $NiFe_2O_4$, in order to understand their function as spin filters within tunnel barriers. Experiment has found a positive spin filtering efficiency for these materials. This is in contrast to what would be expected from the lower energy position of the bottom of the minority conduction band. It was suggested that symmetry selection in the ferrites could result in a lower decay rate for majority electrons. Our results suggest that the solution is not so simple and requires knowledge of the electronic structure of the electrodes as well as the barrier and ultimately a full *ab initio* calculation of the heterostructure is needed in order to determine the band alignment.

We also presented initial investigations into ferroelectric tunnel junctions comprised of asymmetric electrodes. We found that the asymmetric screening at the interfaces results in the magnitude of ferroelectric distortion being dependent on the direction of ferroelectric polarisation. This impacts on the complex band structure of $BaTiO_3$ which in turn determines the decay rate of tunnelling electrons through the barrier. We predict that this will have a significant influence of the transport properties of such an asymmetric tunnelling device and possibly generate an appreciable tunnelling electroresistance effect.

CHAPTER 8

Conclusions & Future Work

In summary, I have presented a first-principles study of spin-dependent transport in multifunctional oxide tunnel junctions. Due to concurrent improvements in both thin-film deposition techniques and the capabilities of *ab initio* calculations in addressing complex heterostructures, this branch of material science has experienced a surge of popularity in recent years. This has been driven, not only by interest in the fundamental physics at play, but also by the potential to engineer tunnel junctions with properties suitable for device applications. In this thesis, we examine the possibility of using functional barriers to manipulate the current tunnelling through them.

In chapter 2 we described briefly the theoretical formalism of both density functional theory and the NEGF method for transport calculations. These are powerful methods for computing the ground state properties of many-electrons systems and the quantum mechanical transport properties of nanoscale devices at finite bias, respectively. All transport calculations were carried out with the SMEAGOL code, which uses a tight binding-like Hamiltonian calculated with the SIESTA DFT code. The implemention details of both codes were briefly discussed.

Chapter 3 is a detailed discussion of the bulk properties of two materials, one ferromagnetic and one ferroelectric, that form the basis for much of the work in later chapters. $SrRuO_3$, an itinerant ferromagnetic metal, has been found experimentally to exhibit some of the hallmarks of strongly correlated electrons. We discussed the effects of strong electronic correlations in $SrRuO_3$, by comparing the electronic structure calculated with the LDA functional to that calculated with a self-interaction correction functional. We found that $SrRuO_3$ can be described as a moderately correlated ferromagnet. We also considered the choice of exchange-correlation functional on the electronic and structural properties of $BaTiO_3$, a prototypical ferroelectric. We found that the local functionals are capable of describing the ferroelectric transition adequately but fail to accurately describe the electronic structure. In particular we showed how the underestimation of the band gap can lead to errors if $BaTiO_3$ is included as a barrier material in a tunnel junction. We found that by correcting for the self-interaction error a much better agreement in electronic structure was found with experiments but the ferroelectric ground state structure was not correctly described. As a compromise, we chose to relax the structure by using the GGA functional and subsequently calculating the electronic, and transport, properties with the ASIC functional.

The spin-dependent transport properties of a $SrRuO_3/BaTiO_3/SrRuO_3$ tunnel junction were investigated in chapter 4. We showed that the electronic structure of $SrRuO_3$ has a dramatic effect on the tunnelling magnetoresistance effect in this junction. This is due to the the doubly-degenerate minority band alone available at the $SrRuO_3$ Fermi level, which results in the transport properties at zero bias being dominated by the tunnelling of minority carriers. We also considered the effect of the barrier electric state. We found that when in an paraelectric state, tunnelling electrons of both Δ_1 and Δ_5 symmetry decay at similar rates. This changes with ferroelectric ordering so that states with Δ_5 symmetry decay faster than states with Δ_1 symmetry. The TMR versus bias curve presented an interesting result - at low bias the magnetoresistance can reach enormous values. As the bias is increased, the TMR decreases monotonically eventually reaching zero. However, a further increase in bias causes the sign of the TMR to invert. Furthermore the sign inversion was found to occur at different voltages when altering the barrier electric state from paraelectric to ferroelectric. We conclude that it is possible to manipulate the TMR of a ferroelectric tunnel junction by controlling the ferroic state of the barrier. This opens a potential avenue for the electrical control of magnetic devices.

Chapter 5 extends the work of the previous chapter by considering the effect of structural asymmetry on the tunnelling current in a ferroelectric tunnel junction. In order achieve this goal, we considered a composite barrier combining a ferroelectric material and a dielectric one sandwiched between two symmetric ferromagnetic electrodes. We demonstrated a sizable TER effect that increases in a general exponential manner with the thickness of the dielectric layer. The TER effect is generated because of a dramatic change in the magnitude of the barrier height when the direction of polarisation is reversed. This change was attributed to the electrostatic potential of the dielectric material becoming pinned to the barrier height of the ferroelectric material. The TER can be manipulated by changing the thickness of the dielectric layer and it is much larger than any contribution that could arise from interfacial defects. The direction of ferroelectric polarisation can also be used to manipulate the TMR effect. We find a tunnelling electro-magnetoresistance effect of over 400%, in line with recent experimental observations. Due to the coexistence of the TMR and TER effects, we speculate that such a tunnel junction may become the basis of a novel four state memory device.

Spin-dependent tunnelling in a Ge/MgO/Fe tunnel junction was investigated in chapter 6. Such a structure has been considered experimentally as an important structure for the efficient and integrated electric detection of photon helicity at room temperature. If so, it would facilitate the integration of spintronics with existing logic solid-state devices. The variation of the spin polarised photocurrent induced in a Fe/MgO/Ge(001) heterojunction was determined experimentally to be of a similar magnitude for both electron and hole transport. As the spin-flip relaxation time for holes is significantly lower than that for electrons, this was not expected to be the case. One would expect the spin polarised current in forward bias (tunnelling electrons) to be higher than that for reverse bias (tunnelling holes). This unexpected behaviour can be explained by assuming that all electron transport occurs around the bottom of the conduction band. For the case of Ge, this is at the L point of the Brillouin Zone. Hole transport dominates the region of the Brillouin Zone around the Γ point. We showed that the transmission coefficient is significantly spin-polarised at Γ but much less so at L. As such, although the spin polarisation of holes decays relatively quickly compared to electrons, holes have a much higher initial spin polarisation. In this way, the fast decay rate of holes is compensated by their much larger spin polarisation at injection, so that the experimental results are explained.

Finally, in chapter 7 we showed in more detail how the complex band structure of a barrier material must be considered when describing the tunnelling properties of a junction. In the spinel ferrites, the complex band structure of these ferromagnetic insulators is vital to understand the experimental finding of a positive spin filtering efficiency. A density of states analysis of these materials would suggest the spin filtering efficiency should be negative. We showed that such analysis is too elementary and that the barrier can, in effect, filter a particular spin direction. This is a further confirmation of a recent theoretical breakthrough with regard to tunnel junctions: the spin polarisation of the tunnelling current is determined not only by the properties of the ferromagnetic electrodes but also by the electronic structure of the barrier material. We also discussed how asymmetric electrodes can influence the complex band structure of a ferroelectric barrier. We found that the magnitude of ferroelectric distortion is dependent on the direction of ferroelectric polarisation. This modifies the complex band structure which in turn determines the decay rate of tunnelling electrons through the barrier. We predict that this can generate an appreciable tunnelling electroresistance effect.

There are several lines of research arising from the work presented in this thesis which are the subject of on-going and future investigations. These are discussed briefly here:

In order to fully understand the transport characteristics of a ferroelectric tunnel junction, it is necessary to determine the effect of an applied bias. Asymmetry in the tunnel barrier potential profile for different polarisations should be reflected in various asymmetric features in the hysteretic behaviour of the tunnelling current. Some of these effects have been predicted using model calculations [210, 342] and found experimentally in junctions involving $BaTiO_3$ [236, 235] and $Pb(Zr_xTi_{1-x})O_3$ [238]. Extending the work presented in Chapter 5, the conductance of a asymmetric ferroelectric tunnel junction under the application of an external bias can be determined.

The majority of experimental research on ferroelectric tunnel junctions considers systems comprising of different electrode materials. To date, there has been no first-principles calculation of the transport properties of such a junction. In Chapter 7 we presented some initial structural and electronic calculations in a $Fe/BaTiO_3/SrRuO_3$ junction. On-going calculations aim to determine the transport properties of this junction.

The presence of defects in a Fe/MgO/Fe magnetic tunnel junction were found to drastically reduce the value of the TMR achieved [273]. In ferroelectric tunnel junctions the interface is predicted to play a vital role due to the subtle changes in interfacial electronic structure on the reversal of the electric polarisation. It is likely that the introduction of defects in such a junction could have a profound influence on both the TMR and TER effects and so it is a topic worthy of further investigation.

Chapters 4 and 5 considered the impact of the complex band structure on transport in ferroelectric tunnel junctions. However, further questions remain. In order to answer these conclusively, zero bias calculations are underway that directly compare transport in $SrRuO_3/BaTiO_3/SrRuO_3$ and $SrRuO_3/PbTiO_3/SrRuO_3$ tunnel junctions. All other parameters being equal, it should be possible to isolate the effect of the different complex band structures involved.

Finally, further questions remain about the sign of the spin polarisation in the spinel ferrites. Chapter 7 dealt with the possible impact of the complex band structure of these materials on the electronic transport. In order to explain the experimental results, we suggested that a calculation involving the junction in total is required. Using the information already aquired about the symmetry selection of the spinel ferrites, it should be possible to choose electrode materials in order to maximise the spin filtering efficiency. The spin-dependent conductance of such a device could then be determined.

To conclude, spin-dependent transport in magnetic tunnel junctions is a rapidly growing field of research. The possibility of technological progress is driving a deeper understanding of how spin polarisation can be created, maintained and manipulated in a wide variety of materials and revitalising the search for novel multifunctional materials.

Bibliography

[1] N. F. Mott. *Proceedings of the Royal Society of London. Series A - Mathematical and Physical Sciences* **153**, 699 (1936).

[2] B. Behin-Aein, D. Datta, S. Salahuddin, and S. Datta. *Nature Nanotechnology* **5**, 266 (2010).

[3] S. S. P. Parkin, M. Hayashi, and L. Thomas. *Science* **320**, 190 (2008).

[4] Z. Diao, Z. Li, S. Wang, Y. Ding, A. Panchula, E. Chen, L.-C. Wang, and Y. Huai. *Journal of Physics: Condensed Matter* **19**, 165209 (2007).

[5] O. V. Yazyev. *Reports on Progress in Physics* **73**, 056501 (2010).

[6] G. E. Moore. *Electronics Magazine* (1965).

[7] M. N. Baibich, J. M. Broto, A. Fert, F. N. Van Dau, F. Petroff, P. Etienne, G. Creuzet, A. Friederich, and J. Chazelas. *Physical Review Letters* **61**, 2472 (1988).

[8] G. Binasch, P. Grünberg, F. Saurenbach, and W. Zinn. *Physical Review B* **39**, 4828 (1989).

[9] C. Chappert, A. Fert, and F. N. Van Dau. *Nature Materials* **6**, 813–823 (2007).

[10] M. Julliere. *Physics Letters A* **54**, 225 (1975).

[11] T. Miyazaki and N. Tezuka. *Journal of Magnetism and Magnetic Materials* **139**, L231 (1995).

[12] Y. M. Lee, J. Hayakawa, S. Ikeda, F. Matsukura, and H. Ohno. *Applied Physics Letters* **90** (2007).

[13] U. Luders, A. Barthelemy, M. Bibes, K. Bouzehouane, S. Fusil, E. Jacquet, J.-P. Contour, J.-F. Bobo, J. Fontcuberta, and A. Fert. *Advanced Materials* **18**, 1733 (2006).

[14] S. Sanvito. *Chemical Society Reviews* **40**, 3336 (2011).

[15] S. Horiuchi, Y. Tokunaga, G. Giovannetti, S. Picozzi, H. Itoh, R. Shimano, R. Kumai, and Y. Tokura. *Nature* **463**, 789 (2010).

[16] J. M. Lopez-Encarnacion, J. D. Burton, E. Y. Tsymbal, and J. P. Velev. *Nano Letters* **11**, 599 (2011).

[17] A. Cottet, T. Kontos, S. Sahoo, H. T. Man, M.-S. Choi, W. Belzig, C. Bruder, A. F. Morpurgo, and C. Schnenberger. *Semiconductor Science and Technology* **21**, S78 (2006).

[18] A. Barthlmy and R. Mattana. In *Magnetism: A Synchrotron Radiation Approach*, volume 697 of *Lecture Notes in Physics*, 429. (2006).

[19] M. Bibes and A. Barthelemy. *Nature Materials* **7**, 425 (2008).

[20] S. Picozzi and C. Ederer. *Journal of Physics: Condensed Matter* **21**, 303201 (2009).

[21] N. A. Spaldin and M. Fiebig. *Science* **309**, 391 (2005).

[22] G. Schmidt. *Journal of Physics D: Applied Physics* **38**, R107 (2005).

[23] W. H. Butler, X.-G. Zhang, T. C. Schulthess, and J. M. MacLaren. *Physical Review B* **63**, 054416 (2001).

[24] J. Mathon and A. Umerski. *Physical Review B* **63**, 220403 (2001).

[25] R. Parr and W. Yang. *Density-functional theory of atoms and molecules.* International series of monographs on chemistry. Oxford University Press, (1994).

[26] R. M. Martin. *Electronic Structure: Basic Theory and Practical Methods.* International series of monographs on chemistry. Cambridge University Press, (2004).

[27] K. Burke. *The ABC of DFT.*

[28] M. Gell-Mann and K. A. Brueckner. *Physical Review* **106**, 364 (1957).

[29] M. Born and R. Oppenheimer. *Annalen der Physik* **389**, 457 (1927).

[30] R. Martin. *Electronic structure: basic theory and practical methods.* Cambridge University Press, (2004).

[31] P. Hohenberg and W. Kohn. *Physical Review* **136**, B864 (1964).

[32] W. Kohn and L. J. Sham. *Physical Review* **140**, A1133 (1965).

[33] U. von Barth and L. Hedin. *Journal of Physics C: Solid State Physics* **5**, 1629 (1972).

[34] L. M. Sandratskii. *physica status solidi (b)* **136**, 167 (1986).

[35] J. E. Peralta, G. E. Scuseria, and M. J. Frisch. *Physical Review B* **75**, 125119 (2007).

[36] J. P. Perdew and A. Zunger. *Physical Review B* **23**, 5048 (1981).

[37] D. M. Ceperley and B. J. Alder. *Physical Review Letters* **45**, 566 (1980).

[38] J. P. Perdew, K. Burke, and M. Ernzerhof. *Physical Review Letters* **77**, 3865 (1996).

[39] A. D. Becke. *Journal of Chemical Physics* **98**, 5648 (1993).

[40] P. J. Stephens, F. J. Devlin, C. F. Chabalowski, and M. J. Frisch. *The Journal of Physical Chemistry* **98**, 11623 (1994).

[41] V. I. Anisimov, F. Aryasetiawan, and A. I. Lichtenstein. *Journal of Physics: Condensed Matter* **9**, 767 (1997).

[42] Y. Zhang and W. Yang. *Journal of Chemical Physics* **109**, 2604 (1998).

[43] M. Stengel and N. A. Spaldin. *Physical Review B* **77**, 155106 (2008).

[44] J. A. Perdew and A. Zunger. *Physical Review B* **23**, 5048 (1981).

[45] C. D. Pemmaraju, T. Archer, D. Sánchez-Portal, and S. Sanvito. *Physical Review B* **75**, 045101 (2007).

[46] D. Vogel, P. Krüger, and J. Pollmann. *Physical Review B* **54**, 5495 (1996).

[47] A. Filippetti and N. A. Spaldin. *Physical Review B* **67**, 125109 (2003).

[48] T. Archer, C. D. Pemmaraju, S. Sanvito, C. Franchini, J. He, A. Filippetti, P. Delugas, D. Puggioni, V. Fiorentini, R. Tiwari, and P. Majumdar. *Physical Review B* **84**, 115114 (2011).

[49] A. Droghetti, C. D. Pemmaraju, and S. Sanvito. *Physical Review B* **81**, 092403 (2010).

[50] C. D. Pemmaraju, I. Rungger, X. Chen, A. R. Rocha, and S. Sanvito. *Physical Review B* **82**, 125426 (2010).

[51] J. F. Janak. *Physical Review B* **18**, 7165 (1978).

[52] L. J. Sham and M. Schlüter. *Physical Review Letters* **51**, 1888 (1983).

[53] J. M. Soler, E. Artacho, J. D. Gale, A. Garca, J. Junquera, P. Ordejn, and D. Snchez-Portal. *Journal of Physics: Condensed Matter* **14**, 2745 (2002).

[54] E. Artacho, E. Anglada, O. Diguez, J. D. Gale, A. Garca, J. Junquera, R. M. Martin, P. Ordejn, J. M. Pruneda, D. Snchez-Portal, and J. M. Soler. *Journal of Physics: Condensed Matter* **20**, 064208 (2008).

[55] E. Artacho, D. Snchez-Portal, P. Ordejn, A. Garca, and J. M. Soler. *physica status solidi (b)* **215**, 809 (1999).

[56] D. Snchez-Portal, P. Ordejn, E. Artacho, and J. M. Soler. *International Journal of Quantum Chemistry* **65**, 453 (1997).

[57] R. M. Martin. *Electronic Structure: Basic Theory and Practical Methods.* Cambridge University Press, (2004).

[58] W. E. and Pickett. *Computer Physics Reports* **9**, 115 (1989).

[59] N. Troullier and J. L. Martins. *Physical Review B* **43**, 1993 (1991).

[60] N. Troullier and J. L. Martins. *Physical Review B* **43**, 8861 (1991).

[61] D. R. Hamann, M. Schlüter, and C. Chiang. *Physical Review Letters* **43**, 1494 (1979).

[62] R. Landauer. *Philosophical Magazine* **21**, 863 (1970).

[63] M. Büttiker. *Physical Review Letters* **57**, 1761 (1986).

[64] S. Datta. *Nanotechnology* **15**, S433 (2004).

[65] R. Gebauer and R. Car. *Physical Review B* **70**, 125324 (2004).

[66] K. Burke, R. Car, and R. Gebauer. *Physical Review Letters* **94**, 146803 (2005).

[67] S. Datta. *Electronic transport in mesoscopic systems.* Cambridge studies in semiconductor physics and microelectronic engineering. Cambridge University Press, (1997).

[68] A. R. Rocha, V. M. Garcia-Suarez, S. Bailey, C. Lambert, J. Ferrer, and S. Sanvito. *Physical Review B* **73**, 085414 (2006).

[69] A. R. Rocha, V. M. Garcia-Suarez, S. Bailey, C. Lambert, J. Ferrer, and S. Sanvito. *Nature Materials* **4**, 335 (2005).

[70] Supriyo and Datta. *Superlattices and Microstructures* **28**, 253 (2000).

[71] M. Paulsson, F. Zahid, and S. Datta. *Resistance of a Molecule, Handbook of nanoscience, engineering, and technology.* Handbook of nanoscience, engineering, and technology. CRC Press, (2007).

[72] C. Caroli, R. Combescot, P. Nozieres, and D. Saint-James. *Journal of Physics C: Solid State Physics* **5**, 21 (1972).

[73] J. Ferrer, A. Martin-Rodero, and F. Flores. *Physical Review B* **38**, 10113 (1988).

[74] S. Sanvito, C. J. Lambert, J. H. Jefferson, and A. M. Bratkovsky. *Physical Review B* **59**, 11936 (1999).

[75] Y. Meir and N. S. Wingreen. *Physical Review Letters* **68**, 2512 (1992).

[76] M. M. Fadlallah, C. Schuster, U. Eckern, and U. Schwingenschloegl. *Europhysics Letters* **89**, 47003 (2010).

[77] I. Rungger, O. Mryasov, and S. Sanvito. *Physical Review B* **79**, 094414 (2009).

[78] C. Toher and S. Sanvito. *Physical Review B* **77**, 155402 (2008).

[79] A. R. Rocha, T. Archer, and S. Sanvito. *Physical Review B* **76**, 054435 (2007).

[80] A. Garca-Fuente, A. Vega, V. M. Garca-Surez, and J. Ferrer. *Nanotechnology* **21**, 095205 (2010).

[81] X. Shen, L. Sun, Z. Yi, E. Benassi, R. Zhang, Z. Shen, S. Sanvito, and S. Hou. *Physical Chemistry Chemical Physics* **12**, 10805 (2010).

[82] M. Koentopp, K. Burke, and F. Evers. *Physical Review B* **73**, 121403 (2006).

[83] C. Toher, A. Filippetti, S. Sanvito, and K. Burke. *Physical Review Letters* **95**, 146402 (2005).

[84] V. M. Goldschmidt. *Naturwissenschaften* **14**, 477 (1926).

[85] F. L. Marrec, A. Demuer, D. Jaccard, J.-M. Triscone, M. K. Lee, and C. B. Eom. *Applied Physics Letters* **80**, 2338 (2002).

[86] K. S. Takahashi, A. Sawa, Y. Ishii, H. Akoh, M. Kawasaki, and Y. Tokura. *Physical Review B* **67**, 094413 (2003).

[87] W. J. Gallagher and S. S. P. Parkin. *IBM Journal of Research and Development* **50**(1), 5–23 (2006).

[88] H. N. Lee, H. M. Christen, M. F. Chisholm, C. M. Rouleau, and D. H. Lowndes. *Applied Physics Letters* **84**, 4107 (2004).

[89] C. H. Ahn, R. H. Hammond, T. H. Geballe, M. R. Beasley, J.-M. Triscone, M. Decroux, O. Fischer, L. Antognazza, and K. Char. *Applied Physics Letters* **70**, 206 (1997).

[90] K. S. Takahashi, M. Gabay, D. Jaccard, K. Shibuya, T. Ohnishi, M. Lippmaa, and J.-M. Triscone. *Nature* **441**, 195 (2006).

[91] I. Zutić, J. Fabian, and S. D. Sarma. *Review of Modern Physics* **76**, 323 (2005).

[92] D. Awschalom and M. Flatte. *Nature Physics* **3**, 153 (2007).

[93] R. Ramesh and N. A. Spaldin. *Nature Materials* **6**, 21 (2007).

[94] A. Ohtomo, D. A. Muller, J. L. Grazul, and H. Y. Hwang. *Nature* **419**, 378–380 (2002).

[95] A. Ohtomo and H. Y. Hwang. *Nature* **427**, 423–426 (2004).

[96] H. Y. Hwang. *Science* **313**, 1895 (2006).

[97] M. Huijben, G. Rijnders, D. H. A. Blank, S. Bals, S. V. Aert, J. Verbeeck, G. V. Tendeloo, A. Brinkman, and H. Hilgenkamp. *Nature Materials* **5**, 556 (2006).

[98] H. Yamada, Y. Ogawa, Y. Ishii, H. Sato, M. Kawasaki, H. Akoh, and Y. Tokura. *Science* **305**, 646 (2004).

[99] J. M. De Teresa, A. Barthélémy, A. Fert, J. P. Contour, F. Montaigne, and P. Seneor. *Science* **286**, 507 (1999).

[100] A. Brinkman, M. Huijben, M. van Zalk, J. Huijben, U. Zeitler, J. C. Maan, W. G. van der Wiel, G. Rijnders, D. H. A. Blank, and H. Hilgenkamp. *Nature Materials* **6**, 493 (2007).

[101] D. Toyota, I. Ohkuba, H. Kumigashira, M. Oshima, T. Ohnishi, M. Lipmaa, M. Takizawa, A. Fujimori, K. Ono, M. Kawasaki, and H. Koinuma. *Applied Physics Letters* **87**, 162508 (2005).

[102] H.-D. Kim, H.-J. Noh, K. H. Kim, and S.-J. Oh. *Physical Review Letters* **93**, 126404 (2004).

[103] J. Park, S.-J. Oh, J.-H. Park, D. M. Kim, and C.-B. Eom. *Physical Review B* **69**, 085108 (2004).

[104] W. Siemons, G. Koster, A. Vailionis, H. Yamamoto, D. H. A. Blank, and M. R. Beasley. *Physical Review B* **76**, 075126 (2007).

[105] P. B. Allen, H. Berger, O. Chauvet, L. Forro, T. Jarlborg, A. Junod, B. Revaz, and G. Santi. *Physical Review B* **53**, 4393 (1996).

[106] P. Kostic, Y. Okada, N. C. Collins, Z. Schlesinger, J. W. Reiner, L. Klein, A. Kapitulnik, T. H. Geballe, and M. R. Beasley. *Physical Review Letters* **81**, 2498 (1998).

[107] G. Cao, S. McCall, M. Shepard, J. E. Crow, and R. P. Guertin. *Physical Review B* **56**, 321 (1997).

[108] K. Maiti. *Physical Review B* **73**, 235110 (2006).

[109] K. Maiti and R. S. Singh. *Physical Review B* **71**, 161102 (2005).

[110] H.-T. Jeng, S.-H. Lin, and C.-S. Hsue. *Physical Review Letters* **97**, 067002 (2006).

[111] A. T. Zayak, X. Huang, J. B. Neaton, and K. M. Rabe. *Physical Review B* **74**, 094104 (2006).

[112] N. Fukunaga and N. Tsuda. *Journal of the Physical Society of Japan* **63**, 3798 (1994).

[113] A. Kanbayasi. *Journal of the Physical Society of Japan* **41**, 1876 (1976).

[114] D. J. Singh. *Journal of Applied Physics* **79**, 4818 (1996).

[115] I. I. Mazin and D. J. Singh. *Physical Review B* **56**, 2556 (1997).

[116] G. Santi and T. Jarlborg. *Journal of Physics: Condensed Matter* **9**, 9563 (1997).

[117] W. Kohn and L. J. Sham. *Physical Review* **140**, A1133 (1965).

[118] J. M. Soler, E. Artacho, J. D. Gale, A. García, J. Junquera, P. Ordejón, and D. Sánchez-Portal. *Journal of Physics: Condensed Matter* **14**, 2745 (2002).

[119] D. Sánchez-Portal, P. Ordejón, E. Artacho, and J. M. Soler. *International Journal of Quantum Chemistry* **65**, 453–61 (1997).

[120] P. Ordejón, E. Artacho, and J. M. Soler. *Physical Review B* **53**, 10441 (1996).

[121] D. M. Ceperley and B. J. Alder. *Physical Review Letters* **45**, 566 (1980).

[122] L. Kleinman and D. M. Bylander. *Physical Review Letters* **48**, 1425 (1982).

[123] N. Troullier and J. L. Martins. *Physical Review B* **43**, 1993–2006 (1991).

[124] M. Stengel and N. A. Spaldin. *Physical Review B* **77**, 155106 (2008).

[125] R. S. Mulliken. **23**, 1833 (1955).

[126] C. W. Jones, P. D. Battle, P. Lightfoot, and W. T. A. Harrison. *Acta Crystallographica C* **45**, 365 (1989).

[127] J. Okamoto, T. Mizokawa, A. Fujimori, I. Hase, M. N ohara, H. Takagi, Y. Takeda, and M. Takano. *Physical Review B* **60**, 2281 (1999).

[128] K. Fujioka, J. Okamoto, T. Mizokawa, I. Fujimori, A. an d Hase, M. Abbate, H. J. Lin, C. T. Chen, Y. Takeda, and M. T akano. *Physical Review B* **56**, 6380 (1997).

[129] J. Okamoto, (2008). Unpublished data on new samples. The material preparation and characterization follows that outlined in J. Okamoto *et al.*, Phys. Rev. B **60**, 2281 (1999).

[130] Reused with permission from D. Toyota, Appl. Phys. Lett. **87** 162508 (2005). Copyright 2005, American Institute of Physics.

[131] J. Kim, J. Chung, and S.-J. Oh. *Physical Review B* **71**, 121406 (2005).

[132] H. Kumigashira, M. Minohara, M. Takizawa, A. Fujimori, D. Toyota, I. Ohkubo, M. Oshima, M. Lippmaa, and M. Kawasaki. *Applied Physics Letters* **92**, 122105 (2008).

[133] D. C. Worledge and T. H. Geballe. *Physical Review Letters* **85**, 5182 (2000).

[134] I. I. Mazin. *Physical Review Letters* **83**, 1427 (1999).

[135] J. M. D. Coey and S. Sanvito. *Journal of Physics D: Applied Physics* **37**, 988 (2004).

[136] A. F. Andreev. *Soviet physics, JETP* **19**, 1228 (1964).

[137] J. Soulen, R. J., J. M. Byers, M. S. Osofsky, B. . Nadgorny, T. Ambrose, S. F. Cheng, P. R. Broussard, C. T. Tanaka, J. N owak, J. S. Moodera, A. Barry, and J. M. D. Coey. *Science* **282**, 85 (1998).

[138] S. K. Upadhyay, A. Palanisami, and R. A. Louie, Richard N. an d Buhrman. *Physical Review Letters* **81**, 3247 (1998).

[139] P. Raychaudhuri, A. P. Mackenzie, J. W. Reiner, and M. R. Beasley. *Physical Review B* **67**, 020411 (2003).

[140] B. Nadgorny, M. S. Osofsky, D. J. Singh, G. T. Woods, J. R. J . Soulen, M. K. Lee, S. D. Bu, and C. B. Eom. *Applied Physics Letters* **82**, 427 (2003).

[141] J. Sanders, G. T. Woods, P. Poddar, H. Srikanth, B. D. ski, and S. Kolesnik. *49th Annual Conference on Magnetism and Magnetic Materials* **97**, 10C912 (2005).

[142] A. R. Rocha, V. M. Garcia-Suarez, S. Bailey, C. Lambert, J. Ferrer, and S. Sanvito. *Physical Review B* **73**, 085414 (2006).

[143] F. Taddei, S. Sanvito, and C. Lambert. *Journal of Low Temperature Physics* **124**, 305 (2001).

[144] M. Lines and A. M. Glass. *Principles and applications of ferroelectrics and related materials.* Oxford University Press, Oxford, (1977).

[145] B. Wul and J. M. Goldman. *Comptes Rendus Acad. Sci URSS* **46**, 139 (1945).

[146] P. Ghosez, X. Gonze, and J. P. Michenaud. *Ferroelectrics* **206**, 205 (1998).

[147] L. Landau and E. Lifshitz. *Statistical physics.* Course of theoretical physics. Pergamon Press, (1959).

[148] A. Devonshire. *Philosophical Magazine Series 7* **40**, 1040 (1949).

[149] A. Devonshire. *Philosophical Magazine Series 7* **42**, 1065 (1951).

[150] W. J. Merz. *Physical Review* **91**, 513 (1953).

[151] R. D. King-Smith and D. Vanderbilt. *Physical Review B* **47**, 1651 (1993).

[152] R. Resta and D. Vanderbilt. *Theory of Polarization: a modern approach.* Springer, Berlin, (2007).

[153] Z. Wu and R. E. Cohen. *Physical Review B* **73**, 235116 (2006).

[154] D. I. Bilc, R. Orlando, R. Shaltaf, G.-M. Rignanese, J. Íñiguez, and P. Ghosez. *Physical Review B* **77**, 165107 (2008).

[155] A. Stroppa and S. Picozzi. *Physical Chemistry Chemical Physics* **12**, 5405 (2010).

[156] Z. Wu, R. E. Cohen, and D. J. Singh. *Physical Review B* **70**, 104112 (2004).

[157] J. Junquera and P. Ghosez. *Nature* **422**, 506 (2003).

[158] J. P. Velev, C.-G. Duan, J. D. Burton, A. Smogunov, M. K. Niranjan, E. Tosatti, S. S. Jaswal, and E. Y. Tsymbal. *Nano Letters* **9**, 427 (2009).

[159] K. J. Choi, M. Biegalski, Y. L. Li, A. Sharan, J. Schubert, R. Uecker, P. Reiche, Y. B. Chen, X. Q. Pan, V. Gopalan, L.-Q. Chen, D. G. Schlom, and C. B. Eom. *Science* **306**, 1005 (2004).

[160] E. D. Specht, H.-M. Christen, D. P. Norton, and L. A. Boatner. *Physical Review Letters* **80**, 4317 (1998).

[161] S. K. Streiffer, J. A. Eastman, D. D. Fong, C. Thompson, A. Munkholm, M. V. Ramana Murty, O. Auciello, G. R. Bai, and G. B. Stephenson. *Physical Review Letters* **89**, 067601 (2002).

[162] J. H. Haeni, P. Irvin, W. Chang, R. Uecker, P. Reiche, Y. L. Li, S. Choudhury, W. Tian, M. E. Hawley, B. Craigo, A. K. Tagantsev, X. Q. Pan, S. K. Streiffer, L. Q. Chen, S. W. Kirchoefer, J. Levy, and D. G. Schlom. *Nature* **430**, 758 (2004).

[163] H. Tabata, H. Tanaka, and T. Kawai. *Applied Physics Letters* **65**, 1970 (1994).

[164] D. G. Schlom, L. Q. Chen, C. B. Eom, K. M. Rabe, S. K. Streiffer, and J. M. Triscone. *Annual Review of Materials Research* **37**, 589 (2007).

[165] O. Diéguez, S. Tinte, A. Antons, C. Bungaro, J. B. Neaton, K. M. Rabe, and D. Vanderbilt. *Physical Review B* **69**, 212101 (2004).

[166] K. M. Rabe. *Current Opinion in Solid State and Materials Science* **9**, 122 (2005).

[167] O. Diéguez, K. M. Rabe, and D. Vanderbilt. *Physical Review B* **72**, 144101 (2005).

[168] C. Ederer and N. A. Spaldin. *Physical Review Letters* **95**, 257601 (2005).

[169] G. H. Kwei, A. C. Lawson, S. J. L. Billinge, and S. W. Cheong. *The Journal of Physical Chemistry* **97**, 2368 (1993).

[170] F. M. Michel-Calendini and G. Mesnard. *Journal of Physics C: Solid State Physics* **6**, 1709 (1973).

[171] R. E. Cohen. *Nature* **358**, 136 (1992).

[172] P. Ghosez, X. Gonze, P. Lambin, and J.-P. Michenaud. *Physical Review B* **51**, 6765 (1995).

[173] A. Droghetti and S. Sanvito. *Applied Physics Letters* **94**, 252505 (2009).

[174] N. A. Hill. *The Journal of Physical Chemistry B* **104**, 6694 (2000).

[175] S. Parkin, C. Kaiser, A. Panchula, P. Rice, B. Hughes, M. Samant, and S. Yang. *Nature Materials* **3**, 862–867 (2004).

[176] S. Yuasa, T. Nagahama, A. Fukushima, Y. Suzuki, and K. Ando. *Nature Materials* **3**, 868–871 (2004).

[177] S. Ikeda, J. Hayakawa, Y. Ashizawa, Y. M. Lee, K. Miura, H. Hasegawa, M. Tsunoda, F. Matsukura, and H. Ohno. *Applied Physics Letters* **93**, 082508 (2008).

[178] T. Nagahama, T. S. Santos, and J. S. Moodera. *Physical Review Letters* **99**, 016602 (2007).

[179] M. Gajek, M. Bibes, S. Fusil, K. Bouzehouane, J. Fontcuberta, A. Barthelemy, and A. Fert. *Nature Materials* **6**, 296 (2007).

[180] V. Garcia, M. Bibes, L. Bocher, S. Valencia, F. Kronast, A. Crassous, X. Moya, S. Enouz-Vedrenne, A. Gloter, D. Imhoff, C. Deranlot, N. D. Mathur, S. Fusil, K. Bouzehouane, and A. Barthelemy. *Science* **327**, 1106 (2010).

[181] J. Wang, J. B. Neaton, H. Zheng, V. Nagarajan, S. B. Ogale, B. Liu, D. Viehland, V. Vaithyanathan, D. G. Schlom, U. V. Waghmare, N. A. Spaldin, K. M. Rabe, M. Wuttig, and R. Ramesh. *Science* **299**, 1719 (2003).

[182] T. Kimura, T. Goto, H. Shintani, K. Ishizaka, T. Arima, and Y. Tokura. *Nature* **426**, 55 (2003).

[183] N. Hur, S. Park, P. A. Sharma, J. S. Ahn, S. Guha, and S.-W. Cheong. *Nature* **429**, 392 (2004).

[184] I. Sosnowska, T. P. Neumaier, and E. Steichele. *Journal of Physics C: Solid State Physics* **15**, 4835 (1982).

[185] A. Ohtomo, D. A. Muller, J. L. Grazul, and H. Y. Hwang. *Nature* **419**, 378 (2002).

[186] J. B. Neaton, C.-L. Hsueh, and K. M. Rabe. *Materials Research Society Symposium Proceedings* **718**, 311 (2002).

[187] R. A. McKee, F. J. Walker, and M. F. Chisholm. *Physical Review Letters* **81**, 3014 (1998).

[188] J. Ryu, S. Priya, A. Carazo, K. Uchino, and H. Kim. *Journal of the Americal Ceramic Society* **84**, 2905–2908 (2001).

[189] G. Srinivasan, E. Rasmussen, A. Bush, K. Kamentsev, V. Meshcheryakov, and Y. Fetisov. *Applied Physics A: Materials Science & Processing* **78**, p721 – 728 (2004).

[190] H. Zheng, J. Wang, S. E. Lofland, Z. Ma, L. Mohaddes-Ardabili, T. Zhao, L. Salamanca-Riba, S. R. Shinde, S. B. Ogale, F. Bai, D. Viehland, Y. Jia, D. G. Schlom, M. Wuttig, A. Roytburd, and R. Ramesh. *Science* **303**, 661 (2004).

[191] P. Aguado-Puente and J. Junquera. *Physical Review Letters* **100**, 177601 (2008).

[192] Y. W. Cho, S. K. Choi, and G. V. Rao. *Applied Physics Letters* **86**, 202905 (2005).

[193] A. K. Tagantsev and I. A. Stolichnov. *Applied Physics Letters* **74**, 1326 (1999).

[194] A. K. Tagantsev, I. Stolichnov, E. L. Colla, and N. Setter. *Journal of Applied Physics* **90**, 1387 (2001).

[195] P. Ghosez and K. M. Rabe. *Applied Physics Letters* **76**, 2767 (2000).

[196] T. Tybell, C. H. Ahn, and J.-M. Triscone. *Applied Physics Letters* **75**, 856 (1999).

[197] D. J. Kim, J. Y. Jo, Y. S. Kim, Y. J. Chang, J. S. Lee, J.-G. Yoon, T. K. Song, and T. W. Noh. *Physical Review Letters* **95**, 237602 (2005).

[198] Y. S. Kim, D. H. Kim, J. D. Kim, Y. J. Chang, T. W. Noh, J. H. Kong, K. Char, Y. D. Park, S. D. Bu, J.-G. Yoon, and J.-S. Chung. *Applied Physics Letters* **86**, 102907 (2005).

[199] Y. S. Kim, J. Y. Jo, D. J. Kim, Y. J. Chang, J. H. Lee, T. W. Noh, T. K. Song, J.-G. Yoon, J.-S. Chung, S. I. Baik, Y.-W. Kim, and C. U. Jung. *Applied Physics Letters* **88**, 072909 (2006).

[200] J. C. Slonczewski. *Physical Review B* **39**, 6995 (1989).

[201] V. Heine. *Proceedings of the Physical Society* **81**, 300 (1963).

[202] P. Mavropoulos, N. Papanikolaou, and P. H. Dederichs. *Physical Review Letters* **85**, 1088 (2000).

[203] J. P. Velev, K. D. Belashchenko, D. A. Stewart, M. van Schilfgaarde, S. S. Jaswal, and E. Y. Tsymbal. *Physical Review Letters* **95**, 216601 (2005).

[204] H. Wang, J. P. Lewis, and O. F. Sankey. *Physical Review Letters* **93**, 016401 (2004).

[205] J. K. Tomfohr and O. F. Sankey. *Physical Review B* **65**, 245105 (2002).

[206] P. Pomorski, C. Roland, and H. Guo. *Physical Review B* **70**, 115408 (2004).

[207] F. Greullet, C. Tiusan, F. Montaigne, M. Hehn, D. Halley, O. Bengone, M. Bowen, and W. Weber. *Physical Review Letters* **99**, 187202 (2007).

[208] N. M. Caffrey, T. Archer, I. Rungger, and S. Sanvito. *Physical Review B* **83**, 125409 (2011).

[209] M. Y. Zhuravlev, R. F. Sabirianov, S. S. Jaswal, and E. Y. Tsymbal. *Physical Review Letters* **94**, 246802 (2005).

[210] H. Kohlstedt, N. A. Pertsev, J. Rodríguez Contreras, and R. Waser. *Physical Review B* **72**, 125341 (2005).

[211] C.-G. Duan, S. S. Jaswal, and E. Y. Tsymbal. *Physical Review Letters* **97**, 047201 (2006).

[212] M. Stengel and N. A. Spaldin. *Nature* **443**, 679–682 (2006).

[213] J. P. Velev, C.-G. Duan, K. D. Belashchenko, S. S. Jaswal, and E. Y. Tsymbal. *Physical Review Letters* **98**, 137201 (2007).

[214] J. Zhu, X. W. Wang, and S. G. Louie. *Physical Review B* **45**, 8887 (1992).

[215] J. Junquera, M. Zimmer, P. Ordejón, and P. Ghosez. *Physical Review B* **67**, 155327 (2003).

[216] G. Rijnders, D. H. A. Blank, J. Choi, and C.-B. Eom. *Applied Physics Letters* **84**, 505 (2004).

[217] M.-Q. Cai, Y. Zheng, P.-W. Ma, and C. H. Woo. *Journal of Applied Physics* **109**, 024103 (2011).

[218] G. Gerra, A. K. Tagantsev, N. Setter, and K. Parlinski. *Physical Review Letters* **96**, 107603 (2006).

[219] M. F. Chisholm, W. Luo, M. P. Oxley, S. T. Pantelides, and H. N. Lee. *Physical Review Letters* **105**, 197602 (2010).

[220] M. Fechner, I. V. Maznichenko, S. Ostanin, A. Ernst, J. Henk, and I. Mertig. *physica status solidi (b)* **247**, 1600 (2010).

[221] M. K. Niranjan, J. D. Burton, J. P. Velev, S. S. Jaswal, and E. Y. Tsymbal. *Applied Physics Letters* **95**, 052501 (2009).

[222] M. Stengel, P. Aguado-Puente, N. A. Spaldin, and J. Junquera. *Physical Review B* **83**, 235112 (2011).

[223] J. Junquera, M. H. Cohen, and K. M. Rabe. *Journal of Physics: Condensed Matter* **19**, 213203 (2007).

[224] J. Junquera and P. Ghosez. *Journal of Computational and Theoretical Nanoscience* **5**, 2071 (2008).

[225] T. Archer, N. M. Caffrey, and S. Sanvito. In preparation, (2011).

[226] J. M. Rondinelli, N. M. Caffrey, S. Sanvito, and N. A. Spaldin. *Physical Review B* **78**, 155107 (2008).

[227] A. Droghetti and S. Sanvito. *Applied Physics Letters* **94**, 252505 (2009).

[228] I. Rungger and S. Sanvito. *Physical Review B* **78**, 035407 (2008).

[229] C. Tiusan, F. Greullet, M. Hehn, F. Montaigne, S. Andrieu, and A. Schuhl. *Journal of Physics: Condensed Matter* **19**, 165201 (2007).

[230] L. Esaki, R. B. Laibowitz, and P. J. Stiles. *IBM Technical Disclosure Bulletin* **13**, 2161 (1971).

[231] Fujitsu Limited. www.fujitsu.com/global/services/microelectronics/product/memory/fram/. Accessed October 18, 2011.

[232] M. Hambe, A. Petraru, N. A. Pertsev, P. Munroe, V. Nagarajan, and H. Kohlstedt. *Advanced Functional Materials* **20**, 2436 (2010).

[233] M.-Q. Cai, Y. Du, and B.-Y. Huang. *Applied Physics Letters* **98**, 102907 (2011).

[234] E. Y. Tsymbal and H. Kohlstedt. *Science* **313**, 181 (2006).

[235] V. Garcia, S. Fusil, K. Bouzehouane, S. Enouz-Vedrenne, N. D. Mathur, A. Barthelemy, and M. Bibes. *Nature* **460**, 81 (2009).

[236] A. Gruverman, D. Wu, H. Lu, Y. Wang, H. W. Jang, C. M. Folkman, M. Y. Zhuravlev, D. Felker, M. Rzchowski, C.-B. Eom, and E. Y. Tsymbal. *Nano Letters* **9**, 3539 (2009).

[237] A. Crassous, V. Garcia, K. Bouzehouane, S. Fusil, A. H. G. Vlooswijk, G. Rispens, B. Noheda, M. Bibes, and A. Barthelemy. *Applied Physics Letters* **96**, 042901 (2010).

[238] P. Maksymovych, S. Jesse, P. Yu, R. Ramesh, A. P. Baddorf, and S. V. Kalinin. *Science* **324**, 1421 (2009).

[239] M. Y. Zhuravlev, S. Maekawa, and E. Y. Tsymbal. *Physical Review B* **81**, 104419 (2010).

[240] M. Y. Zhuravlev, Y. Wang, S. Maekawa, and E. Y. Tsymbal. *Applied Physics Letters* **95**, 052902 (2009).

[241] Y.-Z. Wu, S. Ju, and Z.-Y. Li. *Applied Physics Letters* **96**, 252905 (2010).

[242] H. J. Monkhorst and J. D. Pack. *Physical Review B* **13**, 5188 (1976).

[243] D. Wortmann and S. Blügel. *Physical Review B* **83**, 155114 (2011).

[244] G. Gerra, A. K. Tagantsev, N. Setter, and K. Parlinski. *Physical Review Letters* **96**, 107603 (2006).

[245] K. A. Müller and H. Burkard. *Physical Review B* **19**, 3593 (1979).

[246] C. Ang, Z. Yu, P. M. Vilarinho, and J. L. Baptista. *Physical Review B* **57**, 7403 (1998).

[247] N. A. Pertsev, A. K. Tagantsev, and N. Setter. *Physical Review B* **61**, R825 (2000).

[248] V. Garcia, M. Bibes, L. Bocher, S. Valencia, F. Kronast, A. Crassous, X. Moya, S. Enouz-Vedrenne, A. Gloter, D. Imhoff, C. Deranlot, N. D. Mathur, S. Fusil, K. Bouzehouane, and A. Barthlmy. *Science* **327**, 1106 (2010).

[249] S. Valencia, A. Crassous, L. Bocher, V. Garcia, X. Moya, R. O. Cherifi, C. Deranlot, K. Bouzehouane, S. Fusil, A. Zobelli, A. Gloter, N. D. Mathur, A. Gaupp, R. Abrudan, F. Radu, A. Barthlmy, and M. Bibes. *Nature Materials* **10**, 753 (2011).

[250] J. M. Kikkawa and D. D. Awschalom. *Physical Review Letters* **80**, 4313 (1998).

[251] G. Schmidt, D. Ferrand, L. W. Molenkamp, A. T. Filip, and B. J. van Wees. *Physical Review B* **62**, R4790 (2000).

[252] A. Fert and H. Jaffrès. *Physical Review B* **64**, 184420 (2001).

[253] E. I. Rashba. *Physical Review B* **62**, R16267 (2000).

[254] V. F. Motsnyi, J. D. Boeck, J. Das, W. V. Roy, G. Borghs, E. Goovaerts, and V. I. Safarov. *Applied Physics Letters* **81**, 265 (2002).

[255] X. Jiang, R. Wang, R. M. Shelby, R. M. Macfarlane, S. R. Bank, J. S. Harris, and S. S. P. Parkin. *Physical Review Letters* **94**, 056601 (2005).

[256] A. Dimoulas, P. Tsipas, A. Sotiropoulos, and E. K. Evangelou. *Applied Physics Letters* **89**, 252110 (2006).

[257] Y. Zhou, M. Ogawa, X. Han, and K. L. Wang. *Applied Physics Letters* **93**, 202105 (2008).

[258] G. Lampel. *Physical Review Letters* **20**, 491 (1968).

[259] S. A. Wolf, D. D. Awschalom, R. A. Buhrman, J. M. Daughton, S. von Molnr, M. L. Roukes, A. Y. Chtchelkanova, and D. M. Treger. *Science* **294**, 1488 (2001).

[260] M. Oestreich, J. Hbner, D. Hgele, M. Bender, N. Gerhardt, M. Hofmann, W. Rhle, H. Kalt, T. Hartmann, P. Klar, W. Heimbrodt, and W. Stolz. In *Advances in Solid State Physics*, B. Kramer, ed., volume 41 of *Advances in Solid State Physics*, 173. Springer Berlin / Heidelberg (2001).

[261] S. Hvel, N. C. Gerhardt, M. R. Hofmann, F.-Y. Lo, D. Reuter, A. D. Wieck, E. Schuster, H. Wende, and W. Keune. *physica status solidi (c)* **6**, 436 (2009).

[262] I. Žutić, J. Fabian, and S. Das Sarma. *Review of Modern Physics* **76**, 323 (2004).

[263] R. Fiederling, M. Keim, G. Reuscher, W. Ossau, G. Schmidt, A. Waag, and L. W. Molenkamp. *Nature* **402**, 787 (1999).

[264] Y. Ohno, D. K. Young, B. Beschoten, F. Matsukura, H. Ohno, and D. D. Awschalom. *Nature* **402**, 790 (1999).

[265] O. M. J. van 't Erve, G. Kioseoglou, A. T. Hanbicki, C. H. Li, B. T. Jonker, R. Mallory, M. Yasar, and A. Petrou. *Applied Physics Letters* **84**, 4334 (2004).

[266] V. F. Motsnyi, P. Van Dorpe, W. Van Roy, E. Goovaerts, V. I. Safarov, G. Borghs, and J. De Boeck. *Physical Review B* **68**, 245319 (2003).

[267] A. Hirohata, Y. B. Xu, C. M. Guertler, and J. A. C. Bland. *Journal of Applied Physics* **85**, 5804 (1999).

[268] T. Taniyama, G. Wastlbauer, A. Ionescu, M. Tselepi, and J. A. C. Bland. *Physical Review B* **68**, 134430 (2003).

[269] M. Cantoni, D. Petti, C. Rinaldi, and R. Bertacco. *Microelectronic Engineering* **88**, 530 (2011).

[270] W. Han, Y. Zhou, Y. Wang, Y. Li, J. Wong, K. Pi, A. Swartz, K. McCreary, F. Xiu, K. L. Wang, J. Zou, and R. Kawakami. *Journal of Crystal Growth* **312**, 44 (2009).

[271] K.-R. Jeon, C.-Y. Park, and S.-C. Shin. *Crystal Growth and Design* **10**, 1346 (2010).

[272] D. M. Roessler and W. C. Walker. *Physical Review* **159**, 733 (1967).

[273] I. Rungger. *Computational methods for electron transport and their application in nanodevices.* PhD thesis, University of Dublin, Trinity College, (2008).

[274] C. Tusche, H. L. Meyerheim, N. Jedrecy, G. Renaud, A. Ernst, J. Henk, P. Bruno, and J. Kirschner. *Physical Review Letters* **95**, 176101 (2005).

[275] H. L. Meyerheim, R. Popescu, N. Jedrecy, M. Vedpathak, M. Sauvage-Simkin, R. Pinchaux, B. Heinrich, and J. Kirschner. *Physical Review B* **65**, 144433 (2002).

[276] H. L. Meyerheim, R. Popescu, J. Kirschner, N. Jedrecy, M. Sauvage-Simkin, B. Heinrich, and R. Pinchaux. *Physical Review Letters* **87**, 076102 (2001).

[277] C. Wang, A. Kohn, S. G. Wang, L. Y. Chang, S.-Y. Choi, A. I. Kirkland, A. K. Petford-Long, and R. C. C. Ward. *Physical Review B* **82**, 024428 (2010).

[278] C. Tusche, H. L. Meyerheim, N. Jedrecy, G. Renaud, and J. Kirschner. *Physical Review B* **74**, 195422 (2006).

[279] D. Wortmann, G. Bihlmayer, and S. Blgel. *Journal of Physics: Condensed Matter* **16**, S5819 (2004).

[280] T. Urano and T. Kanaji. *Journal of the Physical Society of Japan* **57**, 3403 (1988).

[281] H. Oh, S. B. Lee, J. Seo, H. G. Min, and J.-S. Kim. *Applied Physics Letters* **82**, 361 (2003).

[282] Y. Dedkov, M. Fonin, U. Rdiger, and G. Gntherodt. *Applied Physics A: Materials Science & Processing* **82**, 489 (2006).

[283] X.-G. Zhang, W. H. Butler, and A. Bandyopadhyay. *Physical Review B* **68**, 092402 (2003).

[284] P. Bose, A. Ernst, I. Mertig, and J. Henk. *Physical Review B* **78**, 092403 (2008).

[285] M. Sicot, S. Andrieu, P. Turban, Y. Fagot-Revurat, H. Cercellier, A. Tagliaferri, C. De Nadai, N. B. Brookes, F. Bertran, and F. Fortuna. *Physical Review B* **68**, 184406 (2003).

[286] L. Plucinski, Y. Zhao, B. Sinkovic, and E. Vescovo. *Physical Review B* **75**, 214411 (2007).

[287] S. Yuasa and D. D. Djayaprawira. *Journal of Physics D: Applied Physics* **40**, R337 (2007).

[288] F. J. Palomares, C. Munuera, C. M. Boubeta, and A. Cebollada. *Journal of Applied Physics* **97**, 036104 (2005).

[289] W.-Y. Hsu and R. Raj. *Applied Physics Letters* **60**, 3105 (1992).

[290] D. Petti, M. Cantoni, C. Rinaldi, S. Brivio, R. Bertacco, J. Gazquez, and M. Varela. *Journal of Applied Physics* **109**, 084909 (2011).

[291] C. Wang, S. Wang, A. Kohn, R. C. C. Ward, and A. K. Petford-Long. *IEEE Transactions on Magnetics* **43**, 2779–2781 (2007).

[292] E. J. Loren, B. A. Ruzicka, L. K. Werake, H. Zhao, H. M. van Driel, and A. L. Smirl. *Applied Physics Letters* **95**, 092107 (2009).

[293] S. Patibandla, G. Atkinson, S. Bandyopadhyay, and G. Tepper. *Physica E: Low-dimensional Systems and Nanostructures* **42**, 1721 (2010).

[294] G. Mak and H. M. van Driel. *Physical Review B* **49**, 16817 (1994).

[295] J. Park, E. Vescovo, H. Kim, C. Kwon, R. Ramesh, and T. Venkatesan. *Nature* **392**, 794–796 (1998).

[296] M. Bowen, M. Bibes, A. Barthelemy, J. Contour, A. Anane, Y. Lemaitre, and A. Fert. *Applied Physics Letters* **82**, 233 (2003).

[297] R. P. Borges, R. M. Thomas, C. Cullinan, J. M. D. Coey, R. Suryanarayanan, L. Ben-Dor, L. Pinsard-Gaudart, and A. Revcolevschi. *Journal of Physics: Condensed Matter* **11**, L445 (1999).

[298] J. G. Simmons. *Journal of Applied Physics* **34**, 1793 (1963).

[299] M. Bibes, J. E. Villegas, and A. Barthlmy. *Advances in Physics* **60**, 5 (2011).

[300] L. Esaki, P. J. Stiles, and S. v. Molnar. *Physical Review Letters* **19**, 852 (1967).

[301] N. Müller, W. Eckstein, W. Heiland, and W. Zinn. *Physical Review Letters* **29**, 1651 (1972).

[302] G. Baum, E. Kisker, A. Mahan, W. Raith, and B. Reihl. *Applied Physics A: Materials Science & Processing* **14**, 149 (1977).

[303] J. S. Moodera, X. Hao, G. A. Gibson, and R. Meservey. *Physical Review Letters* **61**, 637 (1988).

[304] P. LeClair, J. Ha, H. Swagten, J. Kohlhepp, C. van de Vin, and W. de Jonge. *Applied Physics Letters* **80**, 625 (2002).

[305] J. S. Moodera, R. Meservey, and X. Hao. *Physical Review Letters* **70**, 853 (1993).

[306] T. S. Santos and J. S. Moodera. *Physical Review B* **69**, 241203 (2004).

[307] H. Chiba, T. Atou, and Y. Syono. *Journal of Solid State Chemistry* **132**, 139 (1997).

[308] M. Gajek, M. Bibes, A. Barthélémy, K. Bouzehouane, S. Fusil, M. Varela, J. Fontcuberta, and A. Fert. *Physical Review B* **72**, 020406 (2005).

[309] A. Cormack, G. Lewis, S. Parker, and C. Catlow. *Journal of Physics and Chemistry of Solids* **49**, 53 (1988).

[310] N. Dix, V. Skumryev, V. Laukhin, L. Fbrega, F. Snchez, and J. Fontcuberta. *Materials Science and Engineering: B* **144**, 127 (2007).

[311] M. Terzzoli, S. Duhalde, S. Jacobo, L. Steren, and C. Moina. *Journal of Alloys and Compounds* **369**, 209 (2004).

[312] A. V. Ramos, J.-B. Moussy, M.-J. Guittet, M. Gautier-Soyer, C. Gatel, P. Bayle-Guillemaud, B. Warot-Fonrose, and E. Snoeck. *Physical Review B* **75**, 224421 (2007).

[313] T. Nagahama, H. Kubota, and S. Yuasa. *Thin Solid Films* **519**, 8239 (2011).

[314] Y. Zhang, J. Liu, Y. Lin, and C.-W. Nan. *Journal of Physics D: Applied Physics* **42**, 135413 (2009).

[315] U. Lders, M. Bibes, J. Bobo, and J. Fontcuberta. *Applied Physics A: Materials Science & Processing* **80**, 427 (2005).

[316] M. N. Iliev, D. Mazumdar, J. X. Ma, A. Gupta, F. Rigato, and J. Fontcuberta. *Physical Review B* **83**, 014108 (2011).

[317] D. Fritsch and C. Ederer. *Applied Physics Letters* **99**, 081916 (2011).

[318] H.-T. Jeng and G. Guo. *Journal of Magnetism and Magnetic Materials* **239**, 88 (2002).

[319] H.-T. Jeng and G. Guo. *Journal of Magnetism and Magnetic Materials* **240**, 436 (2002).

[320] D. J. Singh, M. Gupta, and R. Gupta. *Physical Review B* **65**, 064432 (2002).

[321] V. N. Antonov, B. N. Harmon, and A. N. Yaresko. *Physical Review B* **67**, 024417 (2003).

[322] X. Zuo and C. Vittoria. *Physical Review B* **66**, 184420 (2002).

[323] J. Dobson, G. Vignale, and M. Das. *Electronic density functional theory: recent progress and new directions.* Plenum Press, (1998).

[324] Z. Szotek, W. M. Temmerman, D. Ködderitzsch, A. Svane, L. Petit, and H. Winter. *Physical Review B* **74**, 174431 (2006).

[325] U. Lders, A. Barthlmy, M. Bibes, K. Bouzehouane, S. Fusil, E. Jacquet, J.-P. Contour, J.-F. Bobo, J. Fontcuberta, and A. Fert. *Advanced Materials* **18**, 1733 (2006).

[326] U. Luders, M. Bibes, K. Bouzehouane, E. Jacquet, J. Contour, S. Fusil, J. Bobo, J. Fontcuberta, A. Barthelemy, and A. Fert. *Applied Physics Letters* **88**, 082505 (2006).

[327] Z. Szotek, W. M. Temmerman, A. Svane, L. Petit, P. Strange, G. M. Stocks, D. Kdderitzsch, W. Hergert, and H. Winter. *Journal of Physics: Condensed Matter* **16**, S5587 (2004).

[328] X. Zuo, S. Yan, B. Barbiellini, V. G. Harris, and C. Vittoria. *Journal of Magnetism and Magnetic Materials* **303**, e432 (2006).

[329] A. Miszczyk and K. Darowicki. *Anti-Corrosion Methods and Materials* **58**, 13 (2011).

[330] D. Fritsch and C. Ederer. *Physical Review B* **82**, 104117 (2010).

[331] Z. Li, E. Fisher, J. Liu, and M. Nevitt. *Journal of Materials Science* **26**, 2621 (1991).

[332] R. Rai, S. Wilser, M. Guminiak, B. Cai, and M. Nakarmi. *Applied Physics A: Materials Science & Processing* . Online First.

[333] S. Balaji, R. K. Selvan, L. J. Berchmans, S. Angappan, K. Subramanian, and C. Augustin. *Materials Science and Engineering: B* **119**, 119 (2005).

[334] G.H. and Jonker. *Journal of Physics and Chemistry of Solids* **9**, 165 (1959).

[335] U. Lüders, M. Bibes, S. Fusil, K. Bouzehouane, E. Jacquet, C. B. Sommers, J.-P. Contour, J.-F. Bobo, A. Barthélémy, A. Fert, and P. M. Levy. *Physical Review B* **76**, 134412 (2007).

[336] A. V. Ramos, M.-J. Guittet, J.-B. Moussy, R. Mattana, C. Deranlot, F. Petroff, and C. Gatel. *Applied Physics Letters* **91**, 122107 (2007).

[337] A. V. Ramos, T. S. Santos, G. X. Miao, M.-J. Guittet, J.-B. Moussy, and J. S. Moodera. *Physical Review B* **78**, 180402 (2008).

[338] R. H. Fowler and L. Nordheim. *Proceedings of the Royal Society of London. Series A* **119**, 173 (1928).

[339] F. Rigato, S. Piano, M. Foerster, F. Giubileo, A. M. Cucolo, and J. Fontcuberta. *Physical Review B* **81**, 174415 (2010).

[340] U. Lüders, M. Bibes, J.-F. m. c. Bobo, M. Cantoni, R. Bertacco, and J. Fontcuberta. *Physical Review B* **71**, 134419 (2005).

[341] F. Rigato, S. Estrad, J. Arbiol, F. Peir, U. Lders, X. Mart, F. Snchez, and J. Fontcuberta. *Materials Science and Engineering: B* **144**, 43 (2007).

[342] N. A. Zimbovskaya. *Journal of Applied Physics* **106**, 124101 (2009).

Publications

- *Electronic properties of bulk and thin film $SrRuO_3$: Search for the metal - insulator transition,*
  J. M. Rondinelli, N. M. Caffrey, S. Sanvito and N. Spaldin,
  Physical Review B. **78**, 155107 (2008).

- *Prediction of large bias-dependent magnetoresistance in all - oxide magnetic tunnel junctions with a ferroelectric barrier,*
  N. M. Caffrey, T. Archer, I. Rungger and S. Sanvito,
  Physical Review B. **83**, 125409 (2011).

- *Ge based spin-photodiodes for room temperature integrated detection of photons helicity,*
  R. Bertacco, C. Rinaldi, M. Cantoni, D. Petti, M. Leone, N. M. Caffrey and S. Sanvito,
  arXiv:1105.2908, Submitted.

- *$SrRuO_3/BaTiO_3/SrRuO_3$ and $Fe/BaTiO_3/Fe$ hetrostructures: exchange - correletion functional applicability,*
  N. M. Caffrey, T. Archer, S. Sanvito,
  in preparation.

- *Coexistance of giant tunneling electroresistance and magnetoresistance in an all-oxide magnetic tunnel junction,*
  N. M. Caffrey, T. Archer, I. Rungger and S. Sanvito,
  arXiv:1202.4919, Submitted.